

**APPLICATION OF COMPUTER SIMULATION APPROACHES
TO STUDY THE STRUCTURE AND PROPERTIES OF
POLYMERIC SYSTEMS**

by

ESTHER CÓRDOVA-MATEO

Supervised by

PROF. CARLOS ALEMÁN AND DR. OSCAR BERTRAN

A THESIS SUBMITTED FOR THE DEGREE OF DOCTOR OF PHILOSOPHY AT
UNIVERSITAT POLITÈCNICA DE CATALUNYA

BARCELONA, OCTOBER 2014



UNIVERSITAT POLITÈCNICA
DE CATALUNYA



All the investigations displayed throughout this dissertation has been supervised by Prof. Carlos Alemán (Departament d'Enginyeria Química at E.T.S. d'Enginyeria Industrial de Barcelona and Centre for Research in Nano-Engineering, Universitat Politècnica de Catalunya) and Dr. Oscar Bertran (Departament de Física Aplicada at Escola d'Enginyeria d'Igualada, Universitat Politècnica de Catalunya).

Computational work was carried out in IMEM (Innovación, Modelización e Ingeniería de (Bio)Materiales, Universitat Politècnica de Catalunya) and CESSA (Centre de Supercomputació de Catalunya) installations.

Financial support has been in charge of MICINN and FEDER projects (Grants MAT2009-09138 and MAT2012-34498), and the Generalitat de Catalunya (Grants 2009-SGR-925 and XRQTC).

The author of this Thesis has been grant recipient of Formación de Personal Investigador by Ministerio de Ciencia e Innovación BES-2010-033323.



Acta de qualificació de tesi doctoral

Curs acadèmic: 2014-2015

Nom i cognoms

Esther Córdova-Mateo

Programa de doctorat

Polímers i Biopolímers

Unitat estructural responsable del programa

Departament d'Enginyeria Química

Resolució del Tribunal

Reunit el Tribunal designat a l'efecte, el doctorand / la doctoranda exposa el tema de la seva tesi doctoral titulada *Application of Computer Simulation Approaches to Study the Structure and Properties of Polymeric Systems*.

Acabada la lectura i després de donar resposta a les qüestions formulades pels membres titulars del tribunal, aquest atorga la qualificació:

NO APTÉ

APROVAT

NOTABLE

EXCEL·LENT

(Nom, cognoms i signatura)		(Nom, cognoms i signatura)	
President/a		Secretari/ària	
(Nom, cognoms i signatura)	(Nom, cognoms i signatura)	(Nom, cognoms i signatura)	(Nom, cognoms i signatura)
Vocal	Vocal	Vocal	Vocal

_____, _____ d'/de _____ de _____

El resultat de l'escrutini dels vots emesos pels membres titulars del tribunal, efectuat per l'Escola de Doctorat, a instància de la Comissió de Doctorat de la UPC, atorga la MENCIO CUM LAUDE:

SÍ

NO

(Nom, cognoms i signatura)	(Nom, cognoms i signatura)
President de la Comissió Permanent de l'Escola de Doctorat	Secretari de la Comissió Permanent de l'Escola de Doctorat

Barcelona, _____ d'/de _____ de _____

*A Balbina y a Luis,
porque de alguna manera siempre viajáis conmigo.*

AGRADECIMIENTOS

Tras casi cinco años de dedicación a esta tesis; cinco años de aventuras y desventuras que no sólo han constituido un gran aprendizaje científico sino que también han supuesto un intenso crecimiento a nivel personal; llega uno de los momentos más importantes antes de finalizar esta etapa. El momento de poder plasmar mi gratitud a todos aquellos que me han acompañado en este viaje y que de una manera u otra han contribuido a que este sueño se haya hecho realidad.

A mis directores de tesis, Prof. Carlos Alemán y Dr. Oscar Bertran, por brindarme esta oportunidad y por confiar en mí a lo largo de estos años. Gracias por los conocimientos que me habéis transmitido, por enseñarme a ser más pragmática, por descubrirme el mundo de la química computacional, sin duda uno de los grandes hallazgos de mi vida, y sobre todo, gracias por vuestra paciencia y dedicación.

Al Dr. Juan Cortés por brindarme la oportunidad de realizar una estancia en el Laboratoire d'Analyse et d'Architecture des Systèmes en la Université Paul Sabatier y por abrirme las puertas al complejo mundo de los algoritmos de *networks*.

Gracias a todos los que han formado y/o forman parte del grupo IMEM: a los Drs. Manel Canales, David Curcó, Francisco Rodríguez-Ropero y Joan Torras, por ayudarme y poner a mi disposición sus conocimientos para poder seguir avanzando en alguna de las temáticas de mi tesis; a la Dra. Elaine Armelín y al Dr. Francesc Estrany, por iniciarme en el mundo de los polímeros conductores; al Dr. David Aradilla, por esas discusiones *pseudocientíficas* en los *breaks* de la tarde; al Dr. David Zanuy, per compartir amb mi la seva experiència professional, el fantàstic *thinker* . *£*, i les amenes hores de dinar; al Dr. Guillem Revilla, pels cafès a primera hora del matí on escoltava les meves *rallades* mentals tant a nivell de feina com a nivell personal, i sobre tot, pels bons consells que sempre m'ha donat; al Dr. Bruno Teixeira-Dias, por sus consejos y ese bacalao portugués a la brasa; al Dr. Daniel Ernesto López por su amistad, por todas esas horas de debates sin finalidad alguna con los que tanto disfruto y sobre todo por los buenos momentos que compartimos en estos años; a la Dra. Georgina Fabregat, per ser la meva companya de fatigues (així que t'he reservat un *bueco* una mica més endavant); a Silvana Marione, por los consejos estéticos de la portada y por esas horas de *pump* y TBC; a Mar Pérez-Madrugal, per la seva companyia i per ser un gran exemple de constància i sacrifici sempre amb un somriure a la boca, (Mar, moltes forces perquè en breu tindràs un merescudíssim títol de Dra. davant del teu nom).

A todos los compañeros \notin al grupo IMEM pero sí \subset en algún momento en el Departament d'Enginyeria Química de l'ETSEIB (*i.e.* Abdel, Helena, Ainhoa, Cristina, Sara, Yoli, Elena), gracias por las risas compartidas en cafés, comidas, cenas, *cubateos* y otros momentos varios.

Chema, Peje, gracias por casi toda una vida de amistad llena de buenos momentos, por esos viajes a *Mordor* y alrededores, por anécdotas mil y sobre todo por enseñarme a sintetizar en media frase a qué me dedico.

Laura, gracias por todas las risas que compartimos en Maristas y por mostrarme la luz llevándome a la facultad de Físicas el año que empecé Industriales.

Rosalía, gracias por una de esas amistades que no se pierde a pesar de lo poco que conseguimos coexistir en el mismo punto espacio-temporal. Y gracias también por compartir conmigo ese extraño sentido del humor que te caracteriza.

Gema, gracias por una década y pico de cafés en el bar de física y cervezas o *gin tonics* donde se terciara, gracias por tu amistad y esa manera tan *gema* de preocuparte por mí.

Ana, Jordi, gracias por muchos momentos, guardo con especial cariño esas noches en Butsenit y Fuentesstrún mirando las estrellas. Y muchas gracias por vuestro apoyo, una de las sorpresas más gratas que he tenido en estos últimos años.

Georg, ara sí, moltes gràcies per ser com ets, per la teva amistat i per la teva companyia durant aquest *Viaje a lo desconocido*, en el que hem après, hem guanyat i hem perdut. Sens dubte has estat un dels millors descobriments en aquests anys de recerca.

David, gracias, muchas gracias por todo lo que hemos compartido, por tu continuo e incondicional apoyo con el que he contado, cuento y espero seguir contando desde ese *soy la castaña asesina que te espera en cada esquina*. Sin duda eres unos de los pilares que ha hecho que esta tesis salga adelante, así que de nuevo, muchas gracias *loki*.

Gerard, mil gràcies per ensenyar-me a no encallar-me, a tirar cap endavant i a veure que *¡eh chipirón!, todos los días sale el sol chipirón*. Gràcies per compartir amb mi la teva particular visió del món, i sobre tot, gràcies per fer-me riure i somriure. *Sol*, sense tu acabar aquesta tesis hauria estat una mica bastant més complicat.

A los Ochoa-García, por esos viajes surrealistas en furgoneta, por tantas anécdotas y momentos inolvidables y sobre todo por ser parte de la familia, gracias.

A mi *tía del alma*, gracias por estar siempre ahí, por transmitirme tu pasión por la enseñanza y sobre todo por ese regalo llamado Luís.

A mi hermano, Javi de ti he aprendido el significado de serenidad, pragmatismo y coherencia, gracias por estar siempre ahí.

A mi padre, por inculcarme su amor a las ciencias y sobre todo por su paciencia infinita y su saber hacer.

A mi madre, por haberme enseñado que la vida es para los valientes y que siempre hay que *tirar pa'lante*. Gracias por estar siempre ahí, por tu apoyo y por enseñarme que con trabajo y constancia cualquier meta es posible. Por esto y mucho más, este trabajo también te pertenece.

A las personas que, aunque no aparecen aquí con nombres y apellidos, han estado presentes de alguna forma durante el desarrollo de este trabajo y han hecho posible que hoy vea la luz.

A todos mi eterno agradecimiento.

*‘Agradece a la llama su luz, pero no olvides el pie del candil que
constante y paciente la sostiene en la sombra’*

Rabindranath Tagore

ABSTRACT

The study at the nanoscopic level of the polymeric systems is a keystone for a deeper understanding of their internal structure and properties, not only at nanometric scale but also at macroscopic level. The disciplines involved in this scientific field are diverse, including areas such as chemistry, physics, material science, biology and statistics among others. The aforementioned fields converge in a scientific and technologic central branch called nanotechnology. In the last decades, nanotechnology based on polymeric systems has aroused a great interest among the scientific community, as is clearly evidenced by the huge amount of scientific publications and applications developed within this area. However, the experimental complexity for the development of new devices and the economical limitations devoted to this end are barriers that let us think about the use of alternative approaches in this scientific field. In the face of this endeavors, the application of computer simulation methodologies to must be taken into account.

The principal focus of this Thesis is the study at the atomic and molecular level of some polymeric systems through theoretical methodologies based on quantum and classical mechanics formalisms. Such methods allow us to support and understand some chemical and physical observables as well as to analyze and describe these systems at their structural level.

Within the framework of the application of the atomic and molecular simulation methodologies, this Thesis could be divided mainly in three main research lines. The first one focusses on the study and evaluation of the detection ability of some conducting polymers with the final aim of developing a sensor based on these materials. Second line is devoted to the application of atomistic molecular dynamics simulation for the investigation of dynamical and structural properties inside cation exchange membranes. Finally, the last working line of this Thesis is centered on the study at electronic and atomic level of dendritic molecules and dendronized polymers through both quantum and classical mechanics formalisms.

This dissertation is organized in seven chapters followed by a final section (*Chapter 8*) which consists on the final discussion and the conclusions derived from this Thesis. In *Chapter 1* a general introduction about the polymeric systems studied in this Thesis as well as a brief *state of the art* of some of their most prominent applications is performed. *Chapter 2* includes the main objectives of this Thesis. In *Chapter 3* the mathematical formalism of the methodologies used for the computational simulations presented in the following

four chapters is described. Section 3.1 is devoted to the quantum mechanics formalism while section 3.2 describes the key aspects of molecular dynamics methodology.

Chapter 4 is devoted to evaluate the detection ability of different conducting polymers when they interact with dopamine, a neurotransmitter related to some neurological disorders (section 4.1); and morphine, a potent analgesic psychoactive drug (section 4.2). The examination of conducting polymers sensitivity to the analyte detection was carried out *via* inspection of their ability to form secondary interactions (*i.e.* weak and strong hydrogen bonds, π -stacking interactions), which was examined using quantum mechanical calculations.

Chapter 5 reflects the investigations of the influence of the electric field strength (section 5.1) and the temperature (section 5.2) in the dynamical and structural properties of cationic exchange membranes, which were conducted using molecular dynamics simulations. The studies performed in this chapter were essentially focused on the analysis of hydronium transport mechanism, internal structural rearrangements of the membrane and the characteristics of the hydration shell surrounding the diffused hydronium ions.

The following two chapters are devoted to study dendritic molecules and dendronized polymers using quantum and classical mechanics formalisms, respectively. In *Chapter 6* the structural properties and molecular interactions occurring in a particular class of dendronized polymers are analyzed. In section 6.1 a characterization of the inter and intramolecular non bonded interactions of two interacting polymer chains was carried out in an attempt to relate atomistic information to the rheological response of these large cylindrical-shape objects. In section 6.2 the internal structure and solvent absorption ability of positively charged dendronized polymers of generations one to six are investigated and compared with those of their neutral analogues.

Chapter 7 focusses on the study of both dendrimers and dendronized polymers based on all-thiophene dendrons through quantum mechanics and molecular dynamics. Section 7.1 analyzes the electronic properties of symmetric and unsymmetric all-thiophene dendrimers containing up to 45 thiophene rings in neutral and oxidized state. Finally, in section 7.2 the internal organization of second and third generation macromonomers and dendronized polymers based on all-thiophene dendrons is studied using density functional theory calculations and classical molecular dynamics simulations, respectively.

'Begin at the beginning,' the King said gravely, 'and go on till you come to the end: then stop.'

Lewis Carrol, *Alice's Adventures in Wonderland* (1865)

TABLE OF CONTENTS

ACKNOWLEDGMENTS	v
ABSTRACT	ix
TABLE OF CONTENTS.....	xiii
LIST OF ABBREVIATIONS	xix
LIST OF SYMBOLS.....	xxiii
LIST OF FIGURES.....	xxv
LIST OF TABLES.....	xxxiii
LIST OF SCHEMES	xxxvii

CHAPTER 1

INTRODUCTION	1
1.1. APPROACH TO SOME POLYMERIC SYSTEMS.....	4
1.1.1. CONDUCTING POLYMERS.....	5
1.1.1.1. Electronic Structure of Conducting Polymers. Key Concepts.....	6
1.1.1.2. Mechanism of Electronic Transport	6
1.1.1.3. Possible Uses of Conducting Polymers	7
1.1.2. POLYMERIC ION EXCHANGE MEMBRANES	8
1.1.2.1. Classification of Polymeric Ion Exchange Membranes	9
1.1.2.2. Ion Exchange Membrane Properties.....	9
1.1.2.3. Factors Contributing to Ionic Transport.....	9
1.1.3. DENDRITIC POLYMERS.....	10
1.1.3.1. Dendrimers and Dendrons.....	11
<i>Dendrimer Properties</i>	12
1.1.3.2. Dendronized Polymers.....	12
<i>Structural Aspects of Dendronized Polymers</i>	13
1.2. THE ROLE OF COMPUTATIONAL CHEMISTRY IN THE STUDY OF POLYMERIC SYSTEMS	14
1.3. APPLICATIONS.....	15
1.3.1. CHEMICAL SENSORS BASED ON CONDUCTING POLYMERS	15
1.3.1.1. Conducting Polymer Based Dopamine Sensor	17
1.3.1.2. Conducting Polymer Based Morphine Sensor	19
1.3.2. ION EXCHANGE MEMBRANE FOR ELECTRODIALYSIS	20
1.3.2.1. Styrene-divinylbenzene Based Membranes	21
1.3.3. ELECTRONIC DEVICES BASED ON DENDRITIC POLYMERS	22
1.3.3.1. Polythiophene Based Dendrimers and Dendronized Polymers	22
1.3.4. Dendronized Polymers. Applications in Bioscience.....	23
REFERENCES.....	25

CHAPTER 2	
OBJECTIVES	37
CHAPTER 3	
METHODOLOGY	41
3.1. QUANTUM MECHANICAL METHODS	43
3.1.1. THE HAMILTONIAN OPERATOR	44
3.1.2. THE BORN-OPPENHEIMER APPROXIMATION	45
3.1.3. THE WAVE FUNCTION	45
3.1.3.1. Slater determinant	46
3.1.3.2. The LCAO Basis Set Approach	46
3.1.3.3. Gaussian Functions	47
<i>STO-nG Basis Set</i>	48
<i>Split-Valence Basis Set</i>	48
<i>Polarized Basis Sets</i>	48
<i>Diffuse Functions</i>	49
<i>Basis Set Superposition Error</i>	49
3.1.3.4. Closed-Shell and Open-Shell systems	50
3.1.4. HARTREE-FOCK APPROXIMATION	50
3.1.5. ELECTRON DENSITY COMPUTATION	51
3.1.6. AB INITIO CALCULATIONS	51
3.1.6.1. Hartree-Fock Method	51
3.1.6.2. Post Hartree-Fock Methods	51
<i>Møller-Plesset Perturbation Theory</i>	52
<i>Coupled Cluster Method</i>	52
3.1.7. SEMIEMPIRICAL METHODS	53
3.1.8. DENSITY FUNCTIONAL THEORY METHODS	54
3.1.8.1. Hohenberg-Kohn Theorem	54
3.1.8.2. The Self-Consistent Kohn-Sham Equations	54
3.1.8.3. Exchange-Correlation Functionals	55
<i>Local Density Approximation</i>	55
<i>Generalized Gradient Approximation</i>	56
<i>Hybrid Functionals</i>	56
<i>Long-Range Corrected Hybrid Functionals</i>	56
3.1.9. TIME DEPENDENT DENSITY FUNCTIONAL THEORY	57
3.2. MOLECULAR DYNAMICS METHODS	57
3.2.1. EQUATIONS OF MOTION	58
3.2.2. THE FORCE FIELD	58
3.2.3. INTEGRATION OF MOTION EQUATIONS	60
3.2.4. KEY DETAILS IN FORMALISM	62
3.2.4.1. Boundary Conditions	62
3.2.4.2. Truncation of Interactions	63
3.2.4.3. Thermodynamic Ensembles	63
3.2.4.4. Temperature Control	64

<i>Berendsen Temperature Coupling</i>	64
<i>Nosé-Hoover Temperature Coupling</i>	65
3.2.4.5. Pressure Control.....	65
3.2.5. SIMULATION CONVERGENCE.....	66
3.2.6. PROPERTIES MEASUREMENTS.....	66
REFERENCES	69

CHAPTER 4

DETECTION BASED ON CONDUCTING POLYMERS	73
4.1. ULTRATHIN FILMS OF POLYPYRROLE DERIVATIVES FOR DOPAMINE DETECTION	75
4.1.1. INTRODUCTION	76
4.1.2. METHODS	78
4.1.2.1. Materials	78
4.1.2.2. Electrochemical Synthesis, Polymerization Kinetics, and Thickness of the Films	78
4.1.2.3. Preparation of Au Colloidal Nanoparticles.....	79
4.1.2.4. Detection Assays	80
4.1.2.5. Quantum Mechanical Calculations	80
4.1.3. RESULTS AND DISCUSSION.....	81
4.1.3.1. Electropolymerization Kinetics	81
4.1.3.2. Detection of Dopamine	82
4.1.3.3. Stability and Limit of Detection	85
4.1.3.4. Modeling of the Interaction PNMPy··DQ	86
4.1.3.5. Modeling of the Interaction PNCPy··DQ	89
4.1.4. CONCLUSIONS	91
4.2. ELECTROACTIVE POLYMERS FOR THE DETECTION OF MORPHINE	92
4.2.1. INTRODUCTION	93
4.2.2. METHODS	96
4.2.2.1. Computational Details.....	96
4.2.2.2. Experimental Methods.....	97
<i>Materials</i>	97
<i>Preparation</i>	97
<i>Electrochemical measurements for detection of MO</i>	97
4.2.3. RESULTS AND DISCUSSION	98
4.2.3.1. Theoretical calculations: interaction patterns and binding energies.....	98
4.2.3.2. Electrochemical behavior of the electroactive polymers.....	103
4.2.3.3. Voltammetric detection of morphine.....	103
4.2.3.4. Stability for the voltammetric detection of morphine.....	107
4.2.4. CONCLUSIONS	109
REFERENCES	111

CHAPTER 5

HYDRONIUM TRANSPORT IN CATION EXCHANGE MEMBRANES	117
---	------------

TABLE OF CONTENTS

5.1. ELECTRIC FIELD-INDUCED TRANSPORT OF HYDRONIUM IONS IN P(S-DVB) CATION EXCHANGE MEMBRANES	119
5.1.1. INTRODUCTION.....	120
5.1.2. METHODS AND BACKGROUND	122
5.1.2.1. Molecular System and Computational Details.....	122
5.1.2.2. Diffusion Coefficients.....	124
5.1.2.3. Velocity Distribution Functions and Temperature.....	125
5.1.2.4. Conductivity.....	125
5.1.3. RESULTS AND DISCUSSION.....	126
5.1.3.1. Diffusion of Hydronium Cations	126
5.1.3.2. Velocity of Hydronium Cations.....	129
5.1.3.3. Average Transport Velocities and Conductivity.....	131
5.1.3.4. Interactions	133
5.1.4. CONCLUSIONS	136
5.2. INFLUENCE OF THE TEMPERATURE ON THE PROTON TRANSPORT IN P(S-DVB) MEMBRANES	137
5.2.1. INTRODUCTION.....	138
5.2.2. METHODS.....	140
5.2.3. RESULTS AND DISCUSSION.....	142
5.2.3.1. Effect of the Temperature on the Structure.....	142
5.2.3.2. Effect of the Temperature on the Dynamics and Transport of Hydronium Ions	146
5.2.3.3. Effect of the Temperature on the Hydration of Charged Groups.....	156
5.2.4. CONCLUSIONS	161
REFERENCES	163

CHAPTER 6

ATOMISTIC PROPERTIES OF DENDRONIZED POLYMERS	169
6.1. INTERACTIONS IN DENDRONIZED POLYMERS: INTRAMOLECULAR DOMINATES INTER-MOLECULAR	171
6.1.1. INTRODUCTION.....	172
6.1.2. METHODS.....	175
6.1.2.1. Molecular Models	175
6.1.2.2. Computational Details	177
6.1.3. RESULTS AND DISCUSSION.....	178
6.1.3.1. Temporal evolution and stability of the simulated complexes	178
6.1.3.2. Hydrogen Bonds.....	181
6.1.3.3. π , π -Interactions.....	185
6.1.3.4. Experimental Investigation of the Stability of PG4.....	188
6.1.3.5. Density Profiles, Cross-Sectional Radius and Molecular Length	189
6.1.4. CONCLUSIONS	192
6.2. INTERNAL STRUCTURE OF CHARGED DPs	193
6.2.1. INTRODUCTION	194

6.2.2. METHODS	197
6.2.2.1. Molecular Models	197
6.2.2.2. Computational Details	197
6.2.3. RESULTS AND DISCUSSION	198
6.2.3.1. Analysis of <i>de</i> PGg Conformation	198
6.2.3.2. Penetration of Water Molecules	204
6.2.3.3. Water ··· <i>de</i> PGg Interactions	205
6.2.4. CONCLUSIONS	208
REFERENCES	211

CHAPTER 7

THIOPHENE-BASED DENDRIMERS AND DENDRONIZED POLYMERS	215
7.1. PROPERTIES OF OLIGOTHIOPHENE DENDRIMERS	217
7.1.1. INTRODUCTION	218
7.1.2. METHODS	220
7.1.3. RESULTS AND DISCUSSION	222
7.1.3.1. Conformation and Geometric Parameters	222
7.1.3.2. Ionization Potential	223
7.1.3.3. Lowest π - π^* Transition Energy	227
7.1.3.4. Frontier Orbitals	230
7.1.3.5. Modeling ϵ_g of all-Thiophene Dendrimers	233
7.1.4. CONCLUSIONS	235
7.2. INTERNAL ORGANIZATION OF MACROMONOMERS AND DPs BASED ON TH DENDRONS	236
7.2.1. INTRODUCTION	237
7.2.2. METHODS	240
7.2.2.1. Quantum Mechanical Calculations	240
7.2.2.2. Classical Force Field Simulations	240
7.2.3. RESULTS AND DISCUSSION	241
7.2.3.1. MG2 and MG3 Macromonomers	241
7.2.3.2. PG2 and PG3 DPs: Structural characterization	247
7.2.3.3. π - π Stacking Interactions in PG2 and PG3	250
7.2.4. CONCLUSIONS	253
REFERENCES	255

CHAPTER 8

FINAL DISCUSSION AND CONCLUSIONS	263
8.1. FINAL DISCUSSION	265
8.2. CONCLUSIONS	270
ANNEX. LIST OF SCHEMES	275

LIST OF ABBREVIATIONS

Abbreviation	Meaning
μ VT	Grand Canonical Ensemble
3MT	3-methylthiophene
ADF	Amsterdam Density Functional
AFM	Atomic Force Microscopy
AMBER	Assisted Model Building and Energy Refinement
AuNPs	Au Colloidal Nanoparticles
au	Atomic Units
B3LYP	Functional of three parameters of Lee, Yang and Parr
B3PW91	Functional of three parameters of Perdew-Wang's 1991
B95	Becke's 1995 functional
B97-D	Grimme's functional including dispersion
BP86-D	Grimme's functional including dispersion correction
BSSE	Basis Set Superposition Error
CA	Chronoamperometry
cam-B3LYP	Long-range correction modification to the B3LYP functional
CC	Coupled Cluster
CEM	Cation Exchange Membrane
CP	Conducting Polymer
Cp	Counterpoise
CV	Cyclic Voltammetry
CVHS	Completely Variable Hydration Shells
DA	Dopamine
DFS	Dynamic Frequency Sweeps
DFT	Density Functional Theory
DP	Dendronized Polymer
DQ	Dopamine- <i>o</i> -quinone
DVB	Divinylbenzene
EDA	Energy Decomposition Analysis
EDOT	3,4-ethylenedioxythiophene
EP	Electroactive Polymer
FF	Force Field

LIST OF ABBREVIATIONS

Abbreviation	Meaning
GCEs	Glassy Carbon Electrodes
GGA	Generalized Gradient Approximation
GTO	Gaussian Type Orbitals
HF	Hartree-Fock
HOMO	Highest Occupied Molecular Orbital
IEM	Ion Exchange Membrane
IP	Ionization Potential
ITO	Indium Tin Oxide
KT	Koopmans' Theorem
LCAO	Linear Combination of Atomic Orbitals
LDA	Local Density Approximation
LES	Loss of Electrostaticity
LSDA	Local Spin Density Approximation
LUMO	Lowest Unoccupied Molecular Orbital
LYP	Functional of Lee, Yang and Parr
MB	Macromolecular Backbone
MD	Molecular Dynamics
MG	Macromonomer
MINDO	Modified Intermediated Neglect of Differential Overlap
MIP	Molecularly Imprinted Polymer
MK	Merz-Kollman Scheme
MM	Molecular Mechanics
MO	Morphine
MP	Møller Plesset
MPW1K	Adamo and Barone functional
MSD	Mean Square Displacement
NCPy	N-(2-cyanoethyl)pyrrole
NMPy	N-methylpyrrole
NPH	Isobaric-Isoenthalpic Ensemble
NPT	Isobaric-Isothermal Ensemble
NVE	Microcanonical Ensemble
NVT	Canonical Ensemble
OLED	Organic Light Emitting Diode
P(S-DVB)	Poly(styrene-co-divinyl benzene)
P3MT	Poly(3-methylthiophene)
P86	Perdew's 1986 functional
PANI	Polyaniline
PBC	Periodic Boundary Conditions

Abbreviation	Meaning
PBE	Perdew-Burke-Ernzerhof functional
PBS	Phosphate-Buffered Solution
PEDOT	Poly(3,4-ethylenedioxythiophene)
PG _g	Dendronized Polymer of generation <i>g</i>
PL	Local Perdew's 1981 functional
PME	Particle Mesh of Ewald
PNCPy	Poly-[N-(2-cyanoethyl)pyrrole]
PNMPy	Poly(N-methylpyrrole)
PPy	Polypyrrole
PTh	Polythiophene
PVHS	Partially Variable Hydration Shells
PW91	Perdew-Wang's 1991 functional
Py	Pyrrole
QM	Quantum Mechanics
RESP	Restrained Electrostatic Potential
RMSD	Root Mean Square Deviation
RPP	Recurrent Potential Pulses
SCF	Self-Consistent Field
sd	Sum of the Squared Differences
SHS	Static Hydration Shells
SOMO	Single Occupied Molecular Orbital
STO	Slater Type Orbitals
TD-DFT	Time Dependent Density Functional Theory
TEM	Transmission Electron Microscopy
Th	Thiophene
UA	United Atom
UHF	Unrestricted Hartree-Fock
UMP	Unrestricted Møller Plesset
VWN	Functional of Vosko, Wilk and Nusair
wB97X	Chai and Head-Gordon long-range corrected functional
wB97X-D	Functional from Head-Gordon
X3LYP	Functional of Xu and Goddard

LIST OF SYMBOLS

Symbol	Meaning
$\langle \Delta\theta \rangle$	Average angle formed by the helical axes of two polymeric chains
$\langle \Delta E \rangle$	Average interaction energy
$\langle \rho \rangle$	Average density
$\langle D \rangle$	Average distance between the centers of mass
$\langle E \rangle$	Average potential energy
$\langle L \rangle$	Average molecular length
$\langle R \rangle$	Average cross-sectional radius
ΔE	Relative energy
ΔE_b	Binding energy
ΔE_{disp}	Dispersion energy
ΔE_{int}	Interaction energy in the EDA
ΔE_{oi}	Orbital interaction energy
ΔE_{pauli}	Pauli repulsion energy
ΔE_{SOMO}	Relative energy of the SOMO
ΔV_{el}	Electrostatic interaction energy
ΔQ	Electroactivity
D	Diffusion coefficient (referring to Chapter 5)
	Distance between center of masses (referring to Chapter 6)
D_{\parallel}	Diffusion coefficient in direction parallel to an electric field
D_{\perp}	Diffusion coefficient in direction perpendicular to an applied electric field
d_{H-O}	H \cdots O distance
E_z	Electric field in z -direction
$f(\mathbf{v})$	Maxwell velocity distribution function
$f(v_{\parallel})$	Maxwell distribution function in direction parallel to the applied electric field
$f(v_{\perp})$	Maxwell distribution function in direction perpendicular to the applied electric field
G	Viscoelastic moduli
g	Generation number
$g_{X-Y}(\mathbf{r})$	Partial radial distribution function of X-Y pairs
J	Flow
j	Current density

LIST OF SYMBOLS

Symbol	Meaning
j_{max}	Current at the highest potential
K_{drag}	Electro-Osmotic drag coefficient
L_{av}	Average end-to-end distance
l	Thickness
N_h	Number of hydronium ions
N_S	Hydration shell number
N_w	Number of waters
n_α	Number of $\alpha - \alpha$ linkages
$P(\theta)$	Angular probability distribution function
$\overline{p_z^{CS}}$	averaged projection of the C-S bond into the direction of the electric field
Q_{pol}	Polymerization charge consumed
$R_{\alpha-\alpha}$	Average inter-ring distance for $\alpha - \alpha$ linkages
$R_{\alpha-\beta}$	Average inter-ring distance for $\alpha - \beta$ linkages
RT-D	System composed of two DPs, one rotated + translated a distance D from the second
T	Global temperature of simulated system
T_{\parallel}	Temperature of the hydronium ions in the directions parallel to the electric field
T_{\perp}	Temperature of the hydronium ions in the directions perpendicular to the electric field
T_h	Overall temperature of the hydronium ions
T-D	System composed of two DPs, one translated a distance D from the second
V_R	Unoccupied volume
\overline{v}_{\parallel}	Average transport velocity in the direction parallel to the applied electric field
v_0	Peak shifting velocity
W_{ox}	Mass of polymer deposited in the electrode
\mathcal{E}_g	Lowest $\pi-\pi^*$ transition energy
θ	Polymerization time
θ_A, θ_B	Inter-ring dihedral angles
θ_{D-D}	Dihedral angle associated with dimerization
$\theta_{\alpha-\alpha}$	Average inter-ring dihedral angles for the $\alpha - \alpha$ linkages
$\theta_{\alpha-\beta}$	Average inter-ring dihedral angles for the $\alpha - \beta$ linkages
τ_{res}	Residence time
φ_d	Degree of tilting
χ	Conductivity
$\chi_{\alpha-\alpha}$	Fraction of $\alpha - \alpha$ linkages
$\chi_{\alpha-\beta}$	Fraction of $\alpha - \beta$ linkages
ω	Frequency

LIST OF FIGURES

CHAPTER 1 INTRODUCTION

FIGURE 1.1. Schematic representations of (a) linear, (b) branched, and (c) cross-linked molecular structures. Circles designate individual repeat units.....	4
FIGURE 1.2. Formation of polaron and bipolaron in polyheterocycles.....	7
FIGURE 1.3. Band structure of a polymer chain (a) in neutral state, (b) containing one polaron, (c) containing a bipolaron, and (d) with bipolaron bands.	8
FIGURE 1.4. Schematic representation of cationic ion exchange membrane.	10
FIGURE 1.5. Schematic representation of some subclasses of dendritic polymers.	11
FIGURE 1.6. Structural components of a G4 Dendrimer	11
FIGURE 1.7. Schematic representation of a chemical sensor.....	15
FIGURE 1.8. Schematic representation of the electrodiagnosis principle.....	20
FIGURE 1.9. Schematic representation of sulfonated poly(styrene-co-divinylbenzene) membrane. (a) Chemical representation of a sulfonated pseudounit. (b) Scheme of membrane system including the cross-links.....	21

CHAPTER 3 METHODOLOGY

FIGURE 3.1. Schematic representation of the idea of periodic boundary conditions.	62
FIGURE 3.2. The global MD Algorithm	67

CHAPTER 4 DETECTION BASED ON CONDUCTING POLYMERS

4.1. ULTRATHIN FILMS OF POLYPYRROLE DERIVATIVES FOR DOPAMINE DETECTION

FIGURE 4.1. Variation of the weight per unit of area of PNCPy (◆) and PNMPy (◆) deposited on stainless steel from 10 mM monomer solutions in acetonitrile with 0.1 M LiClO ₄ at a constant potential of 1.40 V against the polymerization charge.	81
FIGURE 4.2. Cyclic voltammograms for the oxidation of (a) PNMPy- and (b) PNMPy/AuNP-modified GCEs in the absence and presence of different DA concentrations (from 1 to 10 mM). Scan rate: 100 mV/s. Initial and final potential: -0.40 V; reversal potential: +0.80 V. For each graphic, labels a-e refer to DA concentrations of 0, 1, 3, 6, and 10 mM, respectively.	82
FIGURE 4.3. Cyclic voltammograms for the oxidation of (a) PNCPy- and (b) PNCPy/AuNP-modified GCEs in the absence and presence of different DA concentrations (from 1 to 10 mM). Scan rate: 100	

mV/s. Initial and final potential: -0.40 V; reversal potential: +0.80 V. For each graphic, labels a-e refer to DA concentrations of 0, 1, 3, 6, and 10 mM, respectively.....	83
FIGURE 4.4. Variation of (a) the oxidation potential and (b) the current density for the oxidation peak of DA against the neurotransmitter concentration measured using PNMPy- (▲), PNMPy/AuNP- (■), PNCPy- (△), and PNCPy/AuNP-modified GCEs (□).....	84
FIGURE 4.5. Control voltammograms for 10 consecutive oxidation-reduction cycles of (a) PNMPy/AuNP- and (b) PNCPy/AuNP-modified GCEs in the presence of 10 mM DA.....	85
FIGURE 4.6. Variation of the loss of electrostability (LES) after 10 consecutive oxidation-reduction cycles for PNMPy- (▲), PNMPy/AuNP- (■), PNCPy- (△), and PNCPy/AuNP-modified GCEs (□) against the DA concentration.....	86
FIGURE 4.7. Cyclic voltammograms for the oxidation of (a) PNMPy- and PNMPy/AuNP-modified GCEs and (b) PNCPy- and PNCPy/AuNP-modified GCE in the presence of a 100 μM DA concentration. Scan rate: 100 mV/s. Initial and final potential: -0.40 V; reversal potential:+0.80 V. The second consecutive oxidation-reduction cycle is also displayed for the PNMPy-modified GCE.....	86
FIGURE 4.8. Four structures of lower energy derived from quantum mechanical calculations for (a) 1-NMPy···DQ, (b) 2-NMPy···DQ, and (c) 3-NMPy···DQ complexes. (d) Atomistic model proposed for the detection of DA by PNMPy.....	87
FIGURE 4.9. Structures derived from quantum mechanical calculations for (a) 1-NCPy···DQ, (b) 2-NCPy···DQ, and (c) 3-NCPy···DQ complexes.(d) Atomistic model proposed for the detection of DA by PNCPy.....	90
4.2. ELECTROACTIVE POLYMERS FOR THE DETECTION OF MORPHINE	
FIGURE 4.10. Geometries of the (a) 3-EDOT···MO, (b) 3-3MT···MO, (c) 3-Py···MO, (d) 3-NMPy···MO and (e) 3-NCPy···MO complexes with $\Delta E < 3$ kcal/mol derived from QM calculations. C-H···O and C-H···N interactions are indicated by pink lines, aromatic···aromatic staking by yellow lines and N-H···O hydrogen bonds by green lines. The H···O, H···N and aromatic···aromatic (centers of masses) distances are displayed in Å.....	100
FIGURE 4.11. Control voltammograms for the oxidation of Pt coated with P3MT, PEDOT, PPy, PNMPy and PNCPy in TRIS solutions with pH= (a) 2, (b) 7 and (c) 8.5. The voltammogram recorded for the uncoated Pt electrode has been included for comparison. Initial and final potentials: -0.50 V; reversal potential: 1.60 V; scan rate: 50 mV·s ⁻¹	104
FIGURE 4.12. Control voltammograms for the oxidation of Pt coated with P3MT (a), PEDOT (b), PPy (c), PNMPy (d) and PNCPy (e) in TRIS (solid lines) and MO-containing TRIS (dashed lines) solutions at pH= 2 and incubation times of 3, 12 and 24 h.....	105
FIGURE 4.13. Difference between the incubated and blank samples in terms of electroactivity, ΔQ in % (left), and the current density at the reversal potential Δj_{max} in mA/cm ² (right) for the five studied EPs at pH= (a) 2, (b) 7 and (c) 8.5.....	106
FIGURE 4.14. Control voltammograms for the oxidation of Pt coated with P3MT (a), PEDOT (b), PPy (c), PNMPy (d) and PNCPy (e) in TRIS (solid lines) and MO-containing TRIS (dashed lines) solutions at pH= 7 and incubation times of 3, 12 and 24 h.....	107
FIGURE 4.15. Control voltammograms for the oxidation of Pt coated with P3MT (a), PEDOT (b), PPy (c), PNMPy (d) and PNCPy (e) in TRIS (solid lines) and MO-containing TRIS (dashed lines) solutions at pH= 8.5 and incubation times of 3, 12 and 24 h.....	108

FIGURE 4.16. Control voltammograms for Pt coated with P3MT (a) and PNCPy (b) after ten consecutive oxidation-reduction cycles in TRIS (solid lines) and MO-containing TRIS (dashed lines) solutions at pH= 2 and 7 and the indicated incubation times.109

CHAPTER 5

HYDRONIUM TRANSPORT IN CATION EXCHANGE MEMBRANES

5.1. ELECTRIC FIELD-INDUCED TRANSPORT OF HYDRONIUM IONS IN P(S-DVB) CATION EXCHANGE MEMBRANES

FIGURE 5.1. Schematic view of the simulation system: the polymer and the sulfonate groups are represented by the solid purple matrix and the yellow spheres, respectively. Water molecules and hydronium ions are explicitly represented. A magnification of a small zone, in which the polymer is described by sticks, is provided at the bottom.123

FIGURE 5.2. (a) Mean squared displacement (MSD) of hydronium ions from its origin in the P(S-DVB) membrane as a function of the simulation time for selected electric fields. (b) Variation of D , D_{\parallel} and D_{\perp} , against the electric field.127

FIGURE 5.3. Snapshots (3.5 and 6.0 ns on the left and right, respectively) of the membrane from MD simulations using external electric fields of (a) 0.1 V/nm and (b) 1.0 V/nm. General view (top) and amplification of a selected zone (bottom) are displayed in each case.128

FIGURE 5.4. Velocity distribution functions $f(\mathbf{v})$, $f(v_{\parallel})$ and $f(v_{\perp})$ of hydronium ions derived from MD simulations for selected electric fields (circles). The red line represents the fitting of velocity distribution functions to the corresponding Maxwell distribution functions: (5.6) - (5.8).129

FIGURE 5.5. Variation of the temperature parameters of the hydronium ions (*i.e.* overall temperature, and temperature in the directions parallel and perpendicular to the electric field) against the electric field.131

FIGURE 5.6. Variation of the protonic (a) current density and (b) conductivity against the applied electric field for the hydrated P(S-DVB) membrane. The dashed line in graphic (a) refers to a current density of 0.00 C/cm²·s.132

FIGURE 5.7. Partial distribution functions of S \cdots OT pairs for selected electric fields.134

FIGURE 5.8. Variation of the number of (a) strong and (b) weak sulfonate \cdots hydronium interactions with their life time. Strong interactions refer to those in which the distance between the sulfur atom of the sulfonate and oxygen of the hydronium is lower than 3.9 Å, while in weak interactions such distance is defined within the 3.9–4.4 Å interval.134

FIGURE 5.9. (a) Partial distribution functions of the intermolecular OT \cdots OW pairs, where OT and OW refer to the oxygen of the hydronium and water molecules, respectively, calculated for selected electric fields. (b) Variation of the population of hydration shells containing 0, 1, 2, 3, 4, 5 and 6 water molecules at a OT \cdots OW distance lower than 4.80 Å, against the electric field.135

FIGURE 5.10. (a) Variation of the percentage of hydronium ions showing each of the three types of hydration shells identified in this work against the electric field. Hydration shells have been categorized according to the variability in the number of coordinated water molecules (N_S) and the exchangeability of such water molecules: (i) N_S changes and at least one of the water molecules of the hydration shell are exchanged (black squares) during the MD trajectory; (ii) N_S and the water molecules remain fixed during the whole MD trajectory (red squares); and (iii) N_S remains constant but at least one water molecule is exchanged during the MD trajectory (blue squares). (b) Percentage of exchanged water molecules in hydration shells of type (i) and (ii) (*i.e.* black and blue squares in Figure 5.8a) against the residence time τ_{res} for selected electric fields.136

5.2. INFLUENCE OF THE TEMPERATURE ON THE PROTON TRANSPORT IN P(S-DVB) MEMBRANES

FIGURE 5.11. Sulfonated P(S-DVB) with water molecules and hydronium ions studied in this work. Color code: water in blue, organic membrane in green, sulfonate groups in yellow, and hydronium ions in purple. 141

FIGURE 5.12. Radial distribution functions of C2···C2 and CH···CH backbone pairs (g_{C2-C2} and g_{CH-CH} , respectively) calculated at different temperatures (from 280 to 360 K) in absence and presence ($E_z = 0.70 \text{ Vnm}^{-1}$) of electric field. Labels used to identify the atoms are displayed in Scheme 5.1. Profiles clearly indicate that the structure of the polymeric membrane is not affected by the temperature, independently of the electric field. 143

FIGURE 5.13. Radial distribution functions of S···S, S···OW, and S···OT pairs ($g_{S-S}(r)$, $g_{S-OW}(r)$, and $g_{S-OT}(r)$, respectively) calculated at different temperatures (from 280 to 360 K) in the absence and presence of electric field ($E_z = 0.70 \text{ Vnm}^{-1}$). Labels used to identify the atoms are displayed in Scheme 5.1. 144

FIGURE 5.14. Radial distribution functions of OT···OW pairs (g_{OT-OW}), where OT and OW refer to the oxygen atoms of hydronium and water, respectively, calculated at different temperatures (from 280 to 360 K) in absence and presence of electric field ($E_z = 0.70 \text{ Vnm}^{-1}$). Labels used to identify the atoms are displayed in Scheme 5.1. Profiles clearly indicate that the hydration of hydronium ions slightly decreases with increasing temperature. 145

FIGURE 5.15. Temporal evolution of the averaged projection of the C–S bond into the direction of the electric field (\hat{z} -axis) calculated at different temperatures (from 280 to 360 K) in absence and presence ($E_z = 0.70 \text{ Vnm}^{-1}$) of electric field. The C–S bonds tend to align in the direction of the electric field. 145

FIGURE 5.16. (a) Variation of the average density against the temperature for the membrane in the absence and presence ($E_z = 0.70 \text{ Vnm}^{-1}$) of an electric field. Averages were calculated considering the last 2 ns of each trajectory. (b) Logarithmic variation of the accessible volume to a given spherical penetrant (unoccupied volume, in %) against the radius of the penetrant (R) for sulfonated P(S-DVB) at different temperatures. The accessible volume has been determined using the microstructures provided by MD simulations in the absence and presence ($E_z = 0.70 \text{ Vnm}^{-1}$) of an electric field (solid and dashed line, respectively). Water and hydronium molecules have not been considered for the evaluation of the accessible volume. 146

FIGURE 5.17. Velocity distributions $f(v)$ (right), $f(v_{||})$ (center) and $f(v_{\perp})$ (left) of hydronium ions at temperatures from 280 to 360 K (row 1 to 5) in absence (top) and presence (bottom) of electric field. The red lines represent the fitting of the velocity distribution functions to the corresponding Maxwell distributions functions (5.14-5.16). 148

FIGURE 5.18. (a) Variation of the temperature of the hydronium ions (T_h) against the temperature of simulation (T) in the absence (filled squares) and presence of electric field (empty squares). The linear behavior is illustrated by displaying the linear fittings (solid and dashed lines, respectively). (b) Temporal evolution of the net displacement of the hydronium ions at the studied temperatures in the absence (solid lines) and presence (dashed line) of external electric field. (c) Temporal evolution of the net displacement in the \hat{z} -direction of the hydronium ions at the studied temperatures in the absence (solid lines) and presence (dashed line) of external electric field. 150

FIGURE 5.19. Variation of the temperature of the hydronium ions in the directions parallel and perpendicular to the electric field (red and blue, respectively) against the temperature of simulation (T) in absence (filled squares) and presence of electric field (empty squares). The linear behavior is illustrated by displaying the linear fittings (solid and dashed lines, respectively). 151

- FIGURE 5.20.** (a) Mean square deviation (MSD; (5.22)) of hydronium ions at different temperatures in the absence (solid lines) and presence (dashed line) of external electric field. The MSD in directions (b) parallel (MSD_{\parallel} ; (5.25)) and (c) perpendicular (MSD_{\perp} ; (5.27)) to the applied electric field are also displayed.154
- FIGURE 5.21.** Variation of the population of hydration shells containing N_w water molecules at a (a) OT \cdots OW and (b) S \cdots OW distance lower than 3.5 and 5.0 Å, respectively. (c) Variation of the population of sulfonate groups with a number of hydronium ions (N_h) at a S \cdots OT distance lower than 4.8 Å. Solid and dashed lines correspond to simulations in the absence and presence of an external electric field, respectively.157
- FIGURE 5.22.** Probability distribution functions for observing (a) OT–OW and (b) S–OW vectors at an angle θ with the water dipole in the first solvation shell of hydronium and sulfonate groups (*i.e.*, $r < 3.5$ Å and $r < 5.0$ Å, respectively) at different temperatures. (c) Probability distribution functions for observing the S–OT vector at an angle θ with the hydronium cations located at a S \cdots OT distance lower than 4.8 Å at different temperatures. Solid and dashed lines correspond to simulations in the absence and presence of an external electric field, respectively.158
- FIGURE 5.23.** (a) Variation of the percentage of hydronium ions showing each of the four situations identified in terms of the first solvation shell (see text) against the electric field: $N_w=0$ (hydroniums without hydration shell); CVHS (completely variable hydration shell); PVHS (partially variable hydration shell); and SHS (static hydration shell).(b) Amount of hydronium \cdots water interactions (*i.e.*, considering water molecules included in the first hydration shell) against the residence time (τ_{res}) at different temperatures. Solid and dashed lines correspond to simulations in the absence and presence of an external electric field, respectively159
- FIGURE 5.24.** (a) Variation of the percentage of sulfonate ions showing each of the four situations identified in terms of the first solvation shell (see text) against the electric field: $N_w=0$ (sulfonate without hydration shell); CVHS (completely variable hydration shell); PVHS (partially variable hydration shell); and SHS (static hydration shell).(b) Amount of sulfonate \cdots water interactions (*i.e.*, considering water molecules included in the first hydration shell) against the residence time (τ_{res}) at different temperatures. Solid and dashed lines correspond to simulations in the absence and presence of external electric field, respectively.159
- FIGURE 5.25.** Amount of hydronium \cdots sulfonate interactions (*i.e.* considering ions within a cut-off distance of 4.0 Å) against the residence time (τ_{res}) at different temperatures. Solid and dashed lines correspond to simulations in absence and presence of external electric field, respectively.161

CHAPTER 6

ATOMISTIC PROPERTIES OF DENDRONIZED POLYMERS

6.1. INTERACTIONS IN DENDRONIZED POLYMERS: INTRAMOLECULAR DOMINATES INTERMOLECULAR

- FIGURE 6.1.** Atomistic conformation obtained in ref. 18 for PG4. Detailed views in the section (top) and in the molecular axis (bottom) are displayed at the right.175
- FIGURE 6.2.** Scheme representing the relative positions of the two PG4 chains in (a) T-*D* and (b) RT-*D* systems. In order to clarify the representation, only a few branched dendrons of each chain are explicitly depicted.176
- FIGURE 6.3.** Temporal evolution of the interchain distance D for (a) T-*D* and (b) RT-*D* systems during the re-equilibration and production runs (before and after the grey dashed line, respectively).178
- FIGURE 6.4.** Average interchain distance D against the average energy E for T-*D* and RT-*D* systems. .179

- FIGURE 6.5.** Partial distribution functions of (N-)H \cdots O pairs belonging to (a) different PG4 molecules or (b) to the same PG4 g_{H-O}^d and g_{H-O}^s , respectively for T-D (left) and RT-D (right) systems..... 181
- FIGURE 6.6.** Schematic view displaying representative intermolecular hydrogen bonds in T-D and RT-D dimers: (a) strong hydrogen bond; and (b) weak interaction. The strength of the weak inter-dendron interaction represented in (b) is limited by the reduced mobility of the involved groups, which are constrained to remain at a distance of ~ 4 Å..... 182
- FIGURE 6.7.** Partial distribution functions of (N-)H \cdots O pairs, $g_{H-O}^s(r)$, for an isolated PG4 chain. .. 183
- FIGURE 6.8.** Schematic view displaying representative intramolecular hydrogen bonds in T-D and RT-D dimers: (a) strong hydrogen bond between dendrons of different repeat units; (b) strong hydrogen bond between dendrons of the same repeat unit; and (c) weak interaction. The strength of the weak inter-dendron interaction represented in (c) is limited by the reduced mobility of the involved groups, which are constrained to remain at a distance of ~ 4 Å. Different colors in the amplified view have been used to identify dendrons belonging to different repeat units..... 184
- FIGURE 6.9.** Schematic view displaying representative intramolecular π,π -interactions in T-D and RT-D dimers: (a) sandwich configuration, and (b) T-shaped configuration. Different colors in the amplified view have been used to identify dendrons belonging to different repeat units. 187
- FIGURE 6.10.** Schematic view displaying representative intermolecular π,π -interactions in T-D and RT-D dimers: (a) T-shaped configuration, and (b) sandwich configuration. Different colors in the amplified view have been used to identify dendrons belonging to different chains..... 188
- FIGURE 6.11.** Viscoelastic moduli as a function of frequency at 110 °C for sample PG4. Different symbols correspond to different instruments and annealing times. ○: G' measured with a strain controlled rheometer ARES; ◐: G' measured after annealing the sample for one week; ◑: G' measured with a stress controlled rheometer Physica. ▽: G'' measured with a strain controlled rheometer ARES; ▿: G'' measured after annealing the sample for one week, ▾: G'' measured with a stress controlled rheometer Physica. The lines are viscoelastic moduli data converted from creep tests (Physica)..... 189
- FIGURE 6.12.** Density profile for a PG4 chain in (a) T-D and (b) RT-D dimers representing the density (ρ) against the distance to the backbone measured using the vector perpendicular to the helix axis (r). The profile displayed for each DP corresponds to an average considering different cross-sections within all the analyzed snapshots. The density profile derived from simulations of an isolated PG4 chain is included for comparison..... 190
- FIGURE 6.13.** Comparison of a single PG4 chain extracted from the last snapshot of simulations on T-40 dimer (right), T-70 dimer (middle) and an isolated chain (left). The backbone corresponds to the central solid lines. Differences in the average molecular length, L , are represented..... 191
- 6.2. INTERNAL STRUCTURE OF CHARGED DPs**
- FIGURE 6.14.** a) Chemical formula of PG $_g$ and $dePG_g$ with $g=1, 2, 3, 5$. b) Schemes illustrating the definition of the branching angles α_i used to examine the organization of PG $_g$ and $dePG_g$ dendrons. 195
- FIGURE 6.15.** Atomistic conformations for PG $_g$ (left) and $dePG_g$ (right). The complete axial projections represent the whole calculated systems, the number of repeat units being $N=150$ for PG $_g$ with $g=1-4$, 100 for PG5 and $dePG_g$ with $g=1-4$, and 75 for PG6 and $dePG_g$ with $g=5-6$. The magnified axial projection involves 20 repeat units in all cases, whereas the equatorial projection involves 5 ($g=1-4$) or 10 ($g=5-6$) repeat units. Figures of PG $_g$ and $dePG_g$ are only comparable for the same g since the zoom decreases with increasing g 200
- FIGURE 6.16.** Density profiles for the $dePG_g$ and PG $_g$ models representing the density (ρ) against the distance to the backbone measured using the vector perpendicular to the helical axis (r). The profile

- displayed for each model corresponds to an average considering different cross-sections within a given snapshot. Data were obtained by averaging over the snapshots taken during the last 10 ns of the MD relaxation runs.201
- FIGURE 6.17.** Radial distribution function of the dendrons of the external layer for (a) *dePGg* and (b) *PGg* models measured through the end ammonium (g_{N-b}) and Boc (g_{Boc-b}) groups, respectively.203
- FIGURE 6.18.** (a) Density profile for the *dePGg* models representing the water density (ρ_w) against the distance to the backbone measured using the vector perpendicular to the helical axis (r). The profile displayed for each model corresponds to an average considering different cross-sections within a given snapshot. Data were obtained by averaging over the snapshots recorded during the last 10 ns of the MD relaxation runs. The profile displayed for *dePG5* has been taken from reference [19]. It should be noted that decay of ρ_w at large values of r is due to boundary effects of the spherical solvent cap used for the simulations. (b) Graphical representation of the cross point (r_p ; filled squares) between the DP and water density profiles and the degree of water penetration (W_p ; empty squares) against g for *dePGg*.204
- FIGURE 6.19.** Superposition of the water (red) and *dePGg* (black) density profiles. Profiles were calculated profiles as a function of the radial distance r from the DP backbone, measured using the vector perpendicular to the helical axis.206
- FIGURE 6.20.** Radial distribution function of (a) $H_w \cdots O$ (g_{H_w-o}) and (b) $O_w \cdots H(-N)$ (g_{O_w-H}) pairs for hydrated *dePGg*. H_w and O_w refer to the hydrogen and oxygen atoms of water molecules, respectively.207
- FIGURE 6.21.** Angular distribution functions for water $\cdots dePGg$ hydrogen bonding interactions: (a) $\angle O_w-H_w \cdots O$; and (b) $\angle O_w \cdots H-N$. Hydrogen bonds were defined using a $H \cdots O$ cutoff distance of 2.50 Å209

CHAPTER 7

THIOPHENE-BASED DENDRIMERS AND DENDRONIZED POLYMERS

7.1. PROPERTIES OF OLIGOTHIOPHENE DENDRIMERS

- FIGURE 7.1.** Chemical structure of the dendrimers studied in this work.219
- FIGURE 7.2.** Molecular structures of a) 18Th and 21Th dendrimers in both the neutral (left) and oxidized (right) states derived from (U)B3LYP/6-311++G(d,p) geometry optimizations and b) 42Th and 45Th dendrimers in both the neutral (left) and oxidized (right) states derived from (U)B3LYP/6-31G(d) geometry optimizations.226
- FIGURE 7.3.** Variation of a) IP^{KT} and b) $IP^{\Delta SCF}$ with $1/n$, where n is the number of thiophene rings. Filled and empty squares correspond to the values derived from (U)B3LYP/6-31G(d) and (U)B3LYP/6-311++G(d,p) calculations, respectively. Solid and dashed lines show the linear behavior of the values predicted at these levels of theory.227
- FIGURE 7.4.** Variation of \mathcal{E}_g derived from DFT calculations against $1/n$, where n is the number of thiophene rings, for nTh . The \mathcal{E}_g values determined with both 6-31G(d) (filled symbols) and 6-311++G(d,p) (empty symbols) are displayed. Solid and dashed lines were obtained by linear regressions: $y = a_1x + a_2$228
- FIGURE 7.5.** Plot of the \mathcal{E}_g values derived from DFT and TD-DFT calculations for nTh dendrimers against the experimental ones. Theoretical values were computed by using the 6-311++G(d,p) basis set for $n \leq 21$ and the 6-31G(d) basis set for $n > 21$. The lines, the equations, and regression coefficients correspond to the linear regressions.228

FIGURE 7.6. Variation of \mathcal{E}_g (eV per thiophene ring) derived from TD-DFT calculations against $1/n$, where n is the number of thiophene rings, for n Th. The \mathcal{E}_g values determined by using both the 6-31G(d) (filled symbols) and 6-311++G(d,p) (empty symbols) are displayed. Solid and dashed lines were obtained by linear regressions $y = a_1x + a_2$.	230
FIGURE 7.7. Comparison of HOMO and LUMO for unsymmetric dendrimers in a) the neutral and b) the oxidized state.	231
FIGURE 7.8. Comparison of HOMO and LUMO for symmetric dendrimers in a) the neutral and b) the oxidized state.	232
7.2. INTERNAL ORGANIZATION OF MACROMONOMERS AND DPs BASED ON TH DENDRONS	
FIGURE 7.9. Chemical structure of: (a) MG2 and MG3 macromonomers; and (b) PG2 and PG3 DPs.	239
FIGURE 7.10. Electrostatic parameters determined for the repeat unit of (a) PG2 and (b) PG3. Charges in parenthesis correspond to hydrogen atoms, where $\times n$ refers to the number n of equivalent hydrogens, while charges for carbon, oxygen and sulfur atoms are out of the parenthesis. Charges for equivalent thiophene rings are omitted for clarity. In the repeat unit of PG3, equivalent pairs of thiophene rings have been labelled using letters.	242
FIGURE 7.11. Potential energy surface $E = E(\theta, \theta')$ calculated for MG2. The dihedral angles θ and θ' are displayed in Figure 7.9a	244
FIGURE 7.12. (a) Molecular representation, (b) HOMO, (c) LUMO and (d) electron density of the MG2-1 (left) and MG3-1 (right) structures.	246
FIGURE 7.13. Atomistic conformations for PG2 (left) and PG3 (right). The complete axial projections represent the whole calculated systems, the number of repeat units being $N = 150$. The magnified axial projection involves 20 repeat units in all cases, whereas the equatorial projection involves 10 repeat units.	248
FIGURE 7.14. (a) Density profile for PG2 and PG3 representing the density (ρ) against the distance to the backbone measured using the vector perpendicular to the helical axis (r). The profile displayed for each DP corresponds to an average considering different cross-sections within a given snapshot. (b) Distribution of peripheral methyl groups (g_{Me-b}) as a function of the distance from the backbone for PG2 and PG3. All data were obtained by averaging over 2500 snapshots taken during the last 20 ns of the MD relaxation runs	250
FIGURE 7.15. Partial radial distribution functions for the pairs of centers of masses of Th rings of (a) PG2 and (b) PG3. Data in were obtained by averaging over 2500 snapshots taken during the last 20 ns of the MD relaxation runs.	252

LIST OF TABLES

CHAPTER 1 INTRODUCTION

TABLE 1.1. Names, Structures, and Conductivities of some Common Conducting Polymers.	5
TABLE 1.2. Various Sensors and their Applications.	17
TABLE 1.3. CPs Modified Electrodes Successfully Applied in DA Sensing.	18

CHAPTER 4 DETECTION BASED ON CONDUCTING POLYMERS

4.1. ULTRATHIN FILMS OF POLYPYRROLE DERIVATIVES FOR DOPAMINE DETECTION

TABLE 4.1. Relative Energy (ΔE), Binding Energy (ΔE_{int}), and Inter-Ring Dihedral Angles (θ_A and θ_B) of the Four Structures of Lower Energy Calculated for n -NMPy \cdots DQ Complexes, where n Ranges from 1 to 3.	88
TABLE 4.2. Relative Energy (ΔE), Binding Energy (ΔE_{int}), and Inter-Ring Dihedral Angles (θ_A and θ_B) of the Four Structures of Lower Energy Calculated for n -NCPy \cdots DQ Complexes, where n Ranges from 1 to 3.	91

4.2. ELECTROACTIVE POLYMERS FOR THE DETECTION OF MORPHINE

TABLE 4.3. Relative Energy (ΔE ; in kcal/mol) and Binding Energy after Correct the Basis Set Superposition Error (ΔE_B ; in kcal/mol) for 3-EDOT \cdots MO, 3-3MT \cdots MO, 3-Py \cdots MO, 3-NMPy \cdots MO And 3-NCPy \cdots MO Complexes (see Figure 4.10) at the UMP2/6-31+G(d,p) Level.	99
TABLE 4.4. Energy Decomposition Analysis Terms and Relative Energy of the SOMO with respect to that of 3-CPy, in kcal mol $^{-1}$, and Hirshfeld Charges of MO.	102

CHAPTER 5 HYDRONIUM TRANSPORT IN CATION EXCHANGE MEMBRANES

5.1. ELECTRIC FIELD-INDUCED TRANSPORT OF HYDRONIUM IONS IN P(S-DVB) CATION EXCHANGE MEMBRANES

TABLE 5.1. Diffusion Coefficients of Hydronium Ions in P(S-DVB) Membrane Applying Selected External Electric fields.	127
TABLE 5.2. Temperature Parameters, Peak Shifting Velocity and Average Transport Velocity in the Direction Parallel to the Applied Electric Field of Hydronium Ions in P(S-DVB) Membrane Applying Selected External Electric Fields.	130

5.2. INFLUENCE OF THE TEMPERATURE ON THE PROTON TRANSPORT IN P(S-DVB) MEMBRANES

TABLE 5.3. Average Transport Velocity in the Direction Parallel to the Applied Electric Field of Hydronium Ions ($\bar{v}_{\parallel h}$ and $\bar{v}_{\parallel h}^*$) and Water Molecules ($\bar{v}_{\parallel w}$), Electro-Osmotic Drag Coefficient (K_{drag}), Proton Conductivity (γ), and Diffusion Coefficients of Hydronium Ions (D_h , $D_{h,\parallel}$ and $D_{h,\perp}$) in the P(S-DVB) Membrane at Different Temperatures..... 149

TABLE 5.4. Average Transport Velocity in the Direction Parallel ($\bar{v}_{\parallel w}$) and Perpendicular ($\bar{v}_{x,w}$ and $\bar{v}_{y,w}$) to the Electric Field of Water Molecules in P(S-DVB) Membrane at Different Temperatures..... 152

CHAPTER 6

ATOMISTIC PROPERTIES OF DENDRONIZED POLYMERS

6.1. INTERACTIONS IN DENDRONIZED POLYMERS: INTRAMOLECULAR DOMINATES INTERMOLECULAR

TABLE 6.1. Average Value of the Energy and Structural Properties in T-D and RT-D dimers: $\langle D \rangle$, Average Distance between the Centers of Mass of the two PG4 Chains; $\langle E \rangle$, Average Potential Energy; $\langle \Delta E \rangle$, Average Interaction Energy; $\langle \Delta \theta \rangle$, Average Angle Formed by the Helical Axes of the two PG4 Chains; $\langle R \rangle$, Average Cross-Sectional Radius; $\langle L \rangle$, Average Molecular Length, and $\langle \rho \rangle$, Average Density.. 180

TABLE 6.2. Amount of Intramolecular and Intermolecular Hydrogen Bonds ($H \cdots O$ Distance $< 2.5 \text{ \AA}$ and $\angle N-H \cdots O \geq 120^\circ$) found in the Simulated Systems: Average Values and Standard Deviations. The Concentration of Nitrogen Atoms (in %) forming Hydrogen Bonds is also Displayed.. 185

TABLE 6.3. Amount of intramolecular and intermolecular π,π -interactions (T-shaped configuration: $R \leq 5.5 \text{ \AA}$ and $60^\circ < \beta < 120^\circ$; sandwich configuration: $R \leq 4.5 \text{ \AA}$ and $\beta < 30^\circ$) found in the simulated systems: average values and standard deviations. The concentration of aromatic rings (in %) involved in π,π -interactions is also displayed. 186

6.2. INTERNAL STRUCTURE OF CHARGED DPs

TABLE 6.4. Average Values of α_i (degrees; see Figure 6.14b) Calculated for $dePG_g$ and PG_g with $g = 2, 3, 4, 5$ and 6 . Standard Deviations are also Displayed..... 199

TABLE 6.5. Average Height per Repeat Unit (h), Average Density (ρ_{av}) and Radius (R and R^*) for $dePG_g$ and PG_g . Relative Elongation upon Deprotection and Maximum Water Penetration Degree (W_p) for $dePG_g$ 201

CHAPTER 7

THIOPHENE-BASED DENDRIMERS AND DENDRONIZED POLYMERS

7.1. PROPERTIES OF OLIGOTHIOPHENE DENDRIMERS

TABLE 7.1. Average Inter-Ring Distances (\AA) for the $\alpha - \alpha$ and $\alpha - \beta$ Linkages ($R_{\alpha-\alpha}$ and $R_{\alpha-\beta}$, respectively; see Scheme 7.1) of nT and nT^+ Dendrimers Calculated at the (U)B3LYP/6-31G(d) and (U)B3LYP/6-311++G(d,p) Levels. Standard Deviations (\AA) are Included. 224

TABLE 7.2. Average Inter-Ring Dihedral Angles ($^\circ$) for the $\alpha - \alpha$ and $\alpha - \beta$ Linkages ($\theta_{\alpha-\alpha}$ and $\theta_{\alpha-\beta}$, respectively; see Scheme 7.1) and Inter-Ring Dihedral Angle Associated with Dimerization of Symmetric

Systems (θ_{D-D}) of nT and $nT+$ Dendrimers Calculated at the (U)B3LYP/6-31G(d) and (U)B3LYP/6-311++G(d,p) Levels. Standard Deviations ($^{\circ}$) are Included.225

TABLE 7.3. \mathcal{E}_g Values (eV) Predicted by DFT and TD-DFT Calculations for nT th Dendrimers. The Values Obtained with the Largest Basis Set are Displayed for Each System (*i.e.* 6-311++G(d,p) for $n \leq 21$ and 6-31G(d) for $n > 21$). Experimental Data (eV) Available for nT th are also Displayed.229

TABLE 7.4. Coefficients a_i Obtained by Minimizing the Squared Difference between the \mathcal{E}_g Values Derived from DFT and TD-DFT Calculations (see Table 7.3) and the Mathematical Models Proposed in Equations (7.1) and (7.2).234

7.2. INTERNAL ORGANIZATION OF MACROMONOMERS AND DPs BASED ON TH DENDRONS

TABLE 7.5. Representative Minimum Energy Conformations Calculated for MG2 at the wB97X-D/6-311++G(d,p) Level. Dihedral Angles (θ, θ', ϕ and ϕ' ; in degrees), Bond Lengths ($R_{\alpha\alpha}$ and $R_{\alpha\beta}$; in Å) and Relative Energy (ΔE ; in kcal/mol) are Displayed.245

TABLE 7.6. Representative Minimum Energy Conformations Calculated for MG3 at the wB97X-D/6-311++G(d,p) Level. Dihedral Angles (θ, θ', ϕ and ϕ' ; in degrees), Bond Lengths ($R_{\alpha\alpha}$ and $R_{\alpha\beta}$; in Å) and Relative Energy (ΔE ; in kcal/mol) are Displayed.247

TABLE 7.7. Properties and Interactions Calculated by MD Simulations for PG2 and PG3. Regarding to Properties, L_{av} , R and ρ_{av} Refer to the Average End-to-End Distance, the Radius and the Average Density, respectively. Regarding to Interactions, the Average Number of π - π Stacking Interactions with T-Shaped and Sandwich Configurations in a Polymer Chain made of 150 Repeat Units are supplied. ...249

LIST OF SCHEMES

CHAPTER 1 INTRODUCTION

SCHEME 1.1. Schematic representation of an example of a polymer 3

CHAPTER 4 DETECTION BASED ON CONDUCTING POLYMERS

4.1. ULTRATHIN FILMS OF POLYPYRROLE DERIVATIVES FOR DOPAMINE DETECTION

SCHEME 4.1. Oxidation of DA to DQ..... 80

SCHEME 4.2. Oxidation of DQ to DC 84

4.2. ELECTROACTIVE POLYMERS FOR THE DETECTION OF MORPHINE

SCHEME 4.3. Molecular structure of MO..... 94

SCHEME 4.4. Molecular structure of the investigated CPs. 95

CHAPTER 5 HYDRONIUM TRANSPORT IN CATION EXCHANGE MEMBRANES

5.2. INFLUENCE OF THE TEMPERATURE ON THE PROTON TRANSPORT IN P(S-DVB) MEMBRANES

SCHEME 5.1. Chemical structure and atom types of the species included in the simulated system: P(S-DVB) membrane, water molecules, and hydronium ions. 141

CHAPTER 6 ATOMISTIC PROPERTIES OF DENDRONIZED POLYMERS

6.1. INTERACTIONS IN DENDRONIZED POLYMERS: INTRAMOLECULAR DOMINATES INTERMOLECULAR

SCHEME 6.1. Chemical structure of PG4. 173

SCHEME 6.2. Average distance between N-H atom and each of the six oxygen atoms surrounding it 183

CHAPTER 7 THIOPHENE-BASED DENDRIMERS AND DENDRONIZED POLYMERS

7.1. PROPERTIES OF OLIGOTHIOPHENE DENDRIMERS

SCHEME 7.1. Representation of $R_{\alpha-\alpha}$, $R_{\alpha-\beta}$, $\theta_{\alpha-\alpha}$ and $\theta_{\alpha-\beta}$ parameters in 3Th dendrimer 222

SCHEME 7.2. Schematic molecular representation of 90Th dendrimer 235

7.2. INTERNAL ORGANIZATION OF MACROMONO-MERS AND DPs BASED ON Th DENDRONS	
SCHEME 7.3. Chemical structure of the dendron (3Th) used to construct MG2.....	243
SCHEME 7.4. Chemical structure of the dendron (7Th) used to construct MG3.....	247
SCHEME 7.5. Chemical structure of the DP with $g = 4$ studied in reference [89].....	251
SCHEME 7.6. DP studied in references [86,87].....	251
SCHEME 7.7. Parameters used to define the sandwich and T-shaped configurations.....	253

CHAPTER 1

INTRODUCTION

'The history of science, like the history of all human ideas, is a history of irresponsible dreams, of obstinacy, and of error. But science is one of the very few human activities — perhaps the only one — in which errors are systematically criticized and fairly often, in time, corrected. This is why we can say that, in science, we often learn from our mistakes, and why we can speak clearly and sensibly about making progress there.'

Karl Popper, *Conjectures and Refutations: The Growth of Scientific Knowledge* (1963)

CHAPTER 1

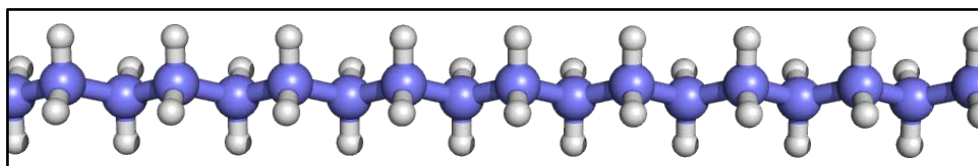
INTRODUCTION

Since the beginning of time natural polymers have been one of the building blocks of life, in the sense that all classes of living organisms are composed of them. However, it was not until the beginning of the 20th century when the origin of polymer science could be considered.

Polymer science was born in the development area of great industrial laboratories due to the need to make and understand some of these materials (*e.g.* plastics, rubber, adhesives, fibers, and coatings), and only much later came to academic world. Because of the wide range of applications that present these compounds, polymer science has become one of the most interdisciplinary fields, which combines chemistry, physics, chemical engineering, material science, and other areas as well. Within this context, modern scientific research tools have made possible the determination of their molecular structures and the synthesis of numerous new polymeric materials with a huge spectrum of possibilities and applications in a great amount of different technological areas [1].

The term polymer comes from the classical Greek words *poly* (meaning “many”) and *meros* (meaning “parts”). Chemically, a polymer is an extremely large molecule (macromolecule) built up by the repetition of small chemical units (see Scheme 1.1) [2].

Key aspects that determine the macroscopic properties of polymers include molecular weight and molecular weight distribution, the organization and configuration of the atoms down the polymer chain, the physical structure of the chain, *etc.* Moreover,



Scheme 1.1

polymers could be classified in several ways; *i.e.* by how the molecules are synthesized, by their molecular structure, by their chemical family, or by their thermal behavior. In view of the foregoing one could guess the huge variability of polymeric systems existing nowadays. However, the aim of this introduction is not an exhaustive description about all kind of polymers and their corresponding properties or applications, but a brief inspection about the main features of polymeric systems studied in this work.

The following section 1.1 is focused on some of the main structural and physical properties of the polymeric systems studied in this Thesis: conducting polymers (CP), polymeric ion exchange membranes (IEM), and dendritic polymers. Section 1.2 is devoted to the role of computational chemistry in the study of some properties of the aforementioned systems, and finally, the last section of this chapter is a review of some applications of these materials.

1.1. APPROACH TO SOME POLYMERIC SYSTEMS

The molecular structure of polymer chains is one of the key elements which determine macroscopical properties of these systems. According to their molecular structure these compounds could be classified on four major types: *linear*, *branched*, *cross-linked* and *dendritic* systems.

Linear polymers are those in which the repeat units are joined together end to end in single chains forming long chains (see Figure 1.1-a). *Branched polymers* are made of relatively short polymer chains covalently bonded to the primary backbone of the macromolecule (see Figure 1.1-b). In *cross-linked polymers*, adjacent linear chains are joined one to another at various positions by covalent bonds, as represented in Figure 1.1-c. Often, this crosslinking is accomplished by additive atoms or molecules that are covalently bonded to the chains [3]. Finally, the *dendritic polymers* could be considered as open, covalent assemblies of branch cells. This special kind of macromolecules has been recently recognized as the fourth major class of polymeric architecture due to the unique repertoire of new properties that these systems manifest [4]. In section 1.1.3 a deeper description of the topological properties of this polymeric species is performed.

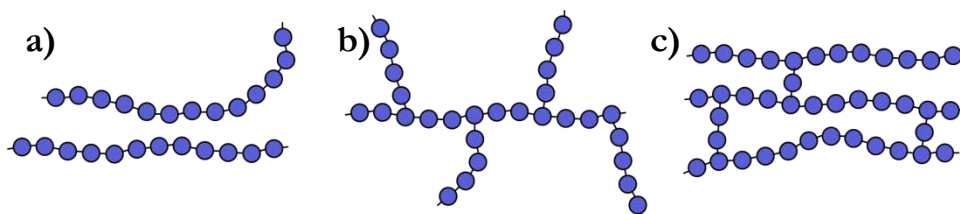


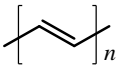
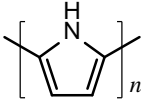
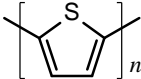
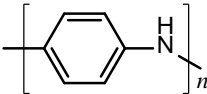
Figure 1.1. Schematic representations of (a) linear, (b) branched, and (c) cross-linked molecular structures. Circles designate individual repeat units.

The molecular architectures previously mentioned appear in the polymeric systems studied in this Thesis. Concretely, works based on CPs present both linear (Chapter 4) and dendritic (Chapter 7) structures; polymer systems studied for IEM applications (Chapter 5) exhibit cross-linked architecture; and finally, Chapter 6 is devoted to a specific subclass of the dendritic architecture: dendronized polymers (DPs).

1.1.1. CONDUCTING POLYMERS

Prior to the 70's, polymeric materials were essentially considered as insulators due to their high resistivity. However, Shirakawa *et al.* [5] reported in 1977 that the conductivity of polyacetylene increases by more than 10 orders of magnitude upon chemical doping. Following the case of polyacetylene, other polymers such as polypyrrole (PPy), polythiophene (PTh) or polyaniline (PANI) have been reported as CPs. Table 1.1 shows the chemical structure of these compounds and their conductivities. The large number of studies developed during the last decades to these unique class of polymers, have opened a new field in materials science extending over solid state and theoretical physics, synthetic chemistry, and device engineering [6].

Table 1.1. Names, Structures, and Conductivities of some Common Conducting Polymers.

Name	Chemical Structure	Conductivity (Scm ⁻¹)
Polyacetylene		~1000
Polypyrrole (PPy)		~40 – 100
Polythiophene (PTh)		~10 – 100
Polyaniline (PANI)		~1 – 100

CPs are mainly organic compounds that have an extended π -orbital system, through which electrons can move from one end of the molecule to the other [7]. The density and mobility of electrons along the π -bonds of the conjugated chain¹, determine the degree of conductivity of the polymer [8].

¹ Organic chain of alternating double and single bonded sp² hybridized atoms.

It is worth noting that the ability of electrons to move along the conjugated chain (that infers the high conductivity to these materials), is mainly achieved after being doped by either an oxidizing or reducing dopant agent [9,10].

1.1.1.1. ELECTRONIC STRUCTURE OF CONDUCTING POLYMERS. KEY CONCEPTS

Some aspects of the electronic structure that play a relevant role in the context of CPs are the ionization potential, the electron affinity, the width of the highest occupied valence band or lowest unoccupied conduction band², and the band gap [11]. In the following lines these parameters will be defined for a deeper understanding of results reported in Chapters 4 and 7.

The *ionization potential* determines whether a given electron acceptor (oxidizing agent) is able to ionize at least partly the polymer chain. *Electron affinity* plays an equivalent role with respect to the reducing case [11].

The *width of the highest occupied valence band or the lowest unoccupied band*, is a measure of the extent of electronic delocalization along the polymer chain. It can be strongly correlated with the mobility of possible charge carriers in that band [11].

The *band gap* is defined as the energy gap between the valence and conduction bands (*i.e.* difference between HOMO and LUMO values), and is an indicative of the intrinsic electrical properties of the polymer. Above 3 eV, the polymer can be considered as insulator. For band gap values smaller than 3 eV, the polymer is described as a semiconductor with electrical conductivities depending mainly on the actual value of the band gap [11].

1.1.1.2. MECHANISM OF ELECTRONIC TRANSPORT

CPs studied in this Thesis have been PPy, PTh and some of their derivatives. These polyheterocyclic macromolecules belong to the *non-degenerate* ground state polymer class; that is, the ground state of such polymers corresponds to a single geometric structure (aromatic-like structure) with lower energy than that of the corresponding resonance quinoid-like structure.

In the neutral state the conjugated backbone of CPs is uncharged and they present aromatic-like structure. After oxidation process, CPs can either lose an electron from one of the bands or can localize the charge over a small segment of the chain. Localizing the charge causes a local distortion due a change in geometry (quinoid-like structure), which requires some energy from the polymer [12-14]. However, the generation of this local geometry decreases the ionization energy of the polymer chain and increases its electron affinity making it more able to accommodate the newly formed charge. This method

² Within the molecular orbital theory the highest occupied molecular orbital, so-called HOMO, is equivalent to the maximum value of the valence band; while the lowest unoccupied molecular orbital, LUMO, corresponds to the minimum value of conduction band.

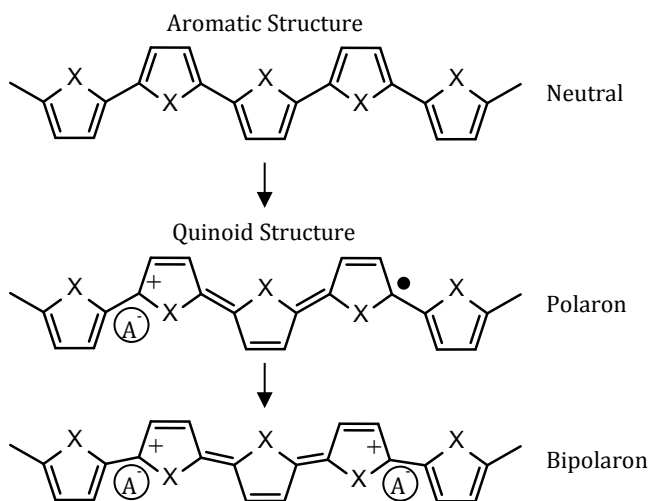


Figure 1.2. Formation of polaron and bipolaron in polyheterocycles.

increases the energy of the polymer less than it would if the charge was delocalized and, hence, this charge localization process is favorable relative to the band process [15]. We then obtain what in physics of condensed-matter is called polaron. In chemically terminology, the polaron is just a radical ion associated with lattice distortion and the presence of localized electronic states in the gap referred to as polaron states [16]. A similar scenario occurs for a reductive process.

If a second electron is removed from the polymer chain, the creation of a so-called bipolaron is observed. The bipolaron is defined as a pair of like charges (dication) associated with a strong local chain distortion. High doping levels provoke a continuous bipolaron bands formation, then the upper and the lower bipolaron bands will merge with the conduction and the valence bands, respectively, to produce partially filled bands and metallic like conductivity [17].

The lattice distortion (aromatic to quinoid-like structure) associated to process of polaron creation and the bipolaron formation is depicted in Figure 1.2. Moreover, Figure 1.3 shows a schematic representation of their corresponding band structures.

1.1.1.3. POSSIBLE USES OF CONDUCTING POLYMERS

The ability that presents extended π conjugated polymer to chemical and electrochemical oxidation or reduction causes the alteration of their electrical and optical properties. That is, by controlling the oxidation and reduction of these materials, it is possible to precisely control their electronic properties. Since these reactions are often reversible, it is possible to systematically control the electrical and optical properties with a great deal of precision. It is even possible to switch from a conducting state to an insulating state.

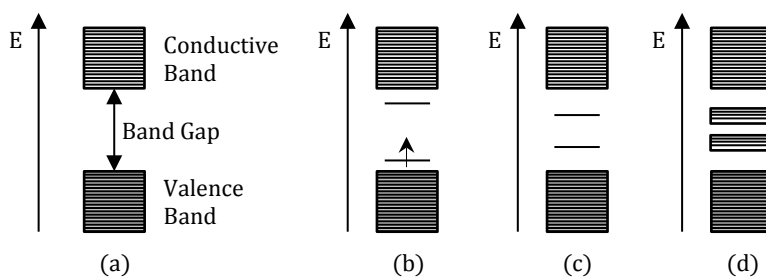


Figure 1.3. Band structure of a polymer chain (a) in neutral state, (b) containing one polaron, (c) containing a bipolaron, and (d) with bipolaron bands.

Taking into account their conductivity properties, CPs could be used for a huge range of applications, such as electrostatic materials, conducting adhesives, artificial nerves, diodes, piezoceramics, *etc.* On the other hand, the utilization of its electroactivity as the main property of CPs gives place to their use for molecular electronics [18,19], chemical and biochemical sensors [20-23], rechargeable batteries [24], electromechanical actuators [25,26], optoelectronic devices [27,28], *etc.*

1.1.2. POLYMERIC ION EXCHANGE MEMBRANES

A membrane is an interphase between two adjacent phases acting as a selective barrier, regulating partial or totally the transport of substances between the two compartments [29]. The key property of a membrane is the ability to selectively control the permeation of particular species through the system. The permselectivity of membranes depend on the intrinsic properties of the material used for their fabrication (*e.g.* porosity and structure), as well as of the solute solubility and diffusivity. However, the flux though the membrane is not only determined by such factors but also by the driving force acting on the permeating component; (*e.g.* electrical potential, concentration, pressure, or temperature gradients) [30].

Although the development of ceramic, metal and liquid membranes is gaining more importance in the last years, the majority of synthetic membranes are and will be based on solid polymeric systems [29]. In general, this is due to the fact that polymeric materials provide a wide variability of barrier structures and chemical and physical properties.

The use of different membrane structures and driving forces has resulted in a number of rather different membrane processes. Within this context, polymeric IEMs represent an important group of technical materials that bear ionic groups that have the ability to selectively permit the transport of ions across themselves. These systems play an important role and present potential applications in a huge number of chemical industry processes, being used as fuel cells, supercapacitors, batteries, sensors, chloro-alkali cells and electrolysers [31].

1.1.2.1. CLASSIFICATION OF POLYMERIC ION EXCHANGE MEMBRANES

Taking into account their functionality, IEMs can be classified as anion or cation exchange membranes depending on the type of ionic groups attached to the membrane matrix. Cation exchange membranes contains negatively charged groups, such as $-\text{SO}_3^-$, $-\text{COO}^-$, $-\text{PO}_3^{2-}$ fixed to the membrane backbone, which allow the passage of cations rejecting anions (Figure 1.4). Anion exchange membranes are positively charged and allow the transport of anions. IEMs can be further classified into homogenous and heterogeneous, depending on whether the charged groups are chemically bonded to or physically mixed with the membrane matrix, respectively [32].

1.1.2.2. ION EXCHANGE MEMBRANE PROPERTIES

Considering the wide range of applications of these materials, the most desired properties that must exhibit IEMs are [33,34]:

- *High permselectivity*; that is, these materials should be highly permeable to counter-ions, but impermeable to co-ions.
- *Low electrical resistance*; IEMs should exhibit low electrical resistance to reduce the potential drop during electro-membrane processes.
- *Good mechanical stability*; the membrane should be mechanically strong and should have a low degree of swelling or shrinking in transition from dilute to concentrated ionic solutions.
- *High chemical stability*; they should be stable over a pH-range from 0 to 14 and in the presence of oxidizing agents.

1.1.2.3. FACTORS CONTRIBUTING TO IONIC TRANSPORT

The investigation of transport and equilibrium phenomena in IEMs have been studied in a large number of papers [32,33,35-37]. Furthermore, some mathematical models have been proposed to explain the macroscopic characteristics of such processes (*e.g.*, proton transport and membrane conductivity) [38-40].

The transport behavior for a given penetrant varies from one polymer to another. Focusing on the structure and chemical nature of the polymer, transport properties depend on its free volume and on the segmental mobility of their chains. The segmental mobility of the polymer chains is affected by factors such as the degree of unsaturation, crosslinking, crystallinity, or the nature of substituents [41]. The transport rate of a charged specie across the membrane is also determined by the nature and density of the electrical charges fixed to the membrane matrix, the properties of the permeating compound (such as its size, its chemical nature and electrical charge) and driving forces, such as electrical potential [42].

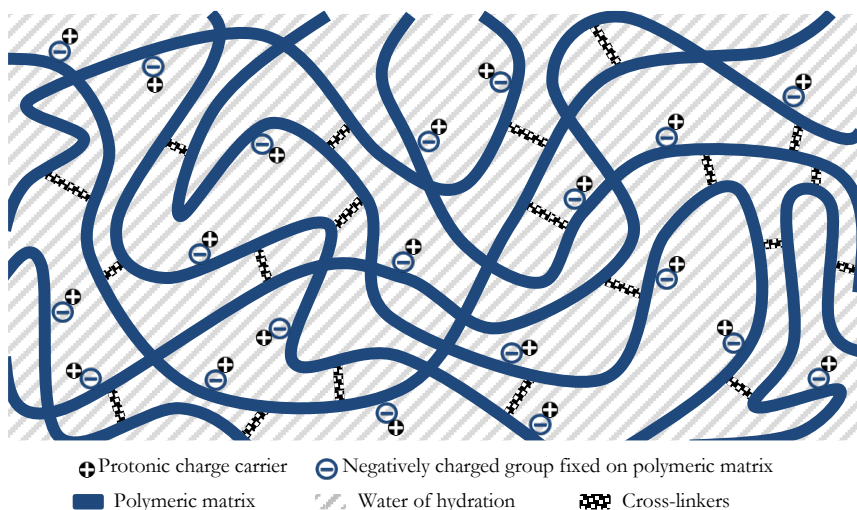


Figure 1.4. Schematic representation of cationic ion exchange membrane.

Taking into account both the skills listed in section 1.1.2.2 which must accomplish IEMs, and the structural properties of the polymeric matrix that affect the transport properties, a great number of materials have been used to develop acidic membranes. Some examples could be matrix membranes based on polyaniline [43] polysulfone [44], polyether sulfone [45], polyphosphazene [46], poly(styrene-ethylene-butylene) [34] and poly(styrene-*co*-divinyl benzene) [47-52].

1.1.3. DENDRITIC POLYMERS

Dendritic polymers are highly branched polymer structures, with complex, secondary architectures and well-defined spatial location of functional groups. Dendritic materials comprise different subclasses, typically divided into monodisperse structures (*i.e.* dendrons and dendrimers), and polydisperse structures such as hyperbranched polymers, dendigrafts and DPs [53,54]. Figure 1.5 represents a schematic overview of some of the aforementioned subclasses of the dendritic polymers.

The highly branched structure associated to this kind of macromolecules gives them unique physical and chemical properties. As a consequence, dendritic materials are being considered as good candidates for a wide range of applications such as; targeted drug-delivery, macromolecular carriers, enzyme-like catalysis, sensors, light harvesting, surface engineering or biomimetic applications [53,55-62].

Among the several subgroups in which dendritic family can be divided, this Thesis focuses on the study of dendrons, dendrimers and DPs. Below, a brief description of some features of the aforementioned subgroups is presented.

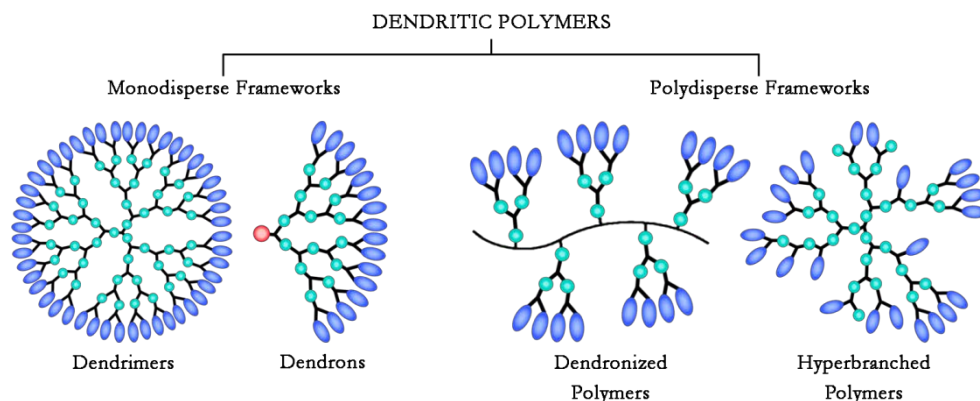


Figure 1.5. Schematic representation of some subclasses of the family of dendritic polymers.

1.1.3.1. DENDRIMERS AND DENDRONS

Ideal dendrimers are structurally perfect monodisperse and highly branched globular macromolecules with well-defined dimensions, surface and interior. They comprise a single core unit that is capped with layers of repeat units radially branched. The number of layers of repeating units between the core and a terminal unit is defined as the generation number (g). Thus, three topological regions coexist in dendrimers: the inner dense core, the dendritic region around the core, and the external surface, as can be seen in Figure 1.6 [4,53-56,63,64].

Associated with dendrimers are dendrons, each dendron represents a wedge of a dendrimer. Hence, a dendrimer is made up of at least 2 dendrons. Each functional group in a dendritic core gives rise to one dendron. Moreover, dendrons with high generation numbers (*i.e.* $g \geq 4$) can be thought of as dendrimers with an active core moiety that can be further functionalized [53].

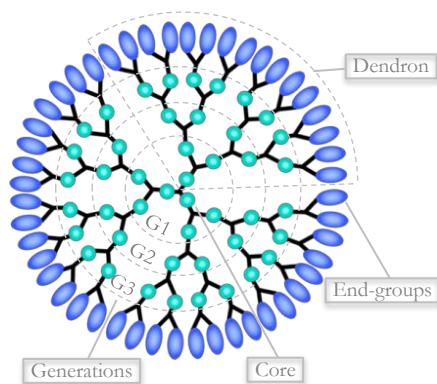


Figure 1.6. Structural components of a G4 Dendrimer.

Each architectural component of the dendrimers has a specific function, inducing unique properties to these structures as they increase their generation number. For instance, the core could be seen as the molecular information point which defines the size, shape, directionality and multiplicity via the covalent bonds to the outer layers. The branched interior region defines the type and volume of internal empty space that may be enclosed by the end-groups while dendrimer is grown. The branch cell multiplicity determines the density and degree

of amplification and increase with the generation number in an exponential way. The last structural component is the peripheral region or surface, which contains the end-groups. Because of the large number of end-groups, the nature of these functional groups affects drastically physical and chemical properties of dendrimers. Hence, the functionalization of a parent dendrimer with a library of different terminal groups is an interesting methodology to produce materials with novel properties [4,53].

Dendrimer Properties

The highly branched structure in combination with the large amount of terminal groups, which in contrast of the only two end-groups of linear polymers increases exponentially with the generation number, is one of the key features of dendrimers and gives rise to a number of unique dendritic properties (*e.g.* high solubility[65,66], unusual rheological behavior [67] and site isolation phenomena [68-70]).

Architecture of dendrimers determines structural features, like size, shape and flexibility. For example, lower generations are generally open, floppy structures, whereas higher generations become robust, less deformable spheroids, ellipsoids or cylinders (this fact depends on the shape and directionality of the core). This transition in overall shape is mainly due to the fact that dendrimer diameters increase linearly as function of generations added, while the number of end-groups grows exponentially. For this reason steric congestion is expected to occur due to the tethered connectivity to the core. As a consequence, generational reiteration of branch cells ultimately will lead to a so-called *dense-packed state* [4,68].

Shape change transitions were firstly confirmed by Turro *et al.* [71-74] through photophysical measurements, followed by the solvatochromic measurements of Hawker *et al.* [75]. Depending upon the accumulative core and branch cell multiplicities of the considered dendrimer family, these transitions were found to occur between third and fifth generation.

Other distinctive features of dendrimers in comparison to their linear analogues are the volume and molecular weight. Dendritic volume increases cubically with generation while dendritic molecular weight increases exponentially. This pattern leads to deviations between the solution properties of dendrimers and linear polymers, especially at the higher molecular weights. These deviations involve changes in the intrinsic viscosity. Generally, the intrinsic viscosity for linear polymers increases continuously with the molecular weight, whereas dendrimers show very low values [58,76-81], reaching a maximum at a certain generation number.

1.1.3.2. DENDRONIZED POLYMERS

Dendronized polymers (DPs) are structures having a linear backbone with dendritic side chains; that is, the polymer is used as a polyfunctional, polydisperse core, in which

each repeat unit is decorated with a dendron (see Figure 1.5). They are in fact a sub-group of comb-polymers where instead of linear polymer chains, the comb's teeth are dendrons.

The research on the field of DPs is fairly new. The first examples were reported in a patent filed by Tomalia *et al.* at Dow in 1987 and results being published in greater detail in 1998 in a scientific paper [82]. Fréchet and Hawker were the first to recognize that the combination of dendrimers with linear polymers might afford materials with interesting molecular architectures, and they attached Fréchet type dendrons to a styrene derivative and copolymerized it with styrene in 1992 [83]. Percec *et al.*, who came from the research area of liquid crystalline polymers, asserted the predominant role of geometry in the self-assembly of polymers equipped with taper-shaped side chains [84-88]. Finally, Schlüter *et al.*, who had synthesized rod-like polymers with conjugated backbones, recognized the importance of dendron decoration for the backbone conformation and the overall shape of the obtained macromolecules, proving their behavior as cylindrical nanoscopic objects [89-92].

Structural Aspects of Dendronized Polymers

The shape of a polymer in bulk and in solution is essentially determined by the chemical constitution of its backbone and its average length. At the submolecular level, a polymer can be seen as a one-dimensional object and, therefore, at the molecular level this may provide the potential for anisotropy. In the case of DPs, dendrons surrounding the polymeric backbone determine the size and shape of the polymer due to a number of factors that affect their conformational behavior. Among these factors one has to distinguish the effects that are purely topological from those induced by chemical functionality of dendrons. Basically, these factors are [55]:

- The repulsive force associated to the steric congestion induced by the dendritic side chains.
- The attractive secondary interactions between the dendrons (*i.e.* hydrogen-bonding or π - π interactions), which also act as a driving force for self-assembly.
- The microphase segregation of incompatible elements, such as backbone, spacers, dendritic branches and the periphery, also acts as a tool for favoring the self-assembly phenomenon.
- The formation of higher ordered phases in the condensed state.

In summary, a dense attachment of high generation dendrons to a polymer converts this linear entity into a shape persistent, rigid, cylindrical molecular objects with nanoscopic dimension and with almost monodisperse diameter [89].

Because of the structural features cited previously, most DPs can be treated as soft elongated colloidal objects [93,94] and currently represent a class of single molecular nanomaterials with potential applications (*e.g.* nanoscopic building blocks [95,96],

functional materials [97,98], organic optoelectronic materials [99,100], self-assembling vectors for complexation with DNA [101,102], stabilizers of therapeutic proteins in the gastrointestinal tract [103], and nanomaterials to both copy [104] and to immobilize enzymes [105]).

1.2. THE ROLE OF COMPUTATIONAL CHEMISTRY IN THE STUDY OF POLYMERIC SYSTEMS

The fast progress in computer technology and the development of both theoretical concepts and models have led the scientific community to use computational chemistry as a powerful tool in a wide range of areas of polymer science (*e.g.* the investigation of the structure, dynamics, surface properties and thermodynamics of polymeric systems). That is, computational chemistry has become a useful way to investigate materials at the microscopic level, helping scientists to make predictions before running the actual experiments.

Among the different theoretical approaches that one can find, theoretical chemistry based on quantum and classical formalisms are probably the most renowned. Depending on both the time-scale and size of the systems studied, this kind of *in silico* methods embraces several formalisms to understand the structure and properties of matter at atomic and molecular scale, such as quantum mechanics (QM), molecular mechanics (MM) and molecular dynamics (MD).

The QM formalism offers the most accurate description of the matter describing its fundamental behavior at the atomic and molecular level. However, due to the computational expensiveness of QM methods, in practice this family of methodologies is only applicable to small systems.

Within classical formalisms, MM and MD do not depict the electronic nature of atoms, but this lower accuracy in the description of the chemical nature allow the inclusion of a bigger quantity of atoms enabling a more realistic representation of the whole system. A more detailed description of QM and MM/MD based methods is included in the chapter devoted to Methodology.

In systems where the number of atoms to be treated becomes too large coarse graining approximations are very useful. Within this approximation a group of atoms is replaced by a pseudo atom. Pseudo-atoms must be parameterized so that they can reproduce as much as possible the experimental data available or the results derived from all atom classical simulations.

The bibliography based on the utilization of computational chemistry to study polymeric systems is really vast. Taking into account this fact, one can conclude that theoretical methods are powerful tools that fit reality properly, saving time and economic

resources for research and contributing significantly to a deeper understanding of the structure and properties of polymeric systems.

1.3. APPLICATIONS

1.3.1. CHEMICAL SENSORS BASED ON CONDUCTING POLYMERS

Global research and development in the field of chemical sensors has made significant strides in the last two decades. According to the definition given by the International Union of Pure and Applied Chemistry (IUPAC), a chemical sensor is:

'a device that transforms chemical information, ranging from the concentration of a specific sample component to total composition analysis, into an analytically useful signal. The chemical information, mentioned above, may originate from a chemical reaction of the analyte or from a physical property of the system investigated' [106].

Chemical sensors are essentially composed of two basic functional units: a chemical (molecular) recognition system (the receptor) and a physiochemical transducer. The sensing part (receptor) interacts with the environment, generates a response, and determines the nature, selectivity and sensitivity of the sensor. On the other hand, the transducer functionality is to read the response of the receptor and converts it into an interpretable and quantifiable data, such as a voltage signal. Figure 1.7 illustrates schematically a chemical sensor device.

Chemical sensors are widely used in areas such as healthcare, lifestyle, environmental sciences and homeland security, covering a wide range of applications (*e.g.* in the field of healthcare from disease diagnosis to discovery and screening of new drugs). Some of the main requirements that have to accomplish an ideal chemical sensor are high sensitivity, selectivity and resolution, fast speed of response, repeatability and small size for *in-situ* measurements. Hence, the development and study of new compounds for the fabrication

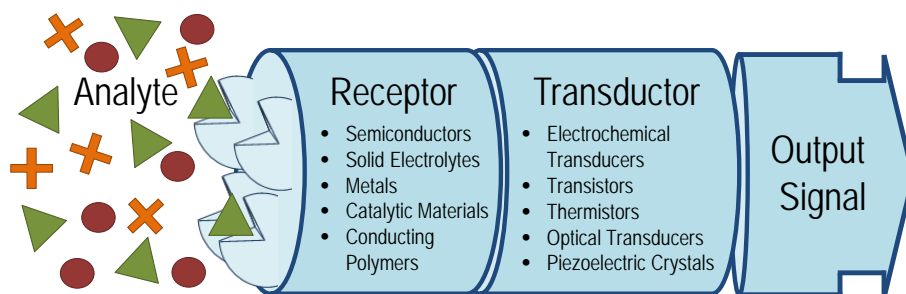


Figure 1.7. Schematic representation of a chemical sensor.

of reliable and inexpensive devices that enable direct and rapid analyses with high sensitivity and selectivity of chemical species is highly desirable.

Due to their unique properties, CPs have emerged in the last two decades as one of the most interesting materials for the fabrication of electrochemical sensors [107]. CPs offer a myriad of opportunities to couple analyte receptor interactions, as well as nonspecific interactions, into transducible responses. The great advantages of CP based sensors over other available devices using small molecule (chemosensor) elements are their potential to exhibit improved response properties and their sensitivity to small perturbations [108]. Moreover, the fact that these materials can be prepared electrochemically guarantees fine control over their synthetic conditions [109]. Consequently, low cost, scalability and material properties, such as large surface area, adjustable transport properties and chemical specificities, make CPs attractive candidates for applications in electrochemical sensing.

Taking into account CPs functionality in the development of sensor devices, they can be employed mainly in three different ways: as receptors components, as matrix for specific molecular immobilization, or as transducers [110]. In the first one, the electronic conductivity related with the oxidized or reduced state of a CP is modulated through the interaction with the analytes (*i.e.* changes in parameters like resistance, current or electrochemical potential, give a straightforward sensor response of the studied phenomena). In the second way, the immobilization of specific molecules able to recognize the analyte can be carried out during, or even after, the electropolymerization process [111]. Finally, the strong and reversible influence of oxidation/reduction processes, protonation/deprotonation reactions and conformational changes on the electrical and optical properties of CPs, enable the use of these materials as transducers [110]. However, as CPs are frequently multifunctional materials, a well-defined separation of their functions in the sensing process is not always possible.

Due to the excellent electrical and chemical properties of CPs, a wide range of different sensor types has been developed in the last years using these materials as receptors (*e.g.* gas sensors, pH sensors, ion-selectivity sensors, humidity sensors and organic sensors) [112]. CPs are also known to be compatible with biological molecules in aqueous solution. Therefore, these materials are also extensively used in the fabrication of biosensors, playing an important role in clinical diagnosis and environmental monitoring [7].

Some of the most commonly used CPs for development of different types of electrochemical sensors are: PANI, PPy and PTh derivatives [113]. Among these, PPy derivatives have been employed more extensively for the development of sensor devices because of their high electrical conductivity and electroactivity, long term environmental stability and ease of being prepared in aqueous environments [114-116]. Table 1.2 summarizes some sensors based in CPs and their applications.

Table 1.2. Various Sensors and their Applications.

Sensor Type	Polymer Used	Fields of Application	Special Features	Ref.
Chemical sensor	PANI ^a and its derivatives	Sensing aliphatic alcohols	Extent of change governed by chain length of alcohol and its chemical	[117]
Chemical sensor	PANI ^a	Measure pH of body fluids and low ionic strength of water	Polymer thin film electrodeposited onto ion-beam etched carbon fiber	[118]
Chemical sensor	P3MT ^b ; PANI ^a ; PPy ^c	Detection of norepinephrine, epinephrine and dopamine	Amperometric detection	[119]
Chemical sensor	P3MT ^b	Detection of phenols	Excellent resistance to electrode fouling in presence of high concentrations of phenolic species	[120]
Chemical sensor	PEDOT ^d	Detection of dopamine and ascorbic acid	PEDOT-modified glassy carbon electrode	[121]
Chemical sensor	PEDOT ^d	Detection of pesticides	PEDOT-modified glassy carbon electrode	[122]
Biosensor	PPy ^c ; PANI ^a ; PTh ^e	Estimation of glucose	Electrode immobilization of an enzyme by electropolymerization of CPs	[123-126]
Biosensor	PPy ^c derivatives	Estimation of glucose	Hemocompatible glucose sensor	[127]
Biosensor	PPy ^c	Can sense fructose	Enzyme entrapped in membrane shows sharp increase in catalytic activity	[128]
Biosensor	PPy ^c ; PANI ^a	Can sense cholesterol	Amperometric detector	[129,130]

^a Polyaniline; ^b Poly(3-methylthiophene); ^c Polypyrrole; ^d Poly(3,4-ethylenedioxythiophene); ^e Polythiophene

1.3.1.1. CONDUCTING POLYMER BASED DOPAMINE SENSOR

Dopamine (3,4-dihydroxyphenyl ethylamine, DA) is one of the most important neurotransmitters in the mammalian central nervous system. The deficiency or excess of DA may result in serious diseases related with neurological disorders (*e.g.* DA has been linked with the debilitating ailment, Parkinson's disease and schizophrenia) [131,132], and is also believed to play a central role in Huntington's disease, a fatal, genetic neurodegenerative movement disorder for which there is no cure [133]. In addition, DA plays a very important role in drug addiction [134], attention disorders [135] and it has even been associated with HIV infection [136]. Accordingly, development of simple analytical methods to measure DA concentration is crucial for clinical diagnoses. This field is receiving special attention because of the necessity of understanding the mechanisms that provoke the neurological disorders mentioned above.

In the last years many research works have been focused on the development of electrochemical sensors for DA detection. This is because the oxidation of DA can be

easily followed using electrochemical techniques. Furthermore, electrochemical approaches have many advantages with respect to other methods: electrodes can be made extremely small, can be conveniently implanted in living organisms with minimal tissue damage and, because the response is very fast, the neurotransmitter can be monitored in real time.

Screening of DA concentration through electrochemical methods is not trivial. One of the primary challenges is that the concentration of dopamine in the extracellular fluid of the caudate nucleus is extremely low (0.01–1 μM for a healthy individual and in the nanomolar range for patients with Parkinson's disease) [137]. In addition DA coexists with many interfering compounds in biological samples. These interfering compounds, which are usually present at concentrations much higher than DA, oxidize at potentials similar to that of the neurotransmitter at most solid electrodes. Consequently, modified electrodes have been employed for the determination of DA. The most popular strategies include polymer modified electrodes [138], self-assembled monolayer modified electrodes [139] and surfactant modified electrodes [140]. However, a wide variety of other modified electrodes have also been used.

Within this context, CP-modified electrodes are widely investigated for the development of DA sensors. Among others, electrodes coated with PPy [141-146], poly(3-methylthiophene) (P3MT) [147-149], poly(N-methylpyrrole) (PNMPy) [150,151], PANI [152-155], and poly(3,4-ethylenedioxythiophene) (PEDOT) [156,157] are the most popular for the detection of DA. Table 1.3 summarized some examples of CPs modified electrodes able of sensing DA electrochemically.

Table 1.3. CPs Modified Electrodes Successfully Applied in DA Sensing.

Polymer	Method	Linear Range	Detection Limit	Ref.
PPy	Incorporation of $\text{Fe}(\text{CN})_6^{3-}$ as dopant during potentiostatic polymerization.	0.2-0.95 $\text{mmol}\cdot\text{L}^{-1}$	15.1 $\mu\text{mol}\cdot\text{L}^{-1}$	[144]
Oxidized PPy	Glassy carbon electrode modified with overoxidized-polypyrrole/gold nanocluster composite	0.075-20 $\mu\text{mol}\cdot\text{L}^{-1}$	0.015 $\mu\text{mol}\cdot\text{L}^{-1}$	[145]
P3MT	Glassy carbon electrode modified with P3MT/gold nanoparticle composites	1.0-35 $\mu\text{mol}\cdot\text{L}^{-1}$	0.24 $\mu\text{mol}\cdot\text{L}^{-1}$	[147]
PANI	Gold nanoparticle/PANI nanocomposite layers obtained through layer-by-layer adsorption	7-148 $\mu\text{mol}\cdot\text{L}^{-1}$	-	[154]
PEDOT	Gold nanoparticles and PEDOT matrix composite	0.5-2 $\mu\text{mol}\cdot\text{L}^{-1}$	0.002 $\mu\text{mol}\cdot\text{L}^{-1}$	[157]
P3MT	Palladium, platinum nanoparticles into P3MT matrix	0.05-1 $\mu\text{mol}\cdot\text{L}^{-1}$	0.009 $\mu\text{mol}\cdot\text{L}^{-1}$	[148]
PNMPy	Electrodeposition of palladium nanoclusters on PNMPy film-coated platinum electrode	0.1-10 $\mu\text{mol}\cdot\text{L}^{-1}$	0.012 $\mu\text{mol}\cdot\text{L}^{-1}$	[151]

Table 1.3. Continuation. CPs Modified Electrodes Successfully Applied in DA Sensing.

Polymer	Method	Linear Range	Detection Limit	Ref.
PANI	Graphene Oxide-Templated PANI Microsheets	1-14 $\mu\text{mol}\cdot\text{L}^{-1}$	0.5 $\mu\text{mol}\cdot\text{L}^{-1}$	[155]
PPy	Composite of PPy and graphene modified electrode	0.1-150 $\mu\text{mol}\cdot\text{L}^{-1}$	0.023 $\mu\text{mol}\cdot\text{L}^{-1}$	[146]
PNMPy, PEDOT	Electrodes based on three-layered films: PEDOT/PNMPy/PEDOT and gold nanoparticles	10-400 $\mu\text{mol}\cdot\text{L}^{-1}$	-	[20] [158]
PNMPy, PEDOT	Microspheres made of alternating layers of PEDOT and PNMPy	500-2000 $\mu\text{mol}\cdot\text{L}^{-1}$	-	[159]

1.3.1.2. CONDUCTING POLYMER BASED MORPHINE SENSOR

Morphine (MO), which is a major component in opium, is used as a powerful pain killing drug in medicine. However, an abusive consumption is toxic and can cause physical dependence, respiratory depression, bradycardia, hypotension or acute lung injury, and death may result from any of these complications [160]. For these reasons it is necessary to monitor the concentrations of morphine in the blood and urine of patients. Some detection techniques based on high-performance liquid chromatography [161], gas chromatography-mass spectroscopy [162], thin-layer chromatography [163], surface plasmon resonance-based immune-sensor [164] or electrochemistry [165,166] have been developed in the last decades, and are currently used for morphine detection in clinical analysis. However, these methods are not only time-consuming but also inconvenient for routine application. Therefore, new methods need to be developed for detecting morphine in a more facile and convenient way.

Recently, novel electrochemical methods have been developed for the detection of MO. Some examples are adsorptive differential pulse stripping method [167] and the fast Fourier transformation with continuous cyclic voltammetry at gold microelectrodes [168,169] in a flow injection system. In addition, different modified electrodes have been fabricated for MO detection. For example, Jin and co-workers prepared a cobalt hexacyanoferrate modified carbon paste electrode able to detect MO *in vivo* [170]. Multiwalled carbon nanotubes modified preheated glassy carbon electrodes were recently used for the amperometric MO detection [171]. Finally, Ho *et al.* devised a Prussian blue-modified indium tin oxide (ITO) electrode [172] and molecularly imprinted electrodes for morphine determination [173,174].

Over the wide range of compounds that are under investigation for the fabrication of modified electrodes for successful MO detection, CPs should be taken into account due to their low density, large specific area, high stability and surface permeability, and rapid electron transfer [175]. Particularly, recent studies have been focussed on the MO sensing with PEDOT [22]. For example, Ho *et al.* carried out MO detection using immobilized

molecularly imprinted polymer (MIP) particles with PEDOT, this procedure being successful for drug concentrations ranging from 0.01 to 0.2 mM [174]. More recently, Atta and co-workers investigated the electrochemical determination of MO at PEDOT modified platinum electrodes in presence of sodium dodecyl sulfate. Specifically, the detection procedure proposed by these authors was based on the oxidation of the phenolic groups of MO at +0.41 V [176].

1.3.2. ION EXCHANGE MEMBRANE FOR ELECTRODIALYSIS

Electrodialysis is a widely used process for desalination of brackish water. In some countries this process is used for the production of potable water [52]. The principle of electrodialysis is based on a mass separation process in which electrically charged membranes and an electrical potential difference are used to separate ionic species from an aqueous solution and other uncharged components [33]. Principle of electrodialysis is illustrated in Figure 1.8, which shows the scheme of a typical electrodialysis cell. This consists of a series of cation- and anion-exchange membranes arranged alternatively between an anode and a cathode. If an ionic solution, such as aqueous salt solution, is passed through these cells under the influence of applied potential gradient between cathode and anode, cations will migrate towards the cathode while anions will move to the anode.

Within this context the development of IEMs with improved thermal, chemical and mechanical properties and lower electrical resistance is crucial for this specific application. Some reported IEMs for electrodialysis which accomplish aforementioned skills are

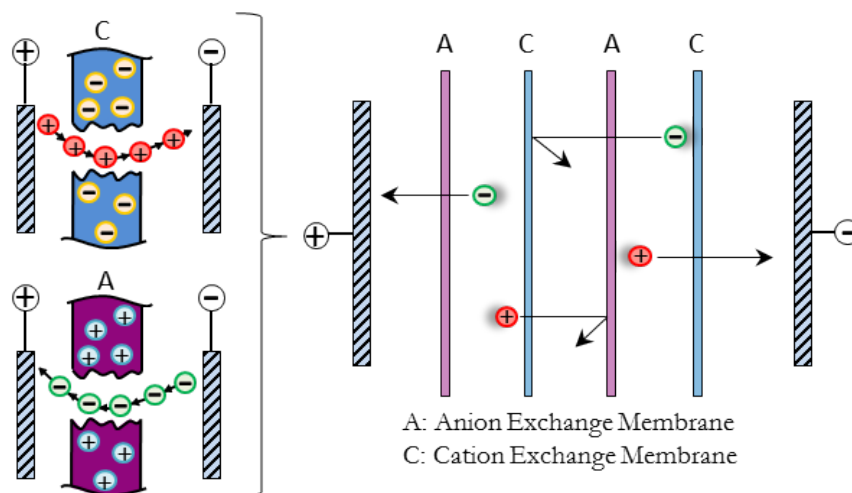


Figure 1.8. Schematic representation of the electrodialysis principle.

polysulfone-based IEMs, which have good electrochemical properties and excellent resistance to degradation by heat and chemical attack [44,47]; sulfonated polyether ether ketone membranes, which present a reduced lifetime because of their mechanical fragility [47]; polyphosphazene, with good thermal and chemical stability, however the resulting polymer present a high hydrophobicity degree [47,177]; sulfonated poly(styrene-ethylene-butylene) which shows high ion diffusion implying a favored cation extraction [34,178]; and poly(styrene-co-divinylbenzene), P(S-DVB), with low protonic resistance, good mechanical properties, and high chemical stability [47,48,179-181].

1.3.2.1. STYRENE-DIVINYLBENZENE BASED MEMBRANES

Copolymers of styrene and divinylbenzene are used to fabricate cation or anion exchange membranes through a sulfonation or amination process, respectively. Sulfonation of the polymer is achieved by chlorosulfonic acid or concentrated sulphuric acid in dichloroethane [33]. Figure 1.9 shows a schematic representation of the chemical structure of sulfonated P(S-DVB) membrane.

It is worth noting that this kind of copolymers are among the best IEMs since cross-linked polystyrene provide a wide number of phenyl rings that act as reactive sites for functionalization with sulfonic acid groups [47]. Moreover, P(S-DVB) supports exhibit excellent mechanical strength and exchange capacities, as well as high resistance to oxidative, hydrolytic or thermal degradation [49].

IEMs based on P(S-DVB) have been commercially applied such as monovalent ion selective filters for the production of table salt, high hydronium ion retention devices to recover acids from the waste water, *etc.* The hydronium ion can pass selectively through the membrane against all other ions in electrodialysis, the development of this kind of cationic membranes with high acid retention being really challenging for the application of the acid recovery [33]. Sata *et al.* have reported significant research work in this field for the production of the table salt from seawater [182]. Moreover, the same author have studied the sieving of the ions by varying the cross-link density, the effect of charge on permselectivity, and the specific interaction between the ion-exchange groups in the membrane matrix and counter-ions [182,183]. Tiihonen *et al.* have investigated the effect

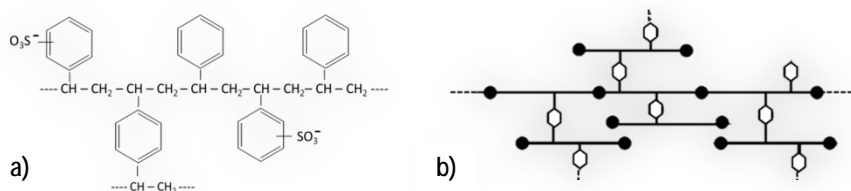


Figure 1.9. Schematic representation of sulfonated poly(styrene-co-divinylbenzene) membrane. (a) Chemical representation of a sulfonated pseudounit. (b) Scheme of membrane system including the cross-links.

of cross-link density on the selectivity and solvent content of the P(S-DVB) resins [51]. On the other hand, theoretical studies based on molecular dynamics simulations are expected to be interesting for the elucidation of details about ionic transport and structural parameters. In this context, Bertran *et al.* used atomistic MD simulations to study the effects of electric field in transport of hydronium ions in a sulfonated P(S-DVB) membrane [184].

1.3.3. ELECTRONIC DEVICES BASED ON DENDRITIC POLYMERS

There are numerous criteria for the design of molecules for application in organic electronics. One of the most important is the charge-carrying properties of the organic material. Within this context, conjugated polymers form an important class of electro- and photoactive materials as has been reported in section 1.1.1. Moreover, dendritic macromolecules provide unique molecular architectures for a wide variety of applications in optoelectronic and electronic devices [185-189]. These architectures have advantages to offer molecules with a well-defined form and structure, a high chemical purity, and high degree of order. On the other hand, they offers the possibility of tuning their photophysical properties by changing the chemical structure (*e.g.* introducing side substituents and/or end-capping groups, inserting specific functional groups and changing the oligomer length).

Some of the most interesting applications in which conjugated based dendritic polymers may be taken into account as active components in organic electronic or electrochemical devices are organic light emitting diodes (OLEDs) [58,186,187,189], photovoltaic cells [185] and field-effect transistors [190].

1.3.3.1. POLYTHIOPHENE BASED DENDRIMERS AND DENDRONIZED POLYMERS

Oligo- and polythiophene derivatives have been extensively investigated in the academic world and industry due to their electro-optic response, which is suitable for potential applications in telecommunications, digital signal processing, phased-array radar, THz generation, and other photonic devices [58]. Currently, due to their fully π -conjugated core, thiophene (Th) based dendrimers and DPs are considered as a new class of organic materials with a very promising conducting properties [191].

Since Advincula and co-workers reported the synthesis of the first Th dendrimer [192,193], several other publications using Th dendrimers for different energy-related applications have appeared [191]. For example, Bäuerle and co-workers [194] by combining divergent/convergent synthetic strategies to build up a new family of structurally well-defined dendritic oligothiophenes containing up to 90 Th rings. The 3D branched structures of these dendritic structures improve the solubility in common organic solvents and, therefore, their processability, which is convenient for the investigation of optoelectronic properties and device performances [195].

Among other Th based dendrimers examples with promising applications as electronic devices, Mitchell *et al.* [196] prepared phenyl-cored Th dendrimers for organic photovoltaic devices, their power-conversion efficiency being recently overtaken by hexaperi-hexabenzocornene-cored Th dendrimers described by Wong *et al.* [197] and the hybrid gold-nanoparticle-cored dendrimers of Deng *et al.* [198].

Bao *et al.* were among the first to report results with respect to DPs as optoelectronic materials. These authors synthesized a dendronized poly(p-phenylene vinylene) with first and second generation of Percec type dendrons [99]. However, Th-based DPs studies are very scarce because of the intrinsic complexity associated to this kind of macromolecular objects. In a groundbreaking work, Schlüter *et al.* [199] reported the synthesis of Th-containing second and third generation dendronized macromonomers with methacrylate polymerizable units as well as their corresponding DPs. More recently, novel all-Th dendritic macromonomers that were subsequently polymerized were prepared by Kimura *et al.* [200]. The study in both cases of their electronic and electrical properties evidenced an enhancement of the electrical conductivity upon doping, which was attributed to the spatial overlapping of the Th dendrons through π - π interactions. Finally, Griffin *et al.* [201] reported the synthesis and characterization of benzodithiophene/Th alternating copolymers decorated with rigid, singly branched pendant side chains. Photoexcitation of these copolymers resulted in excited states primarily localized on the pendant side chains that were rapidly transferred to the polymer backbone.

1.3.4. DENDRONIZED POLYMERS. APPLICATIONS IN BIOSCIENCE

In the last two decades, research on DPs has expanded because of the wide variety of potential applications exhibited by these novel materials. As DPs combine structural features and properties of both dendrimers and polymers, they show set of characteristics that make them unique macromolecules. For instance, their size combined with the polymeric nature of their core promote the behavior of DPs as individual macromolecular objects within nanometer scale, which is not attainable with classical dendrimers. The overall of these properties suggests that DPs are good candidates for applications such as tissue engineering, drug delivery, gene delivery and theranostics [202].

DPs with a variety of shapes, core molecules, carbohydrate residues and valences have been made available for biological evaluation. In fact, the linking of terminal sugar residues, such as heparin, on dendrimers can create a multivalent display that mimic cell-surface glycans to regulate heparin-protein interactions. [203].

Another application in a biochemical context is the use of polycationic and amphiphilic DPs as substrates for DNA complexation, representing an advantage for applications related with gene transfection. Schlüter and Rabe *et al.* used an amine functionalized dendronized poly(styrene) from first to fourth generation as substrates [102]. The polymers were deprotected, yielding polycations, and complexes were obtained by mixing

a solution of the polymer with a DNA solution. Scanning force microscopy images evidenced the formation of complexes between individual dendronized polymer molecules and individual DNA strands [102].

Recently, an intriguing application in the biomedical area has been reported by Leroux *et al.* [103]. They propose the use of a polycationic DP, poly-(3,5-bis(3-aminopropoxy)benzyl)methacrylate, for stabilizing and retaining enzyme activity in the gastrointestinal tract. The purpose of such application is to prevent the enzymes from degrading in the gastrointestinal tract through their attachment to DPs. This opens the door to the development of new therapeutic and imaging strategies based on orally administered proteins to prevent for example, celiac disease, lactose intolerance or exocrine pancreatic disease. It is worth noting that chapter 6 is devoted to the study of internal organization and structure properties of first to sixth generation of the DP used in such study.

REFERENCES

- [1] L.H. Sperling; *Introduction to physical polymer science*, Wiley, 2001.
- [2] R.O. Ebewele; *Polymer science and technology*, CRC Press, Boca Raton, 2000.
- [3] W.D. Callister; *Materials science and engineering: an introduction*, John Wiley & Sons Australia, 2006.
- [4] D.A. Tomalia; *Birth of a new macromolecular architecture: dendrimers as quantized building blocks for nanoscale synthetic polymer chemistry*; *Prog Polym Sci* **30**, 294 (2005).
- [5] H. Shirakawa, E.J. Louis, A.G. Macdiarmid, C.K. Chiang, A.J. Heeger; *Synthesis of electrically conducting organic polymers - halogen derivatives of polyacetylene, (Cb)X*; *J Chem Soc Chem Comm*, 578 (1977).
- [6] Y. Furukawa; *Electronic absorption and vibrational spectroscopies of conjugated conducting polymers*; *J Phys Chem-U.S* **100**, 15644 (1996).
- [7] M.A. Rahman, P. Kumar, D.S. Park, Y.B. Shim; *Electrochemical sensors based on organic conjugated polymers*; *Sensors* **8**, 118 (2008).
- [8] T.A. Skotheim, J. Reynolds; *Conjugated polymers: theory, synthesis, properties, and characterization*, Taylor & Francis, 2006.
- [9] U. Evans, O. Soyemi, M.S. Doescher, U.H.F. Bunz, L. Kloppenburg, M.L. Myrick; *Spectroelectrochemical study of the oxidative doping of polydialkylphenyleneethynylene using iterative target transformation factor analysis*; *Analyst* **126**, 508 (2001).
- [10] M.D. McClain, D.S. Dudis; *Electronic and structural consequences of n-doping: bithiazole oligomers and partially reduced bithiazolium cations*; *Synthetic Met* **116**, 199 (2001).
- [11] J.M. André, J. Delhalle, J.L. Brédas; *Quantum chemistry aided design of organic polymers: an introduction to the quantum chemistry of polymers and its applications*, World Scientific, 1991.
- [12] C. Aleman, L. Julia; *Characterization of the quinoid structure for the 2,2'-bithiophene and 2,2',5',2''-terthiophene dications*; *J Phys Chem-U.S* **100**, 14661 (1996).
- [13] C. Aleman, L. Julia; *Pi conjugation in 2,2'-bithiophene and its dimethyl derivatives: Model compounds of organic conducting polymers based on thiophene rings*; *J Phys Chem-U.S* **100**, 1524 (1996).
- [14] C. Aleman, E. Armelin, J.I. Iribarren, F. Liesa, M. Laso, J. Casanovas; *Structural and electronic properties of 3,4-ethylenedioxythiophene, 3,4-ethylenedisulfanylfurane and thiophene oligomers: A theoretical investigation*; *Synthetic Met* **149**, 151 (2005).
- [15] J. Casanovas, C. Aleman; *Comparative theoretical study of heterocyclic conducting oligomers: Neutral and oxidized forms*; *J Phys Chem C* **111**, 4823 (2007).
- [16] J.L. Bredas, G.B. Street; *Polarons, bipolarons, and solitons in conducting polymers*; *Accounts Chem Res* **18**, 309 (1985).
- [17] C. Aleman; *Spatial extension of the bipolaronic defect in highly conducting polymers based on five-membered aromatic rings*; *Macromol Theor Simul* **6**, 237 (1997).
- [18] D. Aradilla, M.M. Perez-Madrigal, F. Estrany, D. Azambuja, J.I. Iribarren, C. Aleman; *Nanometric ultracapacitors fabricated using multilayer of conducting polymers on self-assembled octanethiol monolayers*; *Org Electron* **14**, 1483 (2013).
- [19] M.M. Perez-Madrigal, E. Armelin, L.J. del Valle, F. Estrany, C. Aleman; *Bioactive and electroactive response of flexible polythiophene: polyester nanomembranes for tissue engineering*; *Polym Chem-Uk* **3**, 979 (2012).
- [20] G. Fabregat, E. Armein, C. Aleman; *Selective detection of dopamine combining multilayers of conducting polymers with gold nanoparticles*; *J Phys Chem B* **118**, 4669 (2014).

- [21] G. Fabregat, E. Cordova-Mateo, E. Armelin, O. Bertran, C. Aleman; *Ultrathin films of polypyrrole derivatives for dopamine detection*; J Phys Chem C **115**, 14933 (2011).
- [22] B. Teixeira-Dias, C. Aleman, F. Estrany, D.S. Azambuja, E. Armelin; *Microstructures of poly(*N*-methylpyrrole) and their interaction with morphine*; Electrochim Acta **56**, 5836 (2011).
- [23] E. Cordova-Mateo, J. Poater, B. Teixeira-Dias, O. Bertran, F. Estrany, L.J. del Valle, M. Sola, C. Aleman; *Electroactive polymers for the detection of morphine*; J Polym Res **21** (2014).
- [24] D. Aradilla, F. Estrany, F. Casellas, J.I. Iribarren, C. Aleman; *All-polythiophene rechargeable batteries*; Org Electron **15**, 40 (2014).
- [25] F. Rodriguez-Ropero, J. Preat, D. Zanuy, J. Torras, C. Aleman; *Sensing mechanism of calix[4]arene-substituted poly(thiophene) ion receptor: effects of the selectivity on the molecular rigidity*; J Phys Chem B **113**, 8284 (2009).
- [26] F. Rodriguez-Ropero, D. Zanuy, C. Aleman; *Molecular dynamics of a calix[4]arene-containing polymer in dichloromethane solution: Ability of the solvent molecules to fill the cavity of the macrocycle*; J Comput Chem **29**, 1233 (2008).
- [27] F. Rodriguez-Ropero, D. Zanuy, C. Aleman; *Electronic characterization of all-thiophene conducting dendrimers: Molecules and assemblies*; Polymer **51**, 308 (2010).
- [28] E. Cordova-Mateo, F. Rodriguez-Ropero, O. Bertran, C. Aleman; *Properties of oligothiophene dendrimers as a function of molecular architecture and generation number*; Chemphyschem **13**, 1354 (2012).
- [29] M. Ulbricht; *Advanced functional polymer membranes*; Polymer **47**, 2217 (2006).
- [30] H. Strathmann, L. Giorno, E. Drioli; *An introduction to membrane science and technology*, CNR-Servizio Pubblicazioni, 2006.
- [31] E. Cordova-Mateo, O. Bertran, C.A. Ferreira, C. Aleman; *Transport of hydronium ions inside poly(styrene-co-divinyl benzene) cation exchange membranes*; J Membrane Sci **428**, 393 (2013).
- [32] T.W. Xu; *Ion exchange membranes: State of their development and perspective*; J Membrane Sci **263**, 1 (2005).
- [33] R.K. Nagarale, G.S. Gohil, V.K. Shahi; *Recent developments on ion-exchange membranes and electro-membrane processes*; Adv Colloid Interfac **119**, 97 (2006).
- [34] F. Muller, C.A. Ferreira, D.S. Azambuja, C. Aleman, E. Armelin; *Measuring the proton conductivity of ion-exchange membranes using electrochemical impedance spectroscopy and through-plane cell*; J Phys Chem B **118**, 1102 (2014).
- [35] J.H. Choi, S.H. Kim, S.H. Moon; *Heterogeneity of ion-exchange membranes: the effects of membrane heterogeneity on transport properties*; J Colloid Interf Sci **241**, 120 (2001).
- [36] P.W. Majsztrik, M.B. Satterfield, A.B. Bocarsly, J.B. Benziger; *Water sorption, desorption and transport in Nafion membranes*; J Membrane Sci **301**, 93 (2007).
- [37] W. Kujawski, M. Staniszewski, T.Q. Nguyen; *Transport parameters of alcohol vapors through ion-exchange membranes*; Sep Purif Technol **57**, 476 (2007).
- [38] N.P. Gnusin, N.P. Berezina, N.A. Kononenko, O.A. Dyomina; *Transport structural parameters to characterize ion exchange membranes*; J Membrane Sci **243**, 301 (2004).
- [39] N.P. Berezina, N.A. Kononenko, O.A. Dyomina, N.P. Gnusin; *Characterization of ion-exchange membrane materials: Properties vs structure*; Adv Colloid Interfac **139**, 3 (2008).
- [40] L. Pisani, M. Valentini, D.H. Hofmann, L.N. Kuleshova, B. D'Aguzzo; *An analytical model for the conductivity of polymeric sulfonated membranes*; Solid State Ionics **179**, 465 (2008).
- [41] S.C. George, S. Thomas; *Transport phenomena through polymeric systems*; Prog Polym Sci **26**, 985 (2001).
-

- [42] M. Ramir Khan, Rafiuddin; *Transport phenomena of inorganic–organic cation exchange nanocomposite membrane: a comparative study with different methods*; J Nanostruct Chem **4**, 1 (2014).
- [43] C.A. Ferreira, J. Casanovas, M.A.S. Rodrigues, F. Muller, E. Armelin, C. Aleman; *Transport of metallic ions through polyaniline-containing composite membranes*; J Chem Eng Data **55**, 4801 (2010).
- [44] M. Ersoz; *The electrochemical properties of polysulfone ion-exchange membranes*; J Colloid Interf Sci **243**, 420 (2001).
- [45] V.K. Shahi; *Highly charged proton-exchange membrane: Sulfonated poly(ether sulfone)-silica polyelectrolyte composite membranes for fuel cells*; Solid State Ionics **177**, 3395 (2007).
- [46] L. Jones, P.N. Pintauro, H. Tang; *Cation exclusion properties of polyphosphazene ion-exchange membranes*; J Membrane Sci **162**, 135 (1999).
- [47] M.Y. Kariduraganavar, R.K. Nagarale, A.A. Kittur, S.S. Kulkarni; *Ion-exchange membranes: preparative methods for electrodialysis and fuel cell applications*; Desalination **197**, 225 (2006).
- [48] O. Okay; *Macroporous copolymer networks*; Prog Polym Sci **25**, 711 (2000).
- [49] F.M.B. Coutinho, S.M. Rezende, B.G. Soares; *Characterization of sulfonated poly(styrene–divinylbenzene) and poly(divinylbenzene) and its application as catalysts in esterification reaction*; J Appl Polym Sci **102**, 3616 (2006).
- [50] L.X. Tuan, B. Hanae, M.V. Lara, C. Buess-Herman; *Cation exchange membranes based on grafted PS/DVB–ETFE films: An investigation of their electrochemical characteristics in sulfuric acid*; Electrochim Acta **54**, 5992 (2009).
- [51] J. Tiihonen, M. Laatikainen, I. Markkanen, E. Paatero; *Sorption of neutral components in ion-exchange resins. 1. Effect of cross-link density and counterion on selective sorption of water–ethanol mixtures in sulfonated PS–DVB resins*; Ind Eng Chem Res **38**, 4832 (1999).
- [52] R. Scherer, A.M. Bernardes, M.M.C. Forte, J.Z. Ferreira, C.A. Ferreira; *Preparation and physical characterization of a sulfonated poly(styrene-co-divinylbenzene) and polypyrrole composite membrane*; Mater Chem Phys **71**, 131 (2001).
- [53] A. Carlmark, C.J. Hawker, A. Hult, M. Malkoch; *New methodologies in the construction of dendritic materials*; Chem Soc Rev **38**, 352 (2009).
- [54] M.V. Walter, M. Malkoch; *Simplifying the synthesis of dendrimers: accelerated approaches*; Chem Soc Rev **41**, 4593 (2012).
- [55] H. Frauenrath; *Dendronized polymers - building a new bridge from molecules to nanoscopic objects*; Prog Polym Sci **30**, 325 (2005).
- [56] J.M.J. Frechet; *Dendrimers and other dendritic macromolecules: From building blocks to functional assemblies in nanoscience and nanotechnology*; J Polym Sci Pol Chem **41**, 3713 (2003).
- [57] C. Gao, D. Yan; *Hyperbranched polymers: from synthesis to applications*; Prog Polym Sci **29**, 183 (2004).
- [58] D. Astruc, E. Boisselier, C. Ornelas; *Dendrimers designed for functions: from physical, photophysical, and supramolecular properties to applications in sensing, catalysis, molecular electronics, photonics, and nanomedicine*; Chem Rev **110**, 1857 (2010).
- [59] P. Ceroni, M. Venturi; *Photoactive and electroactive dendrimers: future trends and applications*; Aust J Chem **64**, 131 (2011).
- [60] Y.Y. Cheng, L.B. Zhao, Y.W. Li, T.W. Xu; *Design of biocompatible dendrimers for cancer diagnosis and therapy: current status and future perspectives*; Chem Soc Rev **40**, 2673 (2011).
- [61] M.A. Mintzer, M.W. Grinstaff; *Biomedical applications of dendrimers: a tutorial*; Chem Soc Rev **40**, 173 (2011).

- [62] L. Roglin, E.H.M. Lempens, E.W. Meijer; *A synthetic "tour de force": well-defined multivalent and multimodal dendritic structures for biomedical applications*; *Angew Chem Int Edit* **50**, 102 (2011).
- [63] D.A. Tomalia, H. Baker, J. Dewald, M. Hall, G. Kallos, S. Martin, J. Roeck, J. Ryder, P. Smith; *A new class of polymers - starburst-dendritic macromolecules*; *Polym J* **17**, 117 (1985).
- [64] A.F. Zhang, L.J. Shu, Z.S. Bo, A.D. Schluter; *Dendronized polymers: Recent progress in synthesis*; *Macromol Chem Phys* **204**, 328 (2003).
- [65] E.M. Harth, S. Hecht, B. Helms, E.E. Malmstrom, J.M.J. Frechet, C.J. Hawker; *The effect of macromolecular architecture in nanomaterials: A comparison of site isolation in porphyrin core dendrimers and their isomeric linear analogues*; *J Am Chem Soc* **124**, 3926 (2002).
- [66] K.L. Wooley, C.J. Hawker, J.M.J. Frechet; *A branched-monomer approach for the rapid synthesis of dendrimers*; *Angew Chem Int Edit* **33**, 82 (1994).
- [67] C.J. Hawker, P.J. Farrington, M.E. Mackay, K.L. Wooley, J.M.J. Frechet; *Molecular ball-bearings - the unusual melt viscosity behavior of dendritic macromolecules*; *J Am Chem Soc* **117**, 4409 (1995).
- [68] J.M.J. Fréchet, D.A. Tomalia; *Dendrimers and other dendritic polymers*, Wiley, 2001.
- [69] S. Hecht, J.M.J. Frechet; *Dendritic encapsulation of function: Applying nature's site isolation principle from biomimetics to materials science*; *Angew Chem Int Edit* **40**, 74 (2001).
- [70] S. Hecht, H. Ihre, J.M.J. Frechet; *Porphyrin core star polymers: Synthesis, modification, and implication for site isolation*; *J Am Chem Soc* **121**, 9239 (1999).
- [71] K.R. Gopidas, A.R. Leheny, G. Caminati, N.J. Turro, D.A. Tomalia; *Photophysical investigation of similarities between starburst dendrimers and anionic micelles*; *J Am Chem Soc* **113**, 7335 (1991).
- [72] S. Jockusch, J. Ramirez, K. Sanghvi, R. Nociti, N.J. Turro, D.A. Tomalia; *Comparison of nitrogen core and ethylenediamine core starburst dendrimers through photochemical and spectroscopic probes*; *Macromolecules* **32**, 4419 (1999).
- [73] M.F. Ottaviani, N.J. Turro, S. Jockusch, D.A. Tomalia; *Characterization of starburst dendrimers by EPR. Aggregational processes of a positively charged nitroxide surfactant*; *J Phys Chem-U* **100**, 13675 (1996).
- [74] N.J. Turro, J.K. Barton, D.A. Tomalia; *Molecular recognition and chemistry in restricted reaction spaces - photophysics and photoinduced electron-transfer on the surfaces of micelles, dendrimers, and DNA*; *Accounts Chem Res* **24**, 332 (1991).
- [75] C.J. Hawker, K.L. Wooley, J.M.J. Frechet; *Solvatochromism as a probe of the microenvironment in dendritic polyethers - transition from an extended to a globular structure*; *J Am Chem Soc* **115**, 4375 (1993).
- [76] S.M. Grayson, J.M.J. Frechet; *Convergent dendrons and dendrimers: from synthesis to applications*; *Chem Rev* **101**, 3819 (2001).
- [77] F.W. Zeng, S.C. Zimmerman; *Dendrimers in supramolecular chemistry: From molecular recognition to self-assembly*; *Chem Rev* **97**, 1681 (1997).
- [78] S. Campidelli, R. Deschenaux, A. Swartz, G.M.A. Rahman, D.M. Guldi, D. Milic, E. Vazquez, M. Prato; *A dendritic fullerene-porphyrin dyad*; *Photoch Photobio Sci* **5**, 1137 (2006).
- [79] B.S. Li, Y.Q. Fu, Y. Han, Z.S. Bo; *Synthesis and optical properties of dendronized porphyrin polymers*; *Macromol Rapid Comm* **27**, 1355 (2006).
- [80] P.L. Burn, S.C. Lo, I.D.W. Samuel; *The development of light-emitting dendrimers for displays*; *Adv Mater* **19**, 1675 (2007).
-

- [81] J.M. Lupton, I.D.W. Samuel, M.J. Frampton, R. Beavington, P.L. Burn; *Control of electrophosphorescence in conjugated dendrimer light-emitting diodes*; Adv Funct Mater **11**, 287 (2001).
- [82] R. Yin, Y. Zhu, D.A. Tomalia, H. Ibuki; *Architectural copolymers: Rod-shaped, cylindrical dendrimers*; J Am Chem Soc **120**, 2678 (1998).
- [83] C.J. Hawker, J.M.J. Frechet; *The synthesis and polymerization of a hyperbranched polyether macromonomer*; Polymer **33**, 1507 (1992).
- [84] V. Percec, J. Heck; *Liquid-crystalline polymers containing mesogenic units based on half-disk and rod-like moieties .1. Synthesis and characterization of 4-(11-undecan-1-yloxy)-4'-[3,4,5-tri(para-normal-dodecan-1-yloxybenzyloxy)benzoate]biphenyl side groups*; J Polym Sci Pol Chem **29**, 591 (1991).
- [85] V. Percec, J. Heck, M. Lee, G. Ungar, A. Alvarezcastillo; *Poly(2-vinyloxyethyl 3,4,5-tris[4-(n-dodecan-yloxy)benzyloxy]benzoate) - a self-assembled supramolecular polymer similar to tobacco mosaic-virus*; J Mater Chem **2**, 1033 (1992).
- [86] V. Percec, J. Heck, D. Tomazos, F. Falkenberg, H. Blackwell, G. Ungar; *Self-assembly of taper-shaped monoesters of oligo(ethylene oxide) with 3,4,5-tris(p-dodecycloxybenzyloxy)benzoic acid and of their polymethacrylates into tubular supramolecular architectures displaying a columnar mesophase*; J Chem Soc Perk T **1**, 2799 (1993).
- [87] V. Percec, J. Heck, G. Ungar; *Liquid-crystalline polymers containing mesogenic units based on half-disk and rodlike moieties .5. Side-chain liquid-crystalline poly(methylsiloxanes) containing hemiphasmidic mesogens based on 4-[[3,4,5-tris(alkan-1-yloxy)benzoyl]oxy]-4'-[[para-(propan-1-yloxy)-benzoyl]oxy]biphenyl groups*; Macromolecules **24**, 4957 (1991).
- [88] V. Percec, M. Lee, J. Heck, H.E. Blackwell, G. Ungar, A. Alvarezcastillo; *Reentrant isotropic-phase in a supramolecular disk-like oligomer of 4-[3,4,5-tris(normal-dodecan-yloxy)benzyloxy]-4'-[(2-vinyloxy)ethoxy]biphenyl*; J Mater Chem **2**, 931 (1992).
- [89] R. Freudenberger, W. Claussen, A.D. Schluter, H. Wallmeier; *Functionalized rod-like polymers - one-dimensional rigid matrices*; Polymer **35**, 4496 (1994).
- [90] Y.F. Guo, J.D. van Beek, B.Z. Zhang, M. Colussi, P. Walde, A. Zhang, M. Kroger, A. Halperin, A.D. Schluter; *Tuning polymer thickness: Synthesis and scaling theory of homologous series of dendronized polymers*; J Am Chem Soc **131**, 11841 (2009).
- [91] B.Z. Zhang, R. Wepf, K. Fischer, M. Schmidt, S. Besse, P. Lindner, B.T. King, R. Sigel, P. Schurtenberger, Y. Talmon, Y. Ding, M. Kroger, A. Halperin, A.D. Schluter; *The largest synthetic structure with molecular precision: towards a molecular object*; Angew Chem Int Edit **50**, 737 (2011).
- [92] A. Kroeger, B.Z. Zhang, C. Rosenauer, A.D. Schluter, G. Wegner; *Solvent induced phenomena in a dendronized linear polymer*; Colloid Polym Sci **291**, 2879 (2013).
- [93] E. Cordova-Mateo, O. Bertran, B.Z. Zhang, D. Vlassopoulos, R. Pasquino, A.D. Schluter, M. Kroger, C. Aleman; *Interactions in dendronized polymers: intramolecular dominates intermolecular*; Soft Matter **10**, 1032 (2014).
- [94] R. Pasquino, B. Zhang, R. Sigel, H. Yu, M. Ottiger, O. Bertran, C. Aleman, A.D. Schluter, D. Vlassopoulos; *Linear viscoelastic response of dendronized polymers*; Macromolecules **45**, 8813 (2012).
- [95] Z.S. Bo, J.P. Rabe, A.D. Schluter; *A poly(para-phenylene) with hydrophobic and hydrophilic dendrons: Prototype of an amphiphilic cylinder with the potential to segregate lengthwise*; Angew Chem Int Edit **38**, 2370 (1999).
- [96] V. Percec, C.H. Ahn, T.K. Bera, G. Ungar, D.J.P. Yeardeley; *Coassembly of a hexagonal columnar liquid crystalline superlattice from polymer(s) coated with a three-cylindrical bundle supramolecular dendrimer*; Chem-Eur J **5**, 1070 (1999).

- [97] C.O. Liang, B. Helms, C.J. Hawker, J.M.J. Frechet; *Dendronized cyclopolymers with a radial gradient of polarity and their use to catalyze a difficult esterification*; Chem Commun, 2524 (2003).
- [98] B.M.J.M. Suijkerbuijk, L.J. Shu, R.J.M.K. Gebbink, A.D. Schluter, G. van Koten; *Single-site catalysts on a cylindrical support beyond nanosize*; Organometallics **22**, 4175 (2003).
- [99] Z.N. Bao, K.R. Amundson, A.J. Lovinger; *Poly(pbenylenevinylene)s with dendritic side chains: Synthesis, self-ordering, and liquid crystalline properties*; Macromolecules **31**, 8647 (1998).
- [100] T. Sato, D.L. Jiang, T. Aida; *A blue-luminescent dendritic rod: Poly(pbenyleneethynylene) within a light-harvesting dendritic envelope*; J Am Chem Soc **121**, 10658 (1999).
- [101] D. Joester, M. Losson, R. Pugin, H. Heinzelmann, E. Walter, H.P. Merkle, F. Diederich; *Amphiphilic dendrimers: Novel self-assembling vectors for efficient gene delivery*; Angew Chem Int Edit **42**, 1486 (2003).
- [102] I. Gossel, L.J. Shu, A.D. Schluter, J.P. Rabe; *Molecular structure of single DNA complexes with positively charged dendronized polymers*; J Am Chem Soc **124**, 6860 (2002).
- [103] G. Fuhrmann, A. Grotzky, R. Lukic, S. Matoori, P. Luciani, H. Yu, B.Z. Zhang, P. Walde, A.D. Schluter, M.A. Gauthier, J.C. Leroux; *Sustained gastrointestinal activity of dendronized polymer-enzyme conjugates*; Nat Chem **5**, 582 (2013).
- [104] A. Grotzky, T. Nauser, H. Erdogan, A.D. Schluter, P. Walde; *A fluorescently labeled dendronized polymer-enzyme conjugate carrying multiple copies of two different types of active enzymes*; J Am Chem Soc **134**, 11392 (2012).
- [105] S. Fornera, T.E. Balmer, B. Zhang, A.D. Schluter, P. Walde; *Immobilization of peroxidase on *sio2* surfaces with the help of a dendronized polymer and the avidin-biotin system*; Macromol Biosci **11**, 1052 (2011).
- [106] A. Hulanicki, S. Glab, F. Ingman; *Chemical sensors definitions and classification*; Pure Appl Chem **63**, 1247 (1991).
- [107] T.A. Skotheim, R.L. Elsenbaumer, J.R. Reynolds; *Handbook of conducting polymers*, 2nd ed., Dekker, New York, 1998.
- [108] D.T. McQuade, A.E. Pullen, T.M. Swager; *Conjugated polymer-based chemical sensors*; Chem Rev **100**, 2537 (2000).
- [109] C.A. Vincent; *Applications of electroactive polymers*. Edited by B. Scrosati. Chapman and Hall, London; Polym Int **33**, 343 (1994).
- [110] U. Lange, N.V. Roznyatovskaya, V.M. Mirsky; *Conducting polymers in chemical sensors and arrays*; Anal Chim Acta **614**, 1 (2008).
- [111] G. Bidan; *Electroconducting conjugated polymers - New sensitive matrices to build up chemical or electrochemical sensors - a review*; Sensor Actuat B-Chem **6**, 45 (1992).
- [112] B. Adhikari, S. Majumdar; *Polymers in sensor applications*; Prog Polym Sci **29**, 699 (2004).
- [113] S. Nambiar, J.T.W. Yeow; *Conductive polymer-based sensors for biomedical applications*; Biosens. Bioelectron. **26**, 1825 (2011).
- [114] A.J. Zhang, J. Chen, D.F. Niu, G.G. Wallace, J.X. Lu; *Electrochemical polymerization of pyrrole in BMIMPF6 ionic liquid and its electrochemical response to dopamine in the presence of ascorbic acid*; Synthetic Met **159**, 1542 (2009).
- [115] S. Tokonami, K. Saimatsu, Y. Nakadoi, M. Furuta, H. Shiigi, T. Nagaoka; *Vertical immobilization of viable bacilliform bacteria into polypyrrole films*; Anal Sci **28**, 319 (2012).
- [116] A. Ramanavicius, A. Ramanaviciene, A. Malinauskas; *Electrochemical sensors based on conducting polymer- polypyrrole*; Electrochim Acta **51**, 6025 (2006).
- [117] A.A. Athawale, M.V. Kulkarni; *Polyaniline and its substituted derivatives as sensor for aliphatic alcohols*; Sensor Actuat B-Chem **67**, 173 (2000).
-

- [118] X.J. Zhang, B. Ogorevc, J. Wang; *Solid-state pH nanoelectrode based on polyaniline thin film electrodeposited onto ion-beam etched carbon fiber*; *Anal Chim Acta* **452**, 1 (2002).
- [119] A. Galal, N.F. Atta, J.F. Rubinson, H. Zimmer, H.B. Mark; *Electrochemistry and detection of some organic and biological molecules at conducting polymer electrodes .2. Effect of nature of polymer electrode and substrate on electrochemical-behavior and detection of some neurotransmitters*; *Anal Lett* **26**, 1361 (1993).
- [120] J. Wang, R.L. Li; *Highly stable voltammetric measurements of phenolic-compounds at poly(3-methylthiophene)-coated glassy-carbon electrodes*; *Anal Chem* **61**, 2809 (1989).
- [121] V.S. Vasantha, S.M. Chen; *Electrocatalysis and simultaneous detection of dopamine and ascorbic acid using poly(3,4-ethylenedioxy)thiophene film modified electrodes*; *J Electroanal Chem* **592**, 77 (2006).
- [122] P. Manisankar, S. Viswanathan, A.M. Puspahalatha, C. Rani; *Electrochemical studies and square wave stripping voltammetry of five common pesticides on poly 3,4-ethylenedioxythiophene modified wall-jet electrode*; *Anal Chim Acta* **528**, 157 (2005).
- [123] M. Umana, J. Waller; *Protein-modified electrodes - the glucose-oxidase polypyrrole system*; *Anal Chem* **58**, 2979 (1986).
- [124] J.J. Wang, N.V. Myung, M.H. Yun, H.G. Monbouquette; *Glucose oxidase entrapped in polypyrrole on high-surface-area Pt electrodes: a model platform for sensitive electroenzymatic biosensors*; *J Electroanal Chem* **575**, 139 (2005).
- [125] K. Ramanathan, S.S. Pandey, R. Kumar, A. Gulati, A. Surya, N. Murthy, B.D. Malhotra; *Covalent immobilization of glucose oxidase to poly(O-Amino benzoic acid) for application to glucose biosensor*; *J Appl Polym Sci* **78**, 662 (2000).
- [126] M. Shimomura, N. Kojima, K. Oshima, T. Yamauchi, S. Miyauchi; *Covalent immobilization of glucose oxidase on film prepared by electrochemical copolymerization of thiophene-3-acetic acid and 3-methylthiophene for glucose sensing*; *Polym J* **33**, 629 (2001).
- [127] M. Yasuzawa, T. Matsuki, H. Mitsui, A. Kunugi, T. Nakaya; *Properties of glucose sensors prepared by the electropolymerization of pyrroles containing phosphatidylcholine (II)*; *Sensor Actuat B-Chem* **66**, 25 (2000).
- [128] G.F. Khan, E. Kobatake, H. Shinohara, Y. Ikariyama, M. Aizawa; *Molecular interface for an activity controlled enzyme electrode and its application for the determination of fructose*; *Anal Chem* **64**, 1254 (1992).
- [129] J.C. Vidal, E. Garcia-Ruiz, J. Espuelas, T. Aramendia, J.R. Castillo; *Comparison of biosensors based on entrapment of cholesterol oxidase and cholesterol esterase in electropolymerized films of polypyrrole and diamionaphthalene derivatives for amperometric determination of cholesterol*; *Anal Bioanal Chem* **377**, 273 (2003).
- [130] S. Singh, P.R. Solanki, M.K. Pandey, B.D. Malhotra; *Cholesterol biosensor based on cholesterol esterase, cholesterol oxidase and peroxidase immobilized onto conducting polyaniline films*; *Sensor Actuat B-Chem* **115**, 534 (2006).
- [131] E. Kandel, J.H. Schwartz, T.M. Jessel, (Eds.), *Principles of neural science*, McGraw-Hill, New York, 2000.
- [132] B.J. Venton, R.M. Wightman; *Psychoanalytical electrochemistry: Dopamine and behavior*; *Anal Chem* **75**, 414a (2003).
- [133] G.S. Wilson, M.A. Johnson; *In-vivo electrochemistry: What can we learn about living systems?*; *Chem Rev* **108**, 2462 (2008).
- [134] P.E.M. Phillips, G.D. Stuber, M.L.A.V. Heien, R.M. Wightman, R.M. Carelli; *Subsecond dopamine release promotes cocaine seeking*; *Nature* **422**, 614 (2003).
- [135] R.D. O'Neill; *Long-term monitoring of brain dopamine metabolism in vivo with carbon paste electrodes*; *Sensors* **5**, 317 (2005).

- [136] E. Koutsilieris, V. ter Meulen, P. Riederer; *Neurotransmission in HIV associated dementia: a short review*; J Neural Transm **108**, 767 (2001).
- [137] S.R. Ali, R.R. Parajuli, Y. Balogun, Y.F. Ma, H.X. He; *A nonoxidative electrochemical sensor based on a self-doped polyaniline/carbon nanotube composite for sensitive and selective detection of the neurotransmitter dopamine: A review*; Sensors **8**, 8423 (2008).
- [138] S.R. Hou, N. Zheng, H.Y. Feng, X.J. Li, Z.B. Yuan; *Determination of dopamine in the presence of ascorbic acid using poly(3,5-dihydroxy benzoic acid) film modified electrode*; Anal Biochem **381**, 179 (2008).
- [139] J. Weng, J.M. Xue, J. Wang, J.S. Ye, H.F. Cui, F.S. Sheu, Q.Q. Zhang; *Gold-cluster sensors formed electrochemically at boron-doped-diamond electrodes: Detection of dopamine in the presence of ascorbic acid and thiols*; Adv Funct Mater **15**, 639 (2005).
- [140] S.M. Chen, W.Y. Chzo; *Simultaneous voltammetric detection of dopamine and ascorbic acid using didodecylmethylammonium bromide (DDAB) film-modified electrodes*; J Electroanal Chem **587**, 226 (2006).
- [141] K. Pihel, Q.D. Walker, R.M. Wightman; *Overoxidized polypyrrole-coated carbon fiber microelectrodes for dopamine measurements with fast-scan cyclic voltammetry*; Anal Chem **68**, 2084 (1996).
- [142] C.C. Harley, A.D. Rooney, C.B. Breslin; *The selective detection of dopamine at a polypyrrole film doped with sulfonated beta-cyclodextrins*; Sensor Actuat B-Chem **150**, 498 (2010).
- [143] S. Shahrokhian, H.R. Zare-Mehrjardi; *Electrochemical synthesis of polypyrrole in the presence of congo red; application to selective voltammetric determination of dopamine in the presence of ascorbic acid*; Electroanal **21**, 157 (2009).
- [144] J.-B. Raoof, R. Ojani, S. Rashid-Nadimi; *Voltammetric determination of ascorbic acid and dopamine in the same sample at the surface of a carbon paste electrode modified with polypyrrole/ferrocyanide films*; Electrochim Acta **50**, 4694 (2005).
- [145] J. Li, X. Lin; *Simultaneous determination of dopamine and serotonin on gold nanocluster/overoxidized-polypyrrole composite modified glassy carbon electrode*; Sensor Actuat B-Chem **124**, 486 (2007).
- [146] P. Si, H. Chen, P. Kannan, D.-H. Kim; *Selective and sensitive determination of dopamine by composites of polypyrrole and graphene modified electrodes*; Analyst **136**, 5134 (2011).
- [147] X. Huang, Y. Li, P. Wang, L. Wang; *Sensitive determination of dopamine and uric acid by the use of a glassy carbon electrode modified with poly(3-methylthiophene)/gold nanoparticle composites*; Anal Sci **24**, 1563 (2008).
- [148] N.F. Atta, M.F. El-Kady; *Novel poly(3-methylthiophene)/Pd, Pt nanoparticle sensor: Synthesis, characterization and its application to the simultaneous analysis of dopamine and ascorbic acid in biological fluids*; Sensor Actuat B-Chem **145**, 299 (2010).
- [149] H.-S. Wang, T.-H. Li, W.-L. Jia, H.-Y. Xu; *Highly selective and sensitive determination of dopamine using a Nafion/carbon nanotubes coated poly(3-methylthiophene) modified electrode*; Biosens Bioelectron **22**, 664 (2006).
- [150] M. Marti, G. Fabregat, F. Estrany, C. Aleman, E. Armelin; *Nanostructured conducting polymer for dopamine detection*; J Mater Chem **20**, 10652 (2010).
- [151] N.F. Atta, M.F. El-Kady, A. Galal; *Simultaneous determination of catecholamines, uric acid and ascorbic acid at physiological levels using poly(N-methylpyrrole)/Pd-nanoclusters sensor*; Anal Biochem **400**, 78 (2010).
- [152] X.M. Feng, C.J. Mao, G. Yang, W.H. Hou, J.J. Zhu; *Polyaniline/Au composite hollow spheres: Synthesis, characterization, and application to the detection of dopamine*; Langmuir **22**, 4384 (2006).
-

- [153] J. Mathiyarasu, S. Senthilkumar, K.L.N. Phani, V. Yegnaraman; *Selective detection of dopamine using a functionalised polyaniline composite electrode*; J Appl Electrochem **35**, 513 (2005).
- [154] A. Stoyanova, S. Ivanov, V. Tsakova, A. Bund; *Au nanoparticle–polyaniline nanocomposite layers obtained through layer-by-layer adsorption for the simultaneous determination of dopamine and uric acid*; Electrochim Acta **56**, 3693 (2011).
- [155] Y. Bao, J. Song, Y. Mao, D. Han, F. Yang, L. Niu, A. Ivaska; *Graphene oxide-templated polyaniline microsbeets toward simultaneous electrochemical determination of AA/DA/UA*; Electroanal **23**, 878 (2011).
- [156] J. Mathiyarasu, S. Senthilkumar, K.L.N. Phani, V. Yegnaraman; *PEDOT-Au nanocomposite films for electrochemical sensing of dopamine and uric acid*; J Nanosci Nanotechno **7**, 2206 (2007).
- [157] S.S. Kumar, J. Mathiyarasu, K.L. Phani; *Exploration of synergism between a polymer matrix and gold nanoparticles for selective determination of dopamine*; J Electroanal Chem **578**, 95 (2005).
- [158] G. Fabregat, J. Casanovas, E. Redondo, E. Armelin, C. Aleman; *A rational design for the selective detection of dopamine using conducting polymers*; Phys Chem Chem Phys **16**, 7850 (2014).
- [159] G. Fabregat, F. Estrany, M.T. Casas, C. Aleman, E. Armelin; *Detection of dopamine using chemically synthesized multilayered hollow microspheres*; J Phys Chem B **118**, 4702 (2014).
- [160] J.H. Jaffe, W.R. Martin; *The pharmacological basis of therapeutics*, Pergamon Press, New York, 1991.
- [161] M.R. Moeller, S. Steinmeyer, T. Kraemer; *Determination of drugs of abuse in blood*; J Chromatogr B **713**, 91 (1998).
- [162] B.H. Chen, E.H. Taylor, A.A. Pappas; *Comparison of derivatives for determination of codeine and morphine by gas chromatography/mass spectrometry*; J. Anal. Toxicol. **14**, 12 (1990).
- [163] R. Jain; *Utility of thin layer chromatography for detection of opioids and benzodiazepines in a clinical setting*; Addict Behav **25**, 451 (2000).
- [164] G. Sakai, K. Ogata, T. Uda, N. Miura, N. Yamazoe; *A surface plasmon resonance-based immunosensor for highly sensitive detection of morphine*; Sensor Actuat B-Chem **49**, 5 (1998).
- [165] J.E. Wallace, S.C. Harris, M.W. Peek; *Determination of morphine by liquid-chromatography with electrochemical detection*; Anal Chem **52**, 1328 (1980).
- [166] W.J. Liaw, S.T. Ho, J.J. Wang, O.Y.P. Hu, J.H. Li; *Determination of morphine by high-performance liquid chromatography with electrochemical detection: application to human and rabbit pharmacokinetic studies*; J Chromatogr B **714**, 237 (1998).
- [167] A. Niazi, A. Yazdanipour; *Determination of trace amounts of morphine in human plasma by anodic adsorptive stripping differential pulse voltammetry*; Chinese Chem Lett **19**, 465 (2008).
- [168] M.R. Ganjali, P. Norouzi, R. Dinarvand, R. Farrokhi, A.A. Moosavi-Movahedi; *Development of fast Fourier transformations with continuous cyclic voltammetry at an Au microelectrode and its application for the sub nano-molar monitoring of methyl morphine trace amounts*; Mater. Sci. Eng. C-Biomimetic Supramol. Syst. **28**, 1311 (2008).
- [169] P. Norouzi, M.R. Ganjali, A.A. Moosavi-movahedi, B. Larijani; *Fast Fourier transformation with continuous cyclic voltammetry at an Au microelectrode for the determination of morphine in a flow injection system*; Talanta **73**, 54 (2007).
- [170] F. Xu, M. Gao, L. Wang, T. Zhou, L. Jin, J. Jin; *Amperometric determination of morphine on cobalt hexacyanoferrate modified electrode in rat brain microdialysates*; Talanta **58**, 427 (2002).
- [171] A. Salimi, R. Hallaj, G.R. Khayatian; *Amperometric detection of morphine at preheated glassy carbon electrode modified with multiwall carbon nanotubes*; Electroanal **17**, 873 (2005).

- [172] K.C. Ho, C.Y. Chen, H.C. Hsu, L.C. Chen, S.C. Shiesh, X.Z. Lin; *Amperometric detection of morphine at a Prussian blue-modified indium tin oxide electrode*; *Biosens Bioelectron* **20**, 3 (2004).
- [173] W.M. Yeh, K.C. Ho; *Amperometric morphine sensing using a molecularly imprinted polymer-modified electrode*; *Anal Chim Acta* **542**, 76 (2005).
- [174] K.C. Ho, W.M. Yeh, T.S. Tung, J.Y. Liao; *Amperometric detection of morphine based on poly(3,4-ethylenedioxythiophene) immobilized molecularly imprinted polymer particles prepared by precipitation polymerization*; *Anal Chim Acta* **542**, 90 (2005).
- [175] F.R.R. Teles, L.R. Fonseca; *Applications of polymers for biomolecule immobilization in electrochemical biosensors*; *Mater. Sci. Eng. C-Biomimetic Supramol. Syst.* **28**, 1530 (2008).
- [176] N.F. Atta, A. Galal, R.A. Ahmed; *Direct and simple electrochemical determination of morphine at PEDOT modified Pt electrode*; *Electroanal* **23**, 737 (2011).
- [177] L. Jones, P.N. Pintauro, H. Tang; *Colon exclusion properties of polyphosphazene ion-exchange membranes*; *J Membrane Sci* **162**, 135 (1999).
- [178] F. Muller, C.A. Ferreira, L. Franco, J. Puiggali, C. Aleman, E. Armelin; *New sulfonated polystyrene and styrene-ethylene/butylene-styrene block copolymers for applications in electro dialysis*; *J Phys Chem B* **116**, 11767 (2012).
- [179] F.M.B. Coutinho, S.M. Rezende, B.G. Soares; *Characterization of sulfonated poly(styrene-divinylbenzene) and poly(divinylbenzene) and its application as catalysts in esterification reaction*; *J Appl Polym Sci* **102**, 3616 (2006).
- [180] L.X. Tuan, B. Hanae, M.V. Lara, B.H. Claudine; *Cation exchange membranes based on grafted PS/DVB-ETFE films: An investigation of their electrochemical characteristics in sulfuric acid*; *Electrochim Acta* **54**, 5992 (2009).
- [181] J. Tiihonen, M. Laatikainen, I. Markkanen, E. Paatero; *Sorption of neutral components in ion-exchange resins. 1. Effect of cross-link density and counterion on selective sorption of water-ethanol mixtures in sulfonated PS-DVB resins*; *Ind Eng Chem Res* **38**, 4832 (1999).
- [182] T. Sata; *Studies on ion-exchange membranes with permselectivity for specific ions in electro dialysis*; *J Membrane Sci* **93**, 117 (1994).
- [183] T. Sata; *Studies on anion exchange membranes having permselectivity for specific anions in electro dialysis - effect of hydrophilicity of anion exchange membranes on permselectivity of anions*; *J Membrane Sci* **167**, 1 (2000).
- [184] O. Bertran, D. Curcò, J. Torras, C.A. Ferreira, C. Aleman; *Field-induced transport in sulfonated poly(styrene-co-divinylbenzene) membranes*; *Macromolecules* **43**, 10521 (2010).
- [185] J.P. Lu, P.F. Xia, P.K. Lo, Y. Tao, M.S. Wong; *Synthesis and properties of multi-tertiaryamine-substituted carbazole-based dendrimers with an oligothiophene core for potential applications in organic solar cells and light-emitting diodes*; *Chem Mater* **18**, 6194 (2006).
- [186] D. Ma, J.M. Lupton, I.D.W. Samuel, S.C. Lo, P.L. Burn; *Bright electroluminescence from a conjugated dendrimer*; *Appl Phys Lett* **81**, 2285 (2002).
- [187] P. Furuta, J. Brooks, M.E. Thompson, J.M.J. Fréchet; *Simultaneous light emission from a mixture of dendrimer encapsulated chromophores: A model for single-layer multichromophoric organic light-emitting diodes*; *J Am Chem Soc* **125**, 13165 (2003).
- [188] A. Pogantsch, F.P. Wenzl, E.J.W. List, G. Leising, A.C. Grimsdale, K. Mullen; *Polyfluorenes with dendron side chains as the active materials for polymer light-emitting devices*; *Adv Mater* **14**, 1061 (2002).
- [189] T.W. Kwon, M.M. Alam, S.A. Jenekhe; *n-Type conjugated dendrimers: Convergent synthesis, photophysics, electroluminescence, and use as electron-transport materials for light-emitting diodes*; *Chem Mater* **16**, 4657 (2004).

-
- [190] S.A. Ponomarenko, S. Kirchmeyer, A. Elschner, B.H. Huisman, A. Karbach, D. Drechsler; *Star-shaped oligothiophenes for solution-processible organic field-effect transistors*; Adv Funct Mater **13**, 591 (2003).
- [191] A. Mishra, C.Q. Ma, P. Bauerle; *Functional oligothiophenes: Molecular design for multidimensional nanoarchitectures and their applications*; Chem Rev **109**, 1141 (2009).
- [192] C.J. Xia, X.W. Fan, J. Locklin, R.C. Advincula; *A first synthesis of thiophene dendrimers*; Org Lett **4**, 2067 (2002).
- [193] C.J. Xia, X.W. Fan, J. Locklin, R.C. Advincula, A. Gies, W. Nonidez; *Characterization, supramolecular assembly, and nanostructures of thiophene dendrimers*; J Am Chem Soc **126**, 8735 (2004).
- [194] C.Q. Ma, E. Mena-Osteritz, T. Debaerdemaeker, M.M. Wienk, R.A.J. Janssen, P. Bauerle; *Functionalized 3D oligothiophene dendrons and dendrimers - Novel macromolecules for organic electronics*; Angew Chem Int Edit **46**, 1679 (2007).
- [195] M.R. Harpham, O. Suzer, C.Q. Ma, P. Bauerle, T. Goodson; *Thiophene dendrimers as entangled photon sensor materials*; J Am Chem Soc **131**, 973 (2009).
- [196] W.J. Mitchell, N. Kopidakis, G. Rumbles, D.S. Ginley, S.E. Shaheen; *The synthesis and properties of solution processable phenyl cored thiophene dendrimers*; J Mater Chem **15**, 4518 (2005).
- [197] W.W.H. Wong, C.Q. Ma, W. Pisula, C. Yan, X.L. Feng, D.J. Jones, K. Mullen, R.A.J. Janssen, P. Bauerle, A.B. Holmes; *Self-assembling thiophene dendrimers with a hexa-perihexabenzocoronene core-synthesis, characterization and performance in bulk heterojunction solar cells*; Chem Mater **22**, 457 (2010).
- [198] S.X. Deng, T.M. Fulghum, G. Krueger, D. Patton, J.Y. Park, R.C. Advincula; *Hybrid gold-nanoparticle-cored conjugated thiophene dendrimers: synthesis, characterization, and energy-transfer studies*; Chem-Eur J **17**, 8929 (2011).
- [199] P. Sonar, H. Benmansour, T. Geiger, A.D. Schluter; *Thiophene-based dendronized macromonomers and polymers*; Polymer **48**, 4996 (2007).
- [200] M. Kimura, A. Kitao, T. Fukawa, H. Shirai; *Rodlike macromolecules through spatial overlapping of thiophene dendrons*; Chem-Eur J **17**, 6821 (2011).
- [201] G.B. Griffin, P.M. Lundin, B.S. Rolczynski, A. Linkin, R.D. McGillicuddy, Z.A. Bao, G.S. Engel; *Ultrafast energy transfer from rigid, branched side-chains into a conjugated, alternating copolymer*; J Chem Phys **140** (2014).
- [202] J.M. Oliveira, A.J. Salgado, N. Sousa, J.F. Mano, R.L. Reis; *Dendrimers and derivatives as a potential therapeutic tool in regenerative medicine strategies-A review*; Prog Polym Sci **35**, 1163 (2010).
- [203] J.L. de Paz, C. Noti, F. Bohm, S. Werner, P.H. Seeberger; *Potential of fibroblast growth factor activity by synthetic heparin oligosaccharide glycodendrimers*; Chem Biol **14**, 879 (2007).
-

CHAPTER 2

OBJECTIVES

"But I don't want to go among mad people," Alice remarked.

"Oh, you can't help that," said the Cat: "we're all mad here. I'm mad. You're mad."

"How do you know I'm mad?" said Alice.

"You must be," said the Cat, "or you wouldn't have come here."

Lewis Carrol, *Alice's Adventures in Wonderland* (1865)

CHAPTER 2

OBJECTIVES

The general objective of this Thesis could be summed up by the attempt to contribute to the nanotechnological scientific branch through the inspection of physicochemical properties of innovative polymeric systems with the aim of providing new information for future applications in the design of nanodevices. Concretely, this global target has been reached through some specific objectives corresponding to each one of the main research lines of this dissertation. The specific purposes related to each chapter are listed below.

CHAPTER 4. DETECTION BASED ON CONDUCTING POLYMERS

Detection studies presented in this Thesis are focused on the comparison of the interactions between different CPs and a given analyte. Comparison of the strength of such interactions with the observed detection abilities is expected to provide important information about the detection mechanisms, which have been related with the molecular recognition process. In particular, the research showed in this chapter is centered in the following issues:

- i. Comparison of the different abilities exhibited by PNCPy and PNMPy to detect DA and analysis of the influence of the substituent attached to the N-position of the methyl ring into the DA detection process.
- ii. Evaluation the intrinsic detection ability of PEDOT, P3MT, PPy, PNMPy and PNCPy to detect MO and analysis of the secondary interactions that participate in the MO recognition process.

CHAPTER 5. HYDRONIUM TRANSPORT IN CATION EXCHANGE MEMBRANES

Following the investigations of our group in electro dialysis membranes, the transport of hydronium ions in sulfonated P(S-DVB) membranes has been investigated in this Thesis. The specific objectives of these studies are the following:

- iii. Influence of both the strength of the electric field and the temperature in the proton transport mechanism and proton transport properties (*i.e.* diffusion, velocity and conductivity).
- iv. Effect of the strength of the electric field and the temperature in the hydration shell surrounding the hydronium ions transported during the electro dialysis process.

CHAPTER 6. ATOMISTIC PROPERTIES OF DENDRONIZED POLYMERS

Molecular dynamics simulations have been used in this Thesis to get new microscopic insights into both the interactions responsible of the particular viscoelastic behavior of protected DPs as well as of the internal organization of deprotected (*i.e.* charged) DPs. More specifically, the issues examined in this work can be summarized as follow:

- v. Inter- and intramolecular hydrogen bonds and π,π -interactions have been characterized for a DP of generation four considering both an isolated chain and complexes formed by chains associated with different degrees of interpenetration.
- vi. The changes in the structure and properties produced by the deprotection of DPs during the divergent synthesis approach have been investigated. Special attention has been given to the relationship between the DP generation and the penetrability of water.

CHAPTER 7. THIOPHENE-BASED DENDRIMERS AND DENDRONIZED POLYMERS

In this Thesis I have extended previous theoretical studies of the group devoted to investigate the properties of all-thiophene dendrimers. For this purpose, QM calculations and MD simulations have been conducted not only on all-thiophene dendrimers but also on macromonomers and the corresponding dendronized polymers. The specific objectives of these studies can be summarized as follows:

- vii. The influence of both the number of thiophene rings (n) and the molecular architecture of all-thiophene dendrimers on the molecular geometry, the ionization potential and the lowest $\pi-\pi^*$ transition energy has been studied considering both the neutral and oxidized state.
- viii. An empirical model to predict the lowest $\pi-\pi^*$ transition energy of all-thiophene dendrimers with a very large number of rings, independently of their symmetric or asymmetric molecular architecture, has been developed using the results derived from quantum mechanical calculations on dendrimers with $n \leq 45$.
- ix. The structure and internal organization of macromonomers and DPs derived from all-thiophene dendrimers have been investigated using a multi-scale approach that combines quantum mechanical calculations with classical MD simulations.

CHAPTER 3

METHODOLOGY

'Une intelligence qui, pour un instant donné, connaîtrait toutes les forces dont la nature est animée, et la situation respective des êtres qui la composent, si d'ailleurs elle était assez vaste pour soumettre ces données à l'Analyse, embrasserait dans la même formule les mouvements des plus grands corps de l'univers et ceux du plus léger atome: rien ne serait incertain pour elle et l'avenir, comme le passé serait présent à ses yeux.'

[Given for one instant an intelligence which could comprehend all the forces by which nature is animated and the respective situation of the beings who compose it -an intelligence sufficiently vast to submit these data to analysis -it would embrace in the same formula the movements of the greatest bodies of the universe and those of the lightest atom; for it, nothing would be uncertain and the future, as the past, would be present to its eyes.]

Pierre-Simon Laplace, *Essai philosophique sur les probabilités*
(1840)

CHAPTER 3

METHODOLOGY

Computational chemistry is a fast-emerging discipline which implements theoretical models with the aim of dealing with the modeling and the computer simulations of systems such as biomolecules, polymers, drugs, inorganic and organic molecules, and so on. Computational chemistry faces chemical problems according to two formalisms: quantum mechanics (QM) and classical mechanics. The main difference between both formalisms is the level of detail in the treatment of the matter. QM calculations require a big amount of CPU time and, since it increases exponentially with the size of the system, only small systems are affordable by using this formalism. Bigger systems are studied using classical methods. It is worth noting that within the huge variety of methodologies developed inside the classical formalism this thesis only has taken into account molecular dynamics (MD).

Since each work presented in the following chapters contains a specific section devoted to the used methodology, only a general overview of QM and MD based methods is presented here. A deeper description of these methods can be found in many text books, such as *Essentials of Computational Chemistry: Theories and Models* by C. Cramer; *Exploring chemistry with electronic structure methods* by J.B.F.E. Foresman; *Understanding Molecular Simulation* by D. Frenkel and B. Smit or *The Art of Molecular Dynamics Simulation* by D.C. Rapaport.

3.1. QUANTUM MECHANICAL METHODS

The postulates and theorems of QM form the rigorous foundation for the prediction of observable chemical properties from first principles. QM postulates that microscopic systems are completely described by wave functions, Ψ , which characterize all the physical properties of matter. In particular, when appropriate quantum mechanical operators (functions) act upon Ψ , they return physical observable properties of the

system; so, that fact allows one to predict the probability of finding the system to exhibit a particular value or range of values [1]. In mathematical notation,

$$\vartheta \psi = e \psi \quad (3.1)$$

where ϑ is an operator and e is a scalar value for some property of the system. Another important aspect in QM formalism is that the product of the wave function with its complex conjugate $|\psi^*\psi|$ has units of probability density¹. Thus, the probability that a chemical system will be found within some region of multi-dimensional space is equal to the integral of $|\psi|^2$ over that region of space. Furthermore, the expectation (average observed) value of any operator can be calculated as

$$e = \frac{\int \psi^* \vartheta \psi}{\int \psi^* \psi} \quad (3.2)$$

3.1.1. THE HAMILTONIAN OPERATOR

The operator in equation (3.1) that returns the energy of the studied system as an eigenvalue E , is called the Hamiltonian operator, H . Thus, equation (3.1) can be rewritten as follows:

$$H \psi = E \psi \quad (3.3)$$

which is known as the Schrödinger time-independent equation. The typical form of the Hamiltonian operator of a polyatomic system can be expressed as:

$$H = - \sum_i \frac{\hbar^2}{2m_e} \nabla_i^2 - \sum_k \frac{\hbar^2}{2m_k} \nabla_k^2 - \sum_i \sum_k \frac{e^2 Z_k}{r_{ik}} + \sum_{i<j} \frac{e^2}{r_{ij}} + \sum_{k<l} \frac{e^2 Z_k Z_l}{r_{kl}} \quad (3.4)$$

where i and j run over electrons, k and l run over nuclei, \hbar is the reduced Planck's constant, m_e and m_k are the mass of the electron and k -nucleus respectively, ∇^2 is the Laplacian operator, e is the electron charge, Z is an atomic number, and r_{ab} is the distance between particles a and b . The five contributions to the Hamiltonian in equation (3.4) correspond to the kinetic energies of the electrons and nuclei, the attraction of the electrons to the nuclei, and the interelectronic and internuclear repulsions.

Unfortunately, the Schrödinger's equation cannot be solved analytically excepting in the case of mono-electronic atoms. For this reason in case of poly-electronic atoms some approximations need to be introduced to provide practical methods.

¹ In case we only work with real, and not complex, wave functions; the complex conjugated symbol (*) is omitted, and the probability density can be expressed as $|\psi|^2$.

3.1.2. THE BORN-OPPENHEIMER APPROXIMATION

The Hamiltonian in equation (3.4) contains pairwise attraction and repulsion terms, implying that no particle is moving independently of all of the others. In order to simplify the problem the robust so-called Born-Oppenheimer approximation is invoked. As the masses of nuclei are much heavier than electrons, nuclei move much more slowly than electrons. Hence, in many cases, one can consider the electrons are moving in a field produced by the fixed nuclei. Under these considerations, the Born-Oppenheimer approximation separates the movement of electrons and nuclei. In consequence, the second term in Hamiltonian expression is neglected, and the final term, the repulsion between nuclei, can be treated as a constant for a fixed configuration of the nuclei. This assumption leads to the so-called electronic Hamiltonian operator,

$$H_{elec} = - \sum_i \frac{\hbar^2}{2m_e} \nabla_i^2 - \sum_i \sum_k \frac{e^2 Z_k}{r_{ik}} + \sum_{i < j} \frac{e^2}{r_{ij}} \quad (3.5)$$

Taking into account (3.3) and (3.5), the solution to the Schrödinger equation involving the electronic Hamiltonian

$$H_{elec} \Psi_{elec} = E_{elec} \Psi_{elec} \quad (3.6)$$

will be the electronic wave function, Ψ_{elec} , which describes the motion of electrons and depends explicitly on the electronic coordinates and parametrically on the nuclear ones. Thus, the total energy of the system, E , will include the constant nuclear repulsion term and the E_{elec} term obtained taking into account (3.2) from solving (3.6).

$$E = E_{elec} + \sum_{k < l} \frac{e^2 Z_k Z_l}{r_{kl}} \quad (3.7)$$

3.1.3. THE WAVE FUNCTION

From QM postulates one can extract certain constraints on what constitutes an acceptable wave function. Thus, as $|\Psi|^2$ is interpreted as probability density for the particle(s) it describes, it must be quadratically integrable. Moreover, as electrons are fermions and obey the Pauli's exclusion principle, the electronic wave function should be antisymmetric with respect to the interchange of the coordinates of any two electrons. However, none of the equations showed above offer us any prescription for obtaining mathematical functions which describe wave functions.

Molecular orbital theory decomposes the wave function, Ψ , into a combination of orthonormal set of molecular orbitals: ϕ_1, ϕ_2, \dots . A typical way to decide the mathematical expression of these set of functions with which to construct a trial wave function is

judging the quality of our wave function (in comparison with one other) by evaluation of the energy eigenvalues associated with each. Then, taking into account the variational principle², the set with the lowest energy will be a best approximation to the ‘real’ wave function, and this will be the best one to be used for computing other properties by the application of other operators.

3.1.3.1. SLATER DETERMINANT

The simplest antisymmetric combination of molecular orbitals is a determinant. Before forming it, one has to take into account that electrons have associated a spin state (up, $+1/2$ or down, $-1/2$). Then, a total wave function, Ψ , can be built up as a combination of spin-orbital functions, where every spin-orbital function is the product of the i -electron molecular orbital (that describes electron spatial location) and their spin function.

Defining $\alpha(i)$ and $\beta(i)$ as the spin functions for the i th electron, where α is equal to 1 when the electron spin is up and β takes the value of unit when the spin is down; one can now build a closed shell wave function as the so-called Slater determinant. Then, in a system with N electrons defined by $N/2$ molecular orbitals and its corresponding opposite spin functions, the Slater determinant will be written as follows.

$$\Psi = \frac{1}{\sqrt{N!}} \begin{vmatrix} \phi_1(\mathbf{r}_1)\alpha(1) & \phi_1(\mathbf{r}_1)\beta(1) & \phi_2(\mathbf{r}_1)\alpha(1) & \phi_2(\mathbf{r}_1)\beta(1) & \cdots & \phi_{\frac{N}{2}}(\mathbf{r}_1)\beta(1) \\ \phi_1(\mathbf{r}_2)\alpha(2) & \phi_1(\mathbf{r}_2)\beta(2) & \phi_2(\mathbf{r}_2)\alpha(2) & \phi_2(\mathbf{r}_2)\beta(2) & \cdots & \phi_{\frac{N}{2}}(\mathbf{r}_2)\beta(2) \\ \vdots & \vdots & \vdots & \vdots & \cdots & \vdots \\ \phi_1(\mathbf{r}_i)\alpha(i) & \phi_1(\mathbf{r}_i)\beta(i) & \phi_2(\mathbf{r}_i)\alpha(i) & \phi_2(\mathbf{r}_i)\beta(i) & \cdots & \phi_{\frac{N}{2}}(\mathbf{r}_i)\beta(i) \\ \vdots & \vdots & \vdots & \vdots & \cdots & \vdots \\ \phi_1(\mathbf{r}_n)\alpha(n) & \phi_1(\mathbf{r}_n)\beta(n) & \phi_2(\mathbf{r}_n)\alpha(n) & \phi_2(\mathbf{r}_n)\beta(n) & \cdots & \phi_{\frac{N}{2}}(\mathbf{r}_n)\beta(n) \end{vmatrix} \quad (3.8)$$

Each row is formed by representing all possible assignments of electron i to all orbital-spin combinations, the initial factor being necessary for normalization.

3.1.3.2. THE LCAO BASIS SET APPROACH

The next approximation for the construction of the wave function expresses the molecular orbitals, ϕ_i , as linear combinations of pre-defined sets of N one-electron functions known as basis set, $\varphi_1, \dots, \varphi_N$. An individual molecular orbital can be represented such as:

$$\phi_i = \sum_{\mu=1}^N c_{\mu i} \varphi_{\mu} \quad (3.9)$$

² The variational principle says that for the ground state of any antisymmetric normalized function of the electronic coordinates, which we will denote Ξ , then the expectation value for the energy corresponding to Ξ will always be greater than the energy for the exact wavefunction: $E(\Xi) > E(\psi)$

where the coefficients $c_{\mu i}$ are known as the molecular expansion coefficients, and the basis functions are chosen to be normalized. This construction is known as the linear combination of atomic orbitals (LCAO) approach.

These basis sets are usually centered on the atomic nuclei and bear some resemblance to atomic orbitals because, from a chemical point of view, one can anticipate that atomic functions will be efficient functions for the representation of molecular orbitals. However, these basis functions do not have to be necessarily atomic orbitals but any set of mathematical functions whose linear combination yield useful representations of molecular orbitals.

3.1.3.3. GAUSSIAN FUNCTIONS

In the early days of quantum chemistry the so-called Slater type orbitals (STOs) were used as basis functions because of their similarity with the solutions of the hydrogen atom. Their general definition is

$$S_{nlm}^{\zeta}(\mathbf{r}, \theta, \varphi) = N r^{n-1} e^{-\zeta r} Y_l^m(\theta, \varphi) \quad (3.10)$$

where N is a normalization constant, Y_l^m refers to the spherical harmonics functions, ζ is called the exponent, and n, l, m are the quantum numbers (*i.e.* principal, angular momentum and magnetic, respectively). However, from a computational point of view the STOs have the severe shortcoming that most of the involved integrals do not have analytical form and, consequently, large computational time is required by this procedure.

In contrast, it is much faster to work with Cartesian Gaussian functions in the evaluation of the two-electron integrals. For this pragmatic reason, Gaussian type orbitals (GTOs) became the most popular basis functions in quantum chemistry. GTOs have the following form in Cartesian coordinates:

$$g_{ijk}^{\zeta}(\mathbf{r}) = N x^i y^j z^k e^{-\zeta r^2} \quad (3.11)$$

It is worth noting that the i, j, k numbers in Cartesian coordinates are not the quantum numbers but instead parameters. However, the sum of them is analogous to the angular momentum for atoms, enabling to mark functions as *s*-type ($L = i + j + k = 0$), *p*-type ($L = 1$), *d*-type ($L = 2$), *etc.*

The Gaussian function described in (3.11) is typically known as a *primitive Gaussian*. Linear combination of *primitive Gaussians* is used to form the actual basis functions. The latter are called *contracted Gaussians* and have the form:

$$\varphi_{\mu} = \sum_p d_{\mu p} g_p \quad (3.12)$$

where $d_{\mu p}$ are fixed constants within a given basis set. Finally, all of these constructions result in the following expansion for molecular orbitals [2].

$$\phi_i = \sum_{\mu} c_{\mu i} \Phi_{\mu} = \sum_{\mu} c_{\mu i} \left[\sum_p d_{\mu p} g_p \right] \quad (3.13)$$

When using Gaussian function basis set, it is far from trivial to decide what set of *contracted Gaussians* are appropriate for the system under investigation. However, the minimum basis set that must be used corresponds to the number of atomic orbitals in the system. In the following lines a brief survey of different kinds of basis sets is given.

STO- n G Basis Set

This kind of basis sets are characterized by the use of n Gaussian primitive functions for each basis function in which coefficients from equation (3.11) are fitted to approximate the corresponding Slater function [3]. In this sense one can distinguish between STO-3G, STO-4G or STO-6G basis sets in which three, four and six Gaussian functions have been used, respectively.

Split-Valence Basis Set

STO- n G basis sets are not flexible enough for accurate representation of orbitals, a more accurate description being necessary. In split-valence basis sets core electrons are described using one single contracted gaussian function, while valence electrons are described by two or more basis functions. In the present thesis double and triple-zeta Pople style basis sets [4,5] have been used. For example, a 6-31G basis set is a double split valence basis set. This notation means that the core orbitals are described by one contracted Gaussian function comprised of six primitive Gaussians. The valence orbital has been split into two contracted Gaussians, one comprised of three primitive Gaussians and the other just one primitive Gaussian. As another example a 6-311G basis set is a triple split valence basis set. The core orbital is still a contraction of six primitive Gaussians. However the valence is now split into three parts which are contractions of three, one, and one primitive Gaussians, respectively.

Polarized Basis Sets

Split-Valence basis sets allow orbitals to change size, but not to change shape. However, when atoms bind each other in order to form molecules, atomic charge distribution is often distorted. Polarized basis sets remove this limitation by adding orbitals with angular momentum beyond what is required for the ground state to the description of each atom. So polarized basis sets add an extra p -orbital for the hydrogen, d -orbitals for the first and second row elements, and f -orbitals for the transition metals will be added. The notation for indicating the addition of polarized functions is to write (d) or (d,p) after the basis set; for example, 6-31G(d,p).

Diffuse Functions

Diffuse functions allow orbitals to occupy a larger region of space, they are added to reproduce in a better way the behavior of electrons that are at a larger distance from the nuclei: molecules with lonely pairs, anions, systems in their excited states, systems with low ionization potentials, *etc.* Diffuse functions are denoted with a plus sign (+) when they are added only to heavy atoms and with two plus signs (++) when they are also added to helium and hydrogen atoms.

Basis Set Superposition Error

Finite basis functions, such as Gaussian functions, undergo a problem known as basis set superposition error (BSSE) [6]. As the atoms of interacting molecules approach one another, their basis functions overlap. Each monomer feels the basis functions of the other, which implies that the basis set is larger than that of isolated monomers and, consequently, an artificial stabilization of the cluster is done. Although BSSE is present in all molecular calculations involving finite basis sets, in practice its effect is important in calculations involving weakly bound complexes.

One widely used method to assess the BSSE is the Counterpoise (Cp) correction scheme of Boys and Bernardi [7]. The Cp approach calculates the BSSE employing ‘ghost orbitals’. In the uncorrected calculation of dimer AB , the dimer basis set is the union of the two monomer basis sets, and the associated interaction energy, E_{int} , is

$$E_{int}(G) = E_{AB}(G, AB) - E_A(A) - E_B(B) \quad (3.14)$$

where G denotes the coordinates that specify the geometry of the dimer, $E_{AB}(G, AB)$ is the total energy of the dimer AB calculated with the full basis set AB at that geometry and, $E_A(A)$ and $E_B(B)$ are the total energy of monomers A and B , respectively, calculated with their corresponding basis sets A and B respectively.

Due to the incompleteness of the basis set for A and B , there exists a BSSE in E_{int} , when using the Counterpoise method, the corrected interaction energy is calculated as,

$$E_{int}^{CP}(G) = E_{AB}(G, AB) - E_A(G, AB) - E_B(G, AB) \quad (3.15)$$

where $E_A(G, AB)$ and $E_B(G, AB)$ denote the total energies of monomers A and B , respectively, computed with the dimer basis set at geometry G (*i.e.* in the calculation of monomer A the basis set of monomer B is present at the same location as in dimer AB , but the nuclei of B are not). The counterpoise corrected energy is:

$$E_{AB}^{CP} = E_{AB}(G, AB) + E_{int}^{CP}(G) - E_{int}(G) \quad (3.16)$$

3.1.3.4. CLOSED-SHELL AND OPEN-SHELL SYSTEMS

Closed-shell systems are those where all orbitals are doubly occupied. In other words, all electrons are split in pairs and, within each pair, electrons with opposite spins occupy the same spatial orbitals. These systems can be handled by using the so-called restricted methods, which use a single molecular orbital twice (one multiplied by the α spin function and the other multiplied by the β spin function) in the Slater determinant (3.8).

Conversely open-shell systems are those where some of the electrons are unpaired, leading to singly occupied molecular orbitals. These systems can be treated by using unrestricted methods, which use different orbitals for different spins.

3.1.4. HARTREE-FOCK APPROXIMATION

The Hartree-Fock (HF) approximation method is typically used to solve in the Born-Oppenheimer approximation the time-independent Schrödinger equation (3.6) for multi-electron systems. Due to the nonlinearities introduced by this approximation, the equations are solved iteratively. The procedure which does so is called the Self-Consistent Field (SCF) method [8-10].

Under this treatment, the approximation to the wave function is equivalent to a mean-field solution of Schrodinger's equation in which each electron moves within an average field due to the presence of all of the other electrons.

Considering a closed-shell system and substituting the Slater determinant (3.8) as a trial wave function into the polyelectronic Hamiltonian (3.5), the expected energy, after simplification of integrals, is given by the following expression:

$$E_{elec} = 2 \sum_{i=1}^{N/2} H_{ii}^{core} + \sum_{i=1}^{N/2} \sum_{j=1}^{N/2} 2(J_{ij} - K_{ij}) \quad (3.17)$$

where H_{ii}^{core} gives the kinetic and potential energy of the electrons moving in the field of the nuclei; J_{ij} gives the electrostatic repulsion between electrons; and K_{ij} gives the so-called exchange interactions. This last term stems from the tendency of electrons with the same spin to 'avoid' each other within the framework of Pauli exclusion principle.

For a more compacted notation we will express the combination of the spatial orbital wave function, ϕ , with the spin function by the symbol χ . Then, terms involved in (3.17) are calculated as

$$H_{ii}^{core} = \int d\tau_1 \chi_i(1) \left[-\frac{1}{2} \nabla_i^2 - \sum_k \frac{Z_k}{r_{1k}} \right] \chi_i(1) \quad (3.18)$$

$$J_{ij} = \int d\tau_1 d\tau_2 \chi_i(1) \chi_j(2) r_{12}^{-1} \chi_i(1) \chi_j(2) \quad (3.19)$$

$$K_{ij} = \int d\tau_1 d\tau_2 \chi_i(1) \chi_j(2) r_{12}^{-1} \chi_i(2) \chi_j(1) \quad (3.20)$$

It should be remarked that all equations have been written in atomic units, and fundamental constants have been omitted for clarity.

3.1.5. ELECTRON DENSITY COMPUTATION

One of the most important properties we can examine using electron structure calculations is the electron density, that is, the probability density with which we expect to see an electron as a function of spatial position. For a set formed by an arbitrary number of one-electron orbitals ϕ_i , the electron expressed using the probabilistic interpretation of the wavefunction is:

$$\rho(\mathbf{r}) = \sum_i |\phi_i(\mathbf{r})|^2 \quad (3.21)$$

3.1.6. AB INITIO CALCULATIONS

Ab initio calculations are grounded on solving the Schrödinger equation without using any empirical adjustment, *i.e.* first principles. Thus *ab initio* calculations are exclusively based on basic physical theory.

3.1.6.1. HARTREE-FOCK METHOD

The simplest *ab initio* method is the HF method or SCF procedure. Taking into account the formalism exposed in previous sections, the basic conceptual approach to these computations consists of building up HF wave function as a single Slater determinant of spin orbitals. Then Schrödinger equation is solved through an iterative process applying the variational principle. The best approximate wave function is obtained by varying iteratively the weighting molecular expansion coefficients, $c_{\mu i}$, until the energy expectation value of the approximate wave function is minimized.

$$\frac{\partial E}{\partial c_{\mu i}} = \frac{\partial}{\partial c_{\mu i}} \left[\frac{\int d\tau \psi^* H_{elec} \psi}{\int d\tau \psi^* \psi} \right] = 0 \quad (3.22)$$

3.1.6.2. POST HARTREE-FOCK METHODS

The major weakness of the HF method is that it does not describe electron correlation properly since each electron is considered to move in an electrostatic field, whereas actually electrons repel each other. This deficiency makes HF method unreliable to get

accurate estimates of systems where electron correlation plays an important role such as π -stacking interactions or chemical reactions. Post-HF methods correct the aforementioned deficiency. Two of the most used post-HF methods are the Møller-Plesset (MP) procedure [11,12] and the Coupled Cluster (CC) method [13,14].

Møller-Plesset Perturbation Theory

Møller Plesset is based on perturbation theory. The basis of this method is the assumption that, while the HF wavefunction ψ_0 and ground-state energy E_0 are approximate solutions to the Schrödinger equation, they are exact solutions to an analogous problem involving the HF Hamiltonian, H_0 , in place of the “exact” Hamiltonian, H . Assuming that the HF wavefunction and energy are, in fact, very close to the exact wavefunction ψ and ground-state energy E , the exact Hamiltonian operator is defined as the addition of a perturbation operator H' to the unperturbed HF Hamiltonian H_0 :

$$H = H_0 + \lambda H' \quad (3.23)$$

where λ is a dimensionless parameter taking values comprised between 0 and 1. Expanding the exact wavefunction and energy in terms of the Hartree-Fock wavefunction and energy as Taylor series in λ yields.

$$\psi = \psi_0 + \lambda\psi^{(1)} + \lambda^2\psi^{(2)} + \dots + \lambda^n\psi^{(n)} \quad (3.24)$$

$$E = E_0 + \lambda E^{(1)} + \lambda^2 E^{(2)} + \dots + \lambda^n E^{(n)} \quad (3.25)$$

Substituting the expansions (3.23) to (3.25) into the Schrödinger equation and considering only equalities involving like powers of λ ,

$$\begin{aligned} H_0\psi_0 &= E_0\psi_0 \\ H_0\psi^{(1)} + H'\psi_0 &= E_0\psi^{(1)} + E^{(1)}\psi_0 \\ H_0\psi^{(2)} + H'\psi^{(1)} &= E_0\psi^{(2)} + E^{(1)}\psi^{(1)} + E^{(2)}\psi_0 \\ &\vdots \end{aligned} \quad (3.26)$$

Multiplying each of the equations (3.26) by ψ_0 and integrating over all space yields the n th order (MP n) energy. In this framework, the HF energy is the sum of the zero and first-order MP energies, electronic correlation corrections to the energy being taken into account from the summation of the next terms, *i.e.* correlation energy in the MP2 methodology will be $E^{(2)}$ and so on.

Coupled Cluster Method

The Coupled Cluster wave function is written as,

$$\Psi_{CC} = e^T \Psi_0 \quad (3.27)$$

Here Ψ_0 is a Slater determinant, and the exponential operator e^T can be expanded as a Taylor series,

$$e^T = 1 + T + \frac{1}{2}T^2 + \frac{1}{3!}T^3 + \dots = \sum_{k=1}^{\infty} \frac{1}{k!} T^k \quad (3.28)$$

where $T = T_1 + T_2 + T_3 + \dots + T_n$ is the cluster operator and n is the total number of electrons. The T_i operator acting on a HF reference wave function generates all i -th excited Slater determinants,

$$\begin{aligned} T_1 \Psi_0 &= \sum_i^{\text{occ}} \sum_a^{\text{vir}} t_i^a \Psi_i^a \\ T_2 \Psi_0 &= \sum_{i < j}^{\text{occ}} \sum_{a < b}^{\text{vir}} t_{ij}^{ab} \Psi_{ij}^{ab} \end{aligned} \quad (3.29)$$

where the amplitudes t are determined by the constraint imposed by equation (3.27), which must be satisfied. The expansion of T ends at n because no more than n excitations are possible.

3.1.7. SEMIEMPIRICAL METHODS

In contrast of *ab initio* techniques, which are based on first principles, semiempirical methods use experimental parameters to improve the cost in terms of computational resources. The main differences between semiempirical and *ab initio* methods lie basically in four points:

- Semiempirical methods restrict treatment only to valence or π electrons (electrons associated with the core are ignored).
- Minimal basis set is used to describe valence electrons.
- Both core and the two electron repulsion integrals are not calculated from first principle but using empirical data.
- Simplifications in the mathematical model by assuming some matrices as unit matrices.

Except for transition metals, parameterizations are based on reproducing a wide variety of experimental data, including equilibrium geometries, heats of formation, dipole moments and ionization potentials.

3.1.8. DENSITY FUNCTIONAL THEORY METHODS

In section 3.1.6 several different ways to approximately solve the electronic Schrödinger equation through first principle methods have been introduced. These methods share one common feature: they rely on the many body wave function as a central quantity. However, the wave function depends on one spin and three spatial coordinates for every electron (assuming fixed nuclear positions) making it particularly complicated and unintuitive.

Density Functional Theory (DFT) differs from wave function based methods in the fact that the former uses the electron density, $\rho(\mathbf{r})$, as the central quantity. This treatment reduces the dimensionality of the problem, which implies a huge advantage with respect to *ab initio* methodologies. Regardless of how many electrons one has in the system, the density is always 3 dimensional. This fact enables DFT to be applied to much larger systems.

3.1.8.1. HOHENBERG-KOHN THEOREM

Density functional theory was born in 1964 with the paper of Hohenberg and Kohn [15]. The two key points proved in this paper are:

- i. For any system of interacting particles in an external potential, the density is uniquely determined (that is, the external potential is a unique functional of the density).
- ii. A universal functional for the energy can be defined in terms of the density. The exact ground state is the global minimum value of this functional and can be found by using the variational principle.

3.1.8.2. THE SELF-CONSISTENT KOHN-SHAM EQUATIONS

In 1965, Kohn and Sham [16] published a paper which transformed density-functional theory into a practical electronic structure theory. To address this problem they decided to replace the many-electron problem by an exactly equivalent set of self-consistent one-electron Schrödinger-like equations. Thus, the central equation in Kohn-Sham DFT can be written as:

$$\left[-\frac{1}{2}\nabla^2 + v(\mathbf{r}) + \int \frac{\rho(\mathbf{r}')}{|\mathbf{r} - \mathbf{r}'|} d\mathbf{r}' + v_{XC}(\mathbf{r}) \right] \phi_i = \varepsilon_i \phi_i \quad (3.30)$$

Here ϕ_i are the Kohn-Sham orbitals and the electron density is expressed as was showed in equation (3.21). The first left-hand term in (3.30) is the kinetic energy of the non-interacting reference system; next term, $v(\mathbf{r})$, is the external potential; the third expression corresponds to the Hartree potential, and the last one is the exchange-

correlation potential. Finally, ε_i is the energy of the Kohn-Sham orbital. Expression (3.30) can be rewritten in a more compact form,

$$\left[-\frac{1}{2}\nabla^2 + v_{eff}\right]\phi_i = \varepsilon_i\phi_i \quad (3.31)$$

Expression (3.31) is clearly like a Hartree-Fock single particle equation which needs to be solved iteratively. Finally, the ground state energy functional can be determined from the resulting density and is written as:

$$E[\rho] = E_K[\rho] + E_V[\rho] + E_J[\rho] + E_{XC}[\rho] \quad (3.32)$$

being E_K the kinetic energy; E_V the term containing the potential attractive energy electron-nucleus and the repulsive term between nuclei, E_J the Coulombic repulsion between electrons and E_{XC} the interchange-correlation energy.

3.1.8.3. EXCHANGE-CORRELATION FUNCTIONALS

The exchange-correlation functional is a universal function independent of the specific system at hand. However, it is not known its exact form. It includes non-classical aspects of the electron-electron interaction along with the component of the kinetic energy of the real system different from the fictitious non-interacting system. Since E_{XC} is not known exactly, it is necessary to approximate it. A large number of approximations have been developed in the last decades for building up efficient exchange-correlation functionals. In the following lines some of the most common types of E_{XC} approximations are briefly discussed.

Local Density Approximation

In Local Density Approximation (LDA), it is assumed that exchange-correlation energy of an electron, ε_{XC} , at some position \mathbf{r} is equal to that of an electron in a homogeneous electron gas of the same density:

$$E_{XC}^{LDA}[\rho] = \int \rho(\mathbf{r})\varepsilon_{XC}[\rho(\mathbf{r})]d\mathbf{r} \quad (3.33)$$

Systems including spin polarization (*i.e.*, open-shell systems) must use the spin-polarized formalism, its greater generality being sometimes distinguished by the sobriquet Local Spin Density Approximation (LSDA).

The LDA worked excellently in solid state physics applications where metals are reasonably approximated by uniform electron gas. Examples of functionals using homogeneous electron density are: Perdew (PL) [17] and Vosko-Wilk-Nusair (VWN) [18].

Generalized Gradient Approximation

Generalized Gradient Approximation (GGA) goes beyond LDA. In this approximation the exchange-correlation functional not only depends on density $\rho(\mathbf{r})$ but also on gradient of the density, which is accounted for the non-homogeneity of the true electron density. These functionals can be generally written according to the following equation:

$$E_{XC}^{GGA}[\rho] = \int \rho(\mathbf{r}) \varepsilon_{XC}[\rho(\mathbf{r})] \nabla \rho(\mathbf{r}) d\mathbf{r} \quad (3.34)$$

Thus, GGAs are semi-local functionals. The most widely used GGAs are Becke's 1995 (B95) [19], Perdew's 1986 (P86) [20], Perdew-Burke-Ernzerhof (PBE) [21], Perdew-Wang's 1991 (PW91) [22] and Lee-Yang-Parr (LYP) [23].

Hybrid Functionals

Hybrid functionals calculate the exchange-correlation term combining a conventional GGA method with a percentage of HF exchange. The most popular hybrid functional is the so-called B3LYP [23,24]. This functional obtains its energy from:

$$E_{XC}^{B3LYP} = E_{XC}^{LDA} + a_1(E_X^{HF} - E_X^{LDA}) + a_2(E_X^{GGA} - E_X^{LDA}) + a_3(E_C^{GGA} - E_C^{LDA}) \quad (3.35)$$

where E_C is the correlation energy and E_X the exchange energy. The three parameters a_1 , a_2 and a_3 are coefficients determined to fit experimental values of energy whose usual values are 0.2, 0.72 and 0.8 respectively.

Examples of other popular hybrid density functionals that combine a part of HF exchange with DFT exchange-correlation are B3PW91 [22,24], MPW1K [25-27], and X3LYP [22,23,28,29].

Long-Range Corrected Hybrid Functionals

Semilocal (LDA, LSDA or GGA) functionals are fundamentally unable to treat long-range interactions in systems with large intramolecular distances. This limitation can be qualitatively resolved using the long-range corrected hybrid density functionals.

Some of the new methods that take into account long range corrections in the energy computation are wB97X [30], cam-B3LYP [31], B97-D [32] and wB97X-D [33].

The wB97X functional, which was developed by Chai and Head-Gordon, incorporates some short-range Hartree-Fock exchange in addition to the short-range Beckes's 1997 [34] density functional exchange to improve thermochemistry performance, and provide non-local correction to the short-range exchange. The cam-B3LYP is the long-range-corrected version of B3LYP using the Coulomb-attenuating method. The B97-D, which is based on Becke's 1997 GGA functional, takes the basic form of the B97 functional and reoptimizes some parameters to include empirical atom-atom dispersion corrections. In a

similar manner to the B97-D functional, the wB97X-D consists on a re-optimization of the Chai and Head-Gordon functional to include empirical atom–atom dispersion corrections.

3.1.9. TIME DEPENDENT DENSITY FUNCTIONAL THEORY

DFT is a very successful methodology to solve the ground state properties of electrons in time-independents potentials. As the density used in conventional DFT is the ground state density, it is necessary to extend DFT towards methods appropriated for solving excited-states problems or for studying systems with a time-dependent potential. Development of time-dependent density functional theory (TD-DFT) corresponds to such extension of DFT.

As Hohenberg-Kohn theorem to DFT, Runge and Gross enounced in 1984 the key points for developing the TD-DFT formalism [35]. These authors proved that for every single-particle potential $v_{ext}(\mathbf{r}, t)$, which can be expanded into a Taylor series around initial time t_0 , the time-dependent Schrodinger equation can be solved if the initial state, $\phi(t_0) = \phi_0$, is invariable. There is a one-to-one correspondence between $v(\mathbf{r}, t)$ and time-dependent density, $\rho(\mathbf{r}, t)$.

Taking into account the time dependence, the Kohn-Sham equation (3.31) for a polyelectronic system must be written as

$$\left[-\frac{1}{2}\nabla^2 + v_s(\mathbf{r}, t) \right] \phi_i(\mathbf{r}, t) = i \frac{\partial}{\partial t} \phi_i(\mathbf{r}, t) \quad (3.36)$$

where the Kohn-Sham potential $v_s(\mathbf{r}, t)$ is composed of three additive parts: the external potential, $v_{ext}(\mathbf{r}, t)$; the Hartree potential, $v_H(\mathbf{r}, t)$; and the exchange-correlation potential, $v_{XC}(\mathbf{r}, t)$. Within this formalism, the time dependence electron density functional can be expressed as

$$\rho(\mathbf{r}, t) = \sum_i |\phi_i(\mathbf{r}, t)|^2 \quad (3.37)$$

Although TD-DFT is a method designed for systems with a time-dependent external potential, it can be also used to improve the ground state DFT (*e.g.* to compute static properties of atoms and molecules such as transition frequencies and oscillation strength).

3.2. MOLECULAR DYNAMICS METHODS

Once the atomic nature of matter became firmly established, quantum mechanics took charge of the microscopic world. However, the study of large systems (over 1000 atoms)

at QM level become very complex and the consume of computer resources is too high. For this reason, and taking into account that a great deal of the behavior of matter in its various states can still be understood in classical terms, molecular dynamics is used to provide a powerful tool for detailed microscopic modeling on the molecular scale. Within this context, as the *behavior* of matter has to be found in the structure and motion of its constituent building blocks, and the dynamics is contained in the solution to the N -body problem, systems made up to several hundred thousand atoms in which electronic properties do not play a crucial role can be understood through this classical approach.

3.2.1. EQUATIONS OF MOTION

Classical molecular dynamics simulation is a technique for computing the equilibrium and transport properties of a classical N -body system, where the positions and velocities of atoms are allowed to evolve according to the Newton's second law [36],

$$m_i \frac{d^2 \mathbf{r}_i}{dt^2} = \mathbf{f}_i = \sum_{\substack{j=1 \\ (j \neq i)}}^N \mathbf{f}_{ij} \quad (3.38)$$

where \mathbf{r}_i is the 3-dimensional position vector of i -atom with atomic mass m_i , and \mathbf{f}_i is the force acting on it in a given moment. The sum is over all N atoms, excluding i itself, and as Newton's third law implies that $\mathbf{f}_{ij} = -\mathbf{f}_{ji}$, each atom pair need only be examined once. These equations must be numerically integrated [37].

Solving equation (3.38) requires on the one hand computing \mathbf{f}_i , and on the other knowing the initial positions (\mathbf{r}_i) and velocities ($\mathbf{v}_i = d\mathbf{r}_i/dt$) of our system. The initial position of the particles should be chosen compatible with the structure that is aimed to simulate. The initial distribution of velocities is usually obtained through a random distribution function (*i.e.* Maxwell-Boltzmann or Gaussian distribution), in such a way that the center of mass of the system is at rest and the mean kinetic energy is adjusted to a desired temperature value.

3.2.2. THE FORCE FIELD

In a system with N interacting atoms, calculation of the force acting on every atom is reached by differentiating the potential energy, $U(\mathbf{r}_1, \mathbf{r}_2, \dots, \mathbf{r}_N)$, through the following expression:

$$\mathbf{f}_i = -\nabla_i U = -\frac{\partial U}{\partial \mathbf{r}_i} \quad (3.39)$$

The potential energy function decides or approximates the interactions between all atoms in the system. In molecular mechanics (MM) potential energies and their

derivatives forces are evaluated by a set of equations and parameters; the combination of these two distinct components is named *Force Field* (FF).

The potential functions evaluated by the FF can be subdivided into 2 terms, bonding and non-bonding interactions. Within the bonding interactions, MM formalism assumes atoms as non-deformable balls and atomic bonds as springs with harmonic potential behavior. Angle bond alterations from its equilibrium position are also described by harmonic potentials, whereas the torsion angle potential function is a rotation around a middle bond described by a dihedral angle and a coefficient of symmetry n .

The non-bonding interactions mainly comprise two terms. One of them expresses van der Waals interactions and is described by a Lennard-Jones potential function, whereas the second one takes into account electrostatic interactions through a coulombic potential function.

Equation (3.40) summarizes the FF function for the *Assisted Model Building and Energy Refinement* (AMBER) [38,39], which has been the force field used for the MD simulations of this thesis.

$$\begin{aligned}
 U_i(\mathbf{r}_1, \mathbf{r}_2, \dots, \mathbf{r}_N) = & \sum_{bonds} k_{stretch}(\mathbf{r}_i - \mathbf{r}_0)^2 + \sum_{angles} k_{bend}(\theta_i - \theta_0)^2 \\
 & + \sum_{dihedrals} \sum_{n=1}^3 \frac{V_n}{2} [1 + \cos(n\phi_i - \gamma)] \\
 & + \sum_{\substack{j=1 \\ (j \neq i)}}^N \left[\frac{A_{ij}}{r_{ij}^{12}} - \frac{B_{ij}}{r_{ij}^6} \right] + \sum_{\substack{j=1 \\ (j \neq i)}}^N \frac{q_i q_j}{4\pi\epsilon_0 r_{ij}}
 \end{aligned} \tag{3.40}$$

U_i represents the potential energy of the i th atom located at position \mathbf{r}_i ; and the right-handed terms included in equation (3.40) correspond to:

- iii. Bond stretching, that is bond elongation and contraction from its equilibrium value (\mathbf{r}_0). This potential is computed as a harmonic potential with a stretching force constant ($k_{stretch}$). It is worth noting that some others FFs use anharmonic functions for this term, however all models have the same behavior around the equilibrium value.
- iv. Angle bending term, which includes the bending force constant (k_{bend}), the angle between three consecutive atoms and its equilibrium value (θ_i and θ_0).
- v. Torsion angle potential function, which models steric barriers between atoms separated by three covalent bonds. This term contains a dihedral constant ($V_n/2$), setting the energy barrier for the rotation profile, the actual dihedral angle (ϕ_i) and the equilibrium one (γ).

- vi. The van der Waals non-bonding term, a mathematical model following the Lennard-Jones potential that takes into account the attractive and repulsive forces between two atoms separated by a distance r_{ij} . A_{ij} and B_{ij} are parameters that depend of the pair of atoms referring to hard core repulsion and dispersive attraction, respectively.
- vii. The electrostatic interactions, where q_i and q_j are the point charges of atoms i and j respectively, r_{ij} is the distance between them and ϵ_0 is vacuum permittivity.

Constants written in equation (3.40) as well as equilibrium values are characteristics of each atom type and are taken from AMBER libraries. All the terms not found in such libraries must be parameterized either using experimental data or by means of *ab initio* or DFT calculations. In particular, charges used in this thesis have been derived from QM calculations according to the so-called Restrained Electrostatic Potential (RESP) [40,41] formalism. This method fits the electrostatic potential at molecular surfaces derived from QM calculations to the one obtained using the atom-centered point charge model.

The calculation of the FF for computing the force acting on every particle is the most time-consuming part of almost all MD simulations. For this reason, in systems with a huge amount of atoms, sometimes it is useful and necessary to reduce the complexity of the system in terms of parameters and interactions number. This reduction entails less resource consumption, some methods focused on this specific purpose being:

- United Atom (UA) FFs embed light atoms (*i.e.* hydrogen atoms) into the heavy ones they are bound to. This is made by adding the van der Waals radii and charges of the light atoms to the heavy ones. With this approximation we can slash down drastically the number of constants and potential functions to be calculated.
- Inclusion of a cut off, that is threshold distance beyond which we do not take into account non-bonded interactions. This is useful to cut down the number of the aforementioned interactions to be computed. It is assumed that, at distances over the cut off, the contributions of electrostatic and van der Waals interactions to the total potential energy are negligible. The remaining electrostatic contribution in distances beyond cut off, which may be significant, can be modelled by Particle Mesh of Ewald (PME) method [42].
- SHAKE algorithm, which takes as rigid (non-vibrating) the bonds between hydrogen and carbon atoms.

3.2.3. INTEGRATION OF MOTION EQUATIONS

Once all forces between particles have been computed, Newton's equations of motion (3.38) must be integrated. These differential equations are integrated numerically to

update particle positions or both positions and velocities. The commonly applied methods are Verlet algorithm [43] and its modifications [44].

Consider a truncated Taylor expansion of the coordinate variable of a particle – typically $\mathbf{r}(t)$, around time t :

$$\mathbf{r}(t + \delta t) = \mathbf{r}(t) + \dot{\mathbf{r}}(t)\delta t + \frac{1}{2}\ddot{\mathbf{r}}(t)\delta t^2 + \mathcal{O}(\delta t^3) \quad (3.41)$$

where, $\dot{\mathbf{r}}(t)$ is the velocity and $\ddot{\mathbf{r}}(t)$ the acceleration. Note that although $\ddot{\mathbf{r}}(t)$ has been expressed as a function of time, it is actually a known function of the coordinates (via the force law). Similarly to (3.41),

$$\mathbf{r}(t - \delta t) = \mathbf{r}(t) - \dot{\mathbf{r}}(t)\delta t + \frac{1}{2}\ddot{\mathbf{r}}(t)\delta t^2 - \mathcal{O}(\delta t^3) \quad (3.42)$$

The expression required to compute the coordinates of the next time step in function of the current and backward time step is obtained by summing and rearranging equations (3.41) and (3.42):

$$\mathbf{r}(t + \delta t) = 2\mathbf{r}(t) - \mathbf{r}(t - \delta t) + \ddot{\mathbf{r}}(t)\delta t^2 + \mathcal{O}(\delta t^4) \quad (3.43)$$

Notice that the coordinate truncation error is of order $\mathcal{O}(\delta t^4)$. Once new positions have been computed, positions at time $t - \delta t$ may be discarded, and the current calculated positions become the old ones while the new positions become the current ones. The velocity is not directly involved in the solution, but if required it can be obtained from subtracting (3.41) and (3.42), then

$$\dot{\mathbf{r}}(t) = \frac{\mathbf{r}(t + \delta t) - \mathbf{r}(t - \delta t)}{2\delta t} + \mathcal{O}(\delta t^2) \quad (3.44)$$

This expression for the velocity is only accurate to order $\mathcal{O}(\delta t^2)$. However, it is possible to obtain more accurate estimations of velocity using Verlet-like algorithm [44]. Particularly, the modified Verlet algorithm, so-called Velocity Verlet algorithm [45], is one of the most commonly used. In this case:

$$\dot{\mathbf{r}}(t + \delta t) = \dot{\mathbf{r}}(t) + \frac{1}{2}[\ddot{\mathbf{r}}(t) + \ddot{\mathbf{r}}(t + \delta t)]\delta t \quad (3.45)$$

Accordingly, this methodology allows to evaluate velocities, coordinates and accelerations at the same value of the time variable.

It is worth noting that, in the integration of equations of motion, the time step δt might be small enough to simulate those movements with the highest frequencies, which normally corresponds to bond vibrations. Consequently time step takes values of the order of femtosecond.

3.2.4. KEY DETAILS IN FORMALISM

A key point in MD simulations is to accurately simulate the experimental conditions to be replicated. However, the application of MD methods in a rigorous way can be useful only to systems that are too small to meaningfully represent actual chemical systems. Moreover, there are various values for physical conditions, such as number of particles, volume, energy, pressure and/or temperature, that must be readily considered and controlled in the simulations. In order to extend the methodology in such a way as to make it useful for interpreting, reproducing or predicting chemical phenomena, a few other approximations, and/or reformulations of MD are often applied.

3.2.4.1. BOUNDARY CONDITIONS

MD simulations take place in a container of some kind (*i.e.* simulation box), but the use of the proper finite size of the box implies to consider walls as rigid boundaries against which atoms collide while trying to escape from the simulation region. In systems of macroscopic size, only a very small fraction of atoms is close enough to a wall to experience any deviation from the environment prevailing in the interior. However, in a typical MD simulation the fraction of atoms that are immediately adjacent cannot be neglected. Thus, unless the goal of the simulation was the study of behavior near real walls, these are best eliminated.

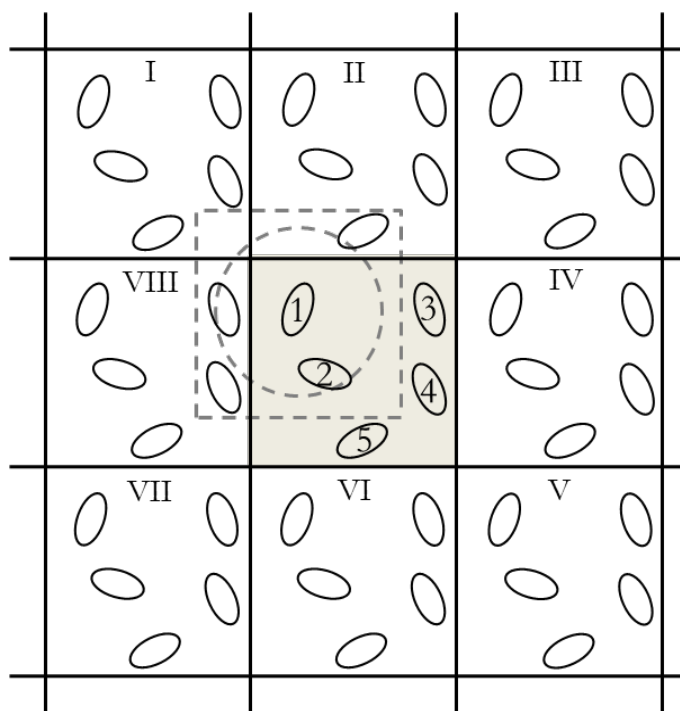


Figure 3.1. Schematic representation of the idea of PBC.

A system that is bounded but free of physical walls can be constructed using periodic boundary conditions (PBC). The introduction of PBC is equivalent to consider an infinite system. The whole system is replicated periodically in all directions, as is shown schematically in Figure 3.1, atoms outside the simulation box being simply images of the atoms simulated in that box. Periodic boundary conditions ensure that all simulated atoms are surrounded by neighboring atoms, either images or not. This condition guarantees that if the trajectory of an individual atom takes it outside the boundary of the simulation cell its image simultaneously enters into the simulation cell from the point related to the exit location by lattice symmetry.

3.2.4.2. TRUNCATION OF INTERACTIONS

The imposition of cutoff distances means that the contribution to the total potential energy of a given particle i is dominated by interactions with neighboring particles located inside such threshold distance. If PBC have been applied, minimum image convention avoids duplicate interactions between atoms i and j by taking into account only the interaction of atom i with the closest j atom, either original or copy (see dashed circle in Figure 3.1). Thus, PBC are useful to correct potential energy errors in the van der Waals non bonded term for those systems in which none of the particles inside the simulation box is covalent bound to a moiety outside the box.

The main problem associated to the evaluation of the Coulombic non bonded term is related with the fact that a sudden cutoff leads to large errors. This entanglement can be solved with the use of the so called Particle Mesh-Ewald summation (PME) [46], which calculates the infinite electrostatic interactions by splitting the summation into short and long range parts. For PME, the cutoff only determines the balance between the two parts, and the long-range part is treated by assigning charges to a grid that is solved in the reciprocal space through Fourier transforms.

3.2.4.3. THERMODYNAMIC ENSEMBLES

An ensemble is a collection of all possible systems having different microscopic states but belonging to a single macroscopic or thermodynamic state [46]. Among the different formal ensembles, the most widely simulated are:

- i. *The canonical ensemble (NVT)*, whose thermodynamic state is characterized by a fixed number of atoms N , fixed volume V and fixed temperature T .
- ii. *The isobaric-isenthalpic ensemble (NPH)*, where the number of atoms N , the pressure P and enthalpy H are fixed.
- iii. *The isobaric-isothermal ensemble (NPT)*, with fixed values of number of atoms N , pressure P and temperature T .
- iv. *The microcanonical ensemble (NVE)*, which corresponds to a closed or isolated system since energy E , besides the number of atoms N and volume V , is fixed.

- v. *The grand canonical ensemble* (μVT), a thermodynamic state characterized by a fixed chemical potential, μ , fixed volume, V , and fixed temperature, T .

As experiments are usually performed at constant temperature and volume (*i.e.*, the canonical ensemble) or constant pressure and temperature (*i.e.*, the isobaric-isothermal ensemble), it is often desirable to simulate these conditions. Consequently, these two distinct ensembles have been employed in the present thesis. Taking into account both canonical and isobaric-isothermal ensembles, it is easy to notice that the control of N and V is trivial in MD simulations by fixing the number of atoms and volume of the simulation box. T can be controlled by applying a thermostat to ensure that the average system temperature is maintained close to the set temperature, and P can be fixed applying a barostat.

3.2.4.4. TEMPERATURE CONTROL

Taking into account that instantaneous temperature T is related to the total kinetic energy of the system (if it is at equilibrium) by

$$T \equiv \frac{1}{k_B N_f} \sum_{i=1}^N m_i \mathbf{v}_i^2 \quad (3.46)$$

where k_B is the Boltzmann constant, N_f the total number of degrees of freedom for a system with N particles, and m_i and \mathbf{v}_i are the mass and velocity of every particle; respectively. In principle velocities of each particle can be scaled at each step to maintain a constant temperature. However, this procedure is undesirable due to it could cause the trajectories to be no longer Newtonian. In order to avoid such limitations, some methods such as Berendsen [47] or Nosé-Hoover [48,49] couplings have been alternatively employed in the present thesis.

Berendsen Temperature Coupling

In this scheme the system is weakly coupled to an external heat bath that is at a constant temperature T_0 . In MD simulations, this corresponds to adding a dissipative Langevin force in the equations of motion according to

$$m_i \frac{d^2 \mathbf{r}_i}{dt^2} = \mathbf{f}_i + \frac{m_i}{\tau} \left(\frac{T_0}{T} - 1 \right) \frac{d\mathbf{r}_i}{dt} \quad (3.47)$$

where τ has units of time (*i.e.*, is an effective relaxation time) and is used to control the strength of the coupling. The larger the value of τ is, the smaller is the perturbing force and the more slowly the system is scaled to T_0 .

The frictional term added to motion equations drives the system (exponentially) towards the desired temperature. In practice, the velocities of the particles are scaled with a factor λ :

$$\lambda = \left[1 + \frac{\delta t}{\tau_T} \left(\frac{T_0}{T} - 1 \right) \right]^{\frac{1}{2}} \quad (3.48)$$

Nosé-Hoover Temperature Coupling

Another popular thermostat is the Nosé-Hoover thermostat, which retains a Boltzmann equilibrium distribution. In this case a thermal reservoir and a friction term are included in the equations of motion. The friction force is proportional to the product of each particle's velocity and a friction parameter, ξ . This friction parameter (or “heat bath” variable) is a fully dynamic quantity with its own momentum (p_ξ) and equation of motion. The time derivative is calculated from the difference between the current kinetic energy and the reference temperature.

In this formulation, the particles' equations of motion are replaced by:

$$\frac{d^2 \mathbf{r}_i}{dt^2} = \frac{\mathbf{f}_i}{m_i} - \frac{p_\xi}{Q} \frac{d\mathbf{r}_i}{dt} \quad (3.49)$$

where the equation of motion for the heat bath parameter ξ is:

$$\frac{dp_\xi}{dt} = (T - T_0) \quad (3.50)$$

The strength of the coupling is determined by the constant Q (so-called the frictional “heat bath mass” of the reservoir) in combination with the reference temperature. Larger values of the heat bath mass implies weak coupling of the system.

The main difference between the weak-coupling Berendsen scheme and the Nosé-Hoover algorithm could be summarized in terms of the relaxation time of the system. Weak coupling involves a strongly damped exponential relaxation, while the Nosé-Hoover approach produces an oscillatory relaxation.

3.2.4.5. PRESSURE CONTROL

In the same spirit as the temperature coupling, the system can also be coupled to a “pressure bath”. The volume is typically modified to adjust the pressure in a simulation. This is accomplished by scaling the location of the particles, *i.e.*, changing the size of the unit cell in the system. In the Berendsen barostat scheme the scaling can be accomplished in a way analogous to that displayed in equation (3.47). In this case, the scale factor μ is

used to scale the lengths of the box of the system. This scale factor can be written (for each dimension) as follows:

$$\mu = \left[1 - \frac{\beta \delta t}{\tau_p} (P_0 - P) \right]^{\frac{1}{3}} \quad (3.51)$$

where P_0 is the desired value of pressure, P the instantaneous pressure, τ_p the coupling time constant for the pressure scaling and β the isothermal compressibility of the system. The scaling is done for all components of the atom positions as well as the simulation cell dimensions.

3.2.5. SIMULATION CONVERGENCE

Convergence is defined as the acquisition of a sufficient number of phase points to ensure that the sampling is ergodic. The statistical convergence of the simulation can be assumed when the average values for all properties of interest appear to remain roughly constant with increased sampling. At this point, one can assume that the system is converged, or, in other word, equilibrated. Then, thermodynamic properties and other quantities can then be calculated after equilibration. Usually, convergence criteria are based on monitoring time evolution of quantities such as energy, root-mean-square deviation (RMSD) or correlation function between two variables [1,44].

3.2.6. PROPERTIES MEASUREMENTS

After MD simulation has been carried out, -Figure 3.2 shows the main steps involved in the MD algorithm;- the analysis of the collected data must be performed. Of course, some of the most interesting properties that could be ‘measured’ are those that can be compared with real experiments to ensure the validity of the system simulated. The simplest among these are thermodynamic properties such as temperature, pressure or heat capacity, which can be directly obtained from simulation. However, there are other thermodynamic functions, such as entropy, Helmholtz free energy or Gibbs free energy that cannot be measured directly, in the sense that they cannot be expressed as a simple average of some function of the coordinates and momenta of all particles of the system. Separate techniques are required to evaluate such thermal quantities in computer simulations.

A second class of observable properties corresponds to that based on the functions used to characterize the local structure of the system. The most notable among these is the so-called radial distribution function, which reflects the correlation between the particles due to the intermolecular interactions.

Both, thermodynamic and structural properties do not depend on the time evolution of the system. However, in addition to these static equilibrium properties, one can also

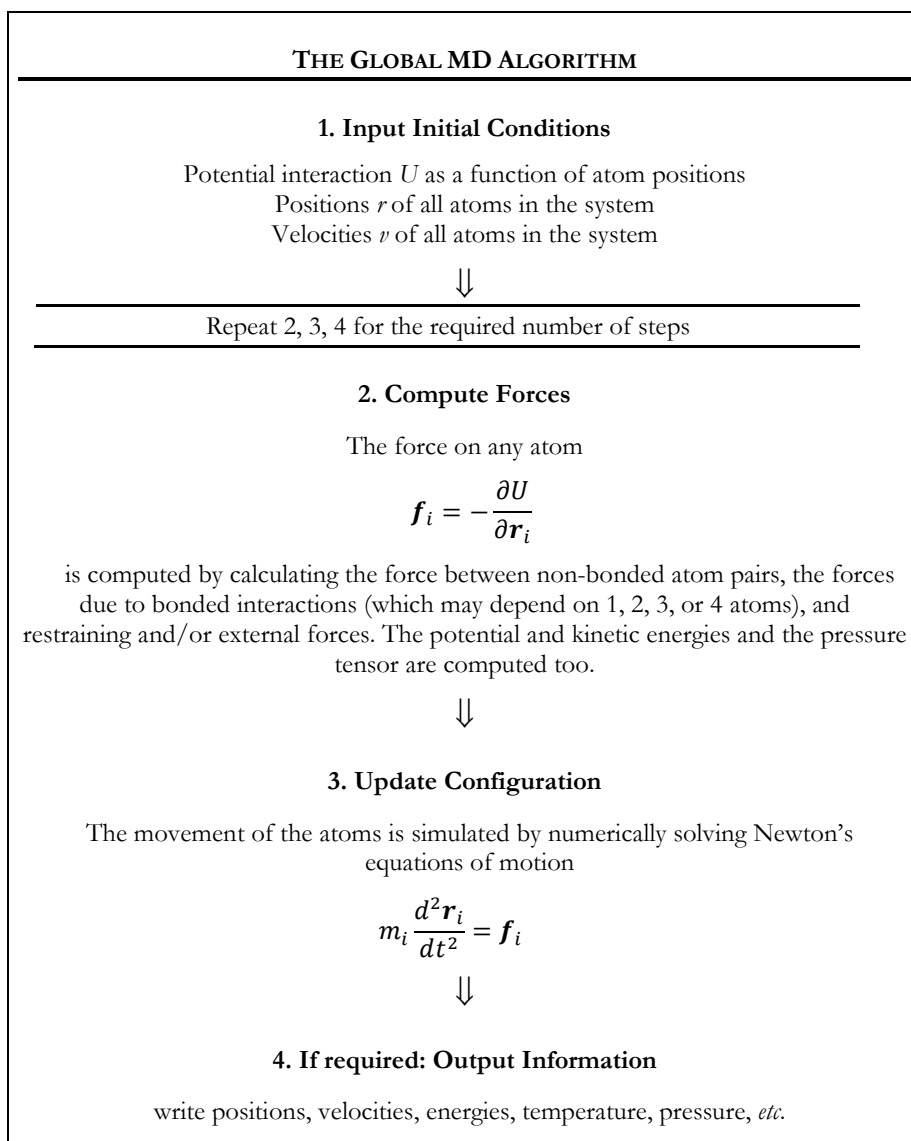


Figure 3.2. The global MD Algorithm

measure dynamic equilibrium properties, so-called time-correlation functions (*i.e.* diffusion).

Statistical mechanics allows obtaining the mentioned properties as time averages from MD simulations after the system is equilibrated. That is, the average value of the property A over all time steps generated by the simulation in the production time can be calculated according to

$$\langle A \rangle_{time} = \lim_{t \rightarrow \infty} \frac{1}{t} \int_{t_0}^{t+t_0} A(\mathbf{v}^N(\tau), \mathbf{r}^N(\tau)) d\tau \approx \frac{1}{M} \sum_i^M A_i(\mathbf{v}^N(t_i), \mathbf{r}^N(t_i)) \quad (3.52)$$

where t is the simulated time, M is the number of times the property is sampled, and A_i is the instantaneous value of A , expressed in terms of the velocities and positions of the particles of the system. The ergodic hypothesis assumes $\langle A \rangle_{time}$ is independent of the choice of the time origin t_0 , and equivalent to the ensemble average $\langle A \rangle$ [1].

REFERENCES

- [1] C. Cramer; *Essentials of computational chemistry: theories and models*, Wiley, 2004.
- [2] J.B.F.E. Foresman; *Exploring chemistry with electronic structure methods*, Gaussian, Pittsburgh, Pa., 1996.
- [3] W.J. Hehre, R.F. Stewart, J.A. Pople; *Self-consistent molecular-orbital methods .I. Use of gaussian expansions of slater-type atomic orbitals*; J Chem Phys **51**, 2657 (1969).
- [4] J.S. Binkley, J.A. Pople, W.J. Hehre; *Self-consistent molecular-orbital methods .21. Small split-valence basis-sets for 1st-row elements*; J Am Chem Soc **102**, 939 (1980).
- [5] Ditchfie.R, W.J. Hehre, J.A. Pople; *Self-consistent molecular-orbital methods .9. Extended gaussian-type basis for molecular-orbital studies of organic molecules*; J Chem Phys **54**, 724 (1971).
- [6] F.B. van Duijneveldt, J.G.C.M. van Duijneveldt-van de Rijdt, J.H. van Lenthe; *State of the art in counterpoise theory*; Chem Rev **94**, 1873 (1994).
- [7] S.F. Boys, F. Bernardi; *Calculation of small molecular interactions by differences of separate total energies - Some procedures with reduced errors*; Mol Phys **19**, 553 (1970).
- [8] D.R. Hartree; *The wave mechanics of an atom with a non-Coulomb central field Part I. Theory and methods*; P Camb Philos Soc **24**, 89 (1928).
- [9] J.C. Slater; *Note on Hartree's method*; Phys Rev **35**, 0210 (1930).
- [10] V. Fock; *Approximation method for the solution of the quantum mechanical multibody problems*; Z Phys **61**, 126 (1930).
- [11] C. Moller, M.S. Plesset; *Note on an approximation treatment for many-electron systems*; Phys Rev **46**, 0618 (1934).
- [12] J.S. Binkley, J.A. Pople; *Moller-Plesset theory for atomic ground-state energies*; Int J Quantum Chem **9**, 229 (1975).
- [13] F. Coester, H. Kummel; *Short-range correlations in nuclear wave functions*; Nucl Phys **17**, 477 (1960).
- [14] J. Paldus, I. Shavitt, J. Cizek; *Correlation problems in atomic and molecular systems .4. extended coupled-pair many-electron theory and its application to bh3 molecule*; Phys Rev A **5**, 50 (1972).
- [15] P. Hohenberg, W. Kohn; *Inhomogeneous electron gas*; Phys Rev B **136**, B864 (1964).
- [16] W. Kohn, L.J. Sham; *Self-consistent equations including exchange and correlation effects*; Phys Rev **140**, 1133 (1965).
- [17] J.P. Perdew, A. Zunger; *Self-interaction correction to density-functional approximations for many-electron systems*; Phys Rev B **23**, 5048 (1981).
- [18] S.H. Vosko, L. Wilk, M. Nusair; *Accurate spin-dependent electron liquid correlation energies for local spin-density calculations - a critical analysis*; Can J Phys **58**, 1200 (1980).
- [19] A.D. Becke; *Density-functional thermochemistry .4. A new dynamical correlation functional and implications for exact-exchange mixing*; J Chem Phys **104**, 1040 (1996).
- [20] J.P. Perdew; *Density-functional approximation for the correlation-energy of the inhomogeneous electron-gas*; Phys Rev B **33**, 8822 (1986).
- [21] J.P. Perdew, K. Burke, M. Ernzerhof; *Generalized gradient approximation made simple*; Phys Rev Lett **77**, 3865 (1996).
- [22] J.P. Perdew, Y. Wang; *Accurate and simple analytic representation of the electron-gas correlation-energy*; Phys Rev B **45**, 13244 (1992).

- [23] C.T. Lee, W.T. Yang, R.G. Parr; *Development of the colle-salvetti correlation-energy formula into a functional of the electron-density*; Phys Rev B **37**, 785 (1988).
- [24] A.D. Becke; *A new mixing of hartree-fock and local density-functional theories*; J Chem Phys **98**, 1372 (1993).
- [25] C. Adamo, V. Barone; *Exchange functionals with improved long-range behavior and adiabatic connection methods without adjustable parameters: The mPW and mPW1PW models*; J Chem Phys **108**, 664 (1998).
- [26] B.J. Lynch, P.L. Fast, M. Harris, D.G. Truhlar; *Adiabatic connection for kinetics*; J Phys Chem A **104**, 4811 (2000).
- [27] B.J. Lynch, Y. Zhao, D.G. Truhlar; *Effectiveness of diffuse basis functions for calculating relative energies by density functional theory*; J Phys Chem A **107**, 1384 (2003).
- [28] A.D. Becke; *Density-functional exchange-energy approximation with correct asymptotic-behavior*; Phys Rev A **38**, 3098 (1988).
- [29] X. Xu, W.A. Goddard; *The X3LYP extended density functional for accurate descriptions of nonbond interactions, spin states, and thermochemical properties*; P Natl Acad Sci USA **101**, 2673 (2004).
- [30] J.D. Chai, M. Head-Gordon; *Systematic optimization of long-range corrected hybrid density functionals*; J Chem Phys **128** (2008).
- [31] T. Yanai, D.P. Tew, N.C. Handy; *A new hybrid exchange-correlation functional using the Coulomb-attenuating method (cam-B3LYP)*; Chem Phys Lett **393**, 51 (2004).
- [32] S. Grimme; *Semiempirical GGA-type density functional constructed with a long-range dispersion correction*; J Comput Chem **27**, 1787 (2006).
- [33] J.D. Chai, M. Head-Gordon; *Long-range corrected hybrid density functionals with damped atom-atom dispersion corrections*; Phys Chem Chem Phys **10**, 6615 (2008).
- [34] A.D. Becke; *Density-functional thermochemistry .5. Systematic optimization of exchange-correlation functionals*; J Chem Phys **107**, 8554 (1997).
- [35] E. Runge, E.K.U. Gross; *Density-functional theory for time-dependent systems*; Phys Rev Lett **52**, 997 (1984).
- [36] D. Frenkel, B. Smit; *Understanding molecular simulation (Second Edition)*, Academic Press, San Diego, 2002.
- [37] D.C. Rapaport; *The art of molecular dynamics simulation*, Cambridge University Press, 1996.
- [38] W.D. Cornell, P. Cieplak, C.I. Bayly, I.R. Gould, K.M. Merz, D.M. Ferguson, D.C. Spellmeyer, T. Fox, J.W. Caldwell, P.A. Kollman; *A 2nd generation force-field for the simulation of proteins, nucleic-acids, and organic-molecules*; J Am Chem Soc **117**, 5179 (1995).
- [39] J.M. Wang, P. Cieplak, P.A. Kollman; *How well does a restrained electrostatic potential (RESP) model perform in calculating conformational energies of organic and biological molecules?*; J Comput Chem **21**, 1049 (2000).
- [40] C.I. Bayly, P. Cieplak, W.D. Cornell, P.A. Kollman; *A well-behaved electrostatic potential based method using charge restraints for deriving atomic charges - the Resp model*; J Phys Chem-Us **97**, 10269 (1993).
- [41] W.D. Cornell, P. Cieplak, C.I. Bayly, P.A. Kollman; *Application of Resp charges to calculate conformational energies, hydrogen-bond energies, and free-energies of solvation*; J Am Chem Soc **115**, 9620 (1993).
- [42] T. Darden, D. York, L. Pedersen; *Particle mesh ewald - an n.log(n) method for ewald sums in large systems*; J Chem Phys **98**, 10089 (1993).
- [43] L. Verlet; *Computer experiments on classical fluids .I. Thermodynamical properties of lennard-jones molecules*; Phys Rev **159**, 98 (1967).
-

- [44] M.P. Allen, D.J. Tildesley; *Computer simulation of liquids*, Oxford University Press, USA, 1989.
- [45] W.C. Swope, H.C. Andersen, P.H. Berens, K.R. Wilson; *A computer simulation method for the calculation of equilibrium constants for the formation of physical clusters of molecules: Application to small water clusters*; *J Chem Phys* **76**, 637 (1982).
- [46] S.A. Adcock, J.A. McCammon; *Molecular dynamics: survey of methods for simulating the activity of proteins*; *Chem Rev* **106**, 1589 (2006).
- [47] H.J.C. Berendsen, J.P.M. Postma, W.F. Vangunsteren, A. Dinola, J.R. Haak; *Molecular-dynamics with coupling to an external bath*; *J Chem Phys* **81**, 3684 (1984).
- [48] S. Nose; *A molecular-dynamics method for simulations in the canonical ensemble*; *Mol Phys* **52**, 255 (1984).
- [49] W.G. Hoover; *Canonical dynamics - Equilibrium phase-space distributions*; *Phys Rev A* **31**, 1695 (1985).

CHAPTER 4
DETECTION BASED ON CONDUCTING POLYMERS

'Everything should be made as simple as possible, but not simpler'

Albert Einstein

CHAPTER 4

DETECTION BASED ON CONDUCTING POLYMERS

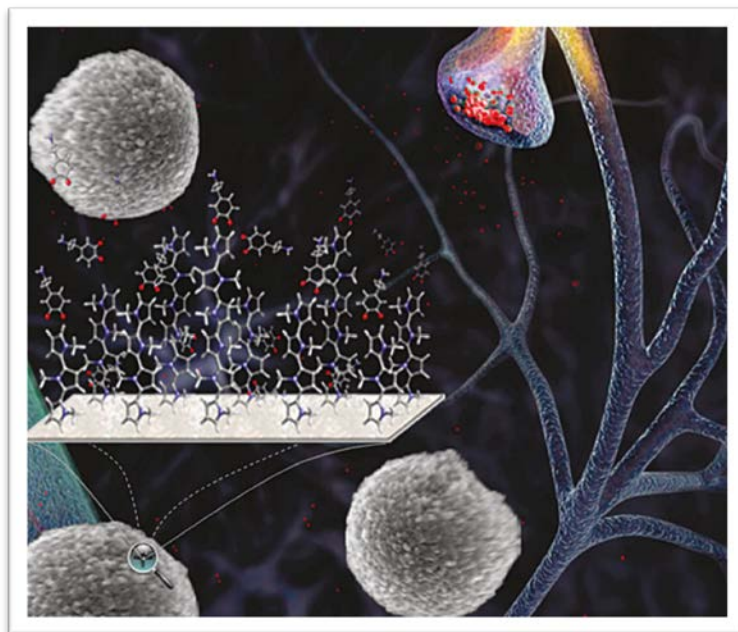
The work reported in this chapter focuses on the study of the mechanism used by some conducting polymers to interact and detect dopamine, a neurotransmitter related to some neurological disorders (section 4.1), and morphine, a potent analgesic psychoactive drug (section 4.2). All results showed in this chapter are based on both theoretical quantum mechanics calculations and experimental measurements. The content reported in the first section previously appeared in *The Journal of Physical Chemistry C* under the title *Ultrathin films of polypyrrole derivatives for dopamine detection* (2011), experimental measures being performed by Dr. Georgina Fabregat¹. Finally, the work described in section 4.2 was published in *Journal of Polymer Research* under the title *Electroactive polymers for the detection of morphine* (2014). The experimental studies were conducted by Dr. Bruno Teixeira-Dias¹ and theoretical results devoted to energy decomposition analysis were conducted by Prof. Miquel Solà² and Dr. Jordi Poater².

4.1. ULTRATHIN FILMS OF POLYPYRROLE DERIVATIVES FOR DOPAMINE DETECTION

Ultrathin films of poly[*N*-(2-cyanoethyl)pyrrole] and poly(*N*-methylpyrrole) and their composites with Au nanoparticles were used for the electrochemical detection of small concentrations (10 mM-100 μ M) of dopamine, a neurotransmitter related with neurological disorders. Results indicated that Au nanoparticles improve the sensing

¹ Center for Research in Nano-Engineering and Departament d'Enginyeria Química (ETSEIB), Universitat Politècnica de Catalunya

² Institut de Química Computacional i Catàlisi (IQCC) and Departament de Química, Universitat de Girona



abilities of the two polymers, even though they are not essential to obtain effective and fast responses toward the presence of dopamine. Furthermore, although both polymers have been found to be highly sensitive to low concentrations of dopamine, the response of poly[*N*-(2-cyanoethyl)pyrrole] is better and more effective than the response of poly(*N*-methylpyrrole). Experimental results were corroborated with quantum mechanical calculations on model systems, which also indicated that the interaction of oxidized dopamine with poly[*N*-(2-cyanoethyl)pyrrole] is stronger than that with poly(*N*-methylpyrrole). This behavior has been attributed to two different factors: (i) the flexibility of the cyanoethyl groups, which allows maximize the number of attractive van der Waals interactions, and (ii) the dipole of the cyano group, which interacts favorably with the dipole of the C=O bonds of oxidized dopamine. Finally, theoretical results were used to propose an atomistic model that explains the interaction behavior between the oxidized dopamine and the conducting polymers.

4.1.1. INTRODUCTION

Dopamine (3,4-dihydroxyphenyl ethylamine, DA) is one of the most important neurotransmitters in the mammalian central nervous system. The deficiency or excess of DA may result in serious diseases related to neurological disorders, including Parkinson's disease and schizophrenia [1,2]. In neurons, DA is stored in synaptic vesicles with other neurotransmitters. When synaptic vesicles receive an electrical stimulus produced by a nerve impulse, the DA molecules are transported to the cell wall, releasing them to the

synapse, which is the tiny gap between the axon ending and the dendrite of the next neuron [3]. Accordingly, the development of sensors to measure the DA concentration in a single synapse is receiving special attention because of the necessity of both an understanding the mechanisms that provoke neurological disorders and the prevention of numerous diseases. Furthermore, detection of DA contained in samples also plays a crucial role in the clinical diagnoses.

Electrochemical techniques have been developed to monitor the concentration of DA [4-15]. Within this context, conducting polymer-modified electrodes have been used to for the determination of DA in biological fluids. Among others, electrodes coated with polypyrrole (PPy) [9-11], poly(*N*-methylpyrrole) (PNMPy) [12], polyaniline [13,14], and poly(3,4-ethylenedioxythiophe) [7] have been used to detect DA. In a very recent study, we prepared DA sensors by coating glassy carbon electrodes (GCEs) and Au colloidal nanoparticles (AuNPs) deposited on GCE with an ultrathin film of PNMPy [12]. Results indicated that PNMPy is highly sensitive to this neurotransmitter, being able to detect DA concentration lower than that estimated for the synapse (1.6 mM). Thus, the constructed PNMPy sensor detected DA concentrations of 1.5 μ M without loss of current density. Moreover, we found that AuNPs are not essential for the sensing abilities of PNMPy, which represents an important practical advantage [12]. These findings suggested that PNMPy-based detectors should be considered to be good candidates for the development of effective, fast, and sensitive systems to be used in diagnosis detection of deficiency or excess DA.

We recently reported the synthesis and characterization poly-[*N*-(2-cyanoethyl)pyrrole] (PNCPy) [16], a *N*-substituted PPy derivative able to form thin and ultrathin films with some properties close to those of PNMPy. Specifically, the electrochemical stability and the electrical conductivity of PNCPy and PNMPy prepared using identical experimental conditions are very similar, whereas the current productivity and the doping level are lower for the former material. PNCPy shows a negligible flow of current density through the electrode for potentials lower than a given threshold (\sim 1.10 V), whereas this flow increases rapidly and significantly after such potential. The incorporation of the cyano to *N*-position of the PPy has been used only to improve the sensing and detection abilities of PPy. Specifically, early PNCPy studies, in which the material was only preliminarily characterized by cyclic voltammetry (CV) and scanning electron microscopy, were focused on the utility of PNCPy to detect organic vapors [17-19] to develop impedimetric immunosensors [20] and to prepare membranes for ions separation [21]. It is worth noting that as far as we know PNCPy has never been used for the detection of biomolecules like DA, even though the cyano functionality is able to participate in a large number of intermolecular interactions (*e.g.*, hydrogen bond and dipole \cdots dipole) [17]. Furthermore, strong electron-withdrawing cyano groups incorporated at positions relatively close to the π system of conjugated conducting polymers induce the reduction

of the barrier for electron injection, increase the oxidation potential, and improve the electron-transporting properties.

In this work, we compare the affinity and sensitivity of PNMPy and PNCPy toward DA molecules. More specifically, the abilities of these two PPy derivatives to immobilize and identify DA molecules have been investigated using the electrochemical oxidation of the neurotransmitter for the detection process. The sensitivity of these two PPy derivatives has been examined by considering submicromolar concentrations of biomolecules. In addition, quantum mechanical calculations have been carried out to examine the geometry and strength of the binding between the conducting polymers and the oxidized DA. Results have allowed us to propose a model that explains the different behaviors experimentally observed for PNMPy and PNCPy.

4.1.2. METHODS

4.1.2.1. MATERIALS

N-(2-Cyanoethyl)pyrrole (NCPy), acetonitrile, anhydrous lithium perchlorate, DA hydrochloride (3-hydroxytyramine hydrochloride), and $\text{HAuCl}_4 \cdot 3\text{H}_2\text{O}$ of analytical reagent grade were purchased from Sigma-Aldrich (Spain), whereas sodium citrate dihydrate was obtained from J. T. Baker. All other chemicals were of analytical-reagent grade and used without further purification. Phosphate-buffered solution (PBS) 0.1M with pH 7.4 was prepared as electrolyte solution by mixing four stock solutions of NaCl, KCl, NaHPO_4 , and KH_2PO_4 . High-purity nitrogen was used for deaeration of the prepared aqueous solutions.

4.1.2.2. ELECTROCHEMICAL SYNTHESIS, POLYMERIZATION KINETICS, AND THICKNESS OF THE FILMS

PNMPy and PNCPy films were prepared by chronoamperometry (CA) under a constant potential of 1.40 V. Electrochemical experiments were performed on an Autolab PGSTAT302N equipped with the ECD module for measuring very low current densities (100 μA -100 pA) (Ecochimie, The Netherlands) using a three-electrode two-compartment cell under a nitrogen atmosphere (99.995% in purity) at room temperature. The reference electrode was a saturated Ag|AgCl electrode, whereas platinum sheets of 0.50 x 0.70 cm^2 were used as counter electrode. A GCE was used as the working electrode (4.11 mm^2), its surface being polished with alumina powder and cleaned by ultrasonication before each trial. PNMPy and PNCPy were electrochemically deposited on the GCE using 70 mL of the corresponding monomer solution (10 mM) in acetonitrile containing 0.1 M LiClO_4 as supporting electrolyte. The polymerization time (θ) was 3 s for PNMPy and PNCPy.

In addition, the polymerization kinetics of PNCPy and PNMPy was investigated considering the same electrochemical conditions discussed above with the exception of: (1) the working and counter electrodes, which were made of steel AISI 316 L sheets of 2.0 x 2.0 cm², and (2) the polymerization time, which ranged from 5 to 70 s. The difference between the masses of the coated and uncoated electrodes was measured with a Sartorius analytical balance with a precision of 10⁻⁶ g.

The thickness of the films (*l*) was estimated using the procedure reported by Schirmeisen and Beck [22]. Accordingly, the current productivity (*m/Q*) was determined through the following relation:

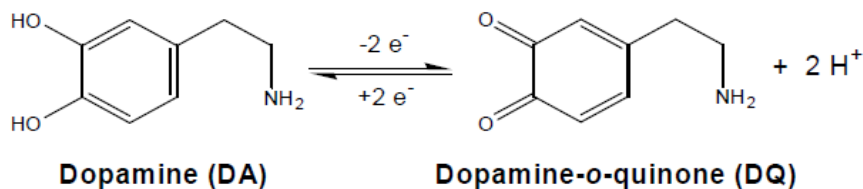
$$W_{ox} = Q_{pol} \cdot \left(\frac{m}{Q}\right) \quad (4.1)$$

where *Q_{pol}* is the polymerization charge consumed in the generation of each layer and *W_{ox}* is the mass of polymer deposited in the electrode. The current productivity was determined as the slope of a plot representing the variation of reproducible film weights (in mg·cm⁻²) against the polymerization charge consumed in each process (in mC·cm⁻²), which was directly obtained from each chronoamperogram. The volume of polymer deposited in the electrode, *V_{pol}*, was obtained using the values of *W_{ox}* and the density. The densities of PNMPy (1.52 g·cm⁻³) and PNCPy (1.42 g·cm⁻³) were determined in previous works [23,24].

4.1.2.3. PREPARATION OF AU COLLOIDAL NANOPARTICLES

For the removal of any adsorbed substance on the GCE surface, prior to the conducting polymer deposition, it was polished repeatedly with alumina slurry, followed by successive sonication in ethanol and doubly distilled water for 5 min and dried under a nitrogen flow.

Preparation of the AuNPs for deposition onto GCEs, which were used to fabricate the nanomembranes of PNCPy and PNMPy, was performed following the standard procedure described in the literature [25,26]. All glassware used in such preparation was thoroughly cleaned in aqua regia (3:1 HCl:HNO₃), rinsed in doubly distilled water, and oven-dried prior to use. In a 1 L round-bottomed flask equipped with a condenser, 500 mL of 1 mM HAuCl₄ was brought to a rolling boil with vigorous stirring. Rapid addition of 50 mL of 38.8 mM sodium citrate to the vortex of the solution produced a color change from pale yellow to burgundy. Boiling was continued for 15 min. After this, the heating mantle was removed while the stirring was continued for 30 min. When the solution reached the room temperature, it was filtered through a 0.2 μm membrane filter. The resulting solution of colloidal particles showed an absorption maximum at 520 nm, indicating that the particle size ranged from 9 to 22 nm. A spherical model for a particle size of 13 nm was used to determine approximately the concentration of mother solution from UV-vis absorption, which was estimated to be 7.4 nM [27].



Scheme 4.1

4.1.2.4. DETECTION ASSAYS.

Detection of DA was performed by CV using a glass cell containing 40 mL of PBS 0.1 M at room temperature and considering DA concentrations ranging from 100 μM to 10 mM. Detection was studied considering PNCPy-, PNMPy-, PNCPy/AuNP-, and PNMPy/AuNP-modified GCE systems. PNCPy and PNMPy GCEs were prepared by depositing the conducting polymer on the GCE bare using CA. PNCPy/AuNP- and PNMPy/AuNP-modified GCEs were prepared by dropping the AuNPs colloidal solution (2 μL) onto the PNCPy and PNMPy-modified GCE surface, respectively, and allowing dry under atmosphere conditions, this process being repeated twice. Cyclic voltammograms were recorded in the potential range from -0.40 to 0.80 V at a scan rate of 100 mV/s, scanning being stopped after 10 oxidation-reduction cycles. All modified electrodes were in contact with the electrolyte solution for 10 min prior to the CV measurements.

4.1.2.5. QUANTUM MECHANICAL CALCULATIONS

Calculations were performed using the Gaussian 03 [28] computer program. PNCPy and PNMPy were modeled considering small oligomers in the radical cation state (charge = +1 and spin multiplicity = 2) made of n repeating units (n -NCPy and n -NMPy, respectively, with $n = 1, 2$ and 3). DA was considered in its oxidized form dopamine-o-quinone, (abbreviated DQ in Scheme 4.1). It is worth noting that the selection of DQ and the oxidized oligomers was based on our own experimental results (Results and Discussion), which indicate that at the detection potential the oxidation from DA to DQ has occurred and the polymer is oxidized. Although the length of the alkyl group has a negligible effect on the electronic properties of N -substituted PPy derivatives, as was found in recent studies on poly[N -(2-cyanoalkyl)pyrrole]s [29] and poly-(N -hydroxyalkylpyrrole)s [30] bearing short alkyl groups (*i.e.*, alkyl = methyl, ethyl, and propyl), the ethyl group of PNCPy was considered explicitly because it may play a crucial role in the detection process.

The structures of the n -NMPy \cdots DQ and n -NCPy \cdots DQ complexes were determined by full geometry optimization in the gas phase at the Hartree-Fock level using the 6-31+G(d,p) basis set. [31,32]. Single-point energy calculations were performed on the HF/6-31+G(d,p) geometries at the B3LYP/6-311++G(d,p) level [33,34]. The binding

energy (ΔE_b) was calculated at the B3LYP/6-311++G(d,p) level as the difference between the total energy of the optimized complex and the energies of the isolated monomers with the geometries obtained from the optimization of the complex. The counterpoise (Cp) method[35] was applied to correct the basis set superposition error from the ΔE_b .

4.1.3. RESULTS AND DISCUSSION

4.1.3.1. ELECTROPOLYMERIZATION KINETICS

The kinetics of oxidation polymerizations yielding PNCPy and PNMPy have been studied by electrogenerating films under a constant potential of 1.40 V and considering polymerization times $\theta = 5, 10, 20, 30, 40, 50, 60$ and 70 s. Figure 4.1 represents the variation of W_{ox} against Q_{pol} for the two PPy derivatives, each value of both Q_{pol} and W_{ox} corresponding to the average of three measures from independent experiments. The linear correlations showed regression coefficient R^2 larger than 0.98 in both cases, which is consistent with the existence of Faradaic processes. The slope of each plot, 0.411 and 0.355 $\text{mg}\cdot\text{C}^{-1}$ for PNCPy and PNMPy, respectively, corresponds to the current productivity, (m/Q), of the polymer. These values are significantly different from those obtained for micrometric films using identical experimental conditions but higher polymerization times (*i.e.*, θ ranged from 300 to 1500 s): 0.531 and 0.619 $\text{mg}\cdot\text{C}^{-1}$ for PNCPy [16] and PNMPy [36], respectively. Such differences affect not only the numerical values but also the relative order in the mass of polymer produced by Coulomb of charge consumed during the anodic polymerization process. These features are fully consistent with previous observations, which evidenced that the growing mechanism, morphology,

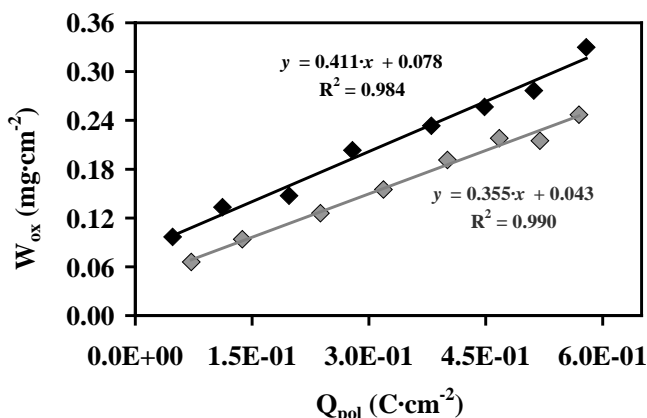


Figure 4.1. Variation of the weight per unit of area of PNCPy (◆) and PNMPy (◆) deposited on stainless steel from 10 mM monomer solutions in acetonitrile with 0.1 M LiClO_4 at a constant potential of 1.40 V against the polymerization charge.

and properties of ultrathin films of conducting polymers (*i.e.*, those produced using $\theta \leq 70$ s) are significantly different from those of micrometric thin films (*i.e.*, $\theta \geq 300$ s) [24,37,38].

The current productivities determined for nanometric PNMPy and PNCpy coatings were used to estimate the thickness of the films used for detection assays, which were produced using a polymerization time of 3 s. The average thickness, which resulted from 12 independent measures, was $l = 54 \pm 11$ and 78 ± 14 nm for PNMPy and PNCpy, respectively. It should be noted that measurement of DA concentration in the brain is not an easy task because of the dimensions of the synapse. However, for both polymers, the thickness of the films is smaller than the synapse diameter, ~ 100 nm.

4.1.3.2. DETECTION OF DOPAMINE

Control voltammograms of the neurotransmitter at isolated GCE and AuNP-modified GCE were reported in our previous study [12]; therefore, they have not been repeated here. The electrochemical behavior of the DA in direct contact with the GCE was found to be less reversible than that with AuNP-modified GCE. Two oxidation peaks were observed for the latter in the presence of DA at 0.43 and 0.56 V, which were attributed to the formation of a polaron and the oxidation of DA molecules to DQ (Scheme 4.1), respectively. This enhancement of the electrochemical response of the DA was attributed to the catalytic role of the AuNPs: the electronic transference between the redox pair and the AuNPs provokes the lowering of the oxidation peak of the neurotransmitter.

Figure 4.2 shows cyclic voltammograms of PNMPy- and PNMPy/AuNP-modified GCEs in the absence and presence of DA concentrations ranging from 1 to 10 mM, whereas Figure 4.3 displays the results corresponding to the PNCpy- and PNCpy/AuNP-modified GCEs. Figure 4.4 represents the variation of the oxidation potential and the current density of the neurotransmitter against the DA concentration for the four systems.

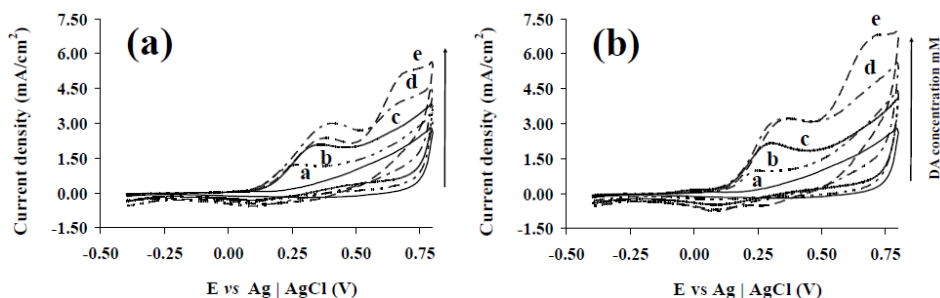


Figure 4.2. Cyclic voltammograms for the oxidation of (a) PNMPy- and (b) PNMPy/AuNP-modified GCEs in the absence and presence of different DA concentrations (from 1 to 10 mM). Scan rate: 100 mV/s. Initial and final potential: -0.40 V; reversal potential: +0.80 V. For each graphic, labels a-e refer to DA concentrations of 0, 1, 3, 6, and 10 mM, respectively.

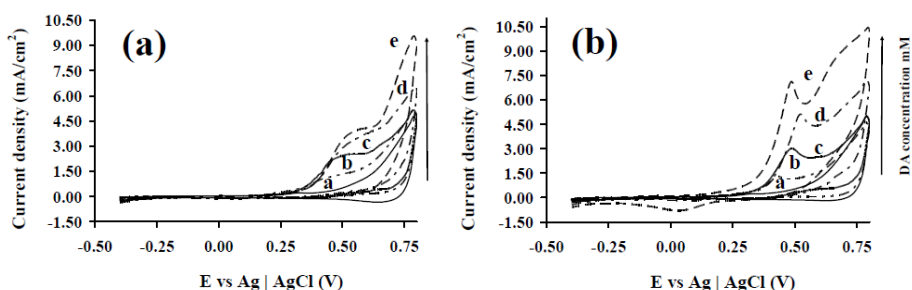


Figure 4.3. Cyclic voltammograms for the oxidation of (a) PNCPy- and (b) PNCPy/AuNP-modified GCEs in the absence and presence of different DA concentrations (from 1 to 10 mM). Scan rate: 100 mV/s. Initial and final potential: -0.40 V; reversal potential: +0.80 V. For each graphic, labels a-e refer to DA concentrations of 0, 1, 3, 6, and 10 mM, respectively.

Results indicate that in both cases AuNPs improve the electrochemical oxidation response of the neurotransmitter. The oxidation potential of DA is clearly lower for the PNMPy/AuNP system than for the PNMPy without AuNPs (Figure 4.4a). This effect is not so evident when PNCPy/AuNP and PNCPy are compared, even though the oxidation peak is much more pronounced in the former than in the latter (Figure 4.3). Cathodic and anodic current densities are significantly higher for PNCPy/AuNP than for the PNCPy (Figure 4.4b). However, although detectable, this effect is much less pronounced for PNMPy-containing systems. This difference should be attributed to the fact that the interaction of AuNPs with PNCPy is better than that with PNMPy, which is probably due to the combination of two effects: the higher roughness of former polymeric matrix [16] and the electron-withdrawing behavior of the cyano group. In addition to the catalytic role mentioned above, the favorable effects produced by AuNPs in the DA detection process should to be attributed to the fact that charge migration through PNMPy and PNCPy is facilitated by the charge hopping in the conductor AuNPs [13].

Comparing the oxidation and reduction processes, we evidence that the oxidation of DA is not a completely reversible process because of the polymerization of DA [39]. Despite this, some reduction peaks, which should be attributed to the reduction of the conducting polymer chains, are observed. This behavior is evidenced by the anodic current density of the first oxidation peak, which is higher than the cathodic current density of the corresponding reduction peak. For the PNCPy-modified GCE, the current density ranges from 1.10 to 3.80 mA·cm⁻² when the DA concentration ranges from 1 to 10 mM, whereas the cathodic current density of the corresponding reduction peak is of only ~ -0.1 mA·cm⁻². In the case of PNCPy/AuNP-modified GCE, there is no reduction peak in the cyclic voltammograms with the exception of that recorded for a DA concentration of 10 mM, which shows a current density of -0.13 mA·cm⁻². Additionally, the oxidation potential increases with the concentration of DA for the four modified electrode systems (Figure 4.4a). This behavior is very evident for concentrations up to 6

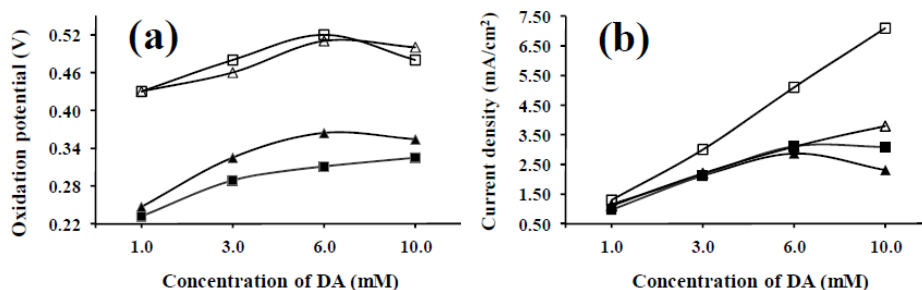
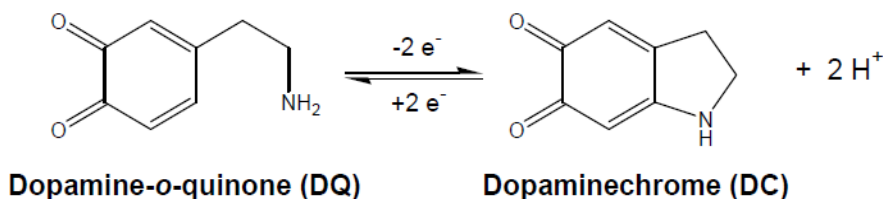


Figure 4.4. Variation of (a) the oxidation potential and (b) the current density for the oxidation peak of DA against the neurotransmitter concentration measured using PNMPy- (▲), PNMPy/AuNP- (■), PNCyPy- (△), and PNCyPy/AuNP-modified GCEs (□).

mM but practically inexistent when DA increases from 6 to 10 mM, which should be attributed to the saturation of the electrode. Thus, after a threshold (6 mM), the accumulation of oxidized DA molecules in the surface makes difficult, or even precludes, the oxidation of other neurotransmitter molecules.

Figure 4.2b and Figure 4.3b show the presence of a second oxidation peak (0.67 and 0.65 V, respectively) and the corresponding reduction peak (0.30 and 0.52 V, respectively) when the concentration of DA is 10 mM. The same behavior is also displayed by the PNMPy system for concentrations of 6 and 10 mM (Figure 4.2a), whereas such a second peak is not observed in the voltammograms recorded using the PNCyPy-modified GCE. The second peak has been attributed to the oxidation of DQ molecules to dopaminechrome (DC in Scheme 4.2) [40].

In a previous study, we reported that PNCyPy films prepared by CA under a constant potential of 1.40 V undergo, upon reduction, an oxidative process in some pyrrole rings [16]. As a consequence of this process, a carbonyl group appears in such rings. This overoxidation process is typically found in PPy derivatives, including PNMPy [41,42]. The onset of overoxidation of PPy derivatives is typically observed at ~ 1.30 V [16,41,42]. Because the cyclic voltammograms used for DA detection were recorded in the potential range from -0.40 to 0.80 V, the proportion of oxidized five-membered rings is expected



Scheme 4.2

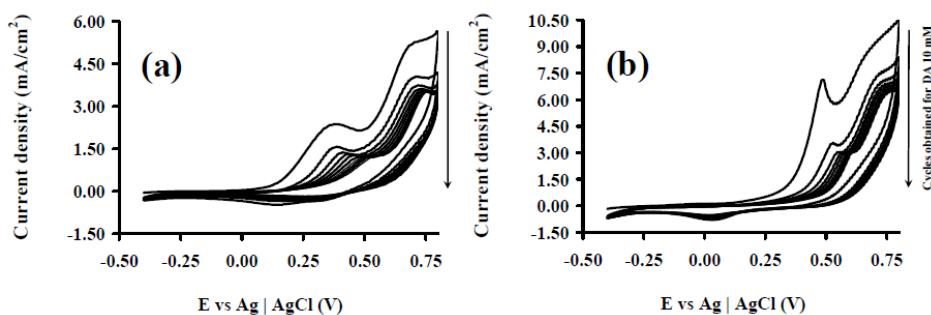


Figure 4.5. Control voltammograms for 10 consecutive oxidation-reduction cycles of (a) PNMPy/AuNP- and (b) PNCPy/AuNP-modified GCEs in the presence of 10 mM DA.

to be considerably low. Accordingly, although the C=O groups may attract oxidized DA molecules, this interaction has been neglected in our subsequent modeling studies. (See below).

4.1.3.3. STABILITY AND LIMIT OF DETECTION

Figure 4.5 displays the control voltammograms recorded for 10 consecutive oxidation-reduction cycles of PNMPy/AuNP and PNCPy/AuNP systems in the presence of a concentration of DA equal to 10 mM. For the two modified electrodes, the DA oxidation peak moves toward higher potentials when the number of oxidation-reduction cycles increases, whereas the current density decreases significantly. Furthermore, the cathodic and anodic areas decrease when the number of cycles increases, the electroactivity determined for the 10th cycle being about 52-54% lower than that of the first one. Accordingly, the electrostability showed by two AuNP-containing conducting polymer films was relatively low. Figure 4.6 represents the variation of the loss of electrostability (LES) after 10 consecutive redox cycles for the PNMPy-, PNMPy/AuNP-, PNCPy-, and PNCPy/AuNP-modified GCEs against the concentration of DA. As it can be seen, the LES decreases when the DA concentration increases. Although the behavior of the four systems is very similar, the electrostability of the electrodes modified with PNCPy is slightly higher than that of the coatings with PNMPy, independently of the presence or absence of AuNPs. Moreover, differences are more remarkable for DA concentrations <6 mM.

Figure 4.7a shows the response of the PNMPy- and PNMPy/AuNP-modified GCEs in the presence of a 100 μ M DA concentration. Oxidation of DA molecules is immediately detected by the latter system (0.19 V and 0.30 mA \cdot cm⁻²), whereas two consecutive oxidation-reduction cycles are required for the electrode without AuNPs. In contrast, the oxidation peak at 0.37 V is clearly detected by both PNCPy and PNCPy/AuNP systems (Figure 4.7b). These results combined with those previously displayed (Figures 4.2-4.6) indicate that, although the two conducting polymers allow the

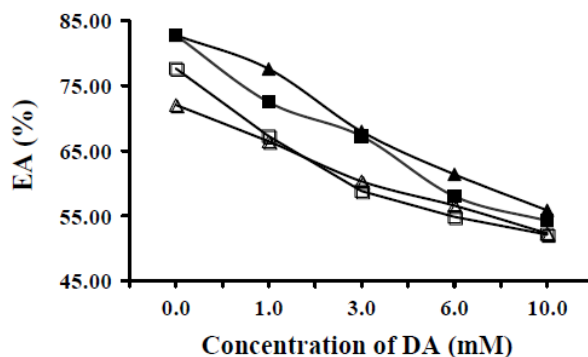


Figure 4.6. Variation of the loss of electrostability (LES) after 10 consecutive oxidation-reduction cycles for PNMPy- (▲), PNMPy/AuNP- (■), PNCPy- (△), and PNCPy/AuNP-modified GCEs (□) against the DA concentration.

detection of very low concentration of DA (*i.e.*, lower than that estimated for the synapse), the response of the PNCPy is better and more effective than the response of PNMPy.

4.1.3.4. MODELING OF THE INTERACTION PNMPY...DQ

The interaction between PNMPy and the oxidized DA was modeled using a build-up scheme. Specifically, the interaction between 1-NMPy and DQ was examined in a first stage, the resulting complexes being used to construct the starting structures for 2-NMPy...DQ. Finally, starting arrangements for 3-NMPy...DQ were constructed using the optimized structures of 2-NMPy...DQ.

Geometry optimizations of 40 starting structures led to 17 1-NMPy...DQ complexes, which were categorized in four groups according to the interaction patterns. The most stable structure of each group is displayed in Figure 4.8a. As it can be seen, complexes 1-

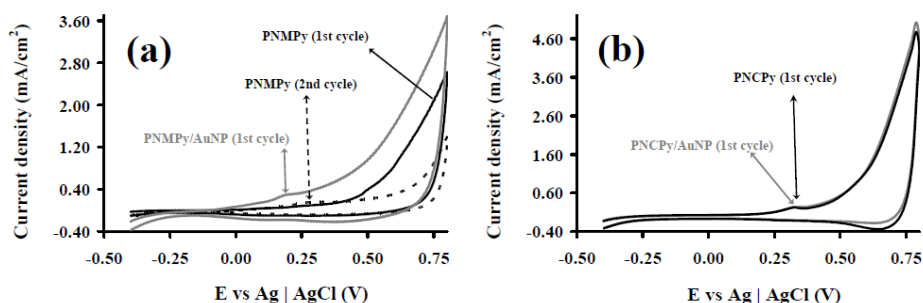


Figure 4.7. Cyclic voltammograms for the oxidation of (a) PNMPy- and PNMPy/AuNP-modified GCEs and (b) PNCPy- and PNCPy/AuNP-modified GCE in the presence of a 100 μM DA concentration. Scan rate: 100 mV/s. Initial and final potential: -0.40 V; reversal potential: +0.80 V. The second consecutive oxidation-reduction cycle is also displayed for the PNMPy-modified GCE.

Ma, 1-Mb, and 1-Mc are stabilized by interactions involving the C–H moieties of the pyrrole ring and the oxygen atoms of DQ, whereas the two rings interact through a $\pi - \pi$ stacking in complex 1-Md. The C–H \cdots O contacts with a H \cdots O distance (d_{H-O}) < 2.65 Å are explicitly indicated in Figure 4.8a. The most stable arrangement corresponds to 1-Ma, the relative energy (ΔE) of 1-Mb, 1-Mc, and 1-Md calculated at the B3LYP/6-311++G(d,p) level being 2.9, 15.5, and 26.2 kcal/mol. Inspection of the binding energies (ΔE_{int}) between 1-NMPy and DQ, which are listed in Table 4.1, indicate that C–H \cdots O interactions are significantly more attractive than the $\pi - \pi$ stacking (*i.e.*, ~ 17 kcal/mol).

The four structures selected for the 1-NMPy \cdots 3DQ complex were used to construct eight starting structures of 2-NMPy \cdots DQ by adding a new NMPy repeating unit to 1-NMPy, both *trans* and *cis* arrangements being considered for the inter-ring dihedral angle (*i.e.*, $\theta_A = 180$ and 0° , respectively). The four structures of lower energy obtained after

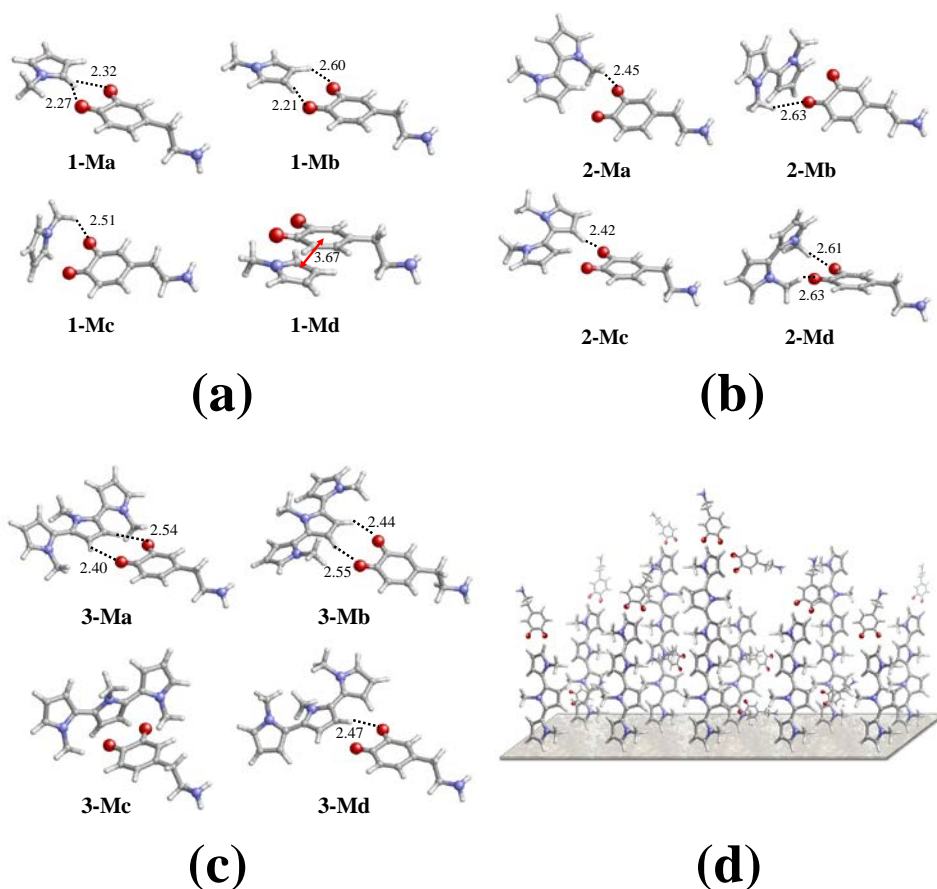


Figure 4.8. Four structures of lower energy derived from quantum mechanical calculations for (a) 1-NMPy \cdots DQ, (b) 2-NMPy \cdots DQ, and (c) 3-NMPy \cdots DQ complexes. (d) Atomistic model proposed for the detection of DA by PNMPy.

geometry optimization are displayed in Figure 4.8b. As it can be seen, the four complexes are essentially stabilized by intermolecular C–H \cdots O interactions. It should be noted that in the past 15 years, a multitude of close contacts between the C–H group and the electronegative oxygen atom were identified as hydrogen bonds, this interaction being found in an enormous variety of chemical systems [43–48]. According to the literature, the threshold chosen for the distance in C–H \cdots O stabilizing hydrogen bonds was ~ 2.6 Å. It should be noted that although C–H \cdots O interactions play a crucial role in the detection of oxidized DA, their chemical nature (*i.e.*, hydrogen bonds or van der Waals contacts) is out of the scope of this work. The inter-ring dihedral angle in the two complexes of lower energy, 2-Ma and 2-Mb, corresponds to an *antigauche*-conformation ($\sim -160^\circ$), whereas structures with the 2-NMPy molecule arranged in *syn-gauche*⁺ ($\sim +20^\circ$), 2-Mc and 2-Md, are destabilized by ~ 4 to 5 kcal/mol with respect to the global minimum. ΔE_b values are relatively similar in the four complexes, ranging from -13.5 to -14.6 kcal/mol. The reduction in the ΔE_b values with respect to those obtained for 1-NMPy \cdots DQ complexes is consistent with the fact that the d_{H-O} values are shorter in the latter than in 2-NMPy \cdots DQ.

The four structures displayed in Figure 4.8b for the 2-NMPy \cdots DQ complex were used to build the starting structures of 3-NMPy \cdots DQ using the procedure previously described (*i.e.*, the third repeating unit was added to the 2-NMPy molecule considering both the *trans* and *cis* arrangements for the inter-ring dihedral angle θ_B). The four

Table 4.1. Relative Energy (ΔE), Binding Energy (ΔE_b), and Inter-Ring Dihedral Angles (θ_A and θ_B) of the Four Structures of Lower Energy Calculated for n -NMPy \cdots DQ Complexes, where n Ranges from 1 to 3^a

Complex	ΔE (kcal/mol)	ΔE_b (kcal/mol)	θ_A ($^\circ$)	θ_B ($^\circ$)
1-Ma	0.0 ^b	-21.9		
1-Mb	2.9	-16.5		
1-Mc	15.5	-20.6		
1-Md	26.2	-2.6		
2-Ma	0.0 ^c	-13.8	-164.0	
2-Mb	2.4	-13.7	-163.0	
2-Mc	4.4	-13.5	21.2	
2-Md	5.4	-14.6	23.2	
3-Ma	0.0 ^d	-12.3	158.9	-159.9
3-Mb	1.8	-12.8	159.0	-159.9
3-Mc	3.3	-11.3	-158.7	157.8
3-Md	8.2	-11.6	22.5	-37.6

^a Molecular geometries have been obtained at the HF/6-31+G(d,p) level, whereas ΔE and ΔE_{int} were derived from single-point calculations at the B3LYP/6-311++G(d,p) level. ^b E = -764.856211 au. ^c E = -1013.243780 au. ^d E = -1261.612486 au.

structures of lower energy, which expand within a relative energy interval of 8.2 kcal/mol, are displayed in Figure 4.8c. The two inter-ring dihedral angles of the three structures of lower energy, 3-Ma, 3-Mb and 3-Mc, which differ only in 3.3 kcal/mol, adopt *antigauche* arrangements. In contrast, structure 3-Md shows two consecutive *syn-gauche* rotamers, which result in a destabilization of 4.9 kcal/mol with respect to 3-Mc.

The ΔE_{int} values range from -11.3 to -12.8 kcal/mol confirming that the strength of the interaction decreases with the length of the polymer chain. The overall of the calculations on *n*-NMPy \cdots DQ complexes indicate that PNMPy detects oxidized DA molecules mainly through the formation of C–H \cdots O interactions. The C–H moieties involved in such interactions belong to the rigid pyrrole rings or to the methyl groups, whose deformability is null or very limited. Accordingly, the strength interaction is determined by the molecular rigidity of both the polymer chains and the neurotransmitter. Figure 4.8d provides a schematic representation of the model proposed to explain the detection of DQ by PNMPy.

4.1.3.5. MODELING OF THE INTERACTION PNCPY \cdots DQ

The structures displayed in Figure 4.9a-c for *n*-NMPy \cdots DQ complexes were modified by replacing the methyl by the cyanoethyl at the N position of each pyrrole ring, being subsequently used as starting structures for geometry optimization of *n*-NCPy \cdots DQ complexes. The optimized structures of 1-NCPy \cdots DQ are displayed in Figure 4.9a, whereas their corresponding ΔE and ΔE_b values are listed in Table 4.2. As can be seen, C–H \cdots O interactions are more important than those in 1-NMPy \cdots DQ complexes, which explains the reduction of the ΔE interval with respect to the latter. This feature is particularly evident in 1-Ca, in which the C–H \cdots O interactions involving the pyrrol ring (with $d_{H-O} < 2.40 \text{ \AA}$) are reinforced by other attractive C–H \cdots O contacts produced by the two methylene units. ΔE_{int} values indicate that the binding with DQ is stronger for 1-NCPy than for 1-NMPy. The four 2-NCPy \cdots DQ complexes are displayed in Figure 4.9b, whereas ΔE and ΔE_b values are listed in Table 4.2. As can be seen, the 2-NCPy tends to surround the DQ favoring the formation of attractive van der Waals interactions in the four structures. This interaction pattern is consistent the fact that the ΔE interval expands by < 1 kcal/mol. The binding of DQ with 2-NCPy is ~ 4 to 5 kcal/mol more favorable than with 2-NMPy. Therefore, the flexibility of the cyanoethyl group, which participates actively in the interaction with DQ, avoids a significant reduction in ΔE_b when *n* grows from 1 to 2. It should be noted that the opposite behavior was predicted for *n*-NMPy \cdots DQ complexes (Table 4.1), where ΔE_b increases considerably with *n*.

Finally, Figure 4.9c depicts the optimized structures of 3-NCPy \cdots DQ, which confirm the trends previously observed for 2-NCPy \cdots DQ. Thus, the four structures are comprised within a ΔE interval of 1.8 kcal/mol only and ΔE_b values, which are similar to those obtained for 2-NCPy \cdots DQ, indicate that DQ forms stronger interactions with

3-NCPy than with 3-NMPy. Therefore, the cyanoethyl groups wrap the DQ molecule forming many attractive C-H \cdots O interactions that stabilize the complex. In addition, the orientation adopted by the cyano groups allows the formation of attractive dipole-dipole interactions with the C=O bonds of the DQ molecule. These interactions are explicitly represented in Figure 4.9c using green arrows. Figure 4.9d describes the model proposed for the interaction between PNCPy and oxidized DA, which is based on the flexibility provided by the methylene units of the substituent at the N-position of the polymer. It is worth noting that the models provided in Figure 4.8d and Figure 4.9d are fully consistent

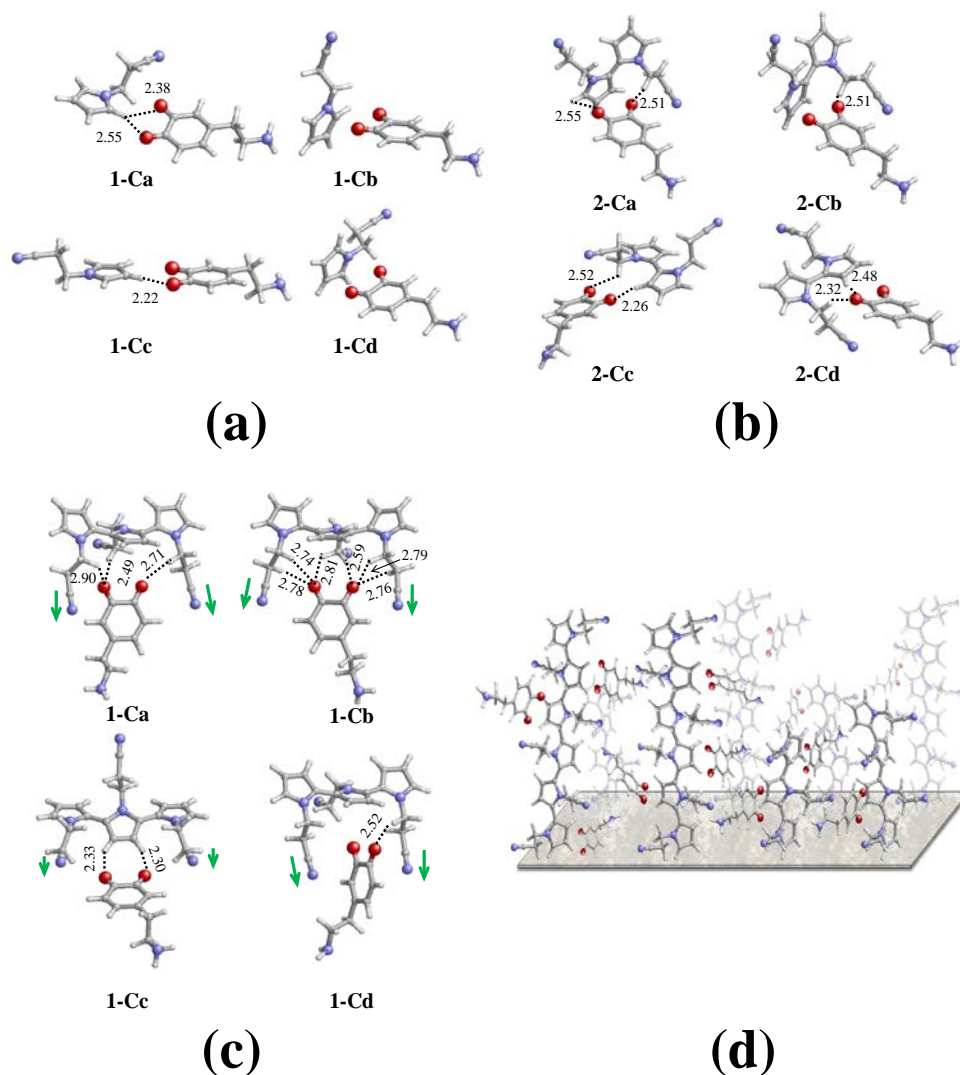


Figure 4.9. Structures derived from quantum mechanical calculations for (a) 1-NCPy \cdots DQ, (b) 2-NCPy \cdots DQ, and (c) 3-NCPy \cdots DQ complexes. (d) Atomistic model proposed for the detection of DA by PNCPy.

Table 4.2. Relative Energy (ΔE), Binding Energy (ΔE_b), and Inter-Ring Dihedral Angles (θ_A and θ_B) of the Four Structures of Lower Energy Calculated for n -NCPy \cdots DQ Complexes, where n Ranges from 1 to 3^a

Complex	ΔE (kcal/mol)	ΔE_b (kcal/mol)	θ_A (°)	θ_B (°)
1-Ca	0.0 ^b	-24.3		
1-Cb	2.1	-22.2		
1-Cc	5.3	-19.1		
1-Cd	14.2	-19.6		
2-Ca	0.0 ^c	-16.0	159.0	
2-Cb	0.1	-19.1	157.1	
2-Cc	0.3	-16.4	-166.4	
2-Cd	0.9	-17.1	163.3	
3-Ca	0.0 ^d	-19.1	158.6	-158.0
3-Cb	0.1	-19.2	158.9	-159.1
3-Cc	0.8	-17.7	-155.7	157.3
3-Cd	1.8	-17.2	152.1	-155.5

^a Molecular geometries have been obtained at the HF/6-31+G(d,p) level, whereas ΔE and ΔE_{int} were derived from single-point calculations at the B3LYP/6-311++G(d,p) level. ^b E = -896.434644 au. ^c E = -1276.398028 au. ^d E = -1656.350539 au.

with the experimental observations reported in the previous sections. Therefore, the relative efficacy of PNCPy and PNMPy as DA detectors is explained by the fact that the interactions of the former polymer are stronger than those of the latter, which in turn is consequence of the flexibility of the cyanoethyl group.

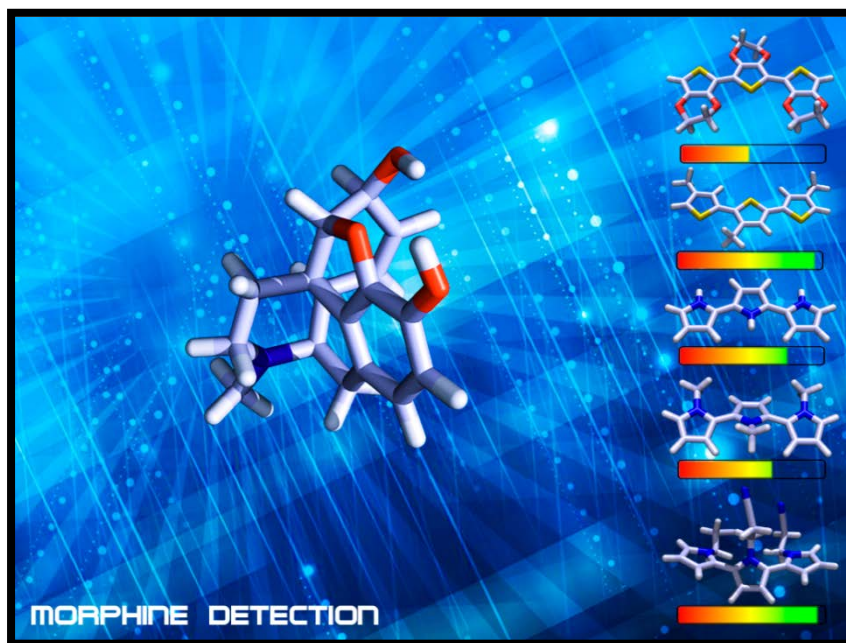
4.1.4. CONCLUSIONS

Nanometric films of PNMPy and PNCPy have been used to examine and compare the abilities of these two conducting polymers to detect small concentrations of DA. Control voltammograms for the oxidation of PNMPy-, PNCPy-, PNMPy/AuNP-, and PNCPy/AuNP-modified GCEs in the presence of DA concentrations ranging from 100 μ M to 10 mM evidenced the sensing abilities of both polymers. AuNPs, which interact more favorably with PNCPy than with PNMPy, enhance the electronic transference and the charge migration processes of the DA oxidation. Despite this, AuNPs are not essential for the detection because of the powerful sensing abilities shown by both PNCPy- and PNMPy-conducting polymers. The response of the two polymers against a DA concentration of only 100 μ M, which is significantly lower than the concentration found in the synapse (1.6 mM), was crucial to discern that the electrochemical response of the PNCPy is more effective than that of PNMPy and facilitates the possible application of these materials to biomedical applications.

Quantum mechanical calculations allowed us to propose atomistic models that explain the interaction of oxidized DA with PNMPy and PNCPy systems. Calculations on n -NMPy \cdots DQ and n -NCPy \cdots DQ complexes with n ranging from 1 to 3 indicate that C–H \cdots O interactions play a crucial role in the detection process. The strength of the interaction between the n -NMPy and DQ molecules decreases when n increases. Thus, the low deformability of the methyl group precludes the reaccommodation of the oxidized DA molecule without energy penalty when the length of the n -NMPy increases. This limitation is also reflected by the distances between the interacting atoms, d_{H-O} , which grow with n . These features allow us to conclude that although PNMPy interacts very satisfactorily with DA molecules, the molecular rigidity of this polymer limits the detection process with respect to other materials. In contrast, analysis of the calculated n -NCPy \cdots DQ complexes indicates that the flexibility of the cyanoethyl group favors not only the rearrangement of the interacting molecules when n increases but also the maximization of the number of attractive C – H \cdots O intermolecular interactions. Consequently, calculations predict that PNCPy interacts more strongly with DQ than PNMPy, which is fully consistent with experimental observations.

4.2. ELECTROACTIVE POLYMERS FOR THE DETECTION OF MORPHINE

The interaction between morphine (MO), a very potent analgesic psychoactive drug, and five electroactive polymers, poly(3,4-ethylenedioxythiophene) (PEDOT), poly(3-methylthiophene) (P3MT), polypyrrole (PPy), poly(N-methylpyrrole (PNMPy) and poly[N-(2-cyanoethyl)pyrrole] (PNCPy), has been examined using theoretical calculations on model complexes and voltammetric measures considering different pHs and incubation times. Quantum mechanical calculations in model polymers predict that the strength of the binding between the different polymers and morphine increases as follows: PEDOT < PNMPy < Ppy < <P3MT \approx PNCPy. The most relevant characteristic of P3MT is its ability to interact with morphine exclusively through non-directional interactions. On the other hand, the variations of the electroactivity and the anodic current at the reversal potential evidence that the voltammetric response towards the presence of MO is considerably higher for P3MT and PNCPy than that for the other polymers at both acid (P3MT > PNMPy) and neutral (P3MT \approx PNCPy) pHs. Energy decomposition analyses of the interaction of MO with different model polymers indicate that the stronger affinity of MO for P3MT and PNCPy as compared to PEDOT, PNMPy, and PPy is due to more favorable orbital interactions. These more stabilizing orbital interactions are the result of the larger charge transfer from MO to P3MT and PNCPy model polymers that takes place because of the higher stability of the single occupied molecular orbital (SOMO) of these model polymers. Therefore, to design

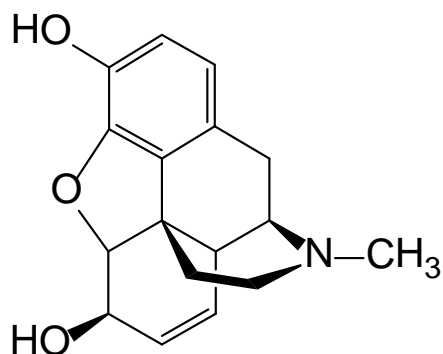


polymers with a large capacity to detect MO we suggest looking at polymers with high electron affinity.

4.2.1. INTRODUCTION

Because their chemical and physical properties may be tailored over a wide range of characteristics, the use of polymers is finding a permanent place in sophisticated electronic measuring devices such as sensors [49-53]. Among this wide family of organic materials, electroactive polymers (EPs) have emerged as attractive candidates for sensing elements due to its unique electrochemical, electrical and optical properties. Thus, properties of these π -conjugated organic materials have been observed to change at room temperature when they are exposed to low concentrations of chemical species, making EPs useful as sensors of gases [54-56], metallic ions [57-60], biomolecules [12,61-66], *etc.*, for environmental and clinical monitoring.

To rationalize and complete experimental sensing information, molecular modeling investigations are extremely useful. Within this context, first principle theoretical studies through sophisticated quantum mechanical (QM) calculations are known to be useful tools for quantifying both intramolecular and intermolecular interactions that govern sensor-analyte binding [60,67-75]. Indeed, such methods provide accurate molecular geometries, give access to the conformational energetic and are able to delineate the sensor-analyte interactions pattern. Thus, QM investigations on complexes formed by



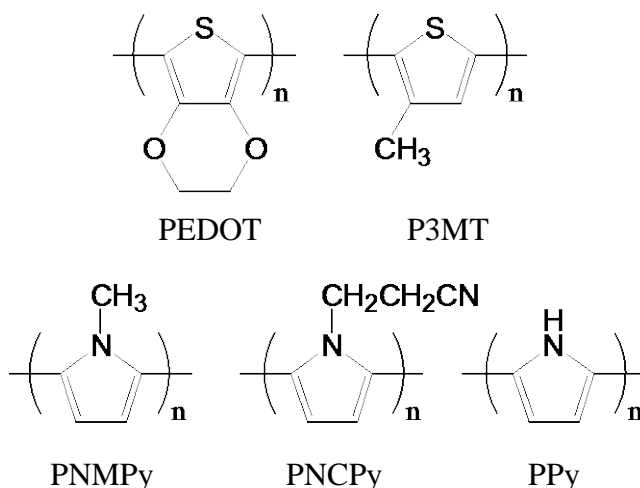
Scheme 4.3. Molecular structure of MO

model EPs and different types of analytes (*e.g.* metallic cations [60,71], neurotransmitters [72], DNA bases [73,74] and vapor of solvents [75]) have been recently devoted to establish a relationship between the experimental sensing information and both the interaction pattern and the binding energies.

We are currently interested in the development of EP-based biosensors to detect certain types of narcotic drugs with clinical applications. Within this specific context, the development of advanced systems to detect morphine (MO; Scheme 4.3), which is the principal active component in opium, is particularly interesting since it is frequently used in medicine to relieve severe pain of patients. However, this extremely potent analgesic psychoactive drug, which affects drastically the individual abilities of the user, is very toxic in excess or when abused.

Currently, detection of MO in clinical assays is carried out using high-performance liquid chromatography followed by UV spectroscopy [76] and conventional electrochemical methods [77,78]. Recently, the excellent properties of poly(3,4-ethylenedioxythiophene) (Scheme 4.4), abbreviated PEDOT, were used to propose a more convenient method to detect MO [79,80]. PEDOT and its derivatives were settled among the most successful EPs due to their high electrochemical and environmental stability, high conductivity, high transparency and high biocompatibility [81-85]. Detection of MO with PEDOT was carried out using immobilized molecularly imprinted polymer (MIP) particles, this procedure being successful for drug concentrations ranging from 0.01 to 0.2 mM [79]. More recently, Atta and co-workers [86] investigated the electrochemical determination of MO at PEDOT modified platinum electrodes in presence of sodium dodecyl sulfate. Specifically, the detection procedure proposed by these authors was based on the oxidation of the phenolic group of MO at +0.41 V.

In this work we present a comprehensive detection study based to compare the affinity of five different EPs (Scheme 4.4) towards MO: PEDOT, poly(3-methylthiophene)



Scheme 4.4. Molecular structure of the investigated EPs.

(P3MT), polypyrrole (PPy), poly(N-methylpyrrole (PNMPy) and poly[N-(2-cyanoethyl)pyrrole] (PNCPy). PEDOT has been successfully used to detect specific nucleotide sequences in DNA [65,87] as well as different small biomolecules, including drugs [41]. Comparison between PEDOT and P3MT is expected to provide useful information about the influence of hydrogen bonding interactions in the detection of MO (*i.e.* the oxygen atoms of the dioxane ring in PEDOT repeat unit were found to form strong intermolecular hydrogen bonds [65,73,74,87]). PPy, PNMPy and PNCPy showed sensing abilities for the detection of dopamine that, as MO, presents aromatic and hydroxyl groups [12,72]. Indeed, the sensing ability of these EPs to detect dopamine was found to increase as follows: PPy < PNMPy < PNCPy. Furthermore, a recent study evidenced the high ability of PPy and PNMPy to capture MO molecules and to retain them for a long period [88].

The present study is based on both theoretical QM calculations and experimental measures to evaluate the intrinsic detection ability of PEDOT, P3MT, PPy, PNMPy and PNCPy. More specifically, QM calculations have been used to provide microscopic understanding of the non-covalent interactions involved in the interaction between the EPs and MO. For this purpose, the geometry and strength of the binding between each EP and MO have been evaluated using model complexes. Furthermore, interactions have been analyzed by means of energy decomposition analyses at the QM level. Finally, experimental studies to examine the sensing ability of the five EPs have been performed using cyclic voltammetry (CV) considering different pHs and incubation times. QM and CV results have been found to be fully consistent, the experimentally measured ability to detect MO increasing with the predicted binding energy.

4.2.2. METHODS

4.2.2.1. COMPUTATIONAL DETAILS

Calculations were performed using the Gaussian 09 rev. A02 computer program [28]. PEDOT, P3MT, PPy, PNMPy and PNCPy were modeled considering small oligomers containing n repeat units in the radical cation state (n -EPs, charge = + 1 and spin multiplicity = 2). It is worth noting that the selection of oxidized n -oligomers was based on our own experimental results (see Results and Discussion section), which indicated that at the detection potential the polymer is oxidized. MO was considered in its neutral form and the molecular geometry used as starting point corresponded to the obtained high resolution X-ray crystallography [89].

The structure of n -EPs \cdots MO complexes was determined by full geometry optimization using the UHF formalism combined with the basis set 6-31+G(d,p) [31,34,90]. Harmonic vibrational frequencies were computed to verify the nature of the minimum state of the resulting stationary points. In order to include electron correlation effects in energy estimations, single-point calculations were performed at the UMP2 level [91] using the 6-31+G(d,p) basis set. The basis set superposition error (BSSE) was corrected using the counterpoise (Cp) method [35].

Binding energies, ΔE_b , were estimated as the difference between the total energy of the optimized complex (E_{AB}) and the energies of the isolated subsystems with the geometries obtained from the optimization of the complex:

$$\Delta E_b = E_{AB} - E_{A(B)} - E_{B(A)} \quad (4.2)$$

where $E_{A(B)}$ and $E_{B(A)}$ refer to energies of the subsystem after correct the BSSE.

In addition, with the aim of achieving a better comprehension of the interaction between MO and the different polymers, energy decomposition analysis [92-95] (EDA) were performed on the UHF/6-31+G(d,p) optimized geometries of 3-EPs model polymers by means of the Amsterdam Density Functional package (ADF) [96,97]. The EDA has been performed with the TZ2P basis set of Slater type orbitals (STOs) [98] of triple- ξ quality containing two sets of polarization functions. The core shells of carbon, nitrogen, oxygen and sulfur were treated by the frozen-core approximation. Energies were calculated with the generalized gradient approximation (GGA) using the BP86-D functional [99-102], which includes the dispersion-correction as developed by Grimme [103-105] for a correct treatment of the stacking interactions.

In the EDA, the interaction energy (ΔE_{int}) between the MO and the model polymer is analyzed in the framework of the Kohn-Sham molecular orbital model using a quantitative decomposition of the bond into electrostatic interaction, Pauli repulsion, orbital interactions, and dispersion energy terms [92-95] represented as:

$$\Delta E_{int} = \Delta V_{el} + \Delta E_{pauli} + \Delta E_{oi} + \Delta E_{disp} \quad (4.3)$$

In particular, the orbital interactions component (ΔE_{oi}) accounts for charge transfer (*i.e.* donor–acceptor interactions between occupied orbitals on one fragment with unoccupied orbitals of the other) and polarization (*i.e.* empty–occupied orbital mixing on one fragment due to the presence of the other fragment). Finally, Hirshfeld charges were also calculated to analyze the charge transfer between MO and the 3-EPs [106].

4.2.2.2. EXPERIMENTAL METHODS

Materials

3,4-ethylenedioxythiophene (EDOT), 3-methylthiophene (3MT), pyrrole (Py), N-methylpyrrole (NMPy) and N-(2-cyanoethyl)pyrrole (NCPy) monomers and acetonitrile (all analytical reagent grade) were purchased from Aldrich and used as received. Anhydrous LiClO₄, analytical reagent grade from Aldrich, was stored in an oven at 80 °C before use in the electrochemical trials. MO solution also was purchased from Aldrich, and used as received. TRIS buffer solutions, purchased from Aldrich, were adjusted to different pH values: pH=2 and 7 with HCl (purchased from Panreac), and pH=8.5 with NaOH (purchased from Panreac).

Preparation

PEDOT, PPy, PNMPy and PNCPy films were prepared by chronoamperometry (CA) under a constant potential of 1.40 V using polymerization times of $\theta = 300, 600, 600$ and 1200 s, respectively. P3MT was obtained using recurrent potential pulses (RPP) of 50 s between 0.70 and 1.70 V, details on the experimental conditions being reported previously [36]. These synthetic procedures allowed us to obtain films of similar thickness in all cases (*i.e.* 2.1–2.6 μm as determined by optical profilometry using a WYKO 9300NT optical profiler - Veeco, Plainview, NY). Anodic electropolymerization and electrochemical experiments were performed on a VersaStat II potentiostat-galvanostat using a three-electrode two-compartment cell under nitrogen atmosphere at 25 °C. For the polymerizations by CA the anodic compartment was filled with 40 ml of a 10 mM monomer solution in acetonitrile containing 0.1 M LiClO₄ as supporting electrolyte, while the cathodic compartment contained 10 ml of the same electrolyte solution. P3MT films were produced using 0.2 M monomer acetonitrile solutions with 0.1 M LiClO₄. Platinum sheets of 1 cm [50] area were employed as working electrodes, whereas counter electrodes were made of steel AISI 316 in all cases. The reference electrode was an Ag|AgCl electrode containing a KCl saturated aqueous solution.

Electrochemical measurements for detection of MO

Electrochemical detection was carried out by CV using an PGSTAT302N AUTOLAB potentiostat-galvanostat (Ecochimie, The Netherlands) equipped with the ECD module

to measure very low current densities (100 μA -100 pA), which was connected to a PC computer controlled through the NOVA 1.6 software. Electrochemical experiments were performed at room temperature using TRIS buffer solutions adjusted to $\text{pH}=2, 7$ and 8.5 . It should be noted that, although the useful buffer range of TRIS solutions is $7-9$, the pH of the solutions adjusted to 2 will not be altered by oxidation and reduction processes carried out in this study because of the used potentials. The glass cell used for detection assays was equipped with saturated $\text{Ag}|\text{AgCl}$ as reference electrode and platinum (Pt) wire as counter electrode. Voltammograms were recorded in the potential range from -0.50 to 1.60 V at a scan rate of $50 \text{ mV}\cdot\text{s}^{-1}$ unless other scan rate is explicitly specified. Before to record the voltammograms, EP films deposited on Pt were subjected to the following experimental conditions:

- a) immersion at room temperature in TRIS buffer solutions at $\text{pH}=2, 7$ and 8.5 during $3, 12$ and 24 h (*blank samples*);
- b) incubation at room temperature during $3, 12$ and 24 h in 3.5 mM MO TRIS buffer solutions at $\text{pH}=2, 7$ and 8.5 (*incubated samples*).

4.2.3. RESULTS AND DISCUSSION

4.2.3.1. THEORETICAL CALCULATIONS: INTERACTION PATTERNS AND BINDING ENERGIES

The interaction between the EPs and MO was modeled using a build-up approach that was previously used to investigate the interaction of dopamine with both PNMPy and PNCPy [72]. For this purpose, $n\text{-EP}\cdots\text{MO}$ model complexes of growing n , where n indicates the number of repeat units, were selectively built. More specifically, the interaction of complexes with $n = 1$ was examined in a first stage, the resulting complexes being used to construct the starting structures for $2\text{-EP}\cdots\text{MO}$. Finally, the starting arrangements of $3\text{-EP}\cdots\text{MO}$ were constructed using the optimized geometries of $2\text{-EP}\cdots\text{MO}$. Analysis of the results has been focused on $3\text{-EP}\cdots\text{MO}$ complexes, which are the most representative.

Geometry optimizations of 12 starting structures for $1\text{-EDOT}\cdots\text{MO}$ led to 9 different arrangements, which were categorized in six different groups according to the interaction patterns. The number of starting structures was increased to 20 for all the remaining $1\text{-EP}\cdots\text{MO}$ complexes, the number of different arrangements derived from their optimization being 9, 11, 8 and 8 for $1\text{-3MT}\cdots\text{MO}$, $1\text{-Py}\cdots\text{MO}$, $1\text{-NMPy}\cdots\text{MO}$ and $1\text{-NCPy}\cdots\text{MO}$, respectively. According to the interaction pattern, the optimized geometries of 1-3MT , 1-Py and 1-NMPy complexes were classified in 6 groups while those of $1\text{-NCPy}\cdots\text{MO}$ were categorized in 8 groups. The most stable structure of each group were used to construct the starting structures of $2\text{-EP}\cdots\text{MO}$ complexes by adding a new repeat unit. After geometry optimization, 5, 4, 5, 4 and 6 different structures were obtained for $2\text{-$

Table 4.3. Relative Energy (ΔE ; in kcal/mol) and Binding Energy after Correct the Basis Set Superposition Error (ΔE_b ; in kcal/mol) for 3-EDOT \cdots MO, 3-3MT \cdots MO, 3-Py \cdots MO, 3-NMPy \cdots MO and 3-NCPy \cdots MO Complexes (see Figure 4.10) at the UMP2/6-31+G(d,p) Level.

	ΔE	ΔE_b		ΔE	ΔE_b
3-EDOTa	0.0	-11.1	3-Pya	0.0	-25.2
3-EDOTb	0.1	-10.9	3-Pyb	0.3	-18.2
3-EDOTc	0.5	-10.5	3-Pyc	0.6	-19.1
3-EDOTd	0.8	-12.3	3-Pyd	2.7	-19.0
3-3MTa	0.0	-48.2	3-NMPya	0.0	-13.2
3-3MTb	1.7	-47.1	3-NMPyb	0.1	-14.4
			3-NMPyc	1.4	-14.1
			3-NCPya	0.0	-50.9

EDOT \cdots MO, 2-3MT \cdots MO, 2-Py \cdots MO, 2-NMPy \cdots MO and 2-NCPy \cdots MO complexes, respectively. As occurred above, the structures obtained for 2-EP \cdots MO were used to build the starting arrangement of 3-EP \cdots MO complexes. For each 3-EP \cdots MO complex, optimized structures with different interaction patterns and relative energies (ΔE) lower than 3.0 kcal/mol with respect to the most stable one were the only considered for analysis. Thus, the number of structure that fulfilled such requirements was 4, 2, 4, 3, and 1 for 3-EDOT \cdots MO, 3-3MT \cdots MO, 3-Py \cdots MO, 3-NMPy \cdots MO and 3-NCPy \cdots MO complexes, which are depicted in Figure 4.10. Both ΔE and ΔE_b values for each complex are listed in Table 4.3.

The four 3-EDOT \cdots MO structures (Figure 4.10a) are within a ΔE interval of only 0.8 kcal/mol. As it can be seen, all four structures are stabilized by C–H \cdots O interactions while, amazingly, no conventional O–H \cdots O hydrogen bond is detected. In addition, the lowest energy structure (3-EDOTa) shows a π -stacking interaction with the two aromatic rings arranged perpendicularly (*i.e.* T-shaped disposition). The remaining 3 structures (3-EDOTa-c) only differ in the relative orientation of the two molecules, which explains their resemblance in terms of ΔE . The strength of the binding is similar for the four structures with ΔE_b values ranging from -10.5 to -12.3 kcal/mol. The two structures obtained for 3-3MT \cdots MO, 3-3MTa and 3-3MTb, are separated by 1.7 kcal/mol. Although these two structures are mainly stabilized by non-specific intermolecular interactions, the ΔE_b values, -48.2 and -47.1 kcal/mol, are significantly lower than those obtained for 3-EDOT \cdots MO structures. This should be attributed to the fact that the contact surface between the two molecules is larger in 3-3MT \cdots MO than in 3-EDOT \cdots MO, enhancing the contribution of the electrostatic interactions provoked by the positive charge localized in the 3-3MT oligomer.

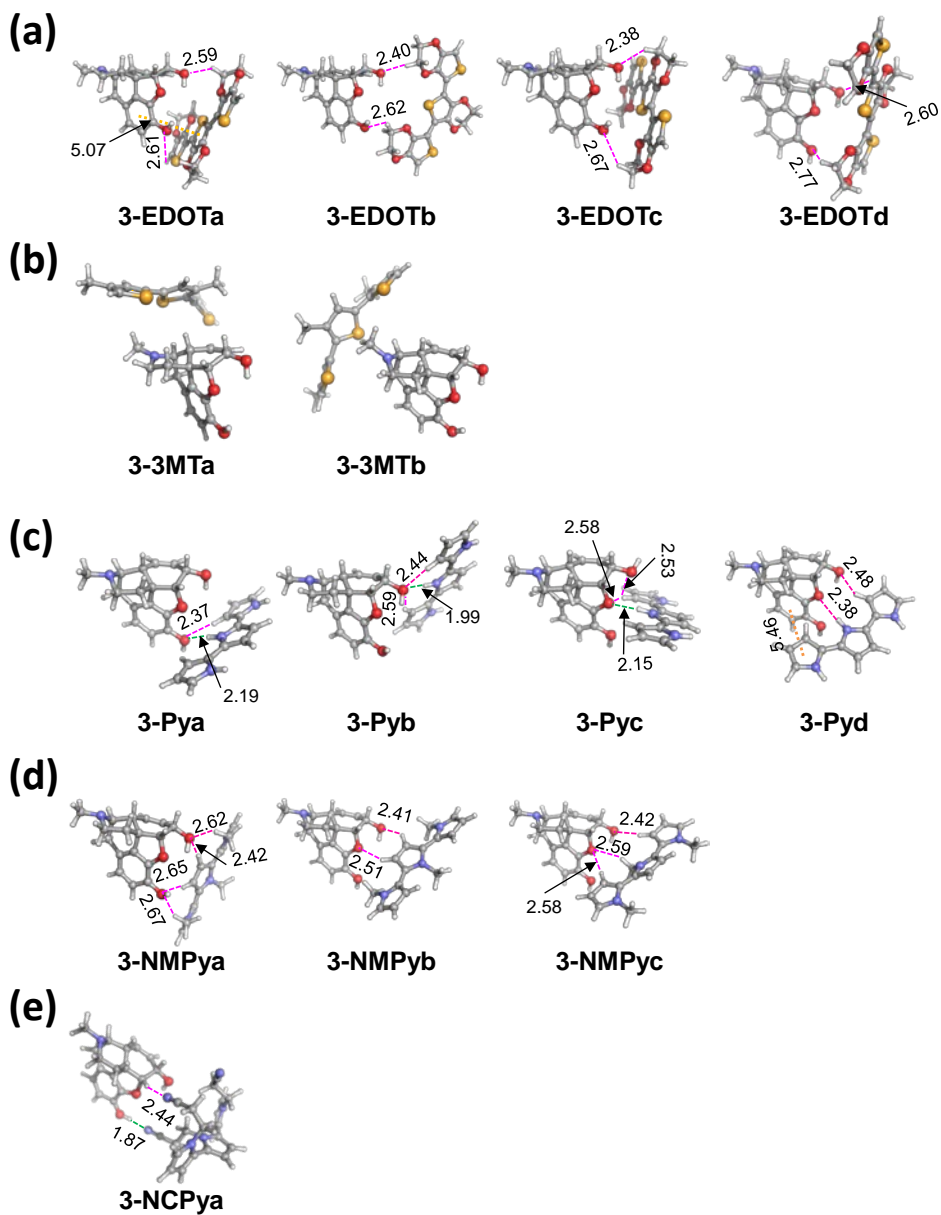


Figure 4.10. Geometries of the (a) 3-EDOT \cdots MO, (b) 3-3MT \cdots MO, (c) 3-Py \cdots MO, (d) 3-NMPy \cdots MO and (e) 3-NCPy \cdots MO complexes with $\Delta E < 3$ kcal/mol derived from QM calculations. C-H \cdots O and C-H \cdots N interactions are indicated by pink lines, aromatic \cdots aromatic staking by yellow lines and N-H \cdots O hydrogen bonds by green lines. The H \cdots O, H \cdots N and aromatic \cdots aromatic (centers of masses) distances are displayed in Å.

Figure 4.10c displays the four structures obtained for 3-Py \cdots MO, which are comprised within a ΔE interval of 2.7 kcal/mol. The lowest energy structure (3-Pya) is stabilized by a N–H \cdots O hydrogen bond and a C–H \cdots O interaction, which involve the same hydroxyl group of MO. Although the nature of the intermolecular interactions in the next structure (3-Pyb), which is destabilized by only 0.3 kcal/mol, is similar to those of 3-Pya, some clear differences are identified. The most relevant ones can be summarized as follows:

- i.* the relative orientation of the two interacting molecules change with respect to the 3-Pya;
- ii.* the MO hydroxyl group involved in the intermolecular interactions of the two structures is different; and
- iii.* the oxygen of MO in 3-Pyb forms one N–H \cdots O hydrogen bond and two C–H \cdots O interactions rather than one interaction of each type, as in 3-Pya.

The third structure (3-Pyc) essentially differs from the lowest energy one in the relative orientation of the two fragments as well as in the fact that intermolecular interactions involve two oxygen atoms of MO. Finally, the fourth structure (3-Pyd) presents a π -stacking, in addition to the N–H \cdots O hydrogen bond and the C–H \cdots O interaction. In spite of the π -stacking is not present in the three previous structures, 3-Pyd is disfavored by 2.1 kcal/mol with respect to 3-Pyc. The ΔE_b of these structures (Table 4.3) ranges from –25.2 kcal/mol (3-Pya) to –18.2 kcal/mol (3-Pyb) indicating that MO interacts more favorably with PPy than with PEDOT but less favorably than with P3MT.

Three different structures separated by a ΔE interval of 1.4 kcal/mol have been identified for 3-NMPy \cdots MO. The two structures of lowest energy are practically isoenergetic (3-NMPya and 3-NMPyb in Figure 4.10d), being stabilized by C–H \cdots O interactions. Although the number of such interactions is higher for 3-NMPya than for 3-NMPyb (*i.e.* 4 and 2, respectively), the strength of such interactions is higher for the latter than for the former (*i.e.* H \cdots O distances are larger for 3-NMPya than for 3-NMPyb). This feature explains not only their isoenergetic behavior but the corresponding ΔE_b values (Table 4.3). Although the third structure, 3-NMPyc, also presents C–H \cdots O interactions, the geometric distortions associated to the binding process provokes a small energy penalty (*i.e.* 1.4 kcal/mol). Results indicate that the affinity of PNMPy towards MO is higher than that of PEDOT but lower than those of PPy and, especially, P3MT.

Finally, the 3-NCPy \cdots MO only presented one structure within a ΔE interval of 3.0 kcal/mol (3-NCPya in Figure 4.10e). This structure, which shows a ΔE_b of –50.9 kcal/mol, is stabilized by a strong O–H \cdots N hydrogen bond, with a H \cdots O distance of only 1.87 Å, and a C–H \cdots N interaction. Comparison of ΔE_b values listed in Table 4.3 allows us to predict that the strength of the binding between the studied EPs and MO increases as follows: PEDOT < PNMPy < PPy < P3MT \approx PNCpy. As it can be seen, these EPs can be categorized in two classes depending on their affinity towards MO:

- a) those with ΔE_b values lower than ~ -25.0 kcal/mol;
 b) those with ΔE_b values about ~ -50.0 kcal/mol.

Unexpectedly, polymers with highest tendency to act as hydrogen bonding acceptor (*i.e.* the oxygen atoms of PEDOT) and donor (*i.e.* the N–H of PPy) belong to the former class.

With the aim to understand this surprising trend, we have performed an EDA of the interaction between MO and 3-EPs model polymers for the most stable structures in each case. From the values in Table 4.4 we find that the main factor determining the different interaction energies is the orbital interaction component. Those polymers that present the strongest interaction, PNCPy and P3MT, are the ones with the most stabilizing orbital interaction term (from -27.8 to -44.3 kcal mol $^{-1}$). On the other hand, the rest of the systems, which present a weaker interaction, have also much less stabilizing ΔE_{oi} values (from -5.0 to -12.1 kcal mol $^{-1}$). The rest of terms of the EDA analysis do not play a determinant role. Hirshfeld charges of MO were calculated to discuss the origin of the different ΔE_{oi} values. Let us remind that initially MO is neutral, whereas the model polymer is charged +1 as a doublet spin state due to its unpaired electron, which is located in a single occupied molecular orbital (SOMO). The Hirshfeld charges of MO in Table 4.4 show a clear difference between the strongly bound 3-PEs models of PNCPy and P3MT and the rest, as for the former a transfer of almost one electron from MO to the polymer is observed with positive charges on MO of $0.74e$ for 3-MT and $0.91e$ for 3-NCPy. On the other hand, for the weaker interacting polymers we find that MO keeps almost neutral and uncharged. The charge transfer in MO \cdots PNCPy and MO \cdots P3MT is favored by the lower energy of their SOMOs as can be seen in Table 4.4, which gathers the relative energies of the SOMOs of the 3-EPs analyzed. The higher charge transfer in 3-Eps models of PNCPy and P3MT justify the more stabilizing ΔE_{oi} component.

Table 4.4. Energy Decomposition Analysis Terms and Relative Energy of the SOMO with respect to that of 3-CPy, in kcal mol $^{-1}$, and Hirshfeld Charges of MO.

	ΔE_{Pauli}	ΔV_{el}	ΔE_{oi}	ΔE_{disp}	ΔE_{int}	ΔE_{SOMO}	$q(\text{MO})$
3-3MTa	4.70	0.45	-27.85	-9.57	-32.27	11.92	0.74
3-3MTb	4.40	0.39	-31.71	-7.84	-34.75	7.53	0.79
3-NCPya	16.10	-14.68	-44.34	-6.17	-49.09	0.00	0.91
3-EDOTa	5.66	-7.36	-4.96	-8.19	-14.85	48.32	0.07
3-EDOTb	4.68	-7.93	-5.33	-4.29	-12.88	48.95	0.02
3-NMPya	5.81	-9.75	-6.65	-5.56	-16.14	39.53	0.04
3-NMPyb	6.13	-10.53	-6.54	-6.02	-16.96	39.53	0.02
3-Pya	11.25	-18.13	-12.10	-10.46	-29.45	33.26	0.06
3-Pyb	11.53	-15.96	-11.36	-6.76	-22.55	33.89	0.05

Therefore to design polymers that improve detection of MO, the determinant factor that one should look at is the energy of the SOMO. Polymers with more stable SOMOs have a high capacity to accept electrons and will result in improved interactions with MO.

In the next section, the interaction between MO and the polymers will be analyzed through voltammetric measures to confirm the above discussed quantum chemical calculations.

4.2.3.2. ELECTROCHEMICAL BEHAVIOR OF THE EPS

Many EPs prepared in aqueous solution are not stable at potentials higher than ~ 1.1 V [88,107,108], which represents a serious limitation. In order to overcome it, EPs were generated in acetonitrile, which allowed us to ensure the stability of this material in the whole potential range used in this study (*i.e.* between -0.50 and 1.60 V). As the detection assays have been performed considering different incubation times in TRIS solutions acid, neutral and basic pHs (see next subsection), in this subsection we examine the electrochemical behavior of the five EPs in absence of MO but using the above mentioned experimental conditions.

Figure 4.11 compares the control voltammograms of fresh modified electrodes before any incubation process (*i.e.* Pt electrodes coated with the EPs after their immediate immersion in TRIS solutions with pHs adjusted at 2, 7 and 8.5) with that of Pt. The electrochemical response of all the EPs, which has been characterized by both the ability to exchange charge reversibly (electroactivity) and the anodic current at the highest potential (j_{max}), depends on the pH. As it can be seen, the electroactivity is significantly higher for P3MT than for the other CPs at pH=2 and 7 (*i.e.* approximately 64–67 and 68–73% at acid and neutral pH, respectively). Interestingly, the electroactivity decreases in all cases with exception of PEDOT when the pH increases from 7 to 8.5, this reduction ranging from 31% (PCNPy) to 60% (P3MT). In the case of PEDOT the electroactivity increases 82%. The same behavior is observed for j_{max} , which for P3MT is higher than 60 mA/cm² at pH=2 and 7 and decreases to 26 mA/cm² at pH=8.5. This reduction is less pronounced for the rest of the EPs (*i.e.* typically from ~ 25 to ~ 10 mA/cm²), an exception being observed for PEDOT (*i.e.* j_{max} increases from 34 to 38 mA/cm² with the pH).

4.2.3.3. VOLTAMMETRIC DETECTION OF MORPHINE

Control voltammograms of blank and incubated samples (*i.e.* those immersed in TRIS solution and MO-containing TRIS solution, respectively) were recorded considering immersion times of 3,12 and 24 h and pHs of 2,7 and 8.5. Figure 4.12 represents the control voltammograms recorded for systems immersed in solutions with pH=2. As it can be seen, the largest difference between blank and incubated samples in this acid environment occurs for P3TM and PNCy, independently of the immersion time. However, differences between blank and incubated samples of some other EPs are also

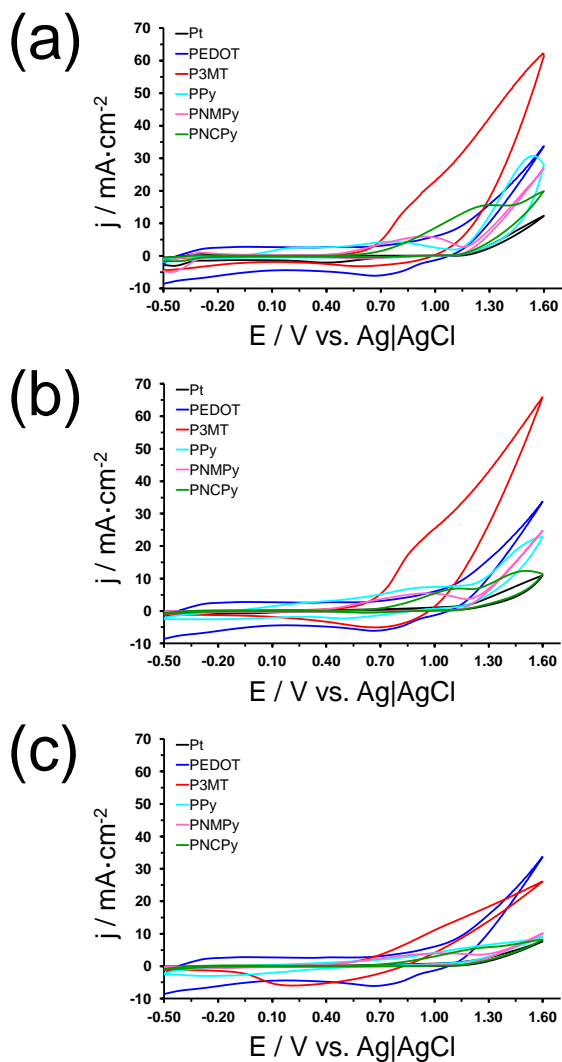


Figure 4.11. Control voltammograms for the oxidation of Pt coated with P3MT, PEDOT, PPy, PNMPy and PNCPy in TRIS solutions with pH= (a) 2, (b) 7 and (c) 8.5. The voltammogram recorded for the uncoated Pt electrode has been included for comparison. Initial and final potentials: -0.50 V; reversal potential: 1.60 V; scan rate: 50 mV·s⁻¹.

clearly appreciable for specific immersion times. The ability to detect MO of the five EPs has been quantified by considering, for each immersion time, the difference of the electroactivity and Δj_{max} values between the incubated and blank samples (ΔQ in % and Δj_{max} in mA/cm², respectively). More specifically, the EP has been considered as appropriated only when the two following conditions are fulfilled simultaneously: (i)

$\Delta Q \geq 125\%$ or $\Delta Q \leq 75\%$; and (ii) $\Delta j \geq |10| \text{ mA/cm}^2$ (i.e. MO provokes significant changes in anodic and cathodic areas as well in the anodic density at the reversal potential). Results, which are depicted in Figure 4.13a and Figure 4.13b, indicate that the ability to detect MO of the different EPs at pH=2 decreases as follows: P3MT > PNCPy >> PPy > PNMPy. Results for PEDOT are completely inappropriate for all immersion times since the change in the voltammetric response of this EP is very weak.

Control voltammograms of samples immersed in solutions with pH=7 are displayed in Figure 4.14 while the variation of ΔQ and Δj_{max} with the immersion time are represented in Figure 4.13c and Figure 4.13d, respectively. Visual inspection of the voltammograms obtained indicates that the results obtained at pH=7 are similar to those achieved in acid environment for P3MT and PNCPy. Thus, such two EPs exhibit the highest variation in the voltammetric response, independently of the immersion time.

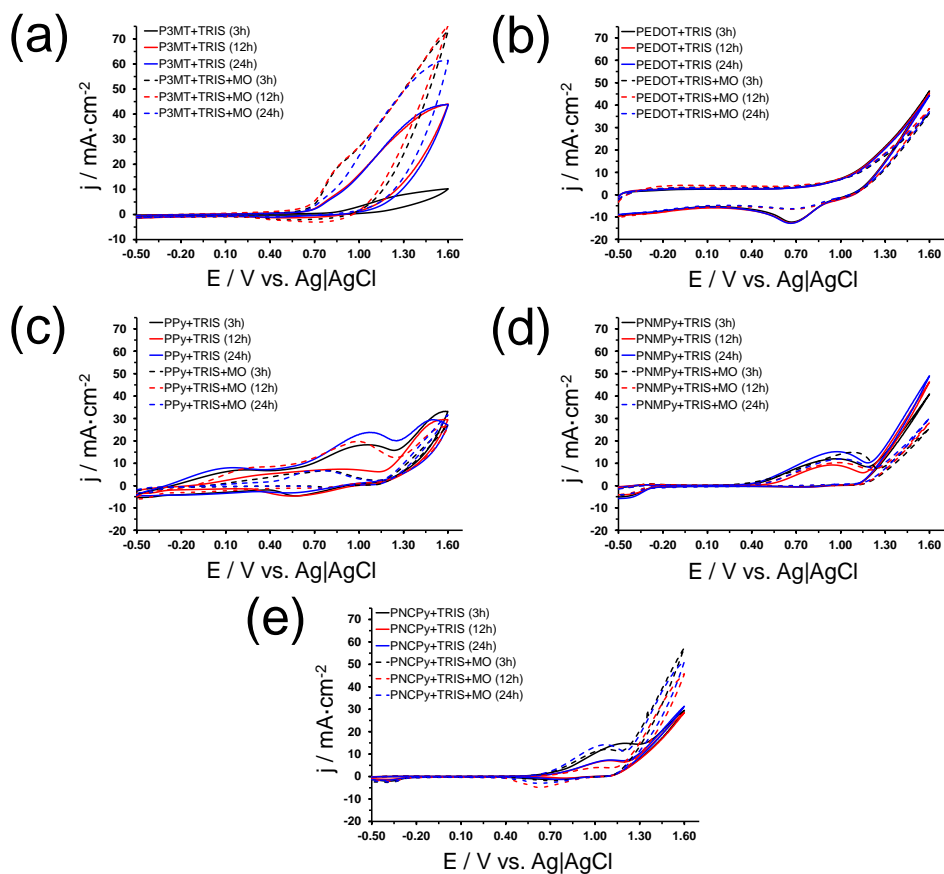


Figure 4.12. Control voltammograms for the oxidation of Pt coated with P3MT (a), PEDOT (b), PPy (c), PNMPy (d) and PNCPy (e) in TRIS (solid lines) and MO-containing TRIS (dashed lines) solutions at pH=2 and incubation times of 3, 12 and 24 h.

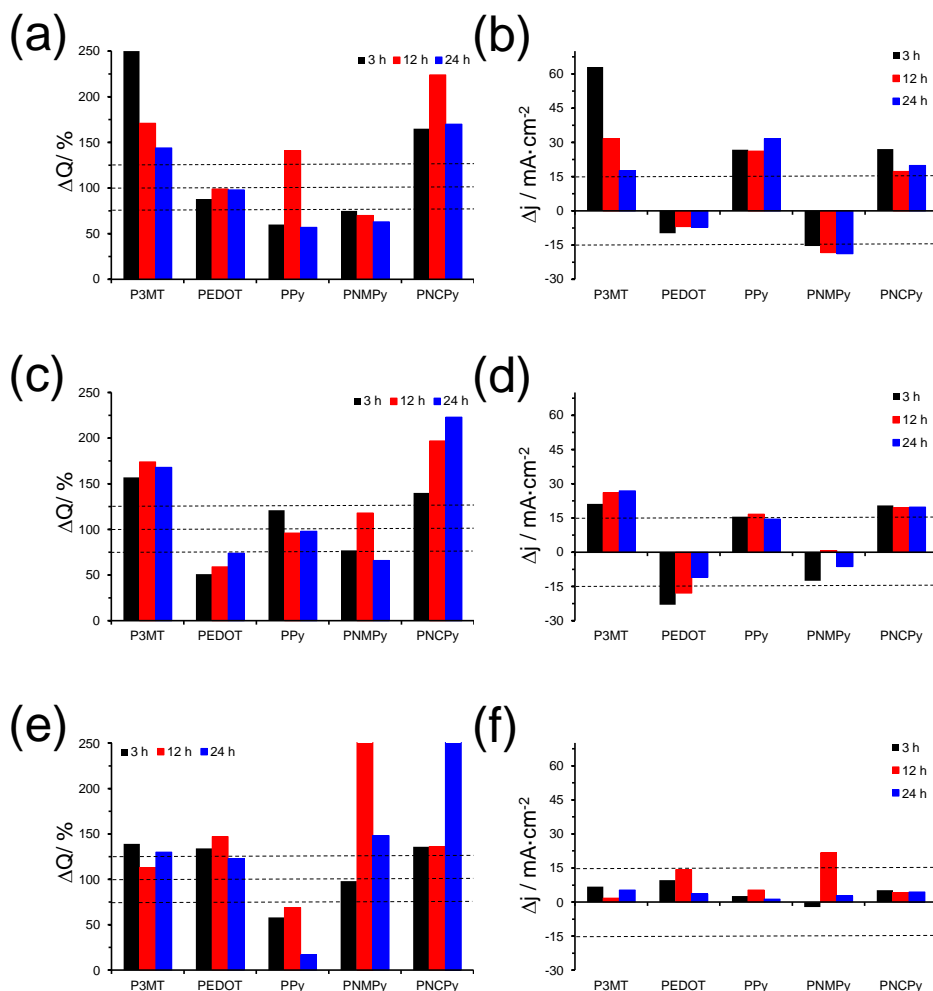


Figure 4.13. Difference between the incubated and blank samples in terms of electroactivity, ΔQ in % (left), and the current density at the reversal potential Δj_{max} in mA/cm^2 (right) for the five studied EPs at pH= (a) 2, (b) 7 and (c) 8.5.

However, some changes are identified for PEDOT and PPy. More specifically, the detection ability of the former exhibits an improvement with respect to pH=2, while the behavior of the latter becomes clearly worse. Considering the criteria used above, the response of EPs towards MO can be described as follows: P3MT \approx PNCpy \gg PEDOT. At neutral pH the response of PPy and PNMPy is not appropriated for MO detection.

Finally, the cyclic voltammograms recorded in solutions with pH=8.5 (Figure 4.15) as well as of ΔQ and Δj_{max} values (Figure 4.13e and Figure 4.13f, respectively) evidence

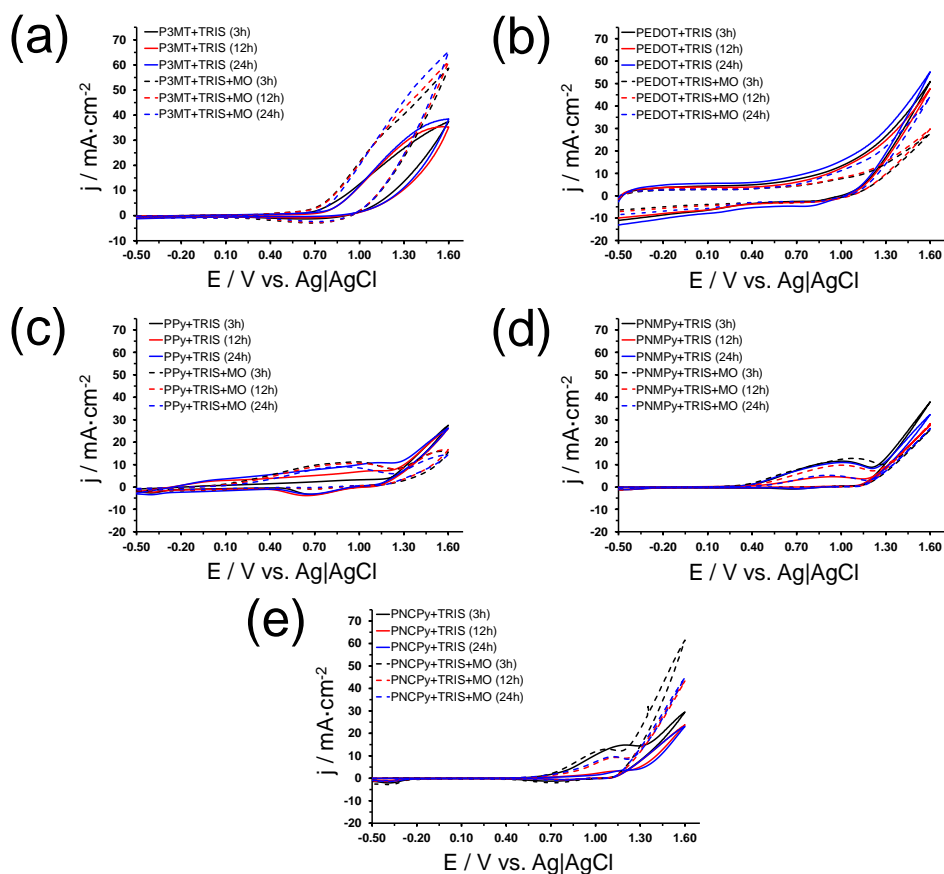


Figure 4.14. Control voltammograms for the oxidation of Pt coated with P3MT (a), PEDOT (b), PPy (c), PNMPy (d) and PNCPy (e) in TRIS (solid lines) and MO-containing TRIS (dashed lines) solutions at pH= 7 and incubation times of 3, 12 and 24 h.

that the response of all EPs towards MO is weak or even very weak. This has been attributed to the competition between the hydroxyl and other negatively charged species, especially dopant anions.

4.2.3.4. STABILITY FOR THE VOLTAMMETRIC DETECTION OF MORPHINE

The electrochemical stability quantifies how the ability to exchange charge reversibly of a material decreases upon consecutive oxidation-reduction cycles. This property has been used to evaluate how repetitive is the measure of electrochemical parameters for the detection of MO without significant detriment in the intensity of the signals. The effect of consecutive oxidation-reduction cycles on the voltammetric response of EPs in absence and presence of MO was examined by considering P3MT (incubation time 3 and

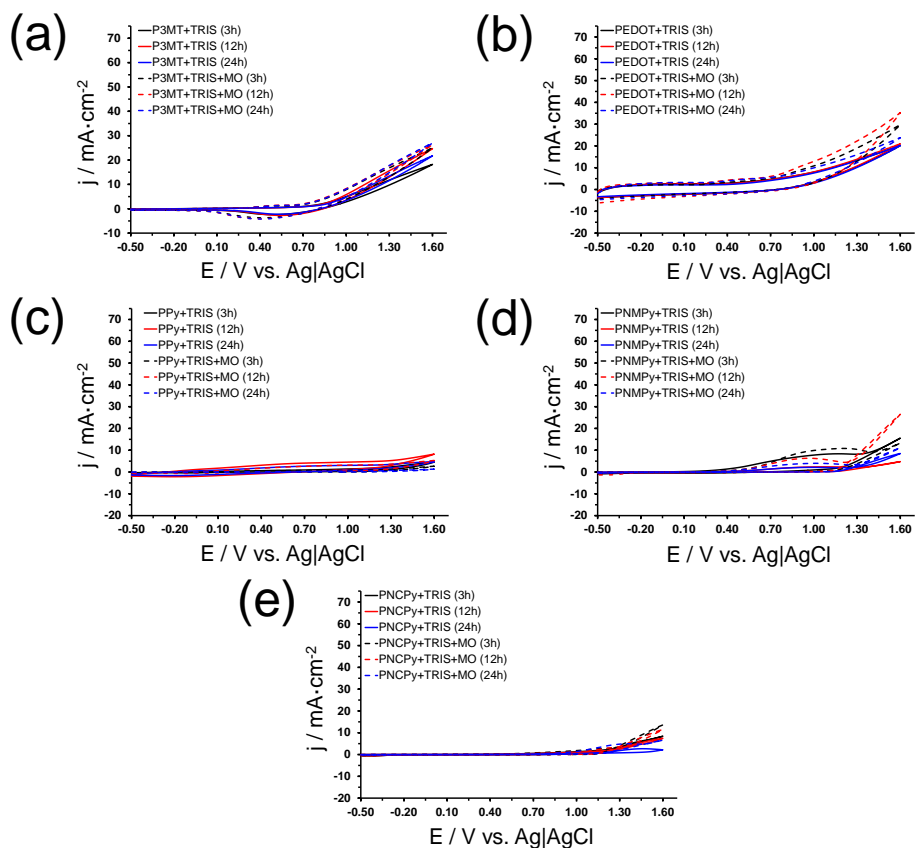


Figure 4.15. Control voltammograms for the oxidation of Pt coated with P3MT (a), PEDOT (b), PPy (c), PNMPy (d) and PNCy (e) in TRIS (solid lines) and MO-containing TRIS (dashed lines) solutions at pH= 8.5 and incubation times of 3, 12 and 24 h.

12 h for pH=2 and 7, respectively) and PNCy (incubation time 12 and 24 h for pH=2 and 7, respectively), which were the more efficient EPs for sensing at acid and neutral pHs. Figure 4.16 represents the voltammograms of blank and incubated samples after 10 consecutive redox cycles. As it can be seen, the largest differences in terms of ΔQ and Δj_{max} at both pH=2 and 7 are detected for PNCy. More specifically, the Δj_{max} measured for P3MT at pH=2 and 7 is -2.1 and 3.7 mA/cm², respectively, which represent a very drastic reduction with respect to the values derived from the first control voltammograms (*i.e.* 157 and 26.1 mA/cm², respectively). However, the Δj_{max} determined for PNCy after 10 cycles, 10.1 and 5.5 mA/cm² at pH=2 and 7, respectively, are relatively close to those obtained in the first control voltammogram (*i.e.* 17.3 and 19.3 mA/cm², respectively). Inspection of ΔQ shows similar trends, redox cycles provoking large and moderate reductions in the difference of electroactivities for P3MT and PNCy,

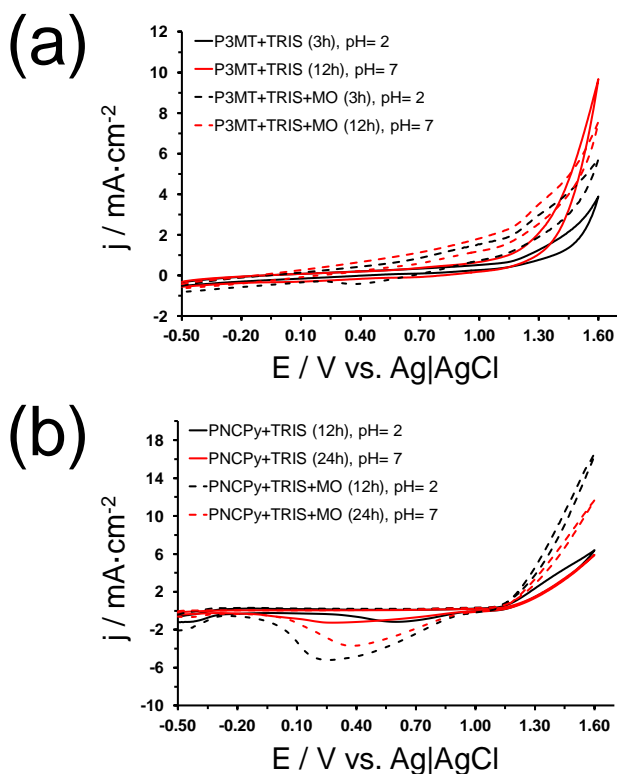


Figure 4.16. Control voltammograms for Pt coated with P3MT (a) and PNCPy (b) after ten consecutive oxidation-reduction cycles in TRIS (solid lines) and MO-containing TRIS (dashed lines) solutions at $\text{pH}= 2$ and 7 and the indicated incubation times.

respectively. The overall of these results indicate that the latter EP is the most stable for the voltammetric detection of MO.

4.2.4. CONCLUSIONS

The ability of five different EPs to interact with MO has been evaluated using QM and voltammetric detection assays. QM calculations on model complexes indicate that the affinity of all these EPs towards morphine, with exception of that of P3MT, is dominated by a combination of different directional interactions: $\text{C-H}\cdots\text{O}$ (PEDOT, PPy and PNMPy), π -stacking (PEDOT and PPy), $\text{N-H}\cdots\text{O}$ (PPy), $\text{O-H}\cdots\text{N}$ (PNCPy) and $\text{C-H}\cdots\text{N}$ (PNCPy). In contrast, P3MT only interacts with MO through non-directional van der Waals interactions. Calculations predict that the strength of the interaction between each EP and MO decreases as follows: $\text{PNCPy} \approx \text{P3MT} \gg \text{PPy} > \text{PNMPy} > \text{PEDOT}$. Cyclic voltammetry assays are fully consistent with these results at acid and neutral pHs.

Thus, the MO-induced changes in both the electroactivity and the anodic current at the reversal potential are larger for P3MT and PNMPy than for PPy, PNMPy and PEDOT at pH=2 (P3MT > PNCPy) and pH=7 (P3MT \approx PNCPy). In contrast, the voltammetric behavior of all investigated polymers is similar in presence and absence of MO at pH=8.5. Although the responses of P3MT and PNCPy for the voltammetric detection of MO are clearly better than those of the other EPs, the stability of such responses is higher for PNMPy than for P3MT. Finally, energy decomposition analyses show that the stronger interaction of MO with P3MT and PNCPy as compared to the other studied polymers is due to the higher stability of their SOMOs, which favors the transfer of charge from MO to the polymers leading to stronger orbital interactions. This allows us to conclude that to design new polymers with a larger capacity of detecting morphine we should focus on the energy of its SOMO and choose those polymers with large electron affinity.

REFERENCES

- [1] B.J. Venton, R.M. Wightman; *Psychoanalytical electrochemistry: Dopamine and behavior*; Anal Chem **75**, 414a (2003).
- [2] E. Kandel, J.H. Schwartz, T.M. Jessel, (Eds.), *Principles of neural science*, McGraw-Hill, New York, 2000.
- [3] K. Powell; *At a lecture at Woods Hole Oceanographic Institute, Tilney heard Jean Dan describe the amazing acrosomal reaction of starfish sperm, which in seven seconds shoots out a process that is 45 times the length of the sperm cell. (vol 170, pg 167, 2005)*; J Cell Biol **170**, 849 (2005).
- [4] B.D. Bath, H.B. Martin, R.M. Wightman, M.R. Anderson; *Dopamine adsorption at surface modified carbon-fiber electrodes*; Langmuir **17**, 7032 (2001).
- [5] B.J. Venton, K.P. Troyer, R.M. Wightman; *Response times of carbon fiber microelectrodes to dynamic changes in catecholamine concentration*; Anal Chem **74**, 539 (2002).
- [6] C.R. Raj, T. Ohsaka; *Electroanalysis of ascorbate and dopamine at a gold electrode modified with a positively charged self-assembled monolayer*; J Electroanal Chem **496**, 44 (2001).
- [7] L. Zhang, J. Jia, X. Zou, S. Dong; *Simultaneous determination of dopamine and ascorbic acid at an in-situ functionalized self-assembled monolayer on gold electrode*; Electroanal **16**, 1413 (2004).
- [8] V.S. Vasantha, S.M. Chen; *Electrocatalysis and simultaneous detection of dopamine and ascorbic acid using poly(3,4-ethylenedioxy)thiophene film modified electrodes*; J Electroanal Chem **592**, 77 (2006).
- [9] K. Pihel, Q.D. Walker, R.M. Wightman; *Overoxidized polypyrrole-coated carbon fiber microelectrodes for dopamine measurements with fast-scan cyclic voltammetry*; Anal Chem **68**, 2084 (1996).
- [10] C.C. Harley, A.D. Rooney, C.B. Breslin; *The selective detection of dopamine at a polypyrrole film doped with sulfonated beta-cyclodextrins*; Sensor Actuat B-Chem **150**, 498 (2010).
- [11] S. Shahrokhian; *Lead phthalocyanine as a selective carrier for preparation of a cysteine-selective electrode*; Anal Chem **73**, 5972 (2001).
- [12] M. Marti, G. Fabregat, F. Estrany, C. Aleman, E. Armelin; *Nanostructured conducting polymer for dopamine detection*; J Mater Chem **20**, 10652 (2010).
- [13] X.M. Feng, C.J. Mao, G. Yang, W.H. Hou, J.J. Zhu; *Polyaniline/Au composite hollow spheres: Synthesis, characterization, and application to the detection of dopamine*; Langmuir **22**, 4384 (2006).
- [14] J. Mathiyarasu, S. Senthilkumar, K.L.N. Phani, V. Yegnaraman; *Selective detection of dopamine using a functionalised polyaniline composite electrode*; J Appl Electrochem **35**, 513 (2005).
- [15] J. Mathiyarasu, S. Senthilkumar, K.L.N. Phani, V. Yegnaraman; *PEDOT-Au nanocomposite films for electrochemical sensing of dopamine and uric acid*; J Nanosci Nanotechnol **7**, 2206 (2007).
- [16] D. Aradilla, F. Estrany, E. Armelin, R. Oliver, J.I. Iribarren, C. Aleman; *Characterization and properties of poly[N-(2-cyanoethyl)pyrrole]*; Macromol Chem Phys **211**, 1663 (2010).
- [17] Z.P. Deng, D.C. Stone, M. Thompson; *Poly N-(2-cyanoethyl)pyrrole as a selective film for the thickness-shear-mode acoustic-wave sensor*; Can J Chem **73**, 1427 (1995).

- [18] Z.P. Deng, D.C. Stone, M. Thompson; *Characterization of polymer films of pyrrole derivatives for chemical sensing by cyclic voltammetry, X-ray photoelectron spectroscopy and vapour sorption studies*; *Analyst* **122**, 1129 (1997).
- [19] Z.P. Deng, D.C. Stone, M. Thompson; *Effect of redox state on the response of poly-N-(2-cyanoethyl)pyrrole coated thickness shear mode acoustic wave sensors to organic vapours*; *Analyst* **121**, 1341 (1996).
- [20] O. Ouerghi, A. Senillou, N. Jaffrezic-Renault, C. Martelet, H. Ben Ouada, S. Cosnier; *Gold electrode functionalized by electropolymerization of a cyano N-substituted pyrrole: application to an impedimetric immunosensor*; *J Electroanal Chem* **501**, 62 (2001).
- [21] A. Naji, C. Marzin, G. Tarrago, M. Cretin, C. Innocent, M. Persin, J. Sarrazin; *Electrodeposition of functionalized pyrrole (N-[3-(dimethylpyridyl-2-yl)aminopropyl], N-(3-aminopropyl), N-(3-acetamidopropyl) and N-(2-cyanoethyl)) on stainless steel gauze for membrane preparation*; *J Appl Electrochem* **31**, 547 (2001).
- [22] M. Schirmeisen, F. Beck; *Electrocoating of iron and other metals with polypyrrole*; *J Appl Electrochem* **19**, 401 (1989).
- [23] R. Oliver, A. Munoz, C. Ocampo, C. Aleman, E. Armelin, F. Estrany; *Electrochemical characteristics of copolymers electrochemically synthesized from N-methylpyrrole and 3,4-ethylenedioxythiophene on steel electrodes: Comparison with homopolymers*; *Chem Phys* **328**, 299 (2006).
- [24] D. Aradilla, F. Estrany, R. Oliver, C. Aleman; *Properties of nanometric and micrometric multilayered films made of three conducting polymers*; *Eur Polym J* **46**, 2222 (2010).
- [25] E.K. Richfield, J.B. Penney, A.B. Young; *Anatomical and affinity state comparisons between dopamine-d1 and dopamine-d2 receptors in the rat central nervous-system*; *Neuroscience* **30**, 767 (1989).
- [26] R.G. Freeman, M.B. Hommer, K.C. Grabar, M.A. Jackson, M.J. Natan; *Ag-clad Au nanoparticles: Novel aggregation, optical, and surface-enhanced Raman scattering properties*; *J Phys Chem-U S* **100**, 718 (1996).
- [27] M.M. Maye, L. Han, N.N. Kariuki, N.K. Ly, W.B. Chan, J. Luo, C.J. Zhong; *Gold and alloy nanoparticles in solution and thin film assembly: spectrophotometric determination of molar absorptivity*; *Anal Chim Acta* **496**, 17 (2003).
- [28] M.J. Frisch, G.W. Trucks, H.B. Schlegel, G.E. Scuseria, M.A. Robb, J.R. Cheeseman, G. Scalmani, V. Barone, B. Mennucci, G.A. Petersson, H. Nakatsuji, M. Caricato, X. Li, H.P. Hratchian, A.F. Izmaylov, J. Bloino, G. Zheng, J.L. Sonnenberg, M. Hada, M. Ehara, K. Toyota, R. Fukuda, J. Hasegawa, M. Ishida, T. Nakajima, Y. Honda, O. Kitao, H. Nakai, T. Vreven, J. Montgomery, J. A., J.E. Peralta, F. Ogliaro, M. Bearpark, J.J. Heyd, E. Brothers, K.N. Kudin, V.N. Staroverov, R. Kobayashi, J. Normand, K. Raghavachari, A. Rendell, J.C. Burant, S.S. Iyengar, J. Tomasi, M. Cossi, N. Rega, J.M. Millam, M. Klene, J.E. Knox, J.B. Cross, V. Bakken, C. Adamo, J. Jaramillo, R. Gomperts, R.E. Stratmann, O. Yazyev, A.J. Austin, R. Cammi, C. Pomelli, J.W. Ochterski, R.L. Martin, K. Morokuma, V.G. Zakrzewski, G.A. Voth, P. Salvador, J.J. Dannenberg, S. Dapprich, A.D. Daniels, Ö. Farkas, J.B. Foresman, J.V. Ortiz, J. Cioslowski, D.J. Fox; *Gaussian*, Gaussian 09, Revision A.1, Gaussian Inc. Wallingford CT, 2009.
- [29] D. Aradilla, J. Torras, C. Aleman; *Structural and electronic properties of poly[N-(2-cyanoalkyl)pyrrole]s bearing small alkyl groups*; *J Phys Chem B* **115**, 2882 (2011).
- [30] J. Casanovas, L.Y. Cho, C. Ocampo, C. Aleman; *A theoretical study of the effects produced by N-hydroxyalkyl substitution in pyrrole oligomers*; *Synthetic Met* **151**, 239 (2005).
- [31] Harihara.Pc, J.A. Pople; *Influence of polarization functions on molecular-orbital hydrogenation energies*; *Theor Chim Acta* **28**, 213 (1973).
-

- [32] A.D. Mclean, G.S. Chandler; *Contracted gaussian-basis sets for molecular calculations .1. 2nd row atoms, Z=11-18*; J Chem Phys **72**, 5639 (1980).
- [33] K. Burke, J. Perdew, Y. Wang, J. Dobson, G. Vignale, M. Das; *Electronic density functional theory: recent progress and new directions*; Dobson, JF, 81 (1998).
- [34] M.J. Frisch, J.A. Pople, J.S. Binkley; *Self-consistent molecular-orbital methods .25. supplementary functions for gaussian-basis sets*; J Chem Phys **80**, 3265 (1984).
- [35] S.F. Boys, F. Bernardi; *Calculation of small molecular interactions by differences of separate total energies - some procedures with reduced errors*; Mol Phys **19**, 553 (1970).
- [36] C. Ocampo, E. Armelin, F. Estrany, L.J. del Valle, R. Oliver, F. Sepulcre, C. Aleman; *Copolymers of 3,4-ethylenedioxythiophene and 3-methylthiophene: Properties, applications and morphologies*; Macromol Mater Eng **292**, 85 (2007).
- [37] F. Estrany, D. Aradilla, R. Oliver, E. Armelin, C. Aleman; *Properties of nanometric and submicrometric multilayered films of poly(3,4-ethylenedioxythiophene) and poly(N-methylpyrrole)*; Eur Polym J **44**, 1323 (2008).
- [38] D. Aradilla, F. Estrany, E. Armelin, C. Aleman; *Morphology and growing of nanometric multilayered films formed by alternated layers of poly(3,4-ethylenedioxythiophene) and poly(N-methylpyrrole)*; Thin Solid Films **518**, 4203 (2010).
- [39] Q. Wei, F.L. Zhang, J. Li, B.J. Li, C.S. Zhao; *Oxidant-induced dopamine polymerization for multifunctional coatings*; Polym Chem-Uk **1**, 1430 (2010).
- [40] F. Yu, S.G. Chen, Y. Chen, H.M. Li, L. Yang, Y.Y. Chen, Y.S. Yin; *Experimental and theoretical analysis of polymerization reaction process on the polydopamine membranes and its corrosion protection properties for 304 stainless steel*; J Mol Struct **982**, 152 (2010).
- [41] M. Skompska, M.A. Vorotyntsev; *Influence of chloride anions on the electrodeposition and electroactivity of the polymer matrix in polypyrrole, poly(N-methylpyrrole) and polypyrrole derivatives functionalized by titanocene centers, in dry non-aqueous solutions*; J Solid State Electr **8**, 360 (2004).
- [42] I. Fernandez, M. Trueba, C.A. Nunez, J. Rieumont; *Some features of the overoxidation of polypyrrole synthesized on austenitic stainless steel electrodes in aqueous nitrate solutions*; Surf Coat Tech **191**, 134 (2005).
- [43] G.R. Desiraju; *The C-H center dot center dot center dot O hydrogen bond: Structural implications and supramolecular design*; Accounts Chem Res **29**, 441 (1996).
- [44] T. Steiner; *Influence of C-H...O interactions on the conformation of methyl groups quantified from neutron diffraction data*; J Phys Chem A **104**, 433 (2000).
- [45] E.S. Meadows, S.L. De Wall, L.J. Barbour, F.R. Fronczek, M.S. Kim, G.W. Gokel; *Structural and dynamic evidence for C-H...hydrogen bonding in lariat ethers: Implications for protein structure*; J Am Chem Soc **122**, 3325 (2000).
- [46] A. Ghosh, M. Bansal; *C-H...O hydrogen bonds in minor groove of A-tracts in DNA double helices*; J Mol Biol **294**, 1149 (1999).
- [47] K.N. Houk, S. Menzer, S.P. Newton, F.M. Raymo, J.F. Stoddart, D.J. Williams; *Molecular meccano. 47. [C-H...O] interactions as a control element in supramolecular complexes: Experimental and theoretical evaluation of receptor affinities for the binding of bipyridinium-based guests by catenated hosts*; J Am Chem Soc **121**, 1479 (1999).
- [48] C. Aleman, J. Casanovas, H.K. Hall; *Systematic evaluation of the conformational properties of aliphatic omega-methoxy methyl esters*; J Org Chem **70**, 7731 (2005).
- [49] S. Cosnier; *Affinity biosensors based on electropolymerized films*; Electroan **17**, 1701 (2005).
- [50] B. Adhikari, S. Majumdar; *Polymers in sensor applications*; Progr Polym Sci **29**, 699 (2004).
- [51] B.D. Malhotra, A. Chaudhary, S.P. Singh; *Prospects of conducting polymers in biosensors*; Anal Chim Acta **578**, 59 (2006).

- [52] L.A. Terry, S.F. White, L.J. Tigwell; *The application of biosensors to fresh produce and the wider food industry*; J Agr Food Chem **53**, 1309 (2005).
- [53] T.G. Drummond, M.G. Hill, J.K. Barton; *Electrochemical DNA sensors*; Nat Biotech **21**, 1192 (2003).
- [54] M.J. Marsella, P.J. Carroll, T.M. Swager; *Design of chemoresistive sensory materials: polythiophene-based pseudopolyrotaxanes*; J Am Chem Soc **117**, 9832 (1995).
- [55] L. Torsi, M. Pezzuto, P. Siciliano, R. Rella, L. Sabbatini, L. Valli, P.G. Zambonin; *Conducting polymers doped with metallic inclusions: New materials for gas sensors*; Sensor Actuat B-Chem **48**, 362 (1998).
- [56] K. Ogura, T. Saino, M. Nakayama, H. Shiigi; *The humidity dependence of the electrical conductivity of a soluble polyaniline-poly(vinyl alcohol) composite film*; J Mater Chem **7**, 2363 (1997).
- [57] M.J. Marsella, T.M. Swager; *Designing conducting polymer-based sensors: selective ionochromic response in crown ether-containing polythiophenes*; J Am Chem Soc **115**, 12214 (1993).
- [58] P. Bäuerle, S. Scheib; *Molecular recognition of alkali-ions by crown-ether-functionalized poly(alkylthiophenes)*; Adv Mater **5**, 848 (1993).
- [59] B. Jousseme, P. Blanchard, E. Levillain, J. Delaunay, M. Allain, P. Richomme, D. Rondeau, N. Gallego-Planas, J. Roncali; *Crown-annulated oligothiophenes as model compounds for molecular actuation*; J Am Chem Soc **125**, 1363 (2003).
- [60] J. Casanovas, J. Preat, D. Zanuy, C. Alemán; *Sensing abilities of crown ether functionalized polythiophenes*; Chem-Eur J **15**, 4676 (2009).
- [61] B.S. Gaylord, A.J. Heeger, G.C. Bazan; *DNA detection using water-soluble conjugated polymers and peptide nucleic acid probes*; P Natl Acad Sci **99**, 10954 (2002).
- [62] H.-A. Ho, M. Boissinot, M.G. Bergeron, G. Corbeil, K. Doré, D. Boudreau, M. Leclerc; *Colorimetric and fluorometric detection of nucleic acids using cationic polythiophene derivatives*; Angew Chem Int Edit **41**, 1548 (2002).
- [63] A. Azioune, M.M. Chehimi, B. Miksa, T. Basinska, S. Slomkowski; *Hydrophobic protein-porphyrrole interactions: the role of van der waals and lewis acid-base forces as determined by contact angle measurements*; Langmuir **18**, 1150 (2002).
- [64] G.G. Wallace, L.A.P. Kane-Maguire; *Manipulating and monitoring biomolecular interactions with conducting electroactive polymers*; Adv Mater **14**, 953 (2002).
- [65] B. Teixeira-Dias, D. Zanuy, J. Poater, M. Sola, F. Estrany, L.J. del Valle, C. Aleman; *Binding of 6-mer single-stranded homo-nucleotides to poly(3,4-ethylenedioxythiophene): specific hydrogen bonds with guanine*; Soft Matter **7**, 9922 (2011).
- [66] B. Teixeira-Dias, L.J. del Valle, F. Estrany, E. Armelin, R. Oliver, C. Alemán; *Specific interactions in complexes formed by polythiophene derivatives bearing polar side groups and plasmid DNA*; Eur Polym J **44**, 3700 (2008).
- [67] M. De Vivo; *Bridging quantum mechanics and structure-based drug design*; Front Biosci **16**, 1619 (2011).
- [68] L.C. Menikarachchi, J.A. Gascon; *QM/MM Approaches in medicinal chemistry research*; Curr Top Med Chem **10**, 46 (2010).
- [69] J.P. Cerón-Carrasco, D. Jacquemin, J. Graton, S. Thany, J.Y. Le Questel; *New insights on the molecular recognition of imidacloprid with aphysia californica achbp: a computational study*; J Phys Chem B **117**, 3944 (2013).
- [70] J.-G. Lee, C. Sagui, C. Roland; *Quantum simulations of the structure and binding of glycopeptide antibiotic aglycons to cell wall analogues*; J Phys Chem B **109**, 20588 (2005).
- [71] D. Zanuy, J. Preat, E.A. Perpète, C. Alemán; *Response of crown ether functionalized polythiophenes to alkaline ions*; J Phys Chem B **116**, 4575 (2012).
-

- [72] G. Fabregat, E. Cordova-Mateo, E. Armelin, O. Bertran, C. Aleman; *Ultrathin films of polypyrrole derivatives for dopamine detection*; J Phys Chem C **115**, 14933 (2011).
- [73] C. Alemán, B. Teixeira-Dias, D. Zanuy, F. Estrany, E. Armelin, L.J. del Valle; *A comprehensive study of the interactions between DNA and poly(3,4-ethylenedioxythiophene)*; Polymer **50**, 1965 (2009).
- [74] D. Zanuy, C. Alemán; *DNA-conducting polymer complexes: a computational study of the hydrogen bond between building blocks*; The Journal of Physical Chemistry B **112**, 3222 (2008).
- [75] D. Aradilla, F. Estrany, C. Aleman; *Polypyrrole derivatives as solvent vapor sensors*; Rsc Adv **3**, 20545 (2013).
- [76] G. Chari, A. Gulati, R. Bhat, I.R. Tebbett; *High-performance liquid chromatographic determination of morphine, morphine-3-glucuronide, morphine-6-glucuronide and codeine in biological samples using multi-wavelength forward optical detection*; J Chromatogr B **571**, 263 (1991).
- [77] J.E. Wallace, S.C. Harris, M.W. Peek; *Determination of morphine by liquid chromatography with electrochemical detection*; Anal Chem **52**, 1328 (1980).
- [78] W.J. Liaw, S.T. Ho, J.J. Wang, O.Y.P. Hu, J.H. Li; *Determination of morphine by high-performance liquid chromatography with electrochemical detection: application to human and rabbit pharmacokinetic studies*; J Chromatogr B **714**, 237 (1998).
- [79] K.C. Ho, W.M. Yeh, T.S. Tung, J.Y. Liao; *Amperometric detection of morphine based on poly(3,4-ethylenedioxythiophene) immobilized molecularly imprinted polymer particles prepared by precipitation polymerization*; Anal Chim Acta **542**, 90 (2005).
- [80] C.H. Weng, W.M. Yeh, K.C. Ho, G.B. Lee; *A microfluidic system utilizing molecularly imprinted polymer films for amperometric detection of morphine*; Sensor Actuat B-Chem **121**, 576 (2007).
- [81] L. Groenendaal, F. Jonas, D. Freitag, H. Pielartzik, J.R. Reynolds; *Poly(3,4-ethylenedioxythiophene) and its derivatives: past, present, and future*; Adv Mater **12**, 481 (2000).
- [82] Q. Pei, G. Zuccarello, M. Ahlskog, O. Inganäs; *Electrochromic and highly stable poly(3,4-ethylenedioxythiophene) switches between opaque blue-black and transparent sky blue*; Polymer **35**, 1347 (1994).
- [83] D.-H. Han, J.W. Kim, S.M. Park; *Electrochemistry of conductive polymers 38. electrodeposited poly(3,4-ethylenedioxy-thiophene) studied by current sensing atomic force microscopy*; J Phys Chem B **110**, 14874 (2006).
- [84] K.E. Aasmundtveit, E.J. Samuelsen, O. Inganäs, L.A.A. Pettersson, T. Johansson, S. Ferrer; *Structural aspects of electrochemical doping and dedoping of poly(3,4-ethylenedioxythiophene)*; Synthetic Met **113**, 93 (2000).
- [85] L.J. del Valle, F. Estrany, E. Armelin, R. Oliver, C. Alemán; *Cellular adhesion, proliferation and viability on conducting polymer substrates*; Macromol Biosci **8**, 1144 (2008).
- [86] N.F. Atta, A. Galal, R.A. Ahmed; *Direct and simple electrochemical determination of morphine at PEDOT modified Pt electrode*; Electroanal **23**, 737 (2011).
- [87] D. Zanuy, B. Teixeira-Dias, L.J. del Valle, J. Poater, M. Sola, C. Aleman; *Examining the formation of specific interactions between poly(3,4-ethylenedioxythiophene) and nucleotide bases*; Rsc Adv **3**, 2639 (2013).
- [88] B. Teixeira-Dias, C. Alemán, F. Estrany, D.S. Azambuja, E. Armelin; *Microstructures of poly(N-methylpyrrole) and their interaction with morphine*; Electrochim Acta **56**, 5836 (2011).
- [89] L. Gylbert; *The crystal and molecular structure of morphine hydrochloride trihydrate*; Acta Crystallogr B **29**, 1630 (1973).
- [90] G.A. Pettersson, M.A. Al-Laham; *A complete basis set model chemistry. II. Open-shell systems and the total energies of the first-row atoms*; J Chem Phys **94**, 6081 (1991).

- [91] C. Møller, M.S. Plesset; *Note on an approximation treatment for many-electron systems*; Phys Rev **46**, 618 (1934).
- [92] K. Morokuma; *Why do molecules interact? The origin of electron donor-acceptor complexes, hydrogen bonding and proton affinity*; Accounts Chem Res **10**, 294 (1977).
- [93] K. Kitaura, K. Morokuma; *A new energy decomposition scheme for molecular interactions within the Hartree-Fock approximation*; Int J Quantum Chem **10**, 325 (1976).
- [94] T. Ziegler, A. Rauk; *On the calculation of bonding energies by the Hartree Fock Slater method*; Theor Chim Acta **46**, 1 (1977).
- [95] T. Ziegler, A. Rauk; *Carbon monoxide, carbon monosulfide, molecular nitrogen, phosphorus trifluoride, and methyl isocyanide as σ -donors and π -acceptors. A theoretical study by the Hartree-Fock-Slater transition-state method*; Inorg Chem **18**, 1755 (1979).
- [96] G. te Velde, F.M. Bickelhaupt, E.J. Baerends, C. Fonseca Guerra, S.J.A. van Gisbergen, J.G. Snijders, T. Ziegler; *Chemistry with ADF*; J Comput Chem **22**, 931 (2001).
- [97] C.F. Guerra, J.G. Snijders, G. te Velde, E.J. Baerends; *Towards an order-N DFT method*; Theor Chem Acc **99**, 391 (1998).
- [98] J.G. Snijders, P. Vernooijs, E.J. Baerends; *Rootbaan-Hartree-Fock-Slater atomic wave functions: Single- ζ , double- ζ , and extended Slater-type basis sets for 87Fr-103Lr*; Atom Data Nucl Data **26**, 483 (1981).
- [99] J.P. Perdew, K. Burke, Y. Wang; *Generalized gradient approximation for the exchange-correlation hole of a many-electron system*; Phys Rev B **54**, 16533 (1996).
- [100] J.P. Perdew, K. Burke, M. Ernzerhof; *Generalized gradient approximation made simple*; Phys Rev Lett **77**, 3865 (1996).
- [101] A.D. Becke; *Density-functional exchange-energy approximation with correct asymptotic behavior*; Phys RevA **38**, 3098 (1988).
- [102] J.P. Perdew; *Density-functional approximation for the correlation energy of the inhomogeneous electron gas*; Phys Rev B **33**, 8822 (1986).
- [103] S. Grimme; *Accurate description of van der Waals complexes by density functional theory including empirical corrections*; J Comput Chem **25**, 1463 (2004).
- [104] S. Grimme; *Semiempirical GGA-type density functional constructed with a long-range dispersion correction*; J Comput Chem **27**, 1787 (2006).
- [105] S. Grimme, J. Antony, S. Ehrlich, H. Krieg; *A consistent and accurate ab initio parametrization of density functional dispersion correction (DFT-D) for the 94 elements H-Pu*; J Chem Phys **132** (2010).
- [106] F.L. Hirshfeld; *Bonded-atom fragments for describing molecular charge densities*; Theor Chim Acta **44**, 129 (1977).
- [107] D. Aradilla, D. Azambuja, F. Estrany, M.T. Casas, C.A. Ferreira, C. Aleman; *Hybrid polythiophene-clay exfoliated nanocomposites for ultracapacitor devices*; J Mater Chem **22**, 13110 (2012).
- [108] D. Aradilla, F. Estrany, D.S. Azambuja, M.T. Casas, J. Puiggali, C.A. Ferreira, C. Alemán; *Conducting poly(3,4-ethylenedioxythiophene)-montmorillonite exfoliated nanocomposites*; Eur Polym J **46**, 977 (2010).

CHAPTER 5
HYDRONIUM TRANSPORT IN CATION EXCHANGE MEMBRANES

'Ideas are like rabbits. You get a couple and learn how to handle them, and pretty soon you have a dozen.'

John Steinbeck, *John Steinbeck : A Biography* (1994)

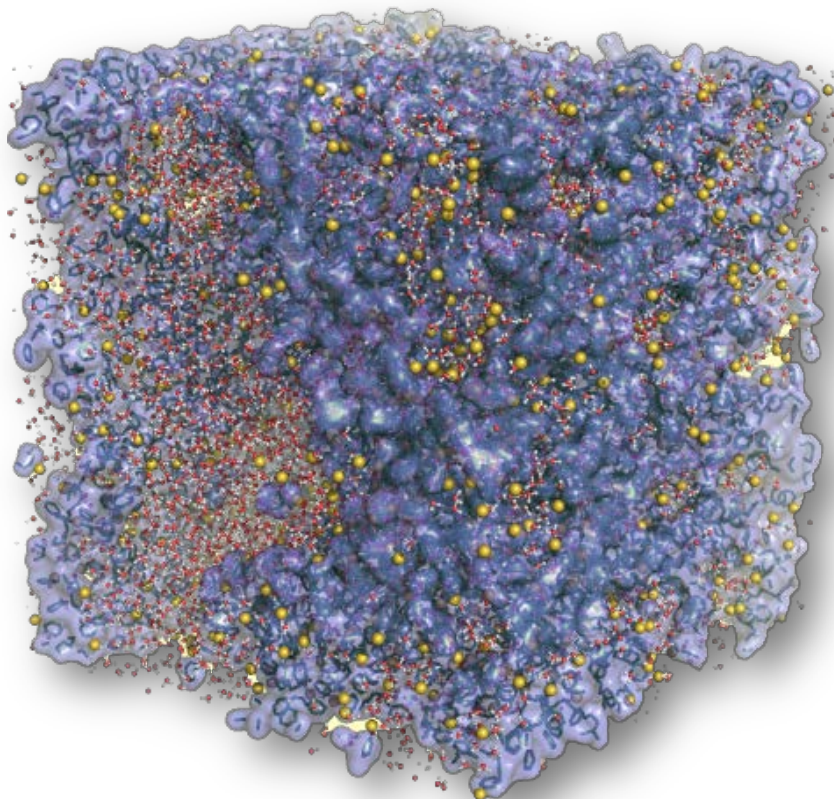
CHAPTER 5

HYDRONIUM TRANSPORT IN CATION EXCHANGE MEMBRANES

This Chapter is devoted to examine the properties of a sulfonated poly(styrene-co-divinyl benzene) membrane, P(S-DVB), through atomistic Molecular Dynamics simulations. Section 5.1 is focused on the transport of hydronium ions inside the cation exchange membrane as a function of the electric field strength. The content of this section has been published in *Journal of Membrane Science* under the title *Transport of hydronium ions inside poly(styrene-co-divinyl benzene) cation exchange membranes* (2013). In section 5.2 the influence of temperature in the acidic membrane in absence and presence of electric field has been studied. For this purpose, the structural properties of the membrane as well as the transport phenomena of both water and hydronium molecules have been analyzed. This work has been published in *The Journal of Physical Chemistry C* under the title *Influence of the temperature on the proton transport in poly(styrene-co-divinylbenzene) membranes from molecular dynamics simulations* (2014).

5.1. ELECTRIC FIELD-INDUCED TRANSPORT OF HYDRONIUM IONS IN P(S-DVB) CATION EXCHANGE MEMBRANES.

The electric field-induced transport of hydronium ions in sulfonated poly(styrene-co-divinyl benzene) membranes has been investigated using atomistic Molecular Dynamics simulations. The diffusive behavior has been found to increase with the electric field, even though the diffusion coefficient is higher in the direction of the applied electric field than in the perpendicular directions. This anisotropy, which has been also detected in the velocities of the hydronium ions, is particularly pronounced for electric fields higher than 1.0 V/nm. Indeed, at such high electric fields the simulated systems are not able to reach the normal diffusive regime. The highest protonic conductivity has been obtained at 0.03



V/nm. At higher electric fields, the protonic current density increases too slowly (*i.e.* for electric fields > 0.7 V/nm) or too rapidly (*i.e.* electric fields ≤ 0.7 V/nm) resulting in a reduction of the conductivity or in significant structural deformations of the membrane, respectively. Finally, the interactions between the hydronium ions and water molecules contained in the hydrated membranes have been analyzed and discussed considering the influence of the applied electric field. Specifically, results have allowed us to discuss the existence of different types of hydration shells, which differ in the number of water molecules contained in the shell and their exchangeability, and residence times.

5.1.1. INTRODUCTION

After the synthesis of ion exchange resins in the beginning of the twentieth century, the dispersion of finely powdered resins into a binding polymer gave rise to the development of ion exchange membranes (IEMs). Currently, these membranes play an important role and present potential applications in an increasing number of processes in chemical industry, being used as fuel cells [1], supercapacitors [2], batteries [3], sensors [4],

chloro-alkali cells [5,6], and electro dialyzers [7-13]. Taking into account such variety of applications, good performance IEMs should exhibit high ionic permselectivity, high ionic conductivity, low permeability to free diffusion of electrolytes as well as chemical stability and mechanical resistance [14-16]. Because of some of these properties are incompatible (*e.g.* high mechanical resistance and high conductivity), in practice good performance membranes exhibit a balance of incompatible properties.

According to their binding preferences IEMs are typically divided in cation and anion exchangers, which exchange positively and negatively charged ions, respectively, even though there are also amphoteric exchangers able to exchange both cations and anions simultaneously. The synthesis of cation exchange membranes, which combines low protonic resistance and good mechanical properties, is nowadays a flourishing field of research. In the last years polymers with high chemical stability and good mechanical skills such as polysulfone [17], polyether sulfone [18], polyphosphazene [19] and poly(styrene-co-divinyl benzene) [7,20-23], hereafter denoted P(S-DVB), have been used to develop acidic membranes. In particular, P(S-DVB)-based membranes have been stated to be among the best for use in electro dialysis because the cross-linked polystyrene has more phenyl rings that act as reactive sites for functionalization with sulfonic acid groups [7]. Thus, the production of commercial sulfonated P(S-DVB) membranes is based on the copolymerization of styrene and divinylbenzene (DVB) in aqueous solution, followed by a sulfonation with concentrated sulfuric acid in dichloroethane.

In recent years some theoretical studies based on Molecular Dynamics (MD) have been used to investigate transport and equilibrium phenomena in IEMs [24-31]. Atomistic MD simulations were used by Goddard and co-workers [24] to investigate Nafions, a polyelectrolyte membrane consisting of non-polar tetrafluoroethylene segments and polar perfluorosulfonic vinyl ether segments. Specifically, these authors studied both the effect of the monomeric sequence in polymer chains on the nanophase-segregation and the transport in hydrated Nafions systems with 20 wt% of water content at room and high temperature (300 and 353 K, respectively). After this seminal study, the electric field-induced transport in Nafions membranes has been simulated by other authors [25-28]. A remarkable contribution within this field was recently reported by Allahyarov and Taylor, who used MD simulations combined with hard coarse-grained models to investigate the effect of stretching-induced structure orientation on the proton conductivity of Nafions-like polymer electrolyte membranes [29]. Pozuelo et al. used atomistic MD simulations to examine the proton conductivity across sulfonated poly(phenyl sulfone)s membranes at temperatures lying in the range 300–360 K [30]. The experimental behavior of the membranes was qualitatively reproduced by these simulations, even though the reduced size of the simulated system (*i.e.* five chains with ten repeating units each one) limited the quantitative agreement.

In a very recent study, we simulated the electric field-induced transport of hydronium ions in P(S-DVB) membranes using atomistic MD simulations [31]. Specifically, we considered a relatively large model (*i.e.* 2165 styrene units, 270 DVB units and 1294 sulfonic acid groups within the simulation box) with a water uptake of 18 wt% (*i.e.* 4756 water molecules), external electric fields ranging from 0.001 to 3.00 V nm⁻¹ being applied to examine structural changes. Results showed that the electric field produced a redistribution of the unoccupied volume modifying the heterogeneity of the resin and a rearrangement of the negatively charged sulfonate groups, which underwent a systematic alignment along the electric field direction [31]. Analyses of the velocities evidenced that, as expected, the mobility of hydronium ions increases with the strength of the electric field [31].

In this work we re-investigate the electric field-induced transport of hydronium ions in P(S-DVB) membranes, extending and complementing our previous work [31]. More specifically, the diffusion, velocity and conductivity of hydronium ions, as well as their variation as a function of the applied electric field, have been quantitatively examined. Furthermore, dynamical aspects of the interaction between the hydronium ions and the sulfonic acid groups have been analyzed and used to discuss the transport mechanism.

5.1.2. METHODS AND BACKGROUND

5.1.2.1. MOLECULAR SYSTEM AND COMPUTATIONAL DETAILS

The chemical system used to represent the transport of hydronium ions inside of sulfonated P(S-DVB) soft membranes involved 2165 styrene units, 270 DVB units, 1294 sulfonic acid groups, 1294 hydronium ions and 4756 water molecules, all them within a cubic simulation box with dimensions $a = 97.83 \text{ \AA}$. Accordingly, the composition, in wt%, of the simulated membrane was: 48.5% of styrene units, 5.9% of DVB units, 22.3% of sulfonic acid groups, 5.2% of hydronium ions and 18.1% of water molecules.

The construction, hydration and equilibration of the membranes were extensively described in our previous study [31]. The main steps can be summarized as follows: (i) the molecular architecture of the P(S-DVB) membrane, including the cross-links, were generated using a stochastic algorithm; and (ii) the sulfonic acid groups were introduced at randomly selected phenyl groups. Once a phenyl group was selected, one of its available free positions (*i.e.* those that are not involved in cross-links) was chosen to add the sulfonic acid group without steric overlaps. After relax the generated structures by energy minimization, water molecules and hydronium ions were randomly introduced in positions previously identified as unoccupied (*i.e.* positions with empty space accessible to such two molecules). Next, the hydrated membrane was relaxed, thermalized and equilibrated using energy minimization and short runs of both NVT- and NPT-MD simulations. The resulting microstructure, which is schematically depicted in Figure 5.1,

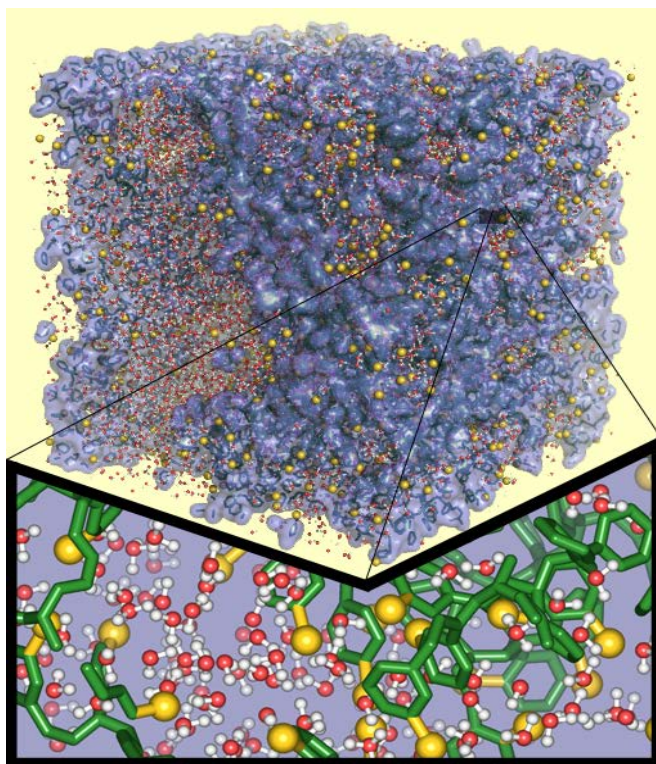


Figure 5.1. Schematic view of the simulation system: the polymer and the sulfonate groups are represented by the solid purple matrix and the yellow spheres, respectively. Water molecules and hydronium ions are explicitly represented. A magnification of a small zone, in which the polymer is described by sticks, is provided at the bottom.

was used as starting point for the independent production MD simulations, which were carry out considering the following electric fields: 0.001, 0.01, 0.03, 0.1, 0.3, 0.7, 1.0, 2.0 and 3.0 V/nm. The electric field was fixed along the z -axis of the simulation box, the force on each atom, i , of the system (\mathbf{F}'_i) being defined by the following expression:

$$\mathbf{F}'_i = \mathbf{F}_i + q_i \mathbf{E}_z \quad (5.1)$$

where \mathbf{F}_i is the force defined by the potential force-field, q_i is the charge of the atom i and \mathbf{E}_z is the electric field. It should be remarked that MD simulations in the presence of an external electric field require huge amounts of computer resources, which prevent us from long trajectories. In order to overcome this limitation and have a quick membrane response, some simulations were carried using very strong electric fields. Although we are aware that very strong electric fields may induce unrealistic structural deformations, simulations with electric fields higher than 0.7 V/nm have allowed us to examine the diffusion of hydronium ions using relatively short trajectories.

The energy of the simulated system was described using the potential energy functions of the AMBER force-field [32]. Force-field parameters for P(S-DVB) were extracted from the General AMBER force-field [33] (GAFF) and the TraPPE united atom force-field of polystyrene [34], whereas those of the sulfonate groups were taken from GAFF.

Water and hydronium ions were described using the TIP3P [35] and Baadem *et al.* [36] models, respectively. The molecular geometry of the water (bond lengths and bond angle) and hydronium (bond lengths, bond angles, and improper torsion) molecules were kept fixed during the whole MD simulations.

MD simulations were carried out using the DLPOLY program [37]. Lennard-Jones and electrostatic interactions were calculated using an atom pair distance cutoff of 14.0 Å. Ewald summations were applied to evaluate electrostatic interactions [38]. The numerical integration step was set to 2 fs using the Verlet algorithm. Both temperature and pressure were controlled by the weak coupling method, the Nosé-Hoover thermo-barostat [39], using a time constant for the heat bath coupling and a pressure relaxation time of 0.15 and 2.85 ps, respectively. Coordinates were stored every 10 ps in the history file while velocities were saved every 40 ps.

5.1.2.2. DIFFUSION COEFFICIENTS

The diffusion coefficient of the hydronium ions (D) was calculated using the so-called Einstein relation:

$$2dD = \lim_{t \rightarrow \infty} \frac{1}{N_h t} \left\langle \sum_{i=1}^{N_h} [\mathbf{r}_i(t) - \mathbf{r}_i(0)]^2 \right\rangle \quad (5.2)$$

where d is the number of dimensions of the trajectory data, the sum at the right hand term is the mean square displacement (MSD), N_h is the number of hydronium ions in the simulation ($N_h = 1294$), t is the time and $\mathbf{r}_i(t)$ is the position vector of hydronium i at the time event t . In evaluating the Einstein equation from MD simulations, a line is fitted to the linear portion of the MSD curve and D is obtained from the limiting slope. This procedure, which is also valid in the presence of external electric fields [26,40], rests on the fact that for sufficiently long times, the MSDs of the diffusing particles increases linearly with time. The criterion used in this work to corroborate that the simulated systems reached this normal diffusive regime was based on the representation of the function $\log(\text{MSD}) = f[\log(t)]$:

$$\text{MSD} \propto t^m \quad (5.3)$$

which shows a slope of $m = 1$ for normal diffusion processes (*i.e.* $m < 1$ and $m > 1$ correspond to accelerated and anomalous diffusive regimes)[41].

Anisotropic diffusion of the hydronium ion was determined by monitoring independently the values of D in directions parallel (\hat{z}) and perpendicular (x and y) to the applied electric field, hereafter denoted D_{\parallel} and D_{\perp} , respectively. These coefficients were computed using the following equations:

$$D_{\parallel} = \lim_{t \rightarrow \infty} \frac{1}{2N_h t} \left\langle \sum_{i=1}^{N_h} [z_i(t) - z_i(0)]^2 \right\rangle \quad (5.4)$$

$$D_{\perp} = \lim_{t \rightarrow \infty} \frac{1}{4N_h t} \left\langle \sum_{i=1}^{N_h} [x_i(t) - x_i(0)]^2 + [y_i(t) - y_i(0)]^2 \right\rangle \quad (5.5)$$

5.1.2.3. VELOCITY DISTRIBUTION FUNCTIONS AND TEMPERATURE

The velocities (\mathbf{v}) recorded during the production MD runs were used to evaluate the velocity distribution functions of the hydronium ions, which were subsequently fitted to the Maxwell velocity distribution function, $f(\mathbf{v})$:

$$f(\mathbf{v}) = 4\pi v^2 \left(\frac{m}{2\pi k_B T_h} \right)^{3/2} \exp\left(-\frac{mv^2}{2k_B T_h} \right) \quad (5.6)$$

where m is the mass, k_B is the Boltzmann constant and T_h is the overall temperature of the hydronium ions. These non-linear fits were used to obtain information about the influence of the electric field in the temperature. Similarly, velocities in the direction parallel and perpendicular to the applied electric field (v_{\parallel} and v_{\perp} , respectively) were fitted to Maxwell distribution functions in such directions:

$$f(v_{\perp}) = \sqrt{\frac{m}{2\pi k_B T_{\perp}}} \exp\left(-\frac{mv_{\perp}^2}{2k_B T_{\perp}} \right) \quad (5.7)$$

$$f(v_{\parallel}) = \sqrt{\frac{m}{2\pi k_B T_{\parallel}}} \exp\left(-\frac{m(v_{\parallel} - v_0)^2}{2k_B T_{\parallel}} \right) \quad (5.8)$$

Non-linear fits to $f(v_{\parallel})$ and $f(v_{\perp})$ allowed us to estimate the temperature of the hydronium ions in the directions parallel and perpendicular to the electric field (T_{\parallel} and T_{\perp} , respectively). Furthermore, the fit to equation (5.8) also provided the peak shifting velocity for hydronium ions (v_0) induced by the electric field.

5.1.2.4. CONDUCTIVITY

The proton conductivity (χ) in a hydrated P(S-DVB) membrane has been calculated by the expression:

$$\mathbf{J} = \chi \mathbf{E} \quad (5.9)$$

which relates the electrical current density (\mathbf{J}) to the applied electric field (\mathbf{E}). In our MD simulations, \mathbf{J} has been evaluated as:

$$J = \frac{1}{V} \bar{v}_{\parallel} \sum_{i=1}^{N_h} q_i \quad (5.10)$$

where \bar{v}_{\parallel} is the average transport velocity of the hydronium ions in the direction parallel to the applied electric field, N_h is the number of hydronium ions in the simulated system, V is the system volume, and q is the charge of the proton. The conductivity of the membrane χ is then found by combining (5.9) and (5.10).

Two different methods have been used to evaluate \bar{v}_{\parallel} . The first one involves the sum of the velocities in the direction parallel to the applied electric field, $v_{\parallel}(i, \delta)$, for every time step δ and over all hydronium ions:

$$\bar{v}_{\parallel} = \frac{1}{\tau} \sum_{\delta=1}^{\tau} \frac{1}{N_h} \sum_{i=1}^{N_h} v_{\parallel}(i, \delta) \quad (5.11)$$

where τ is the total number of time steps. However, this method converges very slowly, being only effective for high electric fields. The second method is based on the integration of the velocity distribution function:

$$\bar{v}_{\parallel} = \int_{-\infty}^{\infty} v_{\parallel} f(v_{\parallel}) dv_{\parallel} \quad (5.12)$$

where $f(v_{\parallel})$ is derived from the data recorded during the production trajectories through equation (5.8). This method provides a satisfactory convergence in all cases, including those with very low electric fields.

5.1.3. RESULTS AND DISCUSSION

5.1.3.1. DIFFUSION OF HYDRONIUM CATIONS

The average MSD profile obtained for selected electric fields (*i.e.* 0.001, 0.01, 0.1, 0.7, 1.0, 2.0 and 3.0 V/nm) are plotted in Figure 5.2. The profiles obtained for 0.03 and 0.3 V/nm (not shown) practically overlap those displayed for 0.01 and 0.7 V/nm, respectively. The MSD increases significantly with the electric field, especially after a threshold value of 0.1 V/nm. However, the slope of the profiles becomes practically zero when the electric field is higher than 1.0 V/nm. This feature is fully consistent with the results reported in our previous structural study [31], in which we showed that electric fields higher than 1.0 V/nm produce important deformations in the membrane. Specifically, the sulfonate groups undergo drastic rearrangements because of the alignment of C–S bond along the direction of the electric field, resulting in a swelling of the membrane (*i.e.* the density decreases). Indeed, this behavior starts at 1.0 V/nm, as is evidenced by the decrease of the slope in the profile displayed in Figure 5.2 with respect to 0.7 V/nm. Accordingly, the normal diffusive regime is not reached for electric fields of

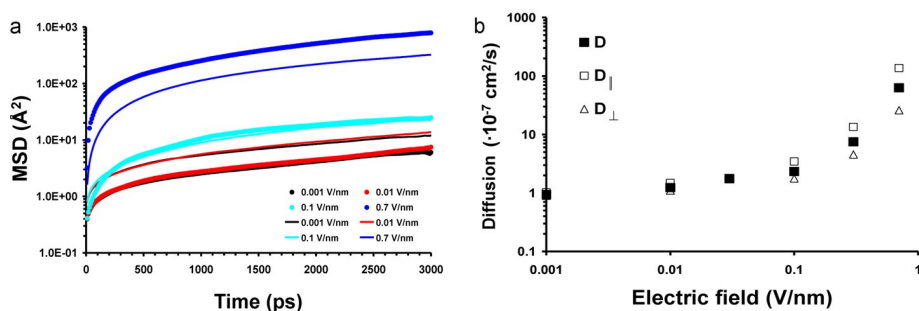


Figure 5.2. (a) Mean squared displacement (MSD) of hydronium ions from its origin in the P(S-DVB) membrane as a function of the simulation time for selected electric fields. (b) Variation of D , $D_{||}$ and D_{\perp} , against the electric field.

≥ 1.0 V/nm and, therefore, diffusion coefficients cannot be obtained using (5.2), (5.4) and (5.5). The structural deformations discussed above for electric fields ≥ 1.0 V/nm are reflected in Figure 5.3, which compares different snapshots of simulations with 0.1 and 1.0 V/nm.

The diffusion coefficient D from (5.2), for electric fields ranging from 0.001 to 0.7 V/nm was determined once the diffusive regime was reached. For this purpose, only the intervals with a slope of 1.00 ± 0.15 in the $\log(\text{MSD})$ vs. $f[\log(t)]$ profiles (5.3), were considered in the fitting process. The D values, which are listed in Table 5.1, increase from $0.9 \cdot 10^{-7}$ cm²/s for 0.001 V/nm to $62.8 \cdot 10^{-7}$ cm²/s for 0.7 V/nm. This represents an increment of two orders of magnitude evidencing the crucial role of the external electric field in the transport process of hydronium ions. These diffusion coefficients are similar to those reported for hydronium ions in sulfonated poly(phenyl sulfone)s [30], Nafions [42], and sulfonated poly(ethersulfone)s[42]. Analysis of $D_{||}$ and D_{\perp} , (equations (5.4) and (5.5), respectively) reflects influence of the electric field in the anisotropy of the diffusive behavior. Thus, the mobility of the hydronium ions is higher in the direction of the

Table 5.1. Diffusion Coefficients of Hydronium Ions in P(S-DVB) Membrane Applying Selected External Electric Fields.

Electric field (V/nm)	D (10^{-7} cm ² /s)	$D_{ }$ (10^{-7} cm ² /s)	D_{\perp} (10^{-7} cm ² /s)
0.001	0.94 ± 0.01	1.02 ± 0.02	0.89 ± 0.01
0.01	1.23 ± 0.01	1.48 ± 0.01	1.10 ± 0.01
0.03	1.75 ± 0.08	1.77 ± 0.13	1.74 ± 0.07
0.1	2.32 ± 0.01	3.44 ± 0.02	1.77 ± 0.01
0.3	7.52 ± 0.04	13.47 ± 0.08	4.55 ± 0.02
0.7	62.83 ± 0.09	136.49 ± 0.03	25.95 ± 0.03

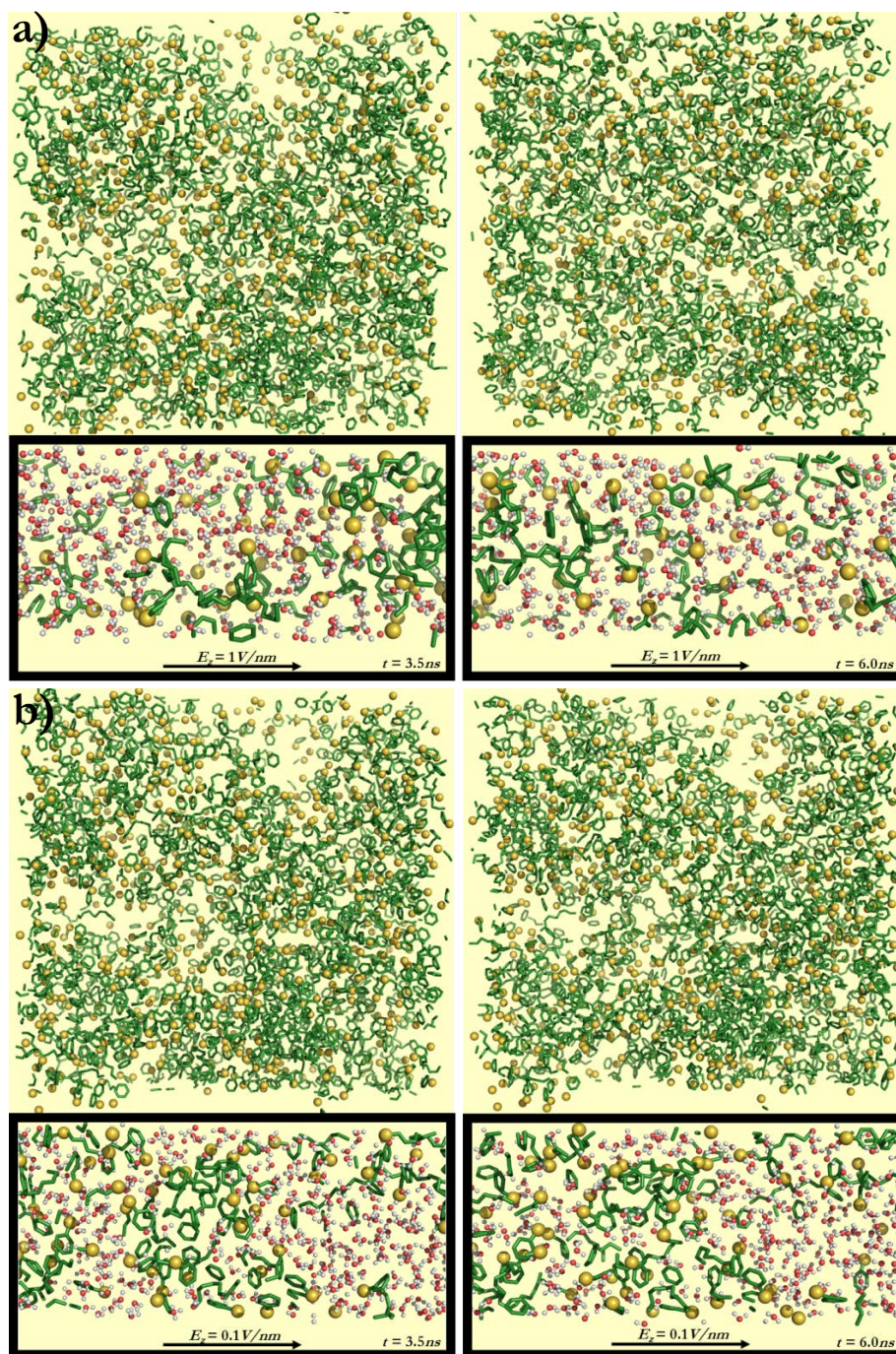


Figure 5.3. Snapshots (3.5 and 6.0 ns on the left and right, respectively) of the membrane from MD simulations using external electric fields of (a) 0.1 V/nm and (b) 1.0 V/nm. General view (top) and amplification of a selected zone (bottom) are displayed in each case.

applied electric field than in the perpendicular directions, this effect being particularly relevant for electric fields higher than 0.03 V/nm. In absolute terms, for electric fields ≤ 0.03 V/nm D_{\perp} values are larger than D_{\parallel} by factors ≤ 1.3 , the latter growing to 2, 3 and 5 for 0.1, 0.3 and 0.7 V/nm, respectively. This remarkable increment should be attributed not only to the influence of the electric field on the hydronium ions but also on the structure of the membrane. Thus, new channels oriented in the z -direction are opened as a consequence of the rearrangement of the sulfonate groups [31]. Figure 5.2b represents the variation of the three diffusion coefficients against the electric field. In all cases a clear exponential behavior is obtained, even though this is more marked for D and D_{\parallel} .

5.1.3.2. VELOCITY OF HYDRONIUM CATIONS

The distribution functions $f(\mathbf{v})$, $f(v_{\parallel})$ and $f(v_{\perp})$ of hydronium ions with different electric fields were obtained using the data recorded from MD production trajectories. Figure 5.4 displays the results obtained for selected electric fields (*i.e.* 0.01, 0.3, 1.0 and 3.0 V/nm), the behavior of the rest of the electric field being intermediate among these ones. The distribution functions $f(\mathbf{v})$ and $f(v_{\parallel})$ show a very good agreement with the Maxwell distribution functions expressed in (5.6) and (5.8), respectively, in all cases with the only exception of the data recorded for 3.0 V/nm, which showed significant deviations at the tails of the profiles. This was attributed to the drastic structural changes

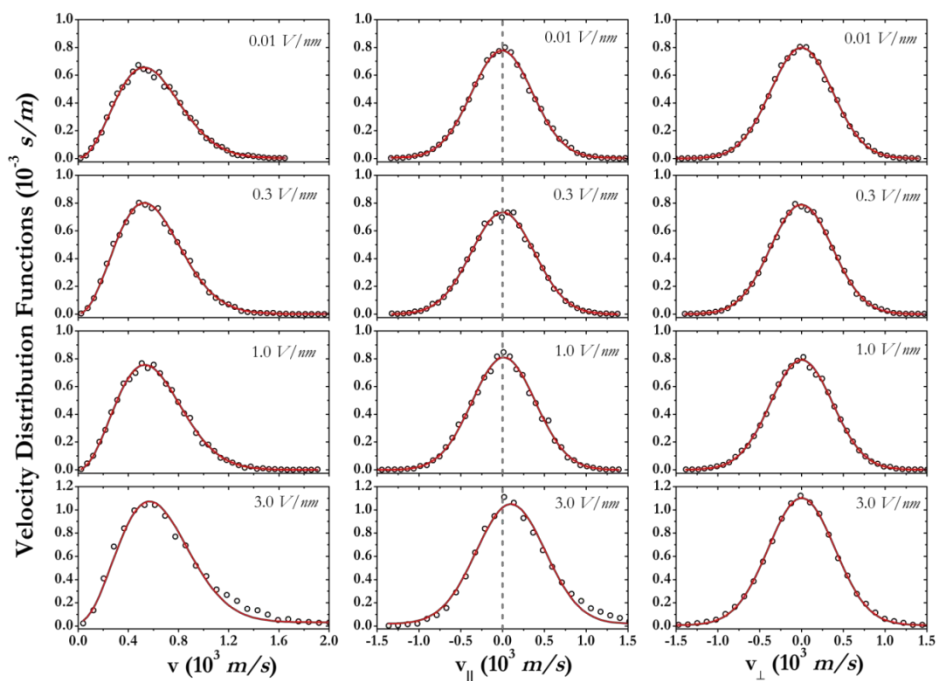


Figure 5.4. Velocity distribution functions $f(\mathbf{v})$, $f(v_{\parallel})$ and $f(v_{\perp})$ of hydronium ions derived from MD simulations for selected electric fields (circles). The red line represents the fitting of velocity distribution functions to the corresponding Maxwell distribution functions: (5.6) - (5.8).

Table 5.2. Temperature Parameters, Peak Shifting Velocity and Average Transport Velocity in the Direction Parallel to the Applied Electric field of Hydronium Ions in P(S-DVB) Membrane Applying Selected External Electric Fields.

E_z (V/nm)	T_h (K)	T_{\parallel} (K)	T_{\perp} (K)	v_0 (m/s)	\bar{v}_{\parallel} (m/s)
0.001	316 ± 3	305 ± 6	315 ± 5	-1.03	-0.04
0.01	318 ± 2	324 ± 5	315 ± 5	-1.12	-0.07
0.03	320 ± 3	319 ± 4	317 ± 6	1.28	1.03
0.1	319 ± 2	319 ± 5	317 ± 6	2.13	1.28
0.3	318 ± 2	327 ± 7	315 ± 4	2.55	1.76
0.7	317 ± 3	324 ± 5	327 ± 6	3.12	2.44
1.0	322 ± 2	329 ± 9	317 ± 5	13.66	10.47
2.0	336 ± 3	346 ± 6	331 ± 4	52.56	45.27
3.0	370 ± 8	390 ± 17	359 ± 4	98.95	105.47

introduced in the P(S-DVB) membrane by such high electric field (see discussion in previous subsection), which perturbs the transport characteristics of the hydronium ions. The adjustment of $f(v_{\perp})$ to (5.7) was excellent in all cases, including that with the highest electric field.

The fit of the velocity distribution functions for hydronium ions to the Maxwell distribution function allowed us to evaluate the temperature parameters, shown in Table 5.2 as T_h , T_{\parallel} and T_{\perp} . The fact that $T_{\parallel} \neq T_{\perp}$ is due to the anisotropic rearrangement of the kinetic energy between the direction of the electric field and the directions perpendicular to the electric field. In MD simulations the temperature can be maintained by removing heat from the system numerically via a procedure called the thermostat [39,43,44]. If the electric heat is too high, as occurs in the case of electric fields higher than 1.0 V/nm, the temperature cannot be controlled even in MD simulations. For example, in this work the system reached 370 K at 3.0 V/nm with the applied Nosé-Hoover thermo-barostat [39].

The temperature of the hydronium ions increases from 300 K in the absence of electric field (not shown) to 316 K when the electric field is 0.001 V/nm (Table 5.2). This increment in the temperature is due to the electric work injected into the system at each simulation step, which cannot be removed quickly enough by the thermostat. The temperature increases slowly with the strength of the electric field until 1.0 V/nm, being always below 325 K. However, the temperature of the hydronium ions is close to the boiling point of water for 3.0 V/nm. The change in the behavior at the threshold value of 1.0 V/nm is clearly reflected in Figure 5.5, which represents the variation of T_h , T_{\parallel} and T_{\perp} against the applied electric field.

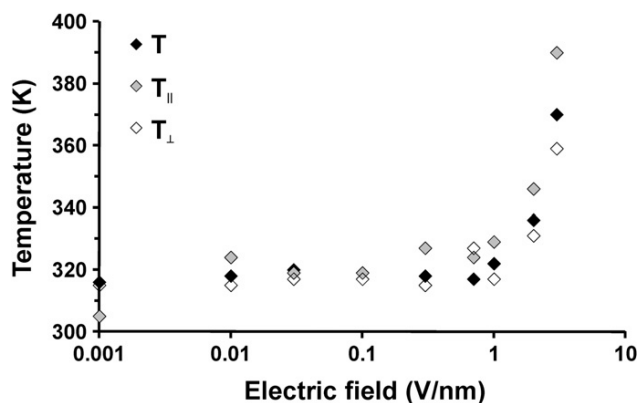


Figure 5.5. Variation of the temperature parameters of the hydronium ions (*i.e.* overall temperature, and temperature in the directions parallel and perpendicular to the electric field) against the electric field.

Another interesting phenomenon is the difference between $T_{||}$ and T_{\perp} , which is relatively unimportant (< 10 K) for electric fields lower than 1.0 V/nm. Thus, the kinetic energy rearrangement between the parallel and perpendicular directions is relatively efficient below this threshold value and the motion of hydronium ions is not significant by the electric field. Indeed, for some of the electric fields (*i.e.* 0.3 and 0.7 V/nm) the kinetic energy is isotropically distributed between the two components of the temperature: $T_{||} \approx T_{\perp} \approx T_h$. However, a relatively pronounced anisotropic behavior, $T_{\perp} < T_h < T_{||}$, is obtained for 2.0 and 3.0 V/nm, in which we observe that the difference between the two directions increases to 15 and 31 K, respectively.

Table 5.2 lists the peak shifting velocity, v_0 , for hydronium ions induced by the different applied electric fields. At 0.001 and 0.01 V/nm, the peak shifting velocity is -1.0 and -1.1 m/s, respectively, slowly increasing to values comprised between 1.3 and 3.1 m/s for electric fields ranging from 0.03 to 0.7 V/nm. The peak shifting velocities sharply increase to 13.7, 52.6 and 98.9 m/s at 1.0, 2.0 and 3.0 V/nm, respectively. This drastic and systematic increment represents another indirect evidence of the structural distortion induced by the electric field in the parallel direction. Specifically, the electric pulling force on the hydronium ions overcomes the intermolecular attraction, which is weakened because of alignment of the C–S bonds, facilitating the movement of the hydronium ions through the channels.

5.1.3.3. AVERAGE TRANSPORT VELOCITIES AND CONDUCTIVITY

The average transport velocities of the hydronium ions in the direction parallel to the applied electric field, $\bar{v}_{||}$ (5.11), which reflect the flow of ions in such direction, are included in Table 5.2. As it can be seen, the hydronium ions move randomly when the electric field is ≤ 0.01 V/nm, the calculated $\bar{v}_{||}$ being practically zero. This indicates that at such low electric fields the thermal motion dominates over the electric field-induced

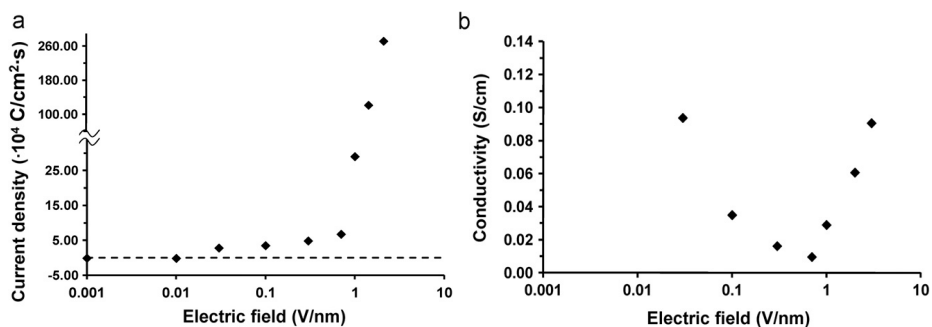


Figure 5.6. Variation of the protonic (a) current density and (b) conductivity against the applied electric field for the hydrated P(S-DVB) membrane. The dashed line in graphic (a) refers to a current density of $0.00 \text{ C/cm}^2 \cdot \text{s}$.

motion, and the ions follow a Brownian behavior. It is worth noting that although for the two lowest electric fields \bar{v}_{\parallel} and v_0 values are very small in comparison with the rest of cases, they are negative. These results may be attributed to the fact that for low electric fields electrostatic interactions between hydronium ions and sulfonated groups are higher than the strength of the electric field. Furthermore, applied electric field could produce a rearrangement of negatively charged sulfonated groups dragging the hydronium ions in the opposite direction to the electric field. At higher electric fields, \bar{v}_{\parallel} grows progressively with the electric field. This increase is slow for electric fields lower than 0.7 V/nm (*i.e.* \bar{v}_{\parallel} is 1.0 and 2.4 m/s for 0.03 and 0.7 V/nm) and rapid for higher electric fields (*i.e.* \bar{v}_{\parallel} suddenly grows from 10.5 to 105.5 m/s when the electric field increases from 1.0 to 3.0 V/nm). The sudden increase in \bar{v}_{\parallel} between 1.0 and 3.0 V/nm reflects the fact that the hydronium ions are pulled out of the sulfonate groups by the electric field or the ions escape because of the thermal motion caused by the accumulated electric heat. On the other hand, Table 5.2 also indicates that \bar{v}_{\parallel} and v_0 are relatively similar in all cases, even though the agreement is higher for weak electric fields. These features indicate that simulations obey the peak-shifted Maxwell distribution function, the importance of the attraction between the hydronium ions and the sulfonate groups decreasing as the electric field increases.

Figure 5.6a represents the variation of the protonic current density for the hydrated P(S-DVB) membrane, \mathbf{J} , against the electric field. As it can be seen, the flux of ions increases progressively with the electric field. This variation is moderate for electric fields lower than 1.0 V/nm (*i.e.* $\mathbf{J} = 2.8 \cdot 10^4$ and $6.7 \cdot 10^4 \text{ C/cm}^2 \cdot \text{s}$ for 0.03 and 0.7 V/nm , respectively) but sharp once this threshold value is reached (*i.e.* $\mathbf{J} = 29 \cdot 10^4$ and $272 \cdot 10^4 \text{ C/cm}^2 \cdot \text{s}$ for 1.0 and 3.0 V/nm , respectively). This drastic change in the flow behavior reflects the influence of high electric fields in the transport of hydronium ions. The protonic current density showed negative values for the lowest electric fields. This has been attributed to the fact that, although at such low electric fields the movement of

the hydronium ions is not dominated by the electric field (*i.e.* ions maintain a strong component of Brownian motion at the lowest electric fields), the C–S groups undergo small deformations, aligning along the direction of the electric field. Consequently, hydronium ions are pulled by the C–S bonds showing small negative displacements. The relationship between \mathbf{J} and the electric field defines the protonic conductivity (χ) through (5.9), the behavior followed by χ for electric fields higher than 0.01 V/nm being displayed in Figure 5.6b.

The maximum value of χ (0.09 S/cm) was reached for an electric field of 0.03 V/nm. This protonic conductivity is lower than that reported for membranes made of graft polymers composed of grafted chains of a macromonomer poly(sodium styrenesulfonate) and a polystyrene backbone when the content of sulfonic acid is maximum (*i.e.* 0.24 S/cm for an ion content of 19.1%) [45]. However, our maximum estimated value is practically identical to those recorded for a polystyrene/polytetra-fluoroethylene composite membranes prepared by adjusting the ratio of DVB to 5–10% in the reaction mixture (0.11–0.09 S/cm) [46] and the Nafions 117 membrane (0.1 S/cm) [47,48]. Moreover, the value for the latter commercial system was in excellent agreement with estimation derived from MD simulations, suggesting the reliability of our results [49]. On the other hand, χ decreases from 0.09 to 0.009 S/cm when the electric field increases from 0.03 to 0.7 V/nm. This behavior is because in such interval the electric field increases faster than the protonic current density. However, the opposite effect is detected for electric fields higher than 0.7 V/nm, χ growing from 0.03 to 0.09 S/cm when the electric field increases from 1.0 to 3.0 V/nm. Thus, the protonic current density increased faster than the electric field at such interval, provoking a change in the tendency of the profile displayed in Figure 5.6b.

5.1.3.4. INTERACTIONS

The partial radial distribution function of the S–OT pairs, $g_{S-OT}(\mathbf{r})$, where S and OT refer to sulfur of the sulfonate groups and the oxygen of the hydronium ions, respectively, is represented in Figure 5.7 for selected electric fields. The profiles show two pronounced sharp peaks at 3.8 and 4.3 Å, independently of the strength of the electric field. These distances correspond to two modes of interaction, which have been denoted as “strong” and “weak”, when the distance S–OT r_{S-OT} is lower than 3.9 Å or is within the interval $3.9 \text{ \AA} \leq r_{S-OT} < 4.4 \text{ \AA}$, respectively. Figure 5.8 represents the variation of the number of strong and weak interactions against their life time (*i.e.* the interval of time in which each interaction remains formed without interruption) for the investigated electric fields. As it can be seen, the weak interactions are two fold more populated than the strong ones, independently of the electric field. Moreover, the number of interactions and their life time remains practically unaltered by the electric field until the threshold value 1.0 V/nm is reached. After that, higher electric fields produce a drastic reduction in both the number of interactions and their corresponding life time, this feature being

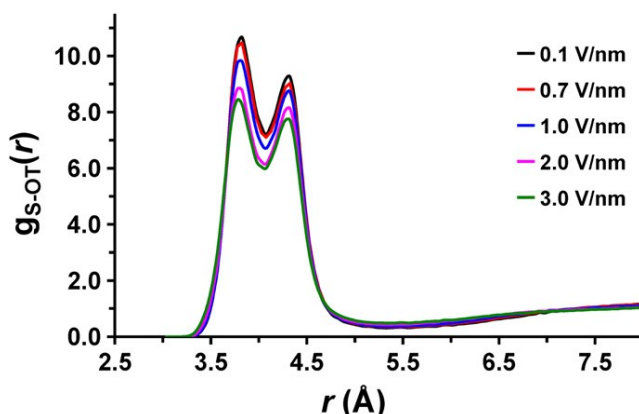


Figure 5.7. Partial distribution functions of $S \cdots OT$ pairs for selected electric fields.

particularly evident for 3.0 V/nm. On the other hand, the number of interactions decays exponentially with their life time in all cases. This behavior is fully consistent with the presence of electric field, which acts against the preservation of the interactions between the sulfonate groups and the hydronium ions. However, the response of both the weak and, especially, the strong interactions against this external force is practically independent of the strength of the electric field for values lower than 1.0 V/nm.

Figure 5.9a shows the partial radial distribution function of the $OT-OW$ pairs (where OT and OW refer to the oxygen of the hydronium and water molecules, respectively), $g_{OT-OW}(r)$, for selected electric fields. The height of the sharp peak centered at 2.97 Å, increases with the electric field suggesting the enhancement of the hydration of the hydronium ions. This was corroborated by examining the amount of water molecules bound to hydronium ions (*i.e.* water molecules involved in the hydration shell of hydronium ions). Thus, the average percentage of water molecules with an $OT-OW$ distance lower than 3.50 Å was 31-33%, 36%, 42%, 49% and 47% for ≤ 0.3 , 0.7, 1.0, 2.0

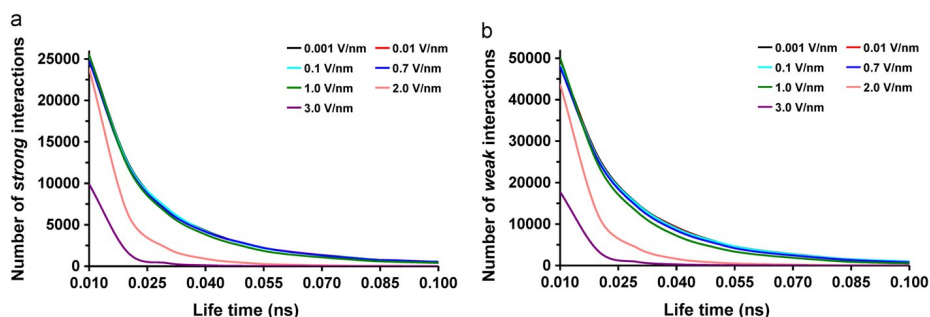


Figure 5.8. Variation of the number of (a) strong and (b) weak sulfonate···hydronium interactions with their life time. Strong interactions refer to those in which the distance between the sulfur atom of the sulfonate and oxygen of the hydronium is lower than 3.9 Å, while in weak interactions such distance is defined within the 3.9–4.4 Å interval.

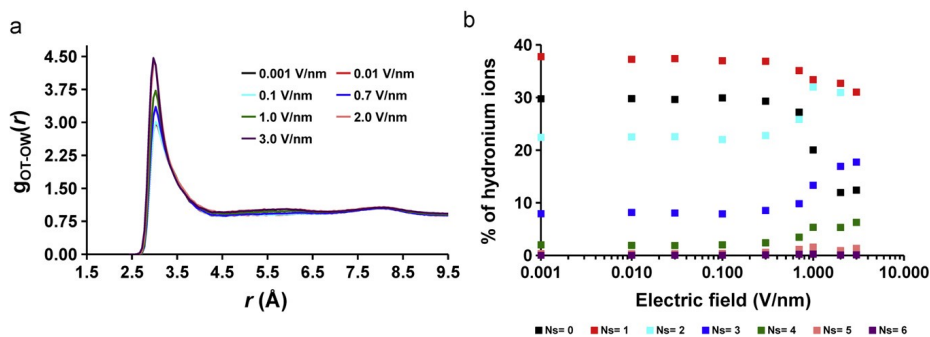


Figure 5.9. (a) Partial distribution functions of the intermolecular OT...OW pairs, where OT and OW refer to the oxygen of the hydronium and water molecules, respectively, calculated for selected electric fields. (b) Variation of the population of hydration shells containing 0, 1, 2, 3, 4, 5 and 6 water molecules at a OT...OW distance lower than 4.80 Å, against the electric field.

and 3.0 V/nm, respectively. Figure 5.9b represents the distribution of such water molecules in the hydration shell against the electric field by counting the number of molecules within a cutoff distance of 3.50 Å (N_S). Specifically, hydronium ions surrounded with $N_S = 0, 1, 2, 3, 4, 5$ and 6 were found, even though the population of the two latter were negligible for electric fields lower than 0.7 V/nm and very small for the rest of the cases. The most populated case was $N_S = 1$ in all cases, even though the percentage of hydronium ions in such situation decreases from 38% to 31% when the electric field increases from 0.001 to 3.0 V/nm. Furthermore, the percentages of hydronium ions with $N_S = 2, 3$ and 4 increase with the electric field while that with $N_S = 0$ follows the opposite behavior.

Analysis of the residence time (τ_{res}) of the water molecules inside the hydration shells of the hydronium ions allowed us to identify three different situations, which were remained unaltered for electric fields ≤ 1.0 V/nm (Figure 5.10a). The first refers to water molecules involved in completely variable hydration shells (black squares in Figure 5.10a): N_S changes with time and one or more of the water molecules defining the hydration shell are exchanged (*i.e.* residence time lower than 3 ns). This category is the most abundant, its population increasing from $\sim 48\%$ (for electric fields lower than 1.0 V/nm) to more 70% for 3.0 V/nm. The second category corresponds to unaltered hydration shells (red squares in Figure 5.10a): N_S and the water molecules of the hydration shell remain unaltered during the trajectories. The population of this category decreases from 37% for electric fields lower than 1.0 V/nm to 4% for the highest electric field. It should be noted that residence time of water molecules involved in this category is higher than 3 ns. The latter value is significantly higher than those predicted by MD simulations for the hydration shells of pure water (5.1 ps) and water surrounding methanol molecules (5.9 ps) [50], which in turn are fully consistent with experimental observations [51]. Finally, the third category involves partially variable hydration shells (blue squares in Figure 5.10a): N_S

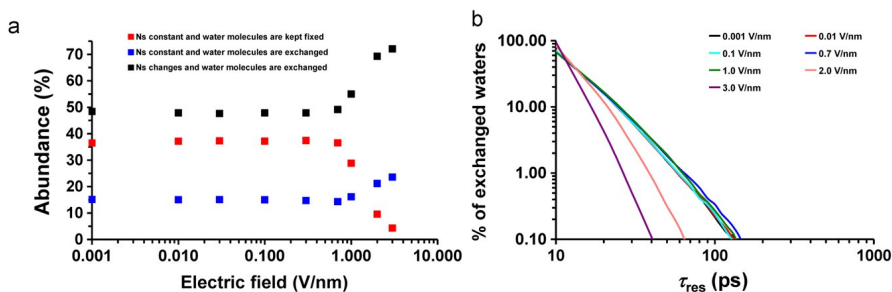


Figure 5.10. (a) Variation of the percentage of hydronium ions showing each of the three types of hydration shells identified in this work against the electric field. Hydration shells have been categorized according to the variability in the number of coordinated water molecules (N_S) and the exchangeability of such water molecules: (i) N_S changes and at least one of the water molecules of the hydration shell are exchanged (black squares) during the MD trajectory; (ii) N_S and the water molecules remain fixed during the whole MD trajectory (red squares); and (iii) N_S remains constant but at least one water molecule is exchanged during the MD trajectory (blue squares). (b) Percentage of exchanged water molecules in hydration shells of type (i) and (ii) (i.e. black and blue squares in Figure 5.8a) against the residence time τ_{res} for selected electric fields.

remains constant during the whole simulation but one or more water molecules contained in the hydration shells are exchanged. This is the least abundant category for electric fields lower than 1.0 V/nm (i.e. 15%), even though its population increases up to 24% when the strength of the electric field is 3.0 V/nm.

Figure 5.10b represents the percentage of exchanged water molecules in completely and partially variable hydration shells of the hydronium ions (i.e. black and blue squares in Figure 5.10b) against τ_{res} for selected electric fields. As it can be seen, the behavior is practically identical for all the electric fields ≤ 1.0 V/nm. Thus, in these cases $\sim 70\%$ of the water molecules contained in the hydration shell present $\tau_{res} \leq 10$ ps, such percentage decreasing to $\sim 16\%$, $\sim 6\%$ and $\sim 3\%$ when τ_{res} increases to 20, 30 and 40 ps, respectively. Electric fields higher than 1.0 V/nm show a reduction of τ_{res} . Thus, for 3.0 V/nm the amount of water molecules with $\tau_{res} \leq 10$ ps increases to 95% and only 4% of water molecules show $\tau_{res} = 20$ ps. These results indicate that, in general, τ_{res} is very short for exchanged water molecules, even though similar to those reported for water molecules at the hydration shell of alkaline ions (i.e. 10-25 ps) [52-54].

5.1.4. CONCLUSIONS

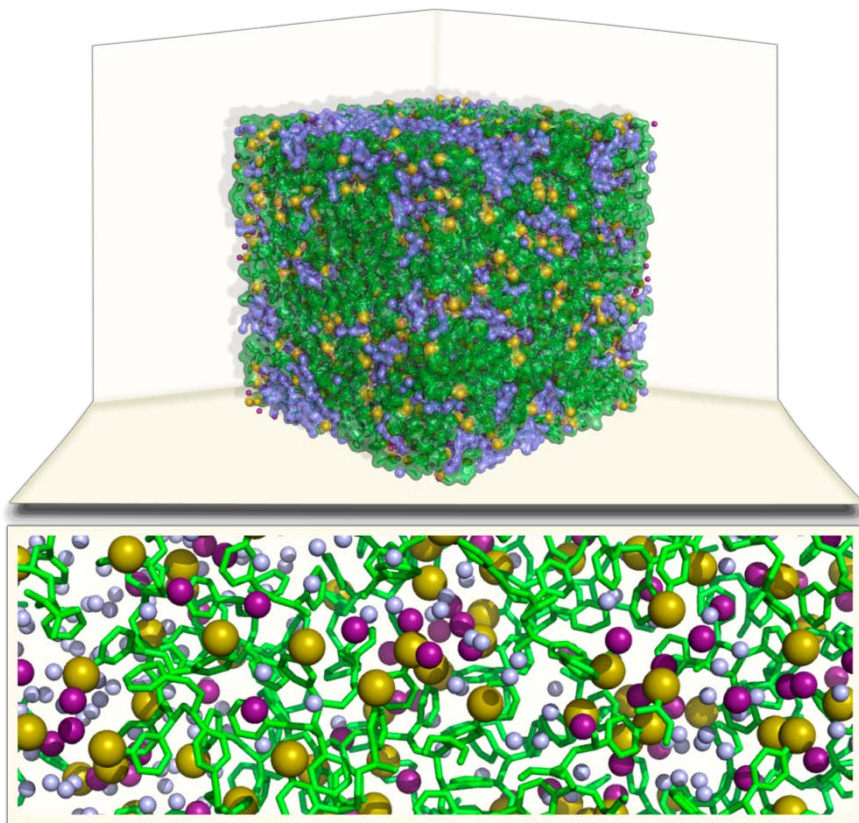
Transport properties of hydronium ions in sulfonated P(S-DVB) membranes are influenced by the strength of the applied electric field. A diffusive regime was only reached for electric fields ≤ 0.7 V/nm, the resulting diffusion coefficients increasing from $0.9 \cdot 10^{-7}$ to $62.8 \cdot 10^{-7}$ cm²/s when the electric field grows from 0.001 to 0.7 V/nm. Moreover, the anisotropy in the diffusive behavior increases with electric field affecting

the diffusion coefficient and velocity of the hydronium ions (*i.e.* the mobility and velocity of the ions is higher in the direction of the applied electric field). Temperature parameters, which were calculated by fitting the velocity distribution functions to the Maxwell distribution functions, indicate that the electric work injected into the system is not efficiently removed by the thermostat. This produces an anisotropic increment of the kinetic energy, resulting in an enhancement of the temperature of the hydronium ions. The protonic conductivity results from the balance between the protonic current density and the strength of the applied electric field. In this work, the highest protonic conductivities have been found for electric fields of 0.03 and 3.0 V/nm. In the former case the current density is moderate and the electric field is very low, whereas in the latter case the protonic current density is extremely high because of the structural deformations induced by the electric field.

The influence of the electric field in hydration shells of hydronium ions has been found to be practically negligible for strengths lower than 1.0 V/nm. Thus, the number of water molecules contained in the shells and both their exchangeability and residence times remained practically unaltered for electric fields ranging from 0.001 to 0.7 V/nm. This behavior should be attributed to the fact that the electric field affects the mobility of charged species, like hydronium ions, more drastically than the mobility of neutral water molecules. However, electric fields ≥ 1.0 V/nm produce an increment in the number of water molecules contained in the hydration shells as well as their exchangeability, the latter being accompanied by a reduction of the residence times.

5.2. INFLUENCE OF THE TEMPERATURE ON THE PROTON TRANSPORT IN P(S-DVB) MEMBRANES

The effect of the temperature on the properties of sulfonated poly(styrene-co-divinylbenzene), P(S-DVB), cation exchange membranes has been examined in the absence and presence of an external electric field of $0.7 \text{ V}\cdot\text{nm}^{-1}$. Results indicate that the temperature provokes local structural deformations around the sulfonate groups, which are manifested by the distortions at the C-S bonds (random and preferential in the absence and presence of the electric field, respectively). These distortions affect both the density and porosity of the membranes, even though the effects of the electric field decrease with increasing temperature. The electric field dominates over the thermal energy in the motion of the hydronium ions, while the external field does not affect the motion water molecules, which follow a Brownian behavior similar to that observed for the two species in the absence of an electric field. The calculated electro-osmotic drag coefficient indicates that the hydronium flow is several times higher than the water flow in the presence of the electric field, and this effect increases the temperature. The diffusion of hydronium ions in the absence of the external field increases slowly and



isotropically with the temperature, this behavior being preserved in the presence of the external electric field once the component associated with the drift velocity is discounted. Finally, the structure and dynamics of hydration shells at hydronium and sulfonate ions have been examined. Interestingly, the shells associated with two such ions as well as their response toward the temperature and electric field are significantly different, which has been attributed to the fact that sulfonate-water interactions are stronger than hydronium-water interactions.

5.2.1. INTRODUCTION

Membranes made of both natural and synthetic polymers comprise a wide range of applications (*e.g.*, water purification, gas separation, solvent dehydration, fuel cells, batteries, biosensors, and biomaterials) [55-65]. In comparison with traditional industrial separation processes, such as adsorption, extraction, and distillation, membrane technology holds inherent advantages (*e.g.*, less reagent and solvent consumption, no chemical additives, and recyclability), leading to the reduction of energy consumption, while the performance of separation processes increases.

Among various kinds of membranes, ion exchange membranes (IEMs) constitute a very useful category. Currently, IEMs play an important role and present potential applications in an increasing number of processes in the chemical industry (*e.g.*, fuel cells, batteries, chloroalkali cells, and electro-dialyzers) [1,3,5,8-11]. IEMs are typically phase-segregated materials, where a percolated network of a hydrophilic domain conducts ions while the hydrophobic phase confers not only mechanical strength but also dimensional and hydrolytic stability during the electro dialysis operation. The properties and performance of IEMs are essentially related to the chemical and physical nature of the polymers used in their fabrication. Consequently, in the last few decades the design of materials able to combine high ionic conductivity and durability, good mechanical strength, reduced permeability, and low cost for high-volume production has become one of the major challenges in the field of new polymer materials for electro dialysis applications [66-70].

IEMs are typically categorized in cation and anion exchangers, which exchange positively and negatively charged ions, respectively. In the last years our efforts have been focused on understanding the electric field-induced transport mechanism of hydronium ions in cation exchange membranes (CEMs) at the microscopic level [31,71]. Among the more useful CEMs for electro dialysis, those based on poly(styrene-co-divinylbenzene) [7,20,22,72,73], hereafter denoted P(S-DVB), deserve special attention. Thus, P(S-DVB) membranes combine several advantages, such as, for example, low protonic resistance, good mechanical properties, and high chemical stability. Furthermore, P(S-DVB)-based membranes are particularly appropriated for sulfonation since the cross-linked polystyrene has more phenyl rings that act as reactive sites for functionalization with sulfonic acid groups [7].

In a recent study, we simulated the electric-field-induced transport of hydronium ions in P(S-DVB) membranes with a water uptake of 18 wt% using atomistic molecular dynamics (MD) simulations [31]. The applied external electric field, which ranged from 0.001 to 3.00 V·nm⁻¹, provoked a redistribution of the unoccupied volume modifying the heterogeneity of the resin. Furthermore, negatively charged sulfonate groups underwent a rearrangement, showing a systematic alignment along the electric field direction. As was expected, the mobility of hydronium ions was found to increase with the strength of the electric field. More recently, we quantitatively examined the diffusion and conductivity of hydronium ions in these membranes, as well as their variation as a function of the applied electric field [71]. We found that the diffusive regime was only reached for electric fields $E_z \leq 0.7 \text{ Vnm}^{-1}$, the resulting diffusion coefficients increasing from $0.9 \cdot 10^{-7}$ to $62.8 \cdot 10^{-7} \text{ cm}^2/\text{s}$ when the electric field grows from 0.001 to 0.7 V·nm⁻¹. The highest protonic conductivities, which resulted from the balance between the protonic current density and the strength of the applied electric field, were detected for electric fields of 0.03 and 3.0 V·nm⁻¹. In the former case the current density was moderate and the electric field very low, whereas in the latter case the protonic current density was extremely high

because of the structural deformations induced by the electric field. Furthermore, the influence of the electric field on hydration shells of hydronium ions was found to be practically negligible for strengths lower than $1.0 \text{ V}\cdot\text{nm}^{-1}$, which was attributed to the fact that the electric field affects the mobility of hydronium ions more drastically than the mobility of neutral water molecules [71]. At this point it should be mentioned that systems containing charged species, such as hydronium and sulfonated ions, are well described by force fields. Thus, classical simulations have been proved to reproduce transport phenomena in which electrostatic interactions play a crucial role [31,71,73-77].

Unfortunately, many microscopic aspects related with the electric-field-induced transport of hydronium ions across CEMs remain unknown. In this work we used atomistic MD simulations to examine the effect of the temperature on both the structure of the P(S-DVB) membrane and the transport of hydronium ions. For this purpose, simulations in the absence and presence of an electric field of $0.7 \text{ V}\cdot\text{nm}^{-1}$ have been performed at $T = 280, 300, 320, 340,$ and 360 K . The properties of the membrane (*i.e.*, structure, density, and porosity), hydronium ions (*i.e.*, dynamics, transport, and conductivity), and water molecules (*i.e.*, dynamics, transport, and distribution in hydration shells around the ions) have been analyzed to compare the influence of the kinetic energy with respect to the electric work.

5.2.2. METHODS

The chemical system used to study the influence of the temperature on the transport of hydronium ions inside of sulfonated P(S-DVB) soft membranes involved 2165 styrene units, 270 DVB units, 1294 sulfonic acid groups, 1294 hydronium ions, and 4756 water molecules, all within a cubic simulation box with dimensions $a = 97.83 \text{ \AA}$. Accordingly, the composition, in wt %, of the simulated membrane was: 48.5% of styrene units, 5.9% of DVB units, 22.3% of sulfonic acid groups, 5.2% of hydronium ions, and 18.1% of water molecules. The chemical structure of the P(S-DVB) membrane is depicted in Scheme 5.1, and labels are used to identify the different atom types in P(S-DVB), water molecules, and hydronium ions. The strategy used to construct this molecular system, which is identical to that used to study the influence of the strength of the electric field on the transport of hydronium ions inside of sulfonated P(S-DVB), was previously described [31]. The three main steps of this approach can be summarized as follows: (*i*) the molecular architecture of the sulfonated P(S-DVB) membrane, including the cross-links, was generated using a stochastic algorithm; (*ii*) water molecules and hydronium ions were randomly introduced at positions with empty space accessible to such two molecules; and (*iii*) the hydrated membrane was relaxed, thermalized, and equilibrated using energy minimization and short runs of both NVT- and NPT-MD simulations.

field of $E_z = 0.7 \text{ Vnm}^{-1}$. The electric field was fixed along the z -axis of the simulation box, the force on each atom, i , of the system (\mathbf{F}'_i) being defined by the following expression

$$\mathbf{F}'_i = \mathbf{F}_i + q_i E_z \quad (5.13)$$

where \mathbf{F}_i is the force defined by the potential force field, q_i is the charge of the atom i , and E_z is the electric field.

MD simulations were carried out using the DLPOLY program [37]. The energy of the simulated system was described using the potential energy functions of the AMBER force field [32]. Force-field parameters for P(S-DVB) were extracted from the general AMBER force field (GAFF) [33] and the TraPPE united atom force field of polystyrene [34], whereas those of the sulfonate groups were taken from GAFF. Water and hydronium ions were described using the TIP3P [35] and Baadem *et al.* [36] models, respectively. The molecular geometry of the water (bond lengths and bond angle) and hydronium (bond lengths, bond angles, and improper torsion) molecules was kept fixed during the whole MD simulations.

Lennard-Jones and electrostatic interactions were calculated using an atom pair distance cutoff of 14.0 Å. Ewald summations were applied to evaluate electrostatic interactions [38]. The numerical integration step was set to 2 fs using the Verlet algorithm. Both temperature and pressure were controlled by the weak coupling method and the Nosé-Hoover thermo-barostat [39], using a time constant for the heat bath coupling and a pressure relaxation time of 0.15 and 2.85 ps, respectively. Coordinates and velocities were stored every 4 ps in the history file.

5.2.3. RESULTS AND DISCUSSION

5.2.3.1. EFFECT OF THE TEMPERATURE ON THE STRUCTURE

In general, the structure of the polymeric resin remains practically unaltered by the temperature, independently of the electric field. This is clearly evidenced in Figure 5.12, which represents the partial radial distribution functions of C2...C2 and CH...CH backbone pairs (atom labeling is indicated in Scheme 5.1). However, temperature provokes small rearrangements of the sulfonate groups, which are an active part of the polymer membrane. This is clearly reflected in Figure 5.13, which represents the sulfonate...sulfonate and sulfonate...water interactions through the partial radial distribution functions of S...S and S...OW pairs (Scheme 5.1), g_{S-S} and g_{S-OW} , respectively. The $g_{S-S}(r)$ function shows a pronounced peak centered at 5.5 Å in all cases, whereas the $g_{S-OW}(r)$ function displays two peaks centered at 4.3 and 7.3 Å, independently of both the temperature and the electric field. However, the height of the $g_{S-S}(r)$ peak increases with increasing temperature, while the height of the two

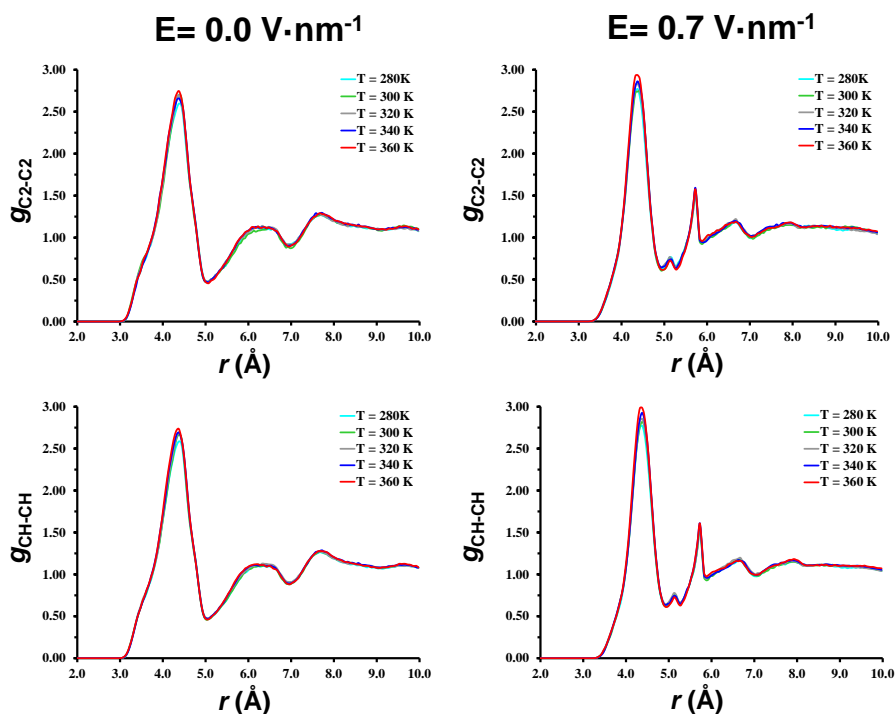


Figure 5.12. Radial distribution functions of C2 \cdots C2 and CH \cdots CH backbone pairs (g_{C2-C2} and g_{CH-CH} , respectively) calculated at different temperatures (from 280 to 360 K) in absence and presence ($E_z = 0.7 \text{ Vnm}^{-1}$) of electric field. Labels used to identify the atoms are displayed in Scheme 5.1. Profiles clearly indicate that the structure of the polymeric membrane is not affected by the temperature, independently of the electric field.

$g_{S-OW}(r)$ peaks decreases. These results indicate that water mediates sulfonate \cdots sulfonate interactions, which are enhanced by the temperature. Moreover, these variations are accompanied by a redistribution of the number of S \cdots OT pairs located at $\sim 4 \text{ \AA}$, which indicate that the attraction between the sulfonate groups and hydronium ions slightly increases with the temperature, as is reflected in the corresponding distribution function, $g_{S-OT}(r)$ (Figure 5.13). In contrast, the hydration of hydronium ions slightly decreases with increasing temperature, which is evidenced in Figure 5.14 through the partial radial distribution functions of OT \cdots OW pairs.

Results allow us to conclude that the temperature provokes local structural distortions around the sulfonate groups. Although these deformations are apparently similar in the absence and presence of electric field, detailed analyses of different geometric parameters revealed an important difference. More specifically, structural distortions at the sulfonate groups of the membrane without electric field, which are only due to the kinetic energy, follow a random distribution. In contrast, these kinetic energy effects are accompanied by a significant rearrangement of the C-S bonds when an electric field of $E_z = 0.7 \text{ Vnm}^{-1}$

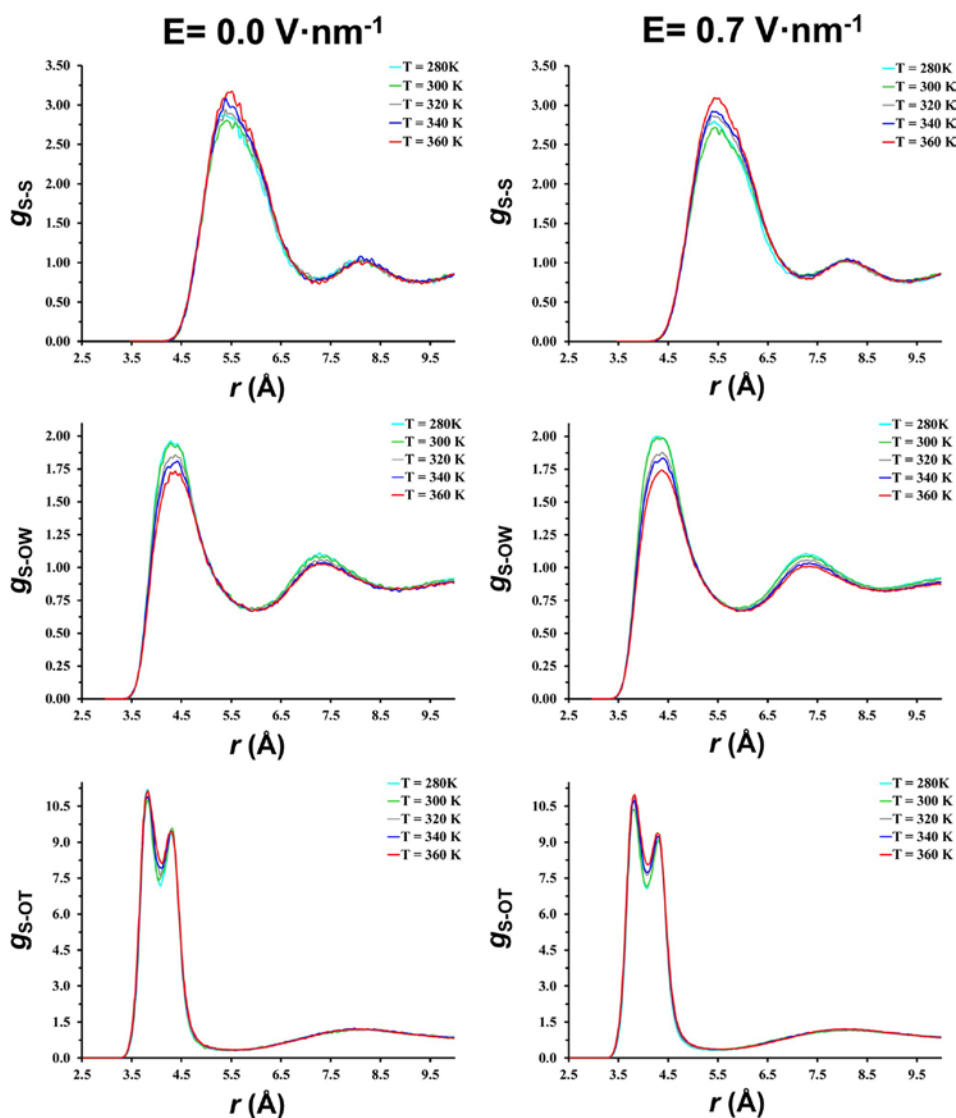


Figure 5.13. Radial distribution functions of $S\cdots S$, $S\cdots OW$, and $S\cdots OT$ pairs ($g_{S-S}(r)$, $g_{S-OW}(r)$, and $g_{S-OT}(r)$, respectively) calculated at different temperatures (from 280 to 360 K) in the absence and presence of electric field ($E_z = 0.7 \text{ Vnm}^{-1}$). Labels used to identify the atoms are displayed in Scheme 5.1.

is applied. This is reflected in Figure 5.15, which represents the temporal evolution of the averaged projection of the C–S bond into the direction of the electric field ($\overline{p_z^{CS}}$). Thus, $\overline{p_z^{CS}}$ is practically zero for the membranes without electric field, increasing to $\sim 4 \text{ \AA}$ upon application of $E_z = 0.7 \text{ Vnm}^{-1}$. Accordingly, C–S bonds tend to align in the direction of the electric field. This behavior corresponds to that observed in polar

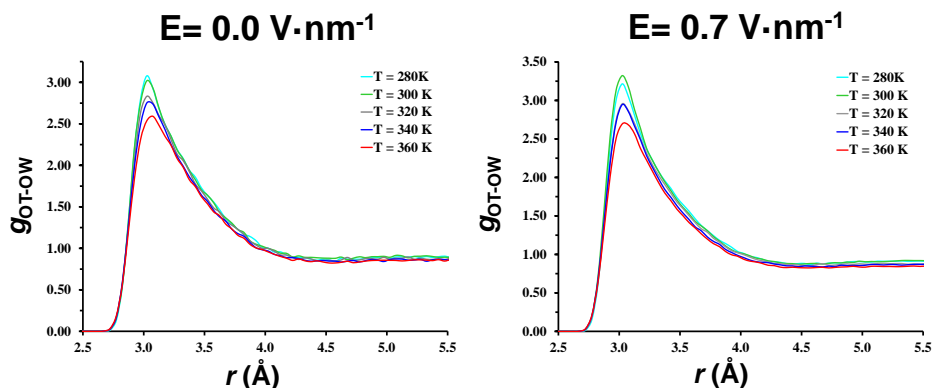


Figure 5.14. Radial distribution functions of OT \cdots OW pairs (g_{OT-OW}), where OT and OW refer to the oxygen atoms of hydronium and water, respectively, calculated at different temperatures (from 280 to 360 K) in absence and presence of electric field ($E_z = 0.7 \text{ Vnm}^{-1}$). Labels used to identify the atoms are displayed in Scheme 5.1. Profiles clearly indicate that the hydration of hydronium ions slightly decreases with increasing temperature.

dielectrics under the action of an external electric field, where their dipole moments are aligned with the electric field [78].

Figure 5.16a displays the variation of the average density, $\langle \rho \rangle$, against the temperature for the membranes with and without electric field. As it was expected, the density decreases with increasing temperature in the two cases, which is consistent with the temperature-induced enlargement of the simulation box. For a given temperature, the membrane with electric field is slightly denser than that without an electric field (*e.g.*,

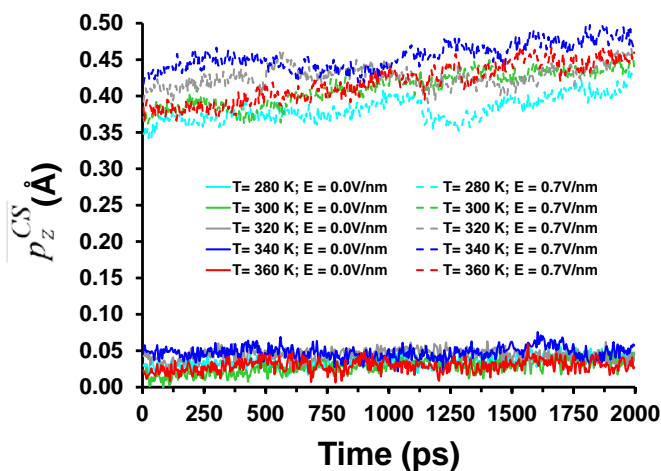


Figure 5.15. Temporal evolution of the averaged projection of the C-S bond into the direction of the electric field (\hat{z} -axis) calculated at different temperatures (from 280 to 360 K) in absence and presence ($E_z = 0.7 \text{ Vnm}^{-1}$) of electric field. The C-S bonds tend to align in the direction of the electric field.

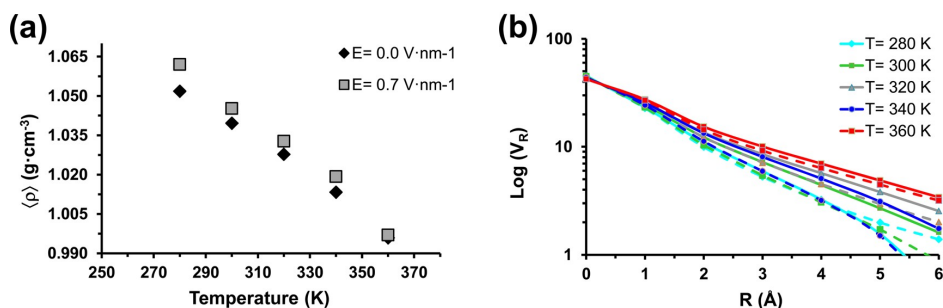


Figure 5.16. (a) Variation of the average density against the temperature for the membrane in the absence and presence ($E_z = 0.7 \text{ Vnm}^{-1}$) of an electric field. Averages were calculated considering the last 2 ns of each trajectory. (b) Logarithmic variation of the accessible volume to a given spherical penetrant (unoccupied volume, in %) against the radius of the penetrant (R) for sulfonated P(S-DVB) at different temperatures. The accessible volume has been determined using the microstructures provided by MD simulations in the absence and presence ($E_z = 0.7 \text{ Vnm}^{-1}$) of an electric field (solid and dashed line, respectively). Water and hydronium molecules have not been considered for the evaluation of the accessible volume.

$\langle \rho \rangle = 1.052 \pm 0.002$ and $1.062 \pm 0.002 \text{ g} \cdot \text{cm}^{-3}$ for $E_z = 0.0$ and 0.7 Vnm^{-1} , respectively, at 280 K), even though such difference becomes practically negligible at the highest temperature (*i.e.*, $\langle \rho \rangle = 0.996 \pm 0.002$ and $0.997 \pm 0.003 \text{ g} \cdot \text{cm}^{-3}$ for $E_z = 0.0$ and 0.7 Vnm^{-1} , respectively, at 360 K). Inspection of the temporal evolution of the density (not shown) indicated a very fast convergence, the error associated with all averages displayed in Figure 5.16a (expressed as ± 2 times the standard deviation) being smaller than $0.003 \text{ g} \cdot \text{cm}^{-3}$ in all cases. This behavior is fully consistent with the variation of the membrane porosity, which has been evaluated by computing the volume accessible to a spherical penetrant of radius R (V_R) [79], against the temperature. Furthermore, the values of V_R for $R = 0 \text{ \AA}$ were determined using the van der Waals radii of atoms involved in the non-hydrated P(S-DVB) membrane (*i.e.*, water and hydronium molecules were omitted in the calculation of V_R). Figure 5.16b, which represents $\log V_R$ against R , indicates that, as expected, the unoccupied volume decreases progressively when R increases, an approximated straight line being obtained in all cases. However, V_R , which decreases slightly upon the application of the electric field, grows systematically with temperature. The latter effect is due to the sulfonate distortions and rearrangements mentioned above. Moreover, the reduction of V_R , with R suggests a heterogeneous distribution of the unoccupied volume, which is essential for the transport of the hydronium ions.

5.2.3.2. EFFECT OF THE TEMPERATURE ON THE DYNAMICS AND TRANSPORT OF HYDRONIUM IONS

The velocity distribution functions of the hydronium ions, which were derived from the velocities (v) stored during the MD simulations at different temperatures (Figure

5.17), were fitted to the Maxwell velocity distribution function, $f(\mathbf{v})$, to obtain the kinetic energy of hydronium ions (T_h)

$$f(\mathbf{v}) = 4\pi v^2 \left(\frac{m}{2\pi k_B T_h} \right)^{3/2} \exp\left(-\frac{mv^2}{2k_B T_h}\right) \quad (5.14)$$

where m is the mass and k_B is the Boltzmann constant. As can be seen in Figure 5.18a, T_h is systematically higher than T by ~ 18 and ~ 24 K for $E_z = 0.0$ and 0.7 Vnm $^{-1}$, respectively. This is because motions are slower on average for polymeric molecules than for hydronium ions. The temperature of the system should be maintained during the production MD run by removing numerically the heat of the system through the thermostat [44,78]. However, results displayed in Figure 5.18a clearly indicate that the applied Nosé-Hoover thermo-barostat has difficulties to remove quickly enough the energy of the system. These difficulties become slightly more evident, especially at low temperature, in the presence of the electric field due to the electric work injected at each simulation step. Despite this, the linear behavior followed by the two profiles indicates that this limitation is practically constant for all examined temperatures.

The fittings of the velocity distribution functions in the direction parallel and perpendicular to the z -axis (v_{\parallel} and v_{\perp} , respectively), which are included in Figure 5.17, to the Maxwell distribution functions in such directions ($f(v_{\parallel})$ and $f(v_{\perp})$, respectively) were used to estimate the temperature of the hydronium ions in the directions parallel and perpendicular to the electric field (T_{\parallel} and T_{\perp} , respectively)

$$f(v_{\parallel}) = \sqrt{\frac{m}{2\pi k_B T_{\parallel}}} \exp\left(-\frac{m(v_{\parallel} - v_0)^2}{2k_B T_{\parallel}}\right) \quad (5.15)$$

$$f(v_{\perp}) = \sqrt{\frac{m}{2\pi k_B T_{\perp}}} \exp\left(-\frac{mv_{\perp}^2}{2k_B T_{\perp}}\right) \quad (5.16)$$

The variation of both T_{\parallel} and T_{\perp} against T (Figure 5.19) shows that $T_{\parallel} \approx T_{\perp} \approx T_h$ for the simulations with and without the electric field, indicating that the kinetic energy and the injected electric work are isotropically distributed between the components of T_h .

The average transport velocity of the hydronium ions in the direction parallel to the electric field ($\bar{v}_{\parallel h}$) has been evaluated by integrating the velocity distribution function

$$\bar{v}_{\parallel h} = \int_{-\infty}^{\infty} v_{\parallel} f(v_{\parallel}) dv_{\parallel} \quad (5.17)$$

where $f(v_{\parallel})$ is derived from the adjustment of the data provided by MD simulations to (5.15). The average transport velocity of the water molecules in the direction parallel to the electric field ($\bar{v}_{\parallel w}$) has been calculated using the same procedure. Table 5.3 compares

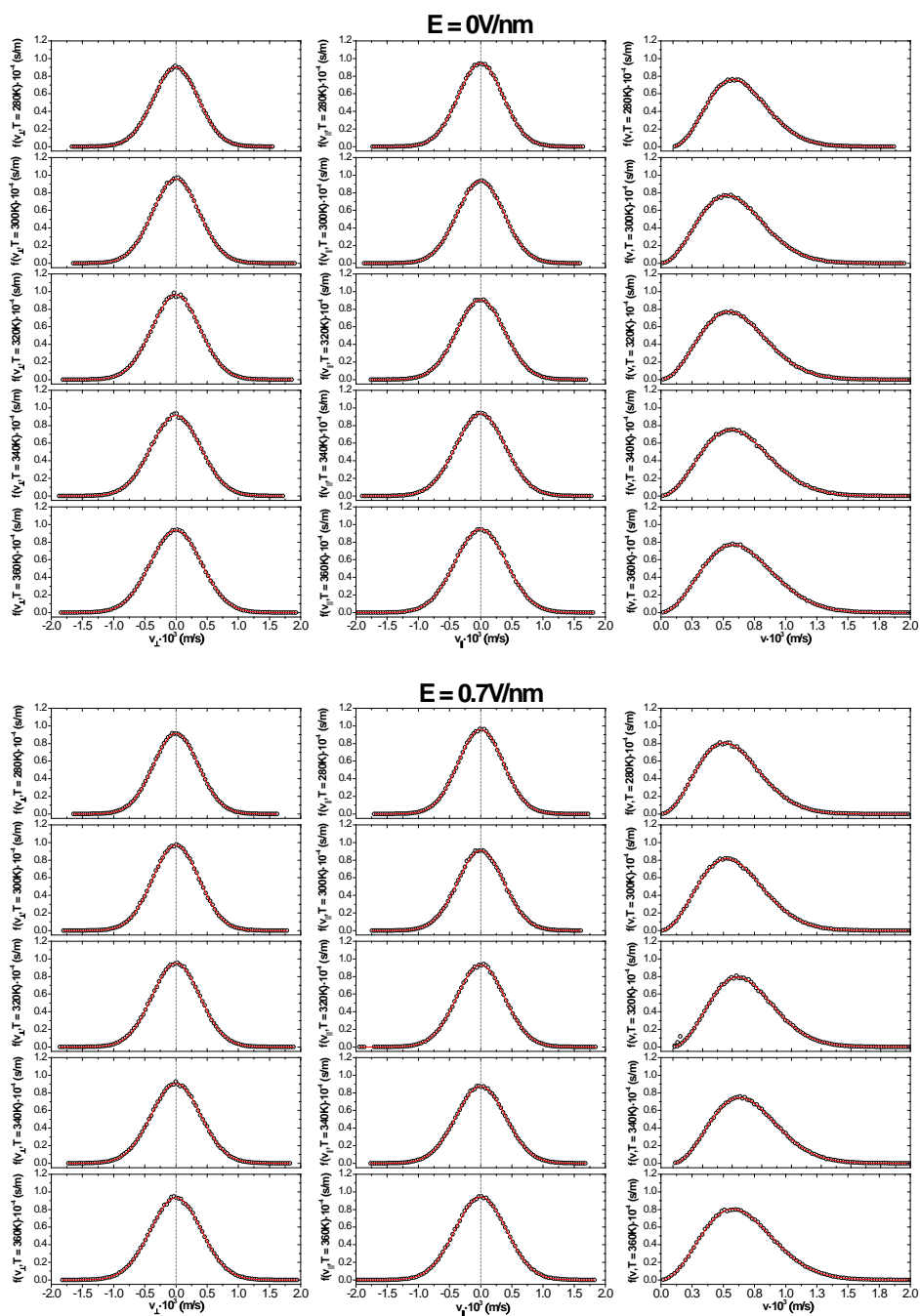


Figure 5.17. Velocity distributions $f(\vec{v})$ (right), $f(v_{\parallel})$ (center) and $f(v_{\perp})$ (left) of hydronium ions at temperatures from 280 to 360 K (row 1 to 5) in absence (top) and presence (bottom) of electric field. The red lines represent the fitting of the velocity distribution functions to the corresponding Maxwell distributions functions (5.14-5.16).

5.2. INFLUENCE OF THE TEMPERATURE ON THE PROTON TRANSPORT IN P(S-DVB) MEMBRANES

 Table 5.3. Average Transport Velocity in the Direction Parallel to the Applied Electric Field of Hydronium Ions ($\bar{v}_{\parallel h}$ and $\bar{v}_{\parallel h}^*$) and Water Molecules ($\bar{v}_{\parallel w}$), Electro-Osmotic Drag Coefficient (K_{drag}), Proton Conductivity (χ), and Diffusion Coefficients of Hydronium Ions (D_h , $D_{h,\parallel}$ and $D_{h,\perp}$) in the P(S-DVB) Membrane at Different Temperatures

Electric Field	T (K)	$\bar{v}_{\parallel h}$ (m/s) ^a	$\bar{v}_{\parallel h}^*$ (m/s) ^b	$\bar{v}_{\parallel w}$ (m/s)	K_{drag}	χ (S/cm)	$D_h \times 10^7$ (cm ² /s) ^c	$D_{h,\parallel} \times 10^7$ (cm ² /s) ^c	$D_{h,\perp} \times 10^7$ (cm ² /s) ^c
$E_z = 0.0 \text{ Vnm}^{-1}$	280	0.597	-0.002	0.005	1.03		0.71/1.17	0.71/1.25	0.69/1.28
	300	-0.095	0.008	0.001	1.03		1.88/1.40	2.08/1.38	1.74/1.40
	320	-0.235	-0.001	-0.012	1.15		1.11/1.49	1.13/1.50	1.14/1.48
	340	0.449	0.002	0.014	1.10		1.79/1.58	1.50/1.57	1.81/1.59
	360	0.653	0.000	-0.014	1.12		2.03/1.68	1.85/1.71	2.21/1.66
$E_z = 0.7 \text{ Vnm}^{-1}$	280	2.934	1.804	0.146	1.18	0.011	-/1.31	-/1.39	-/1.27
	300	2.122	1.748	0.243	1.42	0.008	-/1.42	-/1.50	-/1.38
	320	2.236	2.244	0.244	1.38	0.009	-/1.52	-/1.61	-/1.47
	340	3.365	2.560	0.256	1.40	0.013	-/1.61	-/1.69	-/1.57
	360	2.587	2.513	0.304	1.43	0.010	-/1.72	-/1.82	-/1.67

^aAverage transport velocity in the direction parallel to the applied electric field of hydronium ions calculated using (5.17). ^bAverage transport velocity in the direction parallel to the applied electric field of hydronium ions calculated by adjusting linearly the profiles displayed in Figure 5.18c. ^cDiffusion coefficients calculated using (5.23)/ (5.28) for D_h , (5.24)/(5.29) for $D_{h,\parallel}$, and (5.26)/(5.30) for $D_{h,\perp}$.

$\bar{v}_{\parallel h}$ and $\bar{v}_{\parallel w}$ values obtained at different temperatures in the presence and absence of electric field.

In the absence of an electric field $\bar{v}_{\parallel h}$ and $\bar{v}_{\parallel w}$ are very small, indicating that hydronium ions and water molecules move randomly at the five investigated temperatures. In spite of this, it is worth noting that $\bar{v}_{\parallel h}$ is 1 order of magnitude higher than $\bar{v}_{\parallel w}$. Both $\bar{v}_{\parallel h}$ and $\bar{v}_{\parallel w}$ grow 1 order of magnitude upon the application of an electric field. Thus, $\bar{v}_{\parallel h}$ reaches a value of 2–3 320 m/s when $E_z = 0.7 \text{ Vnm}^{-1}$, indicating that the electric-field-induced motion dominates over the thermal motion in the \tilde{x} -direction. This provokes a flow of ions in the direction of the electric field that is practically independent of the temperature. On the other hand, $\bar{v}_{\parallel w}$ increases from 0.143

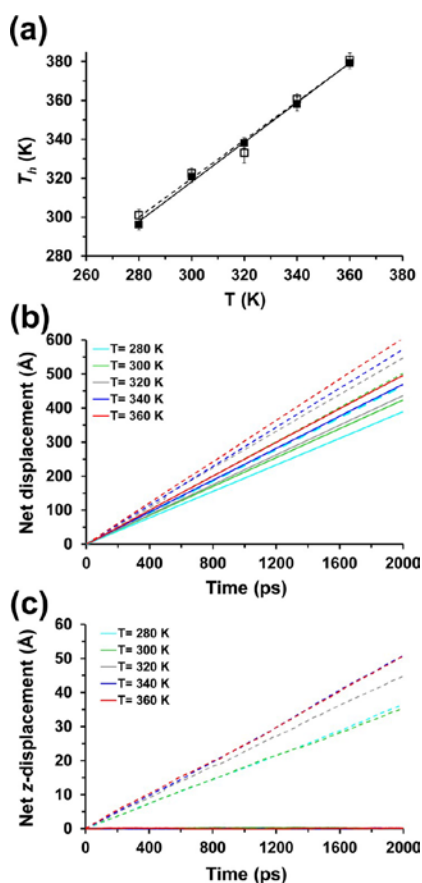


Figure 5.18. (a) Variation of the temperature of the hydronium ions (T_h) against the temperature of simulation (T) in the absence (filled squares) and presence of electric field (empty squares). The linear behavior is illustrated by displaying the linear fittings (solid and dashed lines, respectively). (b) Temporal evolution of the net displacement of the hydronium ions at the studied temperatures in the absence (solid lines) and presence (dashed line) of external electric field. (c) Temporal evolution of the net displacement in the \tilde{z} -direction of the hydronium ions at the studied temperatures in the absence (solid lines) and presence (dashed line) of external electric field.

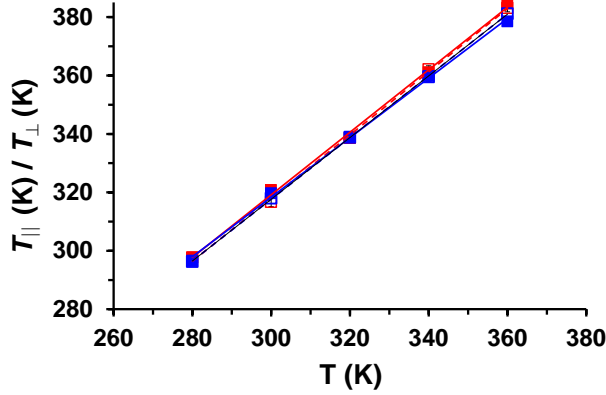


Figure 5.19. Variation of the temperature of the hydronium ions in the directions parallel and perpendicular to the electric field (red and blue, respectively) against the temperature of simulation (T) in absence (filled squares) and presence of electric field (empty squares). The linear behavior is illustrated by displaying the linear fittings (solid and dashed lines, respectively).

to 0.304 m/s when the temperature increases from 280 to 360 K. These values are lower and higher than those obtained for $\bar{v}_{\parallel h}$ and $\bar{v}_{\parallel w}$, respectively, in the absence of an electric field. The difference between $\bar{v}_{\parallel w}$ values in the absence and presence of an electric field has been attributed to the fact that water molecules in the hydration shell of hydronium ions are dragged in the direction of the electric field, resulting in consistently positive net $\bar{v}_{\parallel w}$ values. This feature has been corroborated by calculating the average transport velocity of the water molecules in the directions perpendicular to the electric field ($\bar{v}_{x,w}$ and $\bar{v}_{y,w}$; Table 5.4. Values of $\bar{v}_{x,w}$ and $\bar{v}_{y,w}$, are not only similar but also very small with respect to $\bar{v}_{\parallel w}$, evidencing a Brownian behavior in the directions perpendicular to the electric field.

The hydronium and water flow (J_h and J_w , respectively) has been calculated as a multiplication of the concentration and the average transport velocity

$$J_h = \frac{n_h}{V} \bar{v}_{\parallel h} \quad (5.18)$$

$$J_w = \frac{n_w}{V} \bar{v}_{\parallel w} \quad (5.19)$$

where V is the volume; n_h is the number of hydronium ions; and n_w is the number of water molecules. Then, the electro-osmotic drag coefficient, K_{drag} , is defined as the number of water molecules transported accompanied by the transport of each proton

$$K_{drag} = \frac{J_w + J_h}{J_h} \quad (5.20)$$

Table 5.4. Average Transport Velocity in the Direction Parallel ($\bar{v}_{\parallel w}$) and Perpendicular ($\bar{v}_{x,w}$ and $\bar{v}_{y,w}$) to the Applied Electric Field of Water Molecules in P(S-DVB) Membrane at Different Temperatures.

Electric Field	T (K)	$\bar{v}_{x,w}$ (m/s)	$\bar{v}_{y,w}$ (m/s)	$\bar{v}_{\parallel w}$ (m/s)
$E_z = 0.0 \text{ Vnm}^{-1}$	280	0.011	0.016	0.005
	300	0.001	0.001	0.001
	320	-0.021	-0.015	-0.012
	340	0.001	-0.009	0.014
	360	0.020	0.021	-0.014
$E_z = 0.7 \text{ Vnm}^{-1}$	280	-0.013	-0.007	0.146
	300	0.011	0.029	0.243
	320	-0.015	-0.026	0.244
	340	0.001	0.020	0.256
	360	0.019	0.019	0.304

Table 5.3 indicates that the electro-osmotic drag coefficient in the absence of the electric field increases from 1.03 at $T = 280$ and 300 K to ~ 1.1 at $T = 320 - 360 \text{ K}$. Accordingly, the flow of hydronium ions is always higher than that of water molecules, even though the difference decreases from $J_h \approx 35 \times J_w$ to $J_h \approx 10 \times J_w$ upon increasing the temperature. In the presence of the external electric field, the electro-osmotic drag coefficient increases from 1.18 to 1.43 with the temperature (Table 5.3), indicating that the hydronium flow is 5.4 ($T = 280 \text{ K}$) – 2.3 ($T = 360 \text{ K}$) higher than the water flow. Although experimental values of the electro-osmotic coefficient are not available for P(S-DVB), our theoretical estimations are in good agreement with the values reported for water immersed Nafion ($K_{drag} \approx 2 - 3$) and water vapor equilibrated Nafion ($K_{drag} \approx 1$) [28].

Figure 5.18b displays the temporal evolution of the net displacement of hydronium ions at different temperatures. As expected, the net displacement increases with the temperature in all cases, even though for a given T the displacement is higher in the presence of the electric field. This behavior, which reflects the Brownian motion of the hydronium ions, is fully consistent with the fact that $T_{\parallel} \approx T_{\perp} \approx T_h$ for all simulated temperatures (Figure 5.18a and Figure 5.19). The temporal evolution of the accumulated displacement of hydronium ions in the direction of the electric field at the different temperatures is represented in Figure 5.18c. The net ξ -displacement is null in the absence of an electric field, independently of T , because of the isotropic motion. Although the external electric provokes a linear increment of the ξ -displacement that increases with T , the net ξ -displacement is in all cases 1 order of magnitude lower than that displayed in Figure 5.18b. This feature indicates that the motion of the ions in the ξ -direction is

defined by the electric field, as was concluded from $\bar{v}_{\parallel h}$ values, but the motion in the whole space is essentially due to thermal effects. Indeed, the linear fitting of the profiles displayed in Figure 5.18c provides an alternative estimation of average transport velocity of the hydronium ions in the direction parallel to the electric field, which has been expressed as $\bar{v}_{\parallel h}^*$ in Table 5.3. As can be seen, $\bar{v}_{\parallel h}$ and $\bar{v}_{\parallel h}^*$ values exhibit an excellent agreement.

The protonic conductivity (χ) in a hydrated P(S-DVB) membrane has been calculated by relating the electrical current density (left term in (5.21)), which includes the charge of the hydronium ion (q), to the applied electric field (\mathbf{E})

$$\frac{1}{V} \bar{v}_{\parallel h} \sum_{i=1}^{n_h} q_i = \chi \mathbf{E} \quad (5.21)$$

The values calculated for χ , which are included in Table 5.3, are very similar for the five evaluated temperatures, ranging from 0.008 to 0.013 S/cm. These values, which suggest that the effect of the temperature on the protonic conductivity is very small, are similar to those measured for commercial polystyrene/polytetrafluoroethylene composite membranes prepared adjusting the ratio of DVB to 5-10% in the reaction mixture (0.09–0.11 S/cm) [47,80]. The practically negligible dependence on the temperature displayed in Table 5.3 should be attributed to the fact that the protonic flux induced by the electron field is higher than that provoked by increasing the temperature. The mean square displacement (MSD) has been calculated as

$$\text{MSD} = \left\langle \sum_{i=1}^{n_h} [\mathbf{r}_i(t) - \mathbf{r}_i(0)]^2 \right\rangle \quad (5.22)$$

where $\mathbf{r}_i(t)$ is the position vector of hydronium i at the time event t . Figure 5.20a represents the average MSD profiles obtained at $T = 280, 300, 320, 340,$ and 360 K for the membrane in the absence and presence of an electric field. As can be seen, the mobility of hydronium ions increases with the temperature, even though the influence of the temperature is very small in comparison with that of the electric field. The diffusion coefficient of hydronium ions (D_h) in P(S-DVB) membranes without an external electric field has been calculated by the Einstein diffusion equation

$$D_h = \frac{1}{6n_h} \lim_{t \rightarrow \infty} \frac{d}{dt} \text{MSD} \quad (5.23)$$

where t is time. Equation (5.23) is only valid when the Einstein diffusive regimen is reached (*i.e.*, the motion of the diffusing hydronium follows a random walk). To test the region in which (5.23) is valid, $\log(\text{MSD})$ against $\log(t)$ was plotted for each temperature. For sufficient long times, the MSD of the diffusing particles increases linearly with time, and the slope, m , of such curve is 1.0 (*i.e.*, accelerated and anomalous

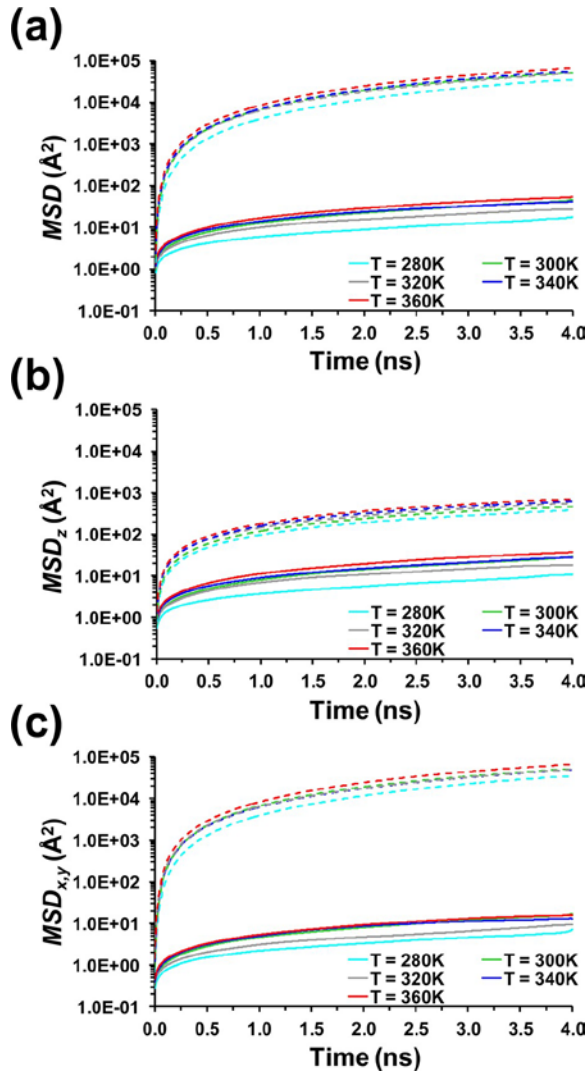


Figure 5.20. (a) Mean square deviation (MSD; (4.22)) of hydronium ions at different temperatures in the absence (solid lines) and presence (dashed line) of external electric field. The MSD in directions (b) parallel (MSD_z ; (4.25)) and (c) perpendicular ($MSD_{x,y}$; (4.27)) to the applied electric field are also displayed.

diffusive regimes exhibit $m < 1$ and $m > 1$, respectively [48]). D_h values calculated using the normal diffusion region of Figure 5.20a are listed in Table 5.3. As can be seen, D_h increases slowly with the temperature changing from $7.10 \times 10^{-8} \text{ cm}^2/\text{s}$ for $T = 280 \text{ K}$ to $430.203 \times 10^{-7} \text{ cm}^2/\text{s}$ for 360 K .

Isotropic or anisotropic diffusion of the hydronium ions was examined by monitoring independently the values of D in directions parallel (z) and perpendicular (x and y) to the

applied electric field, hereafter denoted $D_{h,\parallel}$ and $D_{h,\perp}$, respectively. These coefficients were computed using the following equations

$$D_{h,\parallel} = \frac{1}{2n_h} \lim_{t \rightarrow \infty} \frac{d}{dt} \text{MSD}_z \quad (5.24)$$

$$\text{MSD}_z = \left\langle \sum_{i=1}^{n_h} [z_i(t) - z_i(0)]^2 \right\rangle \quad (5.25)$$

$$D_{h,\perp} = \frac{1}{4n_h} \lim_{t \rightarrow \infty} \frac{d}{dt} \text{MSD}_{x,y} \quad (5.26)$$

$$\text{MSD}_{x,y} = \left\langle \sum_{i=1}^{n_h} ([x_i(t) - x_i(0)]^2 + [y_i(t) - y_i(0)]^2) \right\rangle \quad (5.27)$$

Inspection of the MSD_z and $\text{MSD}_{x,y}$ profiles, which are displayed in Figure 5.20b and Figure 5.20c, does not allow us to appreciate significant changes in the slope of the profiles. Indeed, the partial diffusion coefficients, $D_{h,\parallel}$ and $D_{h,\perp}$, calculated in the absence of the electric field, which are included in Table 5.3, show that motion of the hydronium ions is isotropic at the five examined temperatures with $D_h \approx D_{h,\parallel} \approx D_{h,\perp}$. This feature is consistent with the isotropic structure of the P(S-DVB) membrane in the absence of an electric field.

In the presence of an external electric field, the diffusion coefficients cannot be calculated using (5.23), (5.24) and (5.26) because the mobility of the hydronium ions results from a combination of diffusion and drift, such equations failing to separate the two contributions. The MSD of hydronium ions varies as a function of t ($m = 1$, as discussed above) in diffusive motion and as t^2 ($m = 2$) in drift due to the electric field [41,81]. In principle, the diffusive motion is unaffected by the electric field. To corroborate this feature, the diffusion coefficients D_h , $D_{h,\parallel}$ and $D_{h,\perp}$ have been calculated in the absence and presence of an external electric field using the velocity correlation functions

$$D_h = \frac{1}{3} \int_{t=0}^{t=\infty} \langle \mathbf{v}_i(0) \cdot \mathbf{v}_i(t) \rangle dt \quad (5.28)$$

$$D_{h,\parallel} = \int_{t=0}^{t=\infty} \langle v_{i,z}(0) \cdot v_{i,z}(t) \rangle dt \quad (5.29)$$

$$D_{h,\perp} = \frac{1}{2} \int_{t=0}^{t=\infty} \langle v_{i,x}(0) \cdot v_{i,x}(t) + v_{i,y}(0) \cdot v_{i,y}(t) \rangle dt \quad (5.30)$$

Comparison of the diffusion coefficients calculated using the MSDs and the velocity correlation functions for the membranes calculated in the absence of an external electric field, which are also included in Table 5.3, reflects a very good agreement between the two methodologies. The diffusion coefficients derived from velocity correlation functions

are consistent with both the isotropic structure of the membrane and the enhancement of the hydronium mobility with the temperature. This isotropic behavior is clearly retained in simulations with an electric field. Moreover, diffusion coefficients calculated using (5.28)-(5.30) in the presence and absence of an electric field are very similar since velocity correlation functions discount the drift velocity.

5.2.3.3. EFFECT OF THE TEMPERATURE ON THE HYDRATION OF CHARGED GROUPS

The peaks identified in the distribution functions g_{OT-OW} and g_{S-OW} (Figure 5.14 and Figure 5.13, respectively) were used to define the size of the first hydration shell for hydronium and sulfonate ions, respectively. Thus, the hydration of hydronium ions and sulfonate groups was categorized according to the number of water molecules within the selected cutoff distance (N_w), which was 3.5 and 5.0 Å, respectively. Figure 5.21a and Figure 5.21b represent the variation of the percentage of hydronium and sulfonate ions, respectively, with N_w water molecules contained in the first hydration shell against the temperature. As can be seen, the amount of hydronium without surrounding water molecules ($N_w = 0$) at 280 K is relatively high in the presence and absence of an electric field (*i.e.*, 23% and 28%, respectively), this amount increasing slowly and progressively with the temperature (*e.g.*, 35% and 36%, respectively, at 360 K). Although sulfonate ions display the same behavior from a qualitative point of view, the number of groups with $N_w = 0$ is much less pronounced. Thus, the percentage of dehydrated sulfonate groups grows from 4%/3% to 8%/7% when the temperature increases from 280 to 360 K in the absence/presence of an external electric field. Furthermore, sulfonate and hydronium ions also differ in the structure of the hydration shell. The most populated case (34–38%) was $N_w = 1$ for hydronium ions independently of both the temperature and the presence of electric field, the population of ions with $N_w = 2$ being lower than 25%. In contrast, the sulfonate ions surrounded by 3 and 2 water molecules are the most populated cases at temperatures lower and higher than ~ 320 K, respectively. Moreover, the number of hydronium ions with $N_w \geq 5$ is practically null ($<1\%$) at all the investigated temperatures, while the population of sulfonate ions with $N_w = 5$ is still significant (8–10%), and in addition, some cases with $N_w = 7$ are detected ($\sim 2\%$).

The orientation of water molecules in the vicinity of charged hydronium and sulfonate ions was determined from the orientational distribution function, which has been defined through the angle formed by the dipole moments of such groups, in the first hydration shell. The radius of that shell was defined by the cutoff distance mentioned above (*i.e.*, 3.5 and 5.0 Å, respectively). More specifically, the probability $P(\theta)$ of observing a water dipole at an angle θ to the OT–OW or S–OW vector was calculated. Figure 5.22a and Figure 5.22b show these probabilities as functions of θ for hydronium and sulfonate ions, respectively. The most favorable orientation of a water dipole in the first solvation shell

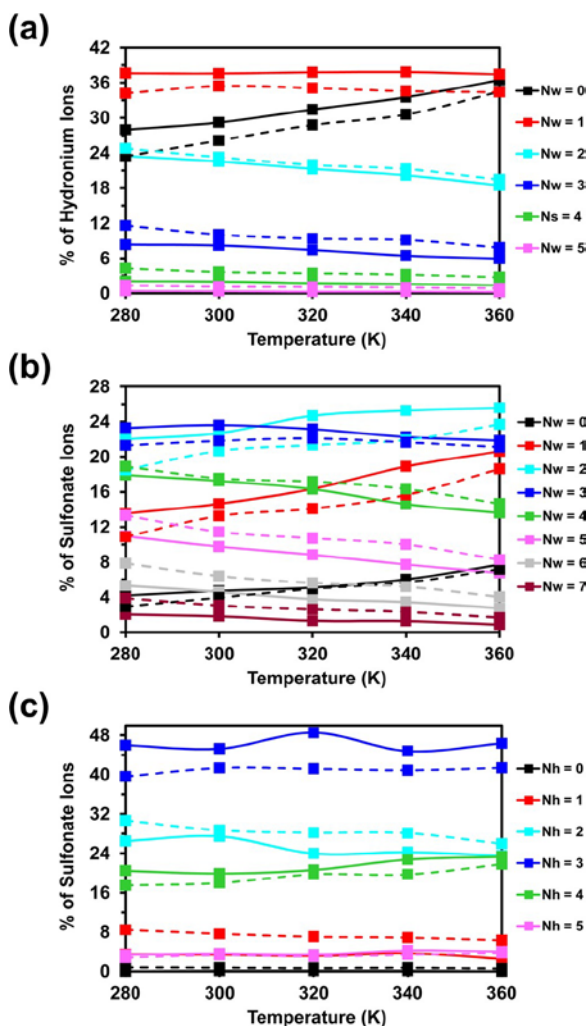


Figure 5.21. Variation of the population of hydration shells containing N_w water molecules at a (a) $OT \cdots OW$ and (b) $S \cdots OW$ distance lower than 3.5 and 5.0 Å, respectively. (c) Variation of the population of sulfonate groups with a number of hydronium ions (N_h) at a $S \cdots OT$ distance lower than 4.8 Å. Solid and dashed lines correspond to simulations in the absence and presence of an external electric field, respectively.

of hydronium is not parallel to the $OT-OW$ but shifts from $\sim 70^\circ$ to $\sim 65^\circ$ (Figure 5.22a) upon the application of the external electric field, independently of the temperature. This small change is probably due to a competition between the strong cation–water electrostatic interaction and the rest of the interactions involving water molecules, including those related with the tendency to maintain hydrogen bonding networks. In contrast, the dipole of water in the first solvation shell of sulfonate anions forms an angle of $59^\circ-61^\circ$ with the $S-OW$ vector (Figure 5.22b), regardless of the electric field. This

feature suggests that water–cation interactions are stronger than water–anion interactions.

On the other hand, analysis of the residence time (τ_{res}) of the water molecules inside the first hydration shell of hydronium and sulfonate ions evidenced the existence of four different situations. The first refers to ions with completely variable hydration shells

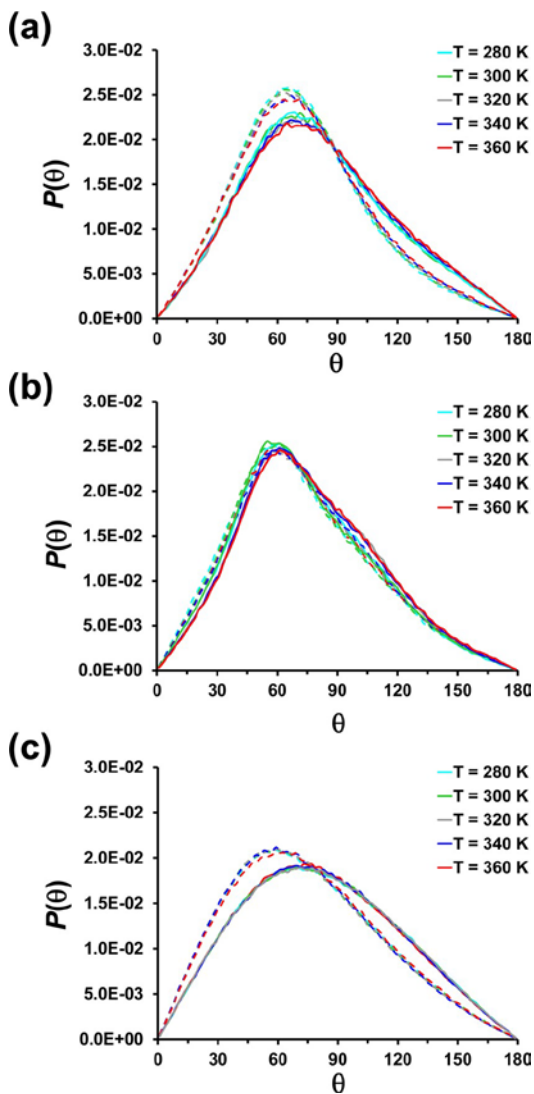


Figure 5.22. Probability distribution functions for observing (a) OT–OW and (b) S–OW vectors at an angle θ with the water dipole in the first solvation shell of hydronium and sulfonate groups (i.e., $r < 3.5 \text{ \AA}$ and $r < 5.0 \text{ \AA}$, respectively) at different temperatures. (c) Probability distribution functions for observing the S–OT vector at an angle θ with the hydronium cations located at a $S \cdots OT$ distance lower than 4.8 \AA at different temperatures. Solid and dashed lines correspond to simulations in the absence and presence of an external electric field, respectively.

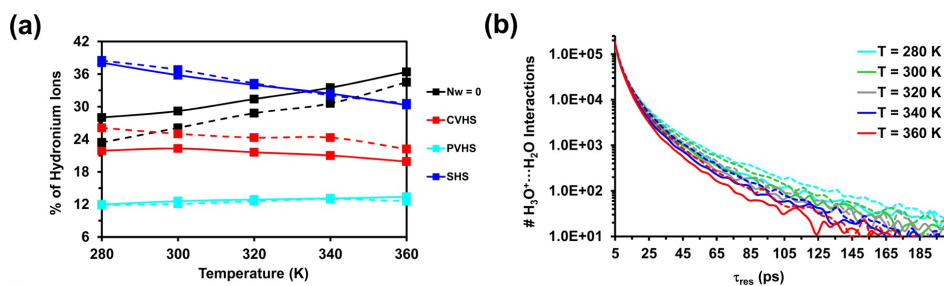


Figure 5.23. (a) Variation of the percentage of hydronium ions showing each of the four situations identified in terms of the first solvation shell (see text) against the electric field: $N_w = 0$ (hydroniums without hydration shell); CVHS (completely variable hydration shell); PVHS (partially variable hydration shell); and SHS (static hydration shell). (b) Amount of hydronium \cdots water interactions (*i.e.*, considering water molecules included in the first hydration shell) against the residence time (τ_{res}) at different temperatures. Solid and dashed lines correspond to simulations in the absence and presence of an external electric field, respectively.

(CVHS), in which N_w changes with time and one or more of the water molecules contained in the first hydration shell are exchanged. Figure 5.23a and Figure 5.24a indicate that the amount of hydronium and sulfonate ions in this situation is practically independent of the temperature, even though the population obtained in the presence of the external electric field ($\sim 24\%$ and $\sim 52\%$, respectively) is slightly larger than in its absence ($\sim 21\%$ and $\sim 50\%$, respectively).

The second situation involves hydronium and sulfonate ions with partially variable hydration shells (PVHS), in which N_w remains constant with time but one or more of the water molecules contained in the first hydration shell are exchanged. This is a relatively infrequent situation, the amount of hydronium and sulfonate ions with PVHS being practically independent of both the temperature and the electric field ($\sim 12\%$ and $\sim 19\%$

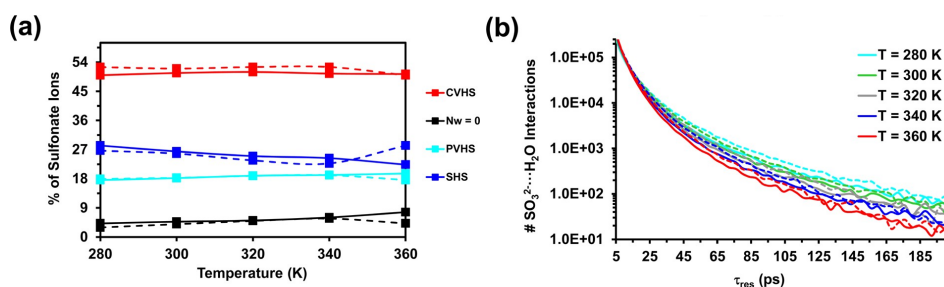


Figure 5.24. (a) Variation of the percentage of sulfonate ions showing each of the four situations identified in terms of the first solvation shell (see text) against the electric field: $N_w = 0$ (sulfonate without hydration shell); CVHS (completely variable hydration shell); PVHS (partially variable hydration shell); and SHS (static hydration shell). (b) Amount of sulfonate \cdots water interactions (*i.e.*, considering water molecules included in the first hydration shell) against the residence time (τ_{res}) at different temperatures. Solid and dashed lines correspond to simulations in the absence and presence of external electric field, respectively.

in Figure 5.23a and Figure 5.24a, respectively). The third situation corresponds to ions with static hydration shells (SHS), in which N_w remains constant with time and no water molecules contained in the first hydration shell are exchanged. This is the most populated situation for hydronium ions, and although the amount of hydronium ions with SHS depends on the temperature (*i.e.*, it decreases from 38% to 30% when the temperature increases from 280 to 360 K), it is practically unaltered by the electric field (Figure 5.23a). A similar but less pronounced behavior is observed for the sulfonate groups, the percentage of ions with SHS decreasing from 28% to 22% when the temperature increases from 280 to 360 K. Finally, the last situation corresponds to dehydrated ions ($N_w = 0$). As was discussed above, the percentage with hydronium ions with $N_w = 0$ increases with temperature and, in addition, depends on the electric field (*i.e.*, its population is higher for $E_z = 0.0$ than for $E_z = 0.7 \text{ Vnm}^{-1}$, independently of the temperature). These dependences are significantly smaller for the sulfonate group, in which the percentage of ions with $N_w = 0$ ranges from 4% to 8%.

Figure 5.23b and Figure 5.24b represent the number of hydronium···water and sulfonate···water interactions, respectively, involving solvent molecules located at CVHS, PVHS, and SHS against τ_{res} . As can be seen, the lifetime of these interactions is practically independent of both the temperature and the electric field for $\tau_{res} < 25 \text{ ps}$. After the latter value, the influence of temperature and the electric field increases with τ_{res} . Thus, results clearly indicate that the amount of hydronium···water and sulfonate···water interactions with $\tau_{res} > 25 \text{ ps}$ increases with decreasing temperature. Furthermore, for a given temperature the number of such long-term interactions is higher in the presence of the external electric field than in its absence. Also, for a given τ_{res} and temperature, sulfonate···water interactions are more abundant than the number of hydronium···water interactions, which is consistent with the highest strength of the former ones.

The relationship between hydronium and sulfonate ions was investigated using the same strategy. More specifically, the sulfonate groups were categorized according to the number of hydronium ions (N_h) within a cutoff distance of 4.0 \AA (Figure 5.13). The variation of N_h against the temperature, which is displayed in Figure 5.21c, indicates that the sulfonate groups tend to be surrounded by three hydronium ions in the absence and presence of an electric field (*i.e.*, populations for $N_h = 3$ are higher than 40%, independently of the temperature). After this, the more populated situations correspond to $N_h = 2$ and 4 with populations of around 25% and 20%, respectively, the number of sulfonate groups without surrounding hydronium ions being practically negligible (<1%). The orientation of hydronium molecules located in the immediate vicinity (cutoff distance: $r < 4 \text{ \AA}$) of sulfonate ions has been determined through the probability $P(\theta)$ of observing a hydronium dipole at an angle θ to the S–OT vector. Although the most favorable orientation of the hydronium dipole in the immediate vicinity remains unaltered

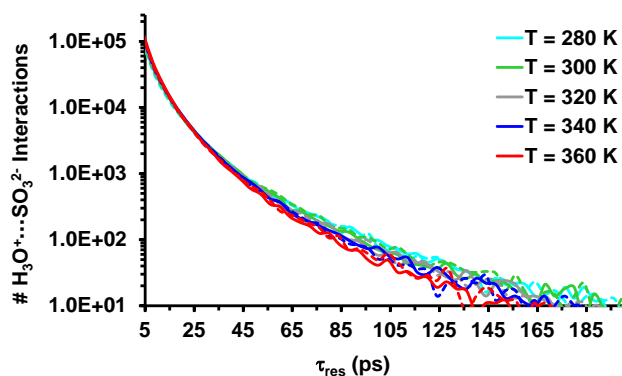


Figure 5.25. Amount of hydronium \cdots sulfonate interactions (*i.e.* considering ions within a cut-off distance of 4.0 Å) against the residence time (τ_{res}) at different temperatures. Solid and dashed lines correspond to simulations in absence and presence of external electric field, respectively.

by the temperature, it is drastically affected by the external electric field shifting from $\sim 90^\circ$ to $\sim 60^\circ$ (Figure 5.22c). Furthermore, the isotropic distribution of hydronium orientations transforms into anisotropic upon the application of the electric field, as is evidenced by the change from a symmetric $P(\theta)$ profile centered at 90° to an asymmetric one centered at lower θ values. Although this behavior is fully consistent with the transport of hydronium ions in the direction of the electric field, it should be noted the τ_{res} for hydronium \cdots sulfonate has practically no temperature and electric field dependence (Figure 5.25).

5.2.4. CONCLUSIONS

Temperature produces random structural distortions localized at the sulfonate groups of the membrane, which become anisotropic upon the application of the external electric field. These changes are accompanied by a variation of the density, which decreases with increasing temperature. Moreover, the temperature-induced rearrangement of the sulfonate groups results in an increment of the porosity, which is slightly higher in the absence of an electric field. On the other hand, the effect of the temperature in the velocity of water molecules and, especially, hydronium ions is relatively small, in comparison with that of the external electric field. Thus, the latter produces an enhancement in flux of water molecules and, especially, hydronium ions that is considerably higher than that induced by increasing the temperature. Consequently, the electro-osmotic drag coefficient and protonic conductivity have very weak temperature dependence. The diffusion coefficients D_h , $D_{h,\parallel}$ and $D_{h,\perp}$ increase with the temperature and are consistent with an isotropic motion of the hydronium ions.

The first hydration shell of hydronium ions tends to involve 1–2 water molecules, independently of the temperature, this number increasing to 2–3 for the sulfonate ions of the membrane. The temperature dependence of the orientation of the water dipole in the first solvation shell is null, even though such a dipole exhibits a reorientation upon the application of the external electric field. However, the residence time of water molecules inside the hydration shell decreases with the temperature, this effect being only appreciable for $\tau_{res} > 25$ ps. Results indicate that sulfonate···water interactions are stronger than hydronium···water ones. This should be attributed to the fact that sulfonate anions tend to be surrounded by three hydronium ions, allowing the formation of a dense attractive network of interactions involving sulfonate anions, hydroniums, and water molecules.

The overall results allows us to establish an important link between the effect of the temperature and both the structure of the P(S-DVB) membrane and the dynamics of water molecules and hydronium ions.

REFERENCES

- [1] V. Neburchilov, J. Martin, H.J. Wang, J.J. Zhang; *A review of polymer electrolyte membranes for direct methanol fuel cells*; J Power Sources **169**, 221 (2007).
- [2] P. Sivaraman, S.K. Rath, V.R. Hande, A.P. Thakur, M. Patri, A.B. Samui; *All-solid-supercapacitor based on polyaniline and sulfonated polymers*; Synthetic Met **156**, 1057 (2006).
- [3] E.L. Dewi, K. Oyaizu, H. Nishide, E. Tsuchida; *Cationic polysulfonium membrane as separator in zinc-air cell*; J Power Sources **115**, 149 (2003).
- [4] K. Shimano, K. Goto, K. Obata, S. Nakata, G. Sakai, N. Yamazoe; *Development of FET-type CO₂ sensor operative at room temperature*; Sensor Actuat B-Chem **102**, 14 (2004).
- [5] J. Balster, D.F. Stamatialis, M. Wessling; *Electro-catalytic membrane reactors and the development of bipolar membrane technology*; Chem Eng Process **43**, 1115 (2004).
- [6] K. Juttner, U. Galla, H. Schmieder; *Electrochemical approaches to environmental problems in the process industry*; Electrochim Acta **45**, 2575 (2000).
- [7] M.Y. Kariduraganavar, R.K. Nagarale, A.A. Kittur, S.S. Kulkarni; *Ion-exchange membranes: preparative methods for electrodialysis and fuel cell applications*; Desalination **197**, 225 (2006).
- [8] S.A. Kalogirou; *Seawater desalination using renewable energy sources*; Prog Energ Combust **31**, 242 (2005).
- [9] T.W. Xu; *Electrodialysis processes with bipolar membranes (EDBM) in environmental protection - a review*; Resour Conserv Recy **37**, 1 (2002).
- [10] F. Faverjon, G. Durand, M. Rakib; *Regeneration of hydrochloric acid and sodium hydroxide from purified sodium chloride by membrane electrolysis using a hydrogen diffusion anode-membrane assembly*; J Membrane Sci **284**, 323 (2006).
- [11] C.H. Huang, T.W. Xu, Y.P. Zhang, Y.H. Xue, G.W. Chen; *Application of electrodialysis to the production of organic acids: State-of-the-art and recent developments*; J Membrane Sci **288**, 1 (2007).
- [12] V.E. Santarosa, F. Peretti, V. Caldart, J. Zoppas, M. Zeni; *Study of ion-selective membranes from electrodialysis removal of industrial effluent metals II: Zn and Ni*; Desalination **149**, 389 (2002).
- [13] M.I. Ahmed, H.T. Chang, J.R. Selman, T.M. Holsen; *Electrochemical chromic acid regeneration process: fitting of membrane transport properties*; J Membrane Sci **197**, 63 (2002).
- [14] Pretoria (South Africa). National Chemical Research Laboratory. Process Development Division., J.R. Wilson; *Demineralization by electrodialysis*, Butterworths Scientific Publications, London,, 1960.
- [15] N. Lakshminarayanaiah; *Transport phenomena in membranes*, Academic Press, New York,, 1969.
- [16] J. Hladik; *Physics of electrolytes*, Academic press, London; New York, 1972.
- [17] M. Ersoz; *The electrochemical properties of polysulfone ion-exchange membranes*; J Colloid Interf Sci **243**, 420 (2001).
- [18] V.K. Shahi; *Highly charged proton-exchange membrane: Sulfonated poly(ether sulfone)-silica polyelectrolyte composite membranes for fuel cells*; Solid State Ionics **177**, 3395 (2007).
- [19] L. Jones, P.N. Pintauro, H. Tang; *Colon exclusion properties of polyphosphazene ion-exchange membranes*; J Membrane Sci **162**, 135 (1999).
- [20] O. Okay; *Macroporous copolymer networks*; Prog Polym Sci **25**, 711 (2000).

- [21] F.M.B. Coutinho, S.M. Rezende, B.G. Soares; *Characterization of sulfonated poly(styrene-divinylbenzene) and poly(divinylbenzene) and its application as catalysts in esterification reaction*; J Appl Polym Sci **102**, 3616 (2006).
- [22] L.X. Tuan, B. Hanae, M.V. Lara, B.H. Claudine; *Cation exchange membranes based on grafted PS/DVB-ETFE films: An investigation of their electrochemical characteristics in sulfuric acid*; Electrochim Acta **54**, 5992 (2009).
- [23] J. Tiihonen, M. Laatikainen, I. Markkanen, E. Paatero; *Sorption of neutral components in ion-exchange resins. 1. Effect of cross-link density and counterion on selective sorption of water-ethanol mixtures in sulfonated PS-DVB resins*; Ind Eng Chem Res **38**, 4832 (1999).
- [24] S.S. Jang, V. Molinero, T. Cagin, W.A. Goddard; *Nanophase-segregation and transport in Nafion 117 from molecular dynamics simulations: Effect of monomeric sequence*; J Phys Chem B **108**, 3149 (2004).
- [25] P.Y. Chen, C.W. Hong; *Nanoscale transport dynamics inside a hydrated nafion membrane with electric field effects*; Fuel Cells **10**, 17 (2010).
- [26] E. Allahyarov, P.L. Taylor, H. Lowen; *Simulation study of field-induced morphological changes in a proton-conducting ionomer*; Phys Rev E **81** (2010).
- [27] C.L. Shao, L.M. Yan, X.B. Ji, S.H. Zhu; *Intermolecular momentum transfer in poly(perfluorosulfonic acid) membrane hydrated by aqueous solution of methanol: A molecular dynamics simulation study*; J Chem Phys **131** (2009).
- [28] L.M. Yan, X.B. Ji, W.C. Lu; *Molecular dynamics simulations of electroosmosis in perfluorosulfonic acid polymer*; J Phys Chem B **112**, 5602 (2008).
- [29] E. Allahyarov, P.L. Taylor; *Simulation study of the correlation between structure and conductivity in stretched nafion*; J Phys Chem B **113**, 610 (2009).
- [30] J. Pozuelo, E. Riande, E. Saiz, V. Compan; *Molecular dynamics simulations of proton conduction in sulfonated poly(phenyl sulfone)s*; Macromolecules **39**, 8862 (2006).
- [31] O. Bertran, D. Curco, J. Torras, C.A. Ferreira, C. Aleman; *Field-induced transport in sulfonated poly(styrene-co-divinylbenzene) membranes*; Macromolecules **43**, 10521 (2010).
- [32] W.D. Cornell, P. Cieplak, C.I. Bayly, I.R. Gould, K.M. Merz, D.M. Ferguson, D.C. Spellmeyer, T. Fox, J.W. Caldwell, P.A. Kollman; *A 2nd generation force-field for the simulation of proteins, nucleic-acids, and organic-molecules*; J Am Chem Soc **117**, 5179 (1995).
- [33] J.M. Wang, R.M. Wolf, J.W. Caldwell, P.A. Kollman, D.A. Case; *Development and testing of a general amber force field*; J Comput Chem **25**, 1157 (2004).
- [34] C.D. Wick, M.G. Martin, J.I. Siepmann; *Transferable potentials for phase equilibria. 4. United-atom description of linear and branched alkenes and alkylbenzenes*; J Phys Chem B **104**, 8008 (2000).
- [35] W.L. Jorgensen, J. Chandrasekhar, J.D. Madura, R.W. Impey, M.L. Klein; *Comparison of simple potential functions for simulating liquid water*; J Chem Phys **79**, 926 (1983).
- [36] M. Baaden, M. Burgard, G. Wipff; *TBP at the water-oil interface: The effect of TBP concentration and water acidity investigated by molecular dynamics simulations*; J Phys Chem B **105**, 11131 (2001).
- [37] W. Smith, T.R. Forester, I. Todorov, Computer Code DL_POLY 2.19, CSE Department, STFC Daresbury Laboratory, England 2008.
- [38] T. Darden, D. York, L. Pedersen; *Particle mesh ewald - an $N \cdot \log(N)$ method for ewald sums in large systems*; J Chem Phys **98**, 10089 (1993).
- [39] W.G. Hoover; *Canonical dynamics - equilibrium phase-space distributions*; Phys Rev A **31**, 1695 (1985).
- [40] A. Vegiri, S.V. Schevkunov; *A molecular dynamics study of structural transitions in small water clusters in the presence of an external electric field*; J Chem Phys **115**, 4175 (2001).
-

- [41] F. Mullerplathe, S.C. Rogers, W.F. Vangunsteren; *Gas sorption and transport in polyisobutylene - equilibrium and nonequilibrium molecular-dynamics simulations*; J Chem Phys **98**, 9895 (1993).
- [42] T. Ohkubo, K. Kidena, N. Takimoto, A. Ohira; *Molecular dynamics simulations of nafion and sulfonated poly ether sulfone membranes II. Dynamic properties of water and hydronium*; J Mol Model **18**, 533 (2012).
- [43] S. Nose; *A unified formulation of the constant temperature molecular-dynamics methods*; J Chem Phys **81**, 511 (1984).
- [44] H.J.C. Berendsen, J.P.M. Postma, W.F. Vangunsteren, A. Dinola, J.R. Haak; *Molecular-dynamics with coupling to an external bath*; J Chem Phys **81**, 3684 (1984).
- [45] J.F. Ding, C. Chuy, S. Holdcroft; *Enhanced conductivity in morphologically controlled proton exchange membranes: Synthesis of macromonomers by SFRP and their incorporation into graft polymers*; Macromolecules **35**, 1348 (2002).
- [46] J.P. Shin, B.J. Chang, J.H. Kim, S.B. Lee, D.H. Suh; *Sulfonated polystyrene/PTFE composite membranes*; J Membrane Sci **251**, 247 (2005).
- [47] Y. Woo, S.Y. Oh, Y.S. Kang, B. Jung; *Synthesis and characterization of sulfonated polyimide membranes for direct methanol fuel cell*; J Membrane Sci **220**, 31 (2003).
- [48] J.M. Bae, I. Honma, M. Murata, T. Yamamoto, M. Rikukawa, N. Ogata; *Properties of selected sulfonated polymers as proton-conducting electrolytes for polymer electrolyte fuel cells*; Solid State Ionics **147**, 189 (2002).
- [49] T. Ohkubo, K. Kidena, N. Takimoto, A. Ohira; *Molecular dynamics simulations of Nafion and sulfonated polyether sulfone membranes. I. Effect of hydration on aqueous phase structure*; J Mol Model **17**, 739 (2011).
- [50] E. Hawlicka, D. Swiatla-Wojcik; *Dynamic properties of the NaCl-methanol-water systems - MD simulation studies*; Phys Chem Chem Phys **2**, 3175 (2000).
- [51] Y. Ishihara, S. Okouchi, H. Uedaira; *Dynamics of hydration of alcohols and diols in aqueous solutions*; J Chem Soc Faraday T **93**, 3337 (1997).
- [52] S. Koneshan, J.C. Rasaiah, R.M. Lynden-Bell, S.H. Lee; *Solvent structure, dynamics, and ion mobility in aqueous solutions at 25 degrees C*; J Phys Chem B **102**, 4193 (1998).
- [53] R.W. Impey, P.A. Madden, I.R. McDonald; *Hydration and mobility of ions in solution*; J Phys Chem-Us **87**, 5071 (1983).
- [54] S. Obst, H. Bradaczek; *Molecular dynamics study of the structure and dynamics of the hydration shell of alkaline and alkaline-earth metal cations*; J Phys Chem-Us **100**, 15677 (1996).
- [55] M.A. Shannon, P.W. Bohn, M. Elimelech, J.G. Georgiadis, B.J. Marinas, A.M. Mayes; *Science and technology for water purification in the coming decades*; Nature **452**, 301 (2008).
- [56] B.D. Freeman, I. Pinnau; *Polymer membranes for gas and vapor separation*, American Chemical Society, 1999.
- [57] V. Compan, D. Zanuy, A. Andrio, M. Morillo, C. Aleman, S. Munoz-Guerra; *Permeation properties of the stereoregular nylon-3 analogue, poly(alpha-bexyl beta-L-aspartate)*; Macromolecules **35**, 4521 (2002).
- [58] P.D. Chapman, T. Oliveira, A.G. Livingston, K. Li; *Membranes for the dehydration of solvents by pervaporation*; J Membrane Sci **318**, 5 (2008).
- [59] M.A. Hickner, H. Ghassemi, Y.S. Kim, B.R. Einsla, J.E. McGrath; *Alternative polymer systems for proton exchange membranes (PEMs)*; Chem Rev **104**, 4587 (2004).
- [60] J.M. Tarascon, M. Armand; *Issues and challenges facing rechargeable lithium batteries*; Nature **414**, 359 (2001).
- [61] D. Aradilla, F. Estrany, F. Casellas, J.I. Iribarren, C. Aleman; *All-polythiophene rechargeable batteries*; Org Electron **15**, 40 (2014).

- [62] C.G.J. Koopal, B. Deruiter, R.J.M. Nolte; *Amperometric biosensor based on direct communication between glucose-oxidase and a conducting polymer inside the pores of a filtration membrane*; J Chem Soc Chem Comm, 1691 (1991).
- [63] B. Adhikari, S. Majumdar; *Polymers in sensor applications*; Progr Polym Sci **29**, 699 (2004).
- [64] M.M. Perez-Madrigal, E. Armelin, L.J. del Valle, F. Estrany, C. Aleman; *Bioactive and electroactive response of flexible polythiophene: polyester nanomembranes for tissue engineering*; Polym Chem **3**, 979 (2012).
- [65] M.M.P. Madrigal, M.I. Giannotti, G. Oncins, L. Franco, E. Armelin, J. Puiggali, F. Sanz, L.J. del Valle, C. Aleman; *Bioactive nanomembranes of semiconductor polythiophene and thermoplastic polyurethane: thermal, nanostructural and nanomechanical properties*; Polym Chem **4**, 568 (2013).
- [66] D. Shi, Z. Ke, J.H. Yang, Y. Gao, J. Wu, J.H. Yin; *Rheology and morphology of reactively compatibilized PP/PA6 blends*; Macromolecules **35**, 8005 (2002).
- [67] Y.J. Li, H. Shimizu; *Morphological investigations on the nanostructured poly(vinylidene fluoride)/polyamide 11 blends by high-shear processing*; Eur Polym J **42**, 3202 (2006).
- [68] R. Scherer, A.M. Bernardes, M.M.C. Forte, J.Z. Ferreira, C.A. Ferreira; *Preparation and physical characterization of a sulfonated poly(styrene-co-divinylbenzene) and polyfyrrole composite membrane*; Mater Chem Phys **71**, 131 (2001).
- [69] F. Muller, C.A. Ferreira, L. Franco, J. Puiggali, C. Aleman, E. Armelin; *New sulfonated polystyrene and styrene-ethylene/butylene-styrene block copolymers for applications in electrodialysis*; J Phys Chem B **116**, 11767 (2012).
- [70] C.A. Ferreira, J. Casanovas, M.A.S. Rodrigues, F. Muller, E. Armelin, C. Aleman; *Transport of metallic ions through polyaniline-containing composite membranes*; J Chem Eng Data **55**, 4801 (2010).
- [71] E. Cordova-Mateo, O. Bertran, C.A. Ferreira, C. Aleman; *Transport of hydronium ions inside poly(styrene-co-divinyl benzene) cation exchange membranes*; J Membrane Sci **428**, 393 (2013).
- [72] F.M.B. Coutinho, S.M. Rezende, B.G. Soares; *Characterization of sulfonated poly(styrene-divinylbenzene) and poly(divinylbenzene) and its application as catalysts in esterification reaction*; J Appl Polym Sci **102**, 3616 (2006).
- [73] J. Tiihonen, M. Laatikainen, I. Markkanen, E. Paatero; *Sorption of neutral components in ion-exchange resins. 1. Effect of cross-link density and counterion on selective sorption of water-ethanol mixtures in sulfonated PS-DVB resins*; Ind Eng Chem Res **38**, 4832 (1999).
- [74] Q.F. Wang, D.J. Keffer, S.X. Deng, J. Mays; *Structure and proton transport in proton exchange membranes based on cross-linked sulfonated poly(1, 3-cyclohexadiene) with varying local acid environment*; Polymer **54**, 2299 (2013).
- [75] M.E. Selvan, Q.P. He, E.M. Calvo-Munoz, D.J. Keffer; *Molecular dynamic simulations of the effect on the hydration of nafion in the presence of a platinum nanoparticle*; J Phys Chem C **116**, 12890 (2012).
- [76] T. Srinophakun, S. Martkumchan; *Ionic conductivity in a chitosan membrane for a PEM fuel cell using molecular dynamics simulation*; Carbohydr Polym **88**, 194 (2012).
- [77] S. Mahajan, R.M. Cole, J.D. Speed, S.H. Pelfrey, A.E. Russell, P.N. Bartlett, S.M. Barnett, J.J. Baumberg; *Understanding the surface-enhanced raman spectroscopy "background"*; J Phys Chem C **114**, 7242 (2010).
- [78] J. Vanderlinde; *Classical electromagnetic theory*, Kluwer Academic Publishers., Dordrecht; London.
- [79] D. Curco, D. Zanuy, C. Aleman; *EVEBAT: A fast strategy for the examination of the empty space in polymer matrices*; J Comput Chem **24**, 1208 (2003).
-

- [80] S.J. Paddison, R. Paul, T.A. Zawodzinski; *Ion and water transport in a Nafion (R) membrane pore: A statistical mechanical model with molecular structure*; Elec Soc S **98**, 106 (1999).
- [81] S. Murad; *The role of external electric fields in enhancing ion mobility, drift velocity, and drift-diffusion rates in aqueous electrolyte solutions*; J Chem Phys **134** (2011).

CHAPTER 6
ATOMISTIC PROPERTIES OF DENDRONIZED POLYMERS

‘La ilusión no se come,’ dijo ella. ‘No se come, pero alimenta,’ replicó el coronel.

[“You can’t eat hope,” the woman said. “You can’t eat it, but it sustains you,” the colonel replied.]

Gabriel García Márquez, *El coronel no tiene quien le escriba*
(1961)

CHAPTER 6

ATOMISTIC PROPERTIES OF DENDRONIZED POLYMERS

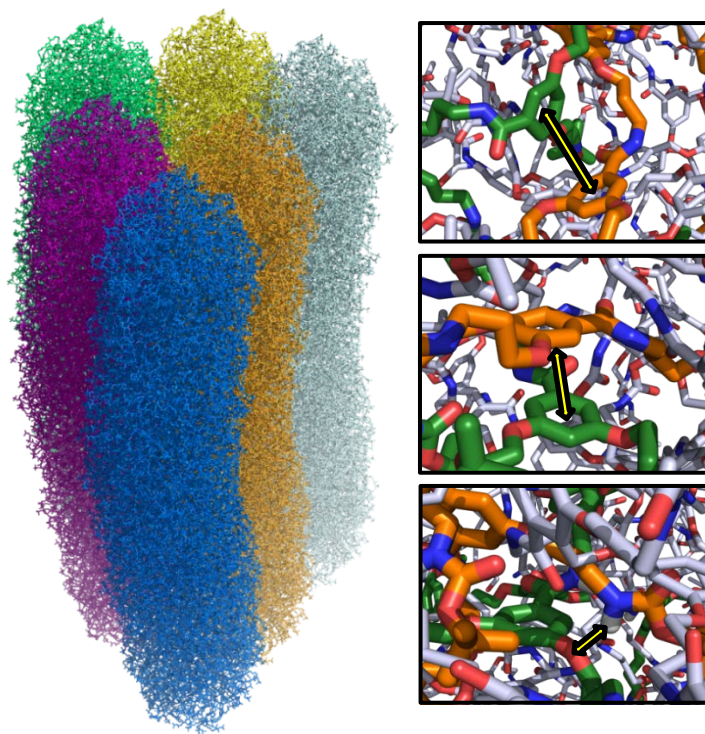
This Chapter is devoted to analyze the structural properties and molecular interactions occurring in dendronized polymers (DPs). For this purpose, simulations have been performed on a well-known and representative family of DPs, which consists of a polymethylmethacrylate backbone with tree-like branches bearing both amide and aromatic groups. Theoretical results presented in the first section have been derived from molecular dynamics simulations while the experimental studies that are included were conducted by Prof. Dimitris Vlassopoulos^{1,2} and Dr. Rossana Pasquino¹. The content of this first section was published in the journal *Soft Matter* under the title *Interactions in Dendronized Polymers: Intramolecular Dominates Intermolecular* (2014). Finally, all the work described in section 6.2 under the title *Internal Structure of Charged Dendronized Polymers* has been carried out through molecular dynamics simulations and has been recently submitted for publication.

6.1. INTERACTIONS IN DPs: INTRAMOLECULAR DOMINATES INTERMOLECULAR

In an attempt to relate atomistic information to the rheological response of a large dendritic object, inter- and intramolecular hydrogen bonds and π,π -interactions have been characterized in a dendronized polymer that consists of a polymethylmethacrylate backbone with tree-like branches of generation four (PG4) and contains both amide and aromatic groups. Extensive atomistic molecular dynamics simulations have been carried

¹ Foundation for Research and Technology (FORTH), Institute of Electronic Structure and Laser, 71110 Heraklion, Crete, Greece

² University of Crete, Department of Materials Science & Technology, 71003 Heraklion, Crete, Greece



out on (i) an isolated PG4 chain and (ii) ten dimers formed by two PG4 chains associated with different degrees of interpenetration. Results indicate that the amount of nitrogen atoms involved in hydrogen bonding is $\sim 11\%$ while $\sim 15\%$ of aromatic groups participate in π,π -interactions. Furthermore, in both cases intramolecular interactions clearly dominate over intermolecular ones, while exhibiting markedly different behaviors. Specifically, the amount of intramolecular hydrogen bonds increases when the interpenetration of the two chains decreases, whereas intramolecular π,π -interactions remain practically insensitive to the amount of interpenetration. In contrast, the strength of the corresponding two types of intermolecular interactions decreases with interpenetration. Although the influence of complexation on the density and cross-sectional radius is relatively small, interpenetration affects significantly the molecular length of the DP. These results support the idea of treating DPs as long colloidal molecules.

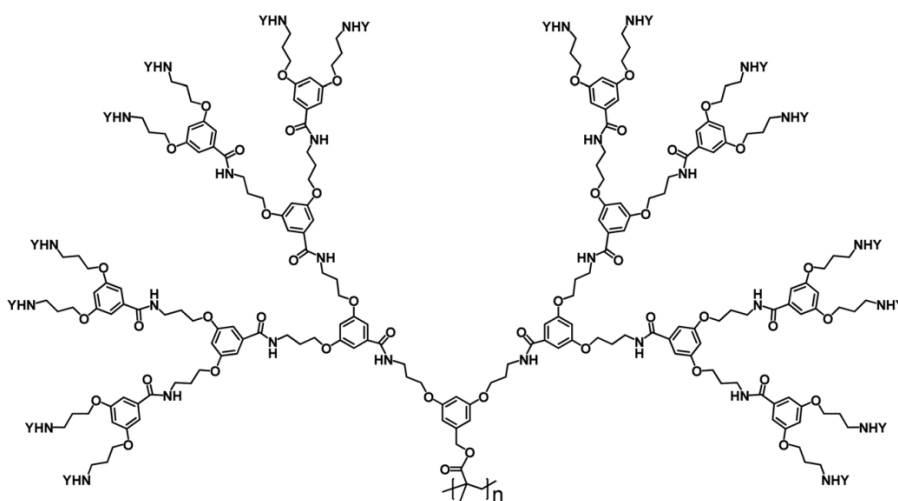
6.1.1. INTRODUCTION

Dendronized polymers (DPs) are linear polymers the repeat units of which are regularly branched tree-like fragments (dendrons). Different synthetic approaches have been developed to precisely control the chemical structure of this unique class of

macromolecules [1-3]. From the structural point of view, these advanced approaches have been used to obtain hierarchically organized macromolecules with tunable thickness and persistence length, which are controlled through the generation number, g [4,5]. Due to this particular architecture, DPs currently represent a class of single molecular nanomaterials with potential applications. Among the most promising applications of DPs are nanoscopic building blocks [6,7], functional materials [8,9], organic optoelectronic materials [10-12], self-assembling vectors for complexation with DNA [13,14], and biosensor systems [15].

The structure of a homologous series of neutral DPs composed of a poly(methacrylic acid) backbone, the repeat units of which are regularly branched dendrons of generation g containing both amide and aromatic groups (Scheme 6.1), was investigated at the nanometric level by atomic force microscopy (AFM) and transmission electron microscopy (TEM) for $g = 1 - 5$ (PG1-PG5) [4,16,17] and at the atomistic level using molecular dynamics (MD) simulations for $g = 1 - 7$ (PG1-PG7) [18,19]. Regarding AFM and TEM studies, the width and height of DPs adsorbed onto attractive mica surfaces were found to exhibit the scaling behavior of a cylinder supporting the visual impression that DPs adsorb as weakly deformed cylinders [4,5]. Atomistic MD simulations indicated that the backbone of DPs with $g \leq 4$ exhibits an elongated shape while DPs with $g = 5$ and 6 exhibit a helical conformation [18,19]. The existence of defect-free DPs with $g \geq 7$ was predicted to be precluded due to stiffness and related strain on the backbone [18].

The physical properties of DPs are severely affected by their molecular rigidity, which



PG4: Y= Boc

Scheme 6.1

increases with g [16-20]. This looks like a point crucial for understanding the dynamics associated with physical properties such as the rheological ones. Dynamics of cylindrical (or spherical) macromolecules with unusual dendritic architecture should be controlled by fluctuations of the outer branching units (*i.e.* dendrons located at the external layers) and the formation of inter- and/or intramolecular interaction patterns. Although the number of systematic rheological investigations on DPs has been very scarce yet [21-23], they do indeed confirm the role of dendritic branches and interactions. Moreover, a generation-dependent study on the viscoelastic properties of homologous PG1–PG4 was recently reported [23]. Results evidenced an unusual viscoelastic response, which was strongly dependent on the generation, ranging from liquid-like (PG1) to solid-like behavior (PG4). This was attributed to their elongated conformation and the combination of topological constraints at the whole macromolecular scale and the competition of intra- and intermolecular interactions [23]. More specifically, it was suggested that DPs can be viewed as soft elongated colloidal objects with reduced ability to interpenetrate, and reduced probability of intermolecular interactions. This scenario was supported and further elucidated in a recent structural investigation in solution [24]. In particular, small angle X-ray scattering measurements in bulk PG4 revealed the presence of Bragg peaks typical of hexagonally dense packed cylindrical objects, reflecting the colloidal nature of this polymer and the related topological arrangements in space. Hence, the dense dendritic shell around the backbone converted the conventional polymers into colloidal filament-like molecules. Based on the molecular details (Scheme 6.1 displays a representative member of this homologous series), these DPs may exhibit in principle two types of specific interactions: hydrogen bonding due to the presence of the NH bonds in the amide groups of the branches and association of the aromatic rings via π,π -stacking.

Atomistic modeling of DPs is very challenging not only due to their intrinsic conformational complexity reflecting crowding and excluded volume interactions but also due to the significant amount of computational resources needed to describe systems with such huge dimensions. Consequently, atomistic modeling has been usually limited to systems with a single molecule, chemical details and physical properties being examined at the molecular level only [18,19,25-30]. Two interacting DPs had been studied in ref. [26] to motivate the Janus chain model that allows investigation of the phase behavior and self-amplifying mechanism for the formation of helically intertwined DP superstructures. In this work we present a detailed atomistic MD study that has allowed examination of the formation and stability of intermolecular interactions in DPs, as well as analysis of their importance and influence on structural properties with respect to intramolecular interactions. Calculations have been carried out on PG4 (Scheme 6.1) interpenetrated dimers, in which DP chains are interspersed at some locations, and results have been used to establish a relationship between the existing interactions and the viscoelastic properties previously reported [23].

6.1.2. METHODS

6.1.2.1. MOLECULAR MODELS

The conformation reported in ref. [18] for a PG4 polymer chain with $N = 150$ repeat units was used as a starting point for this study. This is a homogeneous and regular structure with an elongated or sausage-like shape [24], as is displayed in Figure 6.1, that has a length of about 316 Å and a thickness of approximately 72 Å. Dimers of PG4 were constructed considering two different configurations, five cases being considered for each one. In the first configuration two identical PG4 chains were arranged both parallel to the x -axis at a distance D , where D corresponds to the separation between the centers of mass of the backbones of the two chains. Thus, the second chain was generated by applying a translation of D (Å) along the y -axis to the first one (Figure 6.2a), the values considered for D being 40, 50, 60, 65 and 70 Å. The five complexes resulting for such a configuration have been denoted T- D , where the T refers to translation and the D corres-

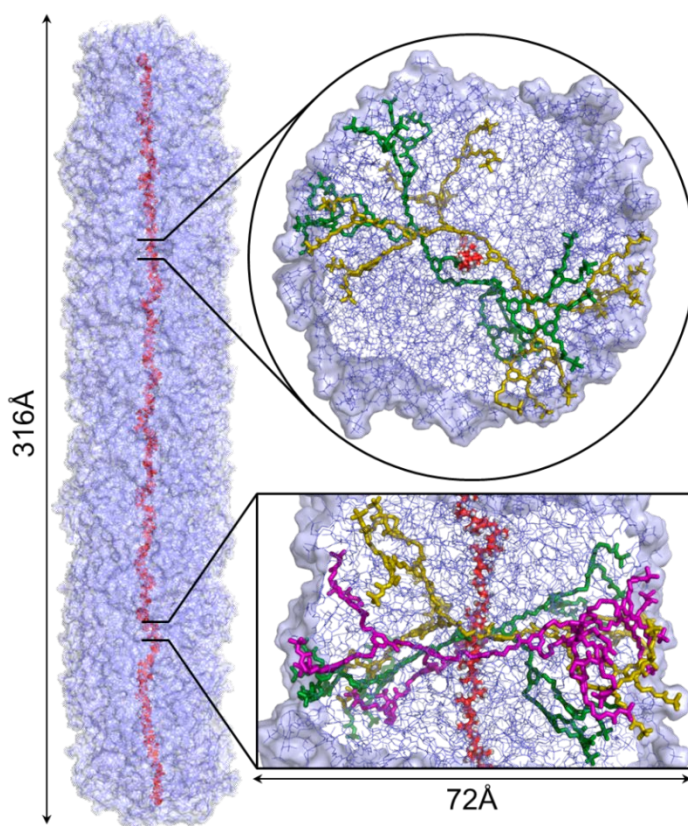


Figure 6.1. Atomistic conformation obtained in ref. 18 for PG4. Detailed views in the section (top) and in the molecular axis (bottom) are displayed at the right.

ponds to each initial interchain distance. The second configuration was constructed by rotating a copy of the first PG4 chain with respect to the y -axis by an angle of $\Delta\theta = 45^\circ$ and then applying a translation of D (Å) along the y -axis (Figure 6.2b), where D adopts the same values as above. The resulting dimers have been denoted RT- D where RT refers to rotation + translation and the meaning of D is the same as that for T- D complexes. It should be noted that RT- D dimers have been considered in this work to examine the ability of PG4 to allow interpenetration of the chains in a well-localized region. Thus, local interpenetration in RT- D (*i.e.* DP chains interspersed in the central region, as shown in Figure 6.2b) may be preferred for complete interpenetration in T- D dimers (*i.e.* DP chains interspersed along the molecular axis, as shown in Figure 6.2a) because of the molecular rigidity induced by the extremely complex chemical architecture of the DP. On the other hand, it should be mentioned that in a realistic system the degree of interpenetration is typically determined by osmotic effects (*i.e.* interactions and concentration). Accordingly, consideration of different D values for T- D and RT- D

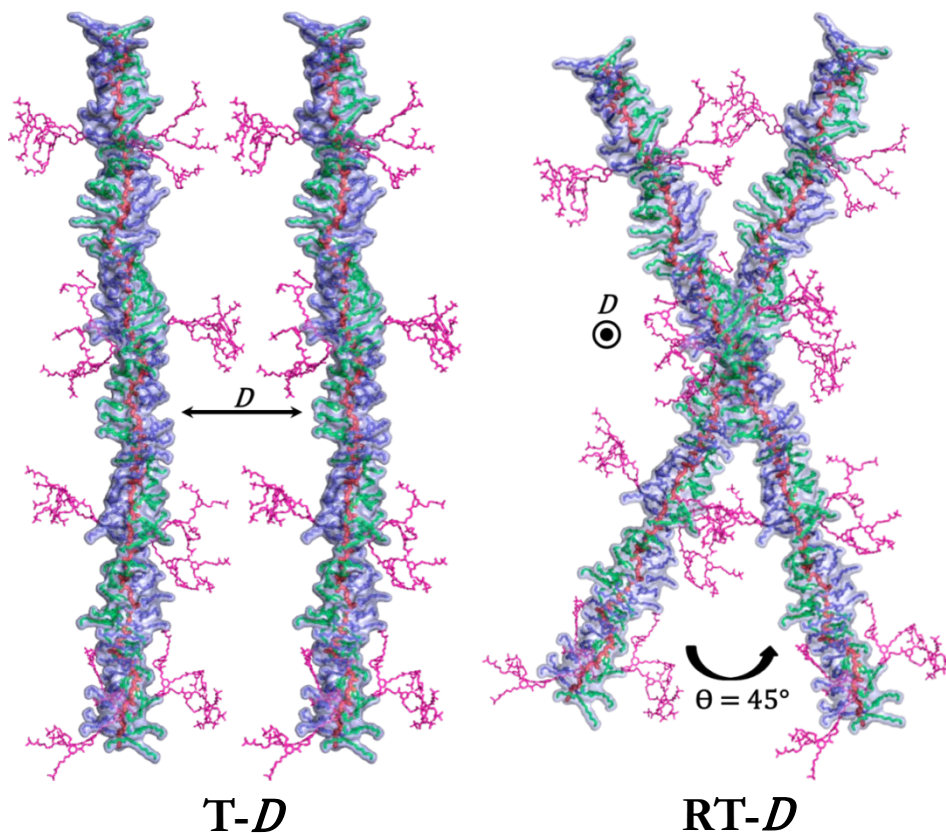


Figure 6.2. Scheme representing the relative positions of the two PG4 chains in (a) T- D and (b) RT- D systems. In order to clarify the representation, only a few branched dendrons of each chain are explicitly depicted.

configurations is also expected to provide information about the influence of such effects on the molecular structure.

Each of the ten dimers constructed for this study (*i.e.* five T-*D* and five RT-*D*) involved a total of 237 904 explicit atoms. Considering the huge dimensions of these dimers, all the simulations were carried out in a completely desolvated environment. Thus, reliable MD simulations with explicit solvent molecules are computationally prohibited because these eventually involve systems with several million explicit particles. Generally speaking, solvent-free simulations can be considered as “poor solvent” situations and, therefore, no swelling effect (“good solvent”) is expected to occur.

6.1.2.2. COMPUTATIONAL DETAILS

Energy minimizations and MD simulations of T-*D* and RT-*D* systems were performed with the NAMD program [31]. The energy was calculated using the AMBER force-field [32]. All the bonding and van der Waals parameters required for PG4 chains were taken from the Generalized AMBER force-field (GAFF) [33] while atomic charges were developed in our previous study [18] using the Restrained ElectroStatic Potential (RESP) strategy [34].

Before starting the production MD trajectories of the T-*D* and RT-*D* series, the geometry of each system was optimized by minimizing the potential energy. This was necessary to relax the tensions produced by overlaps between atoms belonging to different chains. Geometry optimizations were done by applying the conjugate gradient method in 8000 steps. The following rules were imposed during such geometry optimization steps: (i) the distance *D* was kept fixed at the original value to avoid both the separation of the two molecules and undesirable molecular deformations; (ii) the backbone atoms were constrained at their initial relative positions; (iii) the relative positions of the rest of the atoms were allowed to change without any restriction. Then, systems were heated and equilibrated by different consecutive MD runs. Each system was heated from 0 to 298 K using a rate of 3 K for each 1 ps, the temperature being kept at 298 K for 100 additional picoseconds. All the constraints imposed in the minimization were maintained during the heating and equilibration. Upon completion, all the constraints were removed and all atoms of each system were submitted to 5 ns of re-equilibration. Finally, production trajectories, which were 5 ns long, were performed and coordinates were saved every 2.5 ps (2000 snapshots for each system) for subsequent analyses.

Atom pair distance cut-offs were applied at 14.0 Å to compute the van der Waals and electrostatic interactions. The temperature was controlled by the weak coupling method, the Berendsen thermostat [35], the relaxation time used for the coupling being 1 ps. Bond lengths involving hydrogen atoms were constrained using the SHAKE algorithm [36] with a numerical integration step of 1 fs.

6.1.3. RESULTS AND DISCUSSION

6.1.3.1. TEMPORAL EVOLUTION AND STABILITY OF THE SIMULATED COMPLEXES

Figure 6.3 represents the temporal evolution of the interchain distance along the re-equilibration (5 ns) and production (5 ns) trajectories for T- D and RT- D systems, while Table 6.1 lists the average values, $\langle D \rangle$, derived from the production trajectory. As it can be seen, the temporal behavior of D is comparable for the two series of simulations, stabilizing in the first stages of the re-equilibration trajectory for T- D and after 2.5-3.8 ns for RT- D . Accordingly, elimination of unfavorable interactions is easier for the T- D configuration than for the RT- D one. Complexes with initial distances of 40 and 50 Å undergo an expansion during re-equilibration with ΔD values ranging from ~ 4 to ~ 8 Å, whereas complexes with initial distances of 65 and 70 Å experience a contraction of about 3-7 Å. In contrast, the interchain distance of T-60 and RT-60 remains very close to the initial value, $\langle D \rangle$ being 59.97 ± 0.12 and 59.43 ± 0.52 Å, respectively. Although D remains stable in all cases during the production runs, the fluctuations of D are higher for the RT- D complexes than for the T- D ones. This must be attributed to the fact that the dynamics of PG4 chains is more restricted in T- D than in RT- D because the effective contact surface is significantly higher in the former than in the latter. On the other hand, analysis of the temporal evolution of $\Delta\theta$ for RT- D dimers reveals very small changes (*i.e.* 1° - 3°) with respect to the initial value (45°). This is reported in Table 6.1, which includes the average $\Delta\theta$ values ($\langle \Delta\theta \rangle$).

Inspection of Figure 6.4, which represents the variation of the $\langle D \rangle$ values against the average total energies ($\langle E \rangle$), indicates that for each D the RT- D system is favored with respect to the T- D . As the contact surface between polymer chains, which is proportional to the degree of interspersion of one DP with respect to the other in the dimer, and,

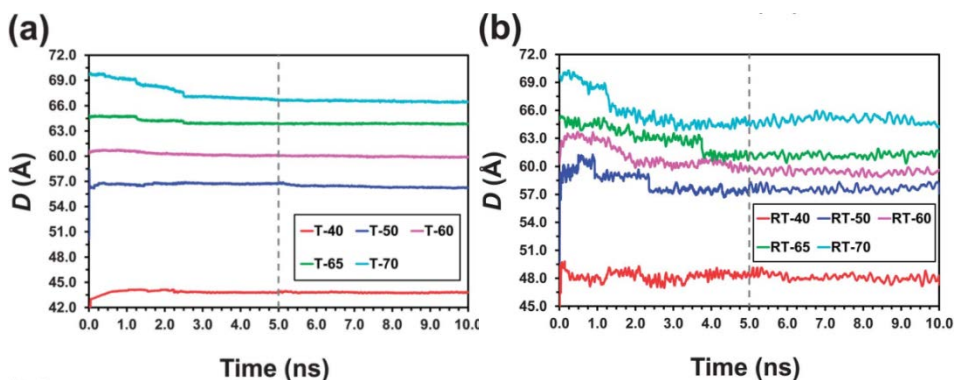


Figure 6.3. Temporal evolution of the interchain distance D for (a) T- D and (b) RT- D systems during the re-equilibration and production runs (before and after the grey dashed line, respectively).

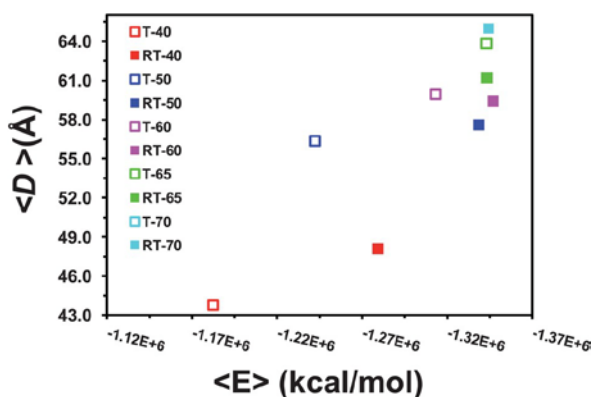


Figure 6.4. Average interchain distance ($\langle D \rangle$) against the average total energy ($\langle E \rangle$) for T- D and RT- D systems.

therefore, the strength of intermolecular interactions is higher for T- D than for RT- D , this result suggests that the contribution of intramolecular interactions to the stability of the complexes is more decisive than that of the intermolecular ones. Moreover, $\langle E \rangle$ increases with $\langle D \rangle$ for both T- D and RT- D complexes until an interchain distance of around 60-65 Å is reached. The poor stability of the dimers with the higher degree of interspersion confirms the crucial role played by intramolecular interactions in the stability of these complexes. The T-65 and RT-60 are the most stable dimers within each series (Table 6.1) as they exhibit the smallest variation between the initial and the final D , the latter being the lowest energy one. Interestingly, both the effective contact surface between the PG4 chains and the interpenetration are lower in RT-60 than in T-65 (*i.e.* $\langle D \rangle = 63.87 \pm 0.08$ and 59.43 ± 0.52 for T-65 and RT-60, respectively), corroborating that intramolecular interactions play a crucial role. On the other hand, energies obtained for T-65, T-70 and RT-65 and RT-70 are relatively similar, which is consistent with the fact that their $\langle D \rangle$ values are also relatively similar (*i.e.* 63.87 ± 0.08 , 66.56 ± 0.16 , 61.19 ± 0.26 and 64.98 ± 0.78 Å, respectively). Accordingly, these four complexes are dominated by intramolecular interactions, the intermolecular contribution being relatively small, independent of the contact surface.

On the other hand, a comparison of the $\langle E \rangle$ values calculated for the dimers with that obtained for an isolated PG4 chain (Table 6.1) indicates complex formation in T- D with $D \leq 60$ and that RT-40 is energetically unfavored. Thus, the energy of the latter dimers is higher than two times the energy of an isolated PG4 chain, which evidences that the repulsive interactions associated with the complexes with a high degree of molecular interpenetration are not fully compensated by the formation of attractive intermolecular interactions. This behavior confirms the predominantly colloidal nature of PG4 put forth recently [23,24], according to which this DP can be represented in the melt as a densely packed weakly interpenetrating elongated core shell system with solid-like behavior.

Table 6.1. Average Value of the Energy and Structural Properties in T-*D* and RT-*D* dimers: $\langle D \rangle$, Average Distance between the Centers of Mass of the two PG4 Chains; $\langle E \rangle$, Average Potential Energy; $\langle \Delta E \rangle$, Average Interaction Energy; $\langle \Delta \theta \rangle$, Average Angle Formed by the Helical Axes of the two PG4 Chains; $\langle R \rangle$, Average Cross-Sectional Radius; $\langle L \rangle$, Average Molecular Length, and $\langle \rho \rangle$, Average Density.

System	$\langle D \rangle$ (Å)	$\langle E \rangle$ (10 ³ kcal/mol)	$\langle \Delta E \rangle$ (10 ³ kcal/mol)	$\langle \Delta \theta \rangle$ (°)	$\langle R \rangle$ (Å)	$\langle L \rangle$ (Å)	$\langle \rho \rangle$ (g cm ⁻³)
T-40	43.79±0.10	-1182.2±6.4	70.02±1.63	-	36.7±0.2	356.9±2.0	0.882±0.002
T-50	56.38±0.26	-1242.0±6.5	43.89±1.38	-	36.2±0.1	328.9±0.7	1.012±0.001
T-60	59.97±0.14	-1313.1±5.4	1.75±0.80	-	35.9±0.1	323.9±0.6	1.051±0.001
T-65	63.87±0.08	-1343.0±5.7	-3.88±0.80	-	35.8±0.1	321.9±0.7	1.073±0.001
T-70	66.56±0.16	-1342.6±5.8	10.23±8.54	-	35.8±0.1	320.8±0.4	1.072±0.001
RT-40	48.09±0.68	-1279.4±6.7	34.12±1.69	44.2±0.6	36.3±0.3	330.4±0.7	1.071±0.001
RT-50	57.60±0.60	-1338.6±6.5	18.41±1.67	43.1±0.7	36.1±0.3	321.6±1.0	1.049±0.001
RT-60	59.43±0.52	-1347.1±5.7	9.68±0.81	43.5±0.6	35.9±0.2	320.0±0.7	1.067±0.001
RT-65	61.19±0.26	-1343.4±5.6	9.80±0.79	42.3±0.6	36.0±0.4	319.4±2.0	1.067±0.001
RT-70	64.98±0.78	-1344.4±5.6	10.42±0.80	43.2±0.6	35.9±0.2	319.2±0.5	1.073±0.001
PG4 ^a	-	-658.1±3.9	-	-	36.2±0.1	315.7±0.6	1.073±0.001

^a Isolated PG4 chain.

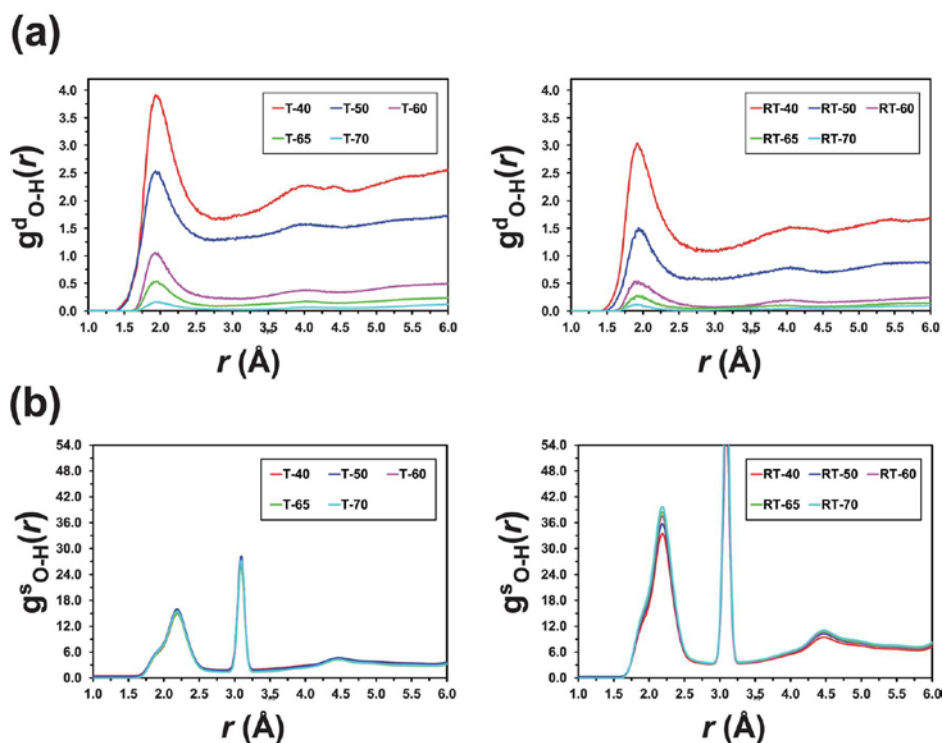


Figure 6.5. Partial distribution functions of (N-)H \cdots O pairs belonging to (a) different PG4 molecules or (b) to the same PG4 molecule $g^d_{H-o}(r)$ and $g^s_{H-o}(r)$, respectively for T- D (left) and RT- D (right) systems.

The average interaction energy, $\langle \Delta E \rangle$, has been estimated as the difference between the average energy of the dimer and the sum of the average energies calculated for each individual PG4 chain in the complex, $\langle \Delta E \rangle = \langle E \rangle - (\langle E1 \rangle + \langle E2 \rangle)$. Results included in Table 6.1 indicate that although PG4 chains remain stable as shown above, the formation of the dimer is energetically unfavored in all cases with the exception of T-65. Furthermore, $\langle \Delta E \rangle$ decreases with the interpenetration for low D values while the opposite behavior is observed for large D values.

6.1.3.2. HYDROGEN BONDS

The existence of N-H \cdots O intermolecular hydrogen bonds is evidenced in Figure 6.5a, which displays the partial distribution function of (N-)H \cdots O pairs belonging to different PG4 molecules, $g^d_{H-o}(r)$, for T- D and RT- D dimers. It can be seen that all profiles show a sharp and well-defined peak centered at 1.9 Å, evidencing the existence of strong intermolecular hydrogen bonds in the two series of complexes. However, the height of such a peak decreases with increasing D , which indicates that the amount of such interactions depends considerably on the degree of interpenetration of the PG4 molecu-

les. This is consistent with observations recently reported for different generations [23]: DPs of low generations, as PG1, are polymer-like, present an enhanced probability of interpenetration and their viscoelastic response is mainly dependent on the strength of intermolecular hydrogen bonds and π -stacking interactions, a fluid-like behavior being observed at temperatures higher than 120 °C (*i.e.* such secondary bonds break). In contrast, molecular colloid PG4 exhibits a solid-like response dominated by topological constraints, which are not released with temperature, resembling the kinetic frustration of repulsive colloidal glasses [23]. Furthermore, all the $g_{H-o}^d(r)$ profiles show a broad shoulder centered at ~ 4 Å that is consistent with the formation of very weak interactions. The structural rigidity of PG4 chains prevents conformational rearrangements needed to increase the strength of such weak hydrogen bonding interactions. As occurred above for the first peak, the visibility and height of the shoulder at ~ 4 Å decrease with increasing D .

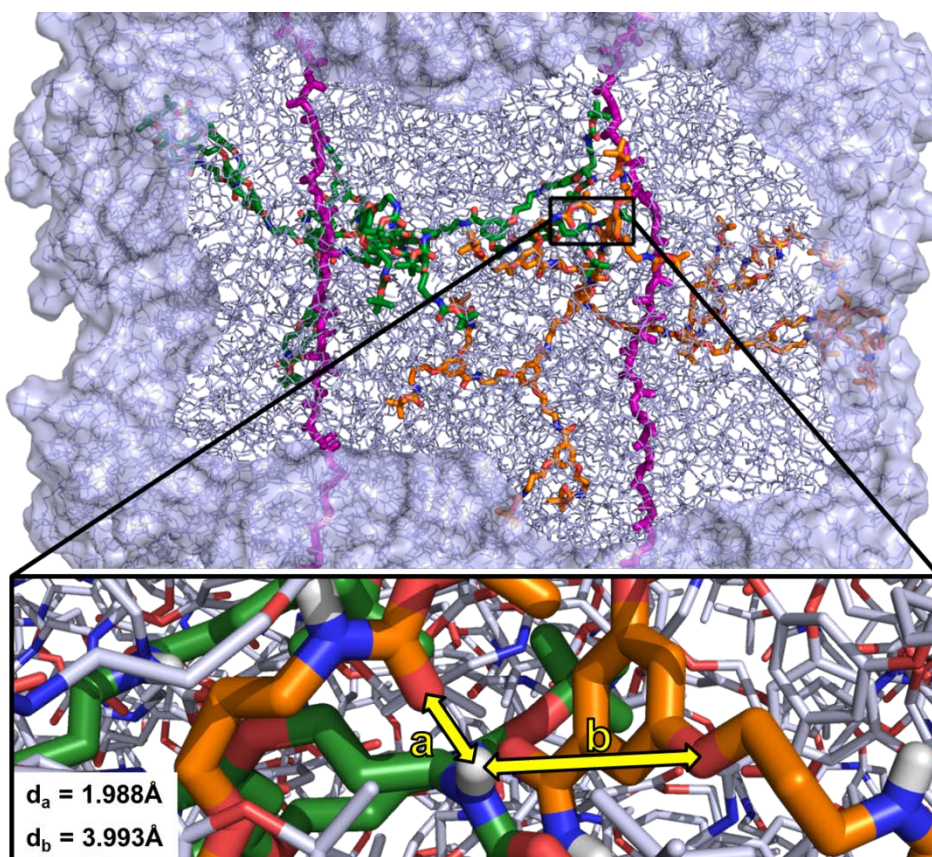


Figure 6.6. Schematic view displaying representative intermolecular hydrogen bonds in T- D and RT- D dimers: (a) strong hydrogen bond; and (b) weak interaction. The strength of the weak inter-dendron interaction represented in (b) is limited by the reduced mobility of the involved groups, which are constrained to remain at a distance of ~ 4 Å.

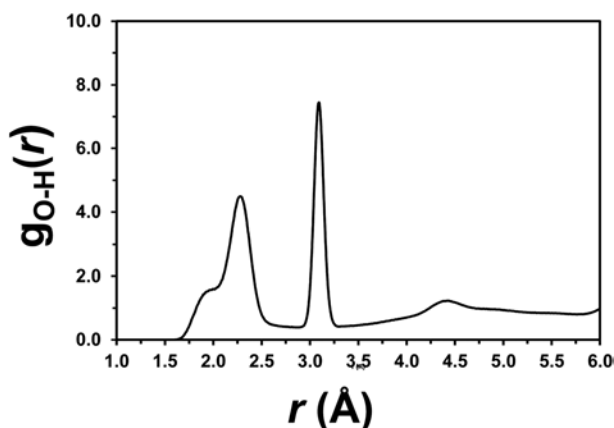
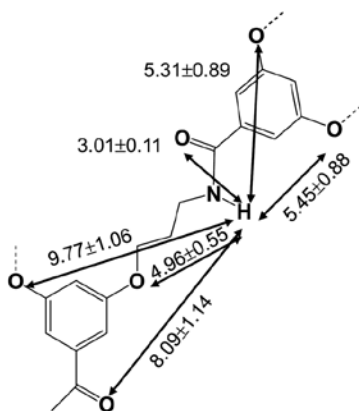


Figure 6.7. Partial distribution functions of (N-)H \cdots O pairs, $g_{H-O}^S(r)$, for an isolated PG4 chain.

Figure 6.6a and Figure 6.6b show schematic views of the representative intermolecular interactions associated with the $g_{H-O}^d(r)$ peaks at 1.9 and ~ 4 Å, respectively.

The partial distribution functions of (N-)H \cdots O pairs belonging to the same PG4 molecule, $g_{H-O}^S(r)$, are displayed in Figure 6.5b. As expected, the shape of the profiles obtained for the T-*D* and RT-*D* dimers is practically identical to the $g_{H-O}^S(r)$ derived from simulations on a single PG4 chain, the latter being displayed in Figure 6.7. Some peaks found in all the profiles calculated for both T-*D* and RT-*D* dimers, as for example the sharp and high one centered at 3.1 Å, cannot be attributed to formation of intramolecular hydrogen bonds, but to the (N-)H \cdots O distance between atoms belonging to the same amide moiety. This is illustrated in Scheme 6.2, which shows the average distance between a N-H atom and each of the six oxygen atoms surrounding it. Accordingly, the sharp peak and the shoulder at 2.2 and 1.9 Å, respectively, should be



Scheme 6.2

ascribed to strong intramolecular hydrogen bonds, which are frequently formed between dendrons belonging to different repeat units (Figure 6.8a) but occasionally formed between dendrons of the same repeat unit (Figure 6.8b). This behavior has been attributed to the steric constraints of the system. Similarly, the small peak centered at 4.4 Å should be related to the formation of very weak intramolecular interactions restrained by the rigid molecular structure of PG4 (Figure 6.8c). It should be mentioned that the amount of all such intramolecular interactions increases with D for RT- D dimers. This tendency is in contrast to the behavior shown by the $g_{H-O}^d(r)$ profiles, suggesting a competition between inter- and intramolecular hydrogen bonds.

Table 6.2 lists the average number of hydrogen bonds for T- D and RT- D dimers. According to the $g_{H-O}^d(r)$ and $g_{H-O}^s(r)$ profiles displayed in Figure 6.5, both inter- and intramolecular hydrogen bonds were accounted for when the (N-)H \cdots O distance (d_{H-O}) was shorter than 2.5 Å. Additionally, fulfillment of a directional criterion based on the empirical rules observed in early studies [36-38] for the hydrogen bonding angle, which consists of $\angle N-H\cdots O \geq 120^\circ$, was imposed. As it can be seen, the number of intramolecular interactions, ranging from 875 ± 39 (T-40) to 996 ± 23 (RT-70), is

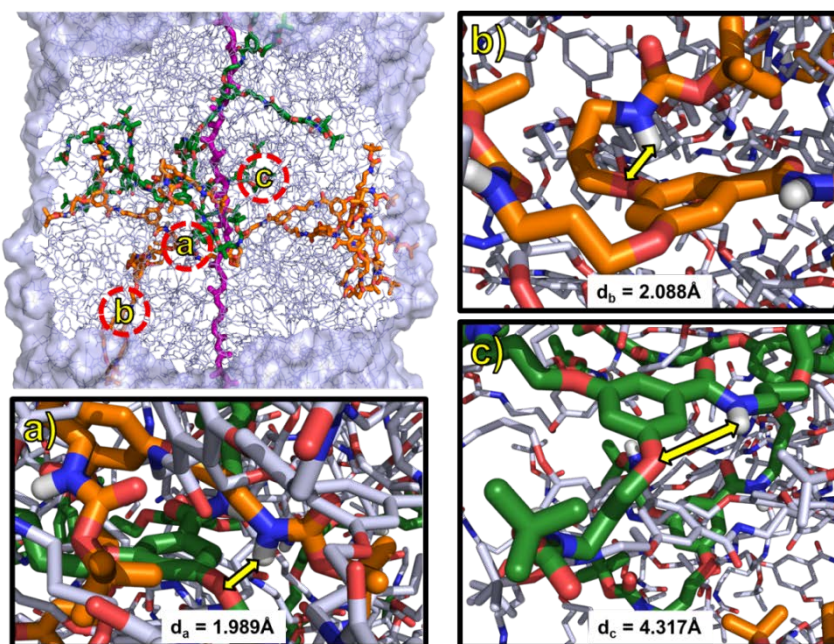


Figure 6.8. Schematic view displaying representative intramolecular hydrogen bonds in T- D and RT- D dimers: (a) strong hydrogen bond between dendrons of different repeat units; (b) strong hydrogen bond between dendrons of the same repeat unit; and (c) weak interaction. The strength of the weak inter-dendron interaction represented in (c) is limited by the reduced mobility of the involved groups, which are constrained to remain at a distance of ~ 4 Å. Different colors in the amplified view have been used to identify dendrons belonging to different repeat units.

considerably higher than the number of intermolecular ones, the latter varying between 4 ± 1 (RT-70) and 72 ± 10 (T-40). These values indicate that 10.5-11.1% of the nitrogen atoms contained in each dimer (*i.e.* 30 nitrogen atoms per repeat unit \times 150 repeat units \times 2 chains = 9000 nitrogen atoms) are involved in the formation of intra- or intermolecular hydrogen bonds, independent of the dimer. The concentration of nitrogen atoms forming hydrogen bonds is slightly higher for an isolated PG4 chain, a total of 516 ± 20 intramolecular hydrogen bonds (*i.e.* 11.5% of the nitrogen atoms) being counted for the latter system. These results indicate that, in general, the amount of hydrogen bonds undergoes a small reduction when PG4 chains interpenetrate. Thus, the concentration of hydrogen bonded nitrogen atoms shows the following variation: T-*D* < RT-*D* < isolated PG4 chain (Table 6.2).

6.1.3.3. π, π -INTERACTIONS

A total of 15 aromatic rings are comprised within each repeat unit, representing a total of $15 \times 150 = 2250$ aromatic rings per simulated chain. Attractive non-covalent interactions between these aromatic rings are expected to play a crucial role in the stability of the system affecting also properties like the molecular stiffness and, consequently, the spatial arrangement [24] and the viscoelastic response [23] of the DP. According to the relative disposition of the aromatic rings, two different configurations are typically considered for π, π -interactions: perpendicular and parallel (also called T-shaped and sandwich, respectively). On the other hand, the potential energy curves for the two configurations of the benzene and toluene dimers were obtained using sophisticated quantum mechanical methods [39,40], which included large basis sets and a proper description of electron correlation effects. Results showed that π, π -interactions in the T-

Table 6.2. Amount of Intramolecular and Intermolecular Hydrogen Bonds (H \cdots O Distance < 2.5 Å and \angle N-H \cdots O \geq 120°) found in the Simulated Systems: Average Values and Standard Deviations. The Concentration of Nitrogen Atoms (in %) forming Hydrogen Bonds is also Displayed.

System	Intramol. H-bonds	Intermol. H-bonds	H-bonded N Atoms (%)
T-40	875 \pm 39	72 \pm 10	10.5
T-50	894 \pm 46	25 \pm 4	10.2
T-60	953 \pm 21	17 \pm 3	10.8
T-65	936 \pm 22	10 \pm 2	10.5
T-70	948 \pm 21	5 \pm 2	10.6
RT-40	967 \pm 40	22 \pm 4	11.0
RT-50	987 \pm 40	6 \pm 2	11.0
RT-60	985 \pm 22	6 \pm 2	11.0
RT-65	998 \pm 21	4 \pm 1	11.1
RT-70	996 \pm 23	4 \pm 1	11.1
PG4 ^a	516 \pm 20 ^b	-	11.5

^a Isolated PG4 chain. ^b The amount of nitrogen atoms involved in hydrogen bonding refers to two polymer chains for T-*D* and RT-*D* dimers and to one polymer chain for isolated PG4.

shaped and sandwich configurations present significant attractive π,π -interactions (*i.e.* ≥ 2 kcal mol⁻¹) for $R \leq 5.5$ and 4.5 \AA [39,40], where R refers to the distance between the centers of mass of the aromatic rings. According to this information, the counting of π,π -interactions was performed using the following criteria: (i) $R \leq 5.5 \text{ \AA}$ and $60^\circ < \beta < 120^\circ$ for the T-shaped configuration and (ii) $R \leq 4.5 \text{ \AA}$ and $\beta < 30^\circ$ for the sandwich one, where β refers to the angle formed by the two aromatic rings.

Table 6.3 lists the amount of intra- and intermolecular π,π -interactions in T- D and RT- D dimers. As occurred for hydrogen bonds, intramolecular π,π -interactions are considerably more frequent than intermolecular ones. The amount of intra-molecular π,π -interactions is practically independent of D for both T- D and RT- D dimers. However, the amount of intramolecular interactions with a sandwich configuration is lower for dimers with $D < 60$ than for dimers with $D \geq 60$. For example, the planar interaction is 35% and 49% more populated than the perpendicular one for T-40 and RT-40, respectively; these percentages increasing to 60% and 68% for R-70 and RT-70 respectively. These features suggest that interpenetration affects the local structure (see next subsections). More specifically, dendrons able to undergo small conformational rearrangements should be related to the formation of interactions in which the rings adopt a planar arrangement, whereas interactions with a perpendicular disposition of the rings should be associated with dendrons with very scarce mobility. This hypothesis is corroborated by the π,π -interactions counted for an isolated PG4 chain (Table 6.3), in which the amount of T-shaped interactions is just half of those found for T- D and RT-

Table 6.3. Amount of Intramolecular and Intermolecular π,π -Interactions (T-shaped Configuration: $R \leq 5.5 \text{ \AA}$ and $60^\circ < \beta < 120^\circ$; Sandwich Configuration: $R \leq 4.5 \text{ \AA}$ and $\beta < 30^\circ$) Found in the Simulated Systems: Average Values and Standard Deviations. The Concentration of Aromatic Rings (in %) Involved in π,π -Interactions is also Displayed.

System	Intramol. π,π -interactions		Intermol. π,π -interactions		Aromatic Rings in π,π -interactions (%)
	T-Shaped	Sandwich	T-Shaped	Sandwich	
T-40	236 ± 22	320 ± 18	85 ± 4	49 ± 6	15
T-50	255 ± 20	379 ± 20	7 ± 3	11 ± 4	14
T-60	253 ± 20	411 ± 20	9 ± 2	5 ± 2	15
T-65	239 ± 22	402 ± 18	-	2 ± 1	14
T-70	253 ± 20	405 ± 20	-	2 ± 1	15
RT-40	249 ± 20	372 ± 18	27 ± 6	7 ± 2	14
RT-50	263 ± 17	404 ± 28	3 ± 1	6 ± 2	15
RT-60	244 ± 22	408 ± 18	-	2 ± 1	14
RT-65	261 ± 22	412 ± 18	-	2 ± 1	15
RT-70	248 ± 22	417 ± 20	-	-	15
PG4 ^a	131 ± 16 ^b	224 ± 14	-	-	16

^a Isolated PG4 chain. ^b The amount of nitrogen atoms involved in π,π -interactions refers to two polymer chains for T- D and RT- D dimers and to one polymer chain for isolated PG4.

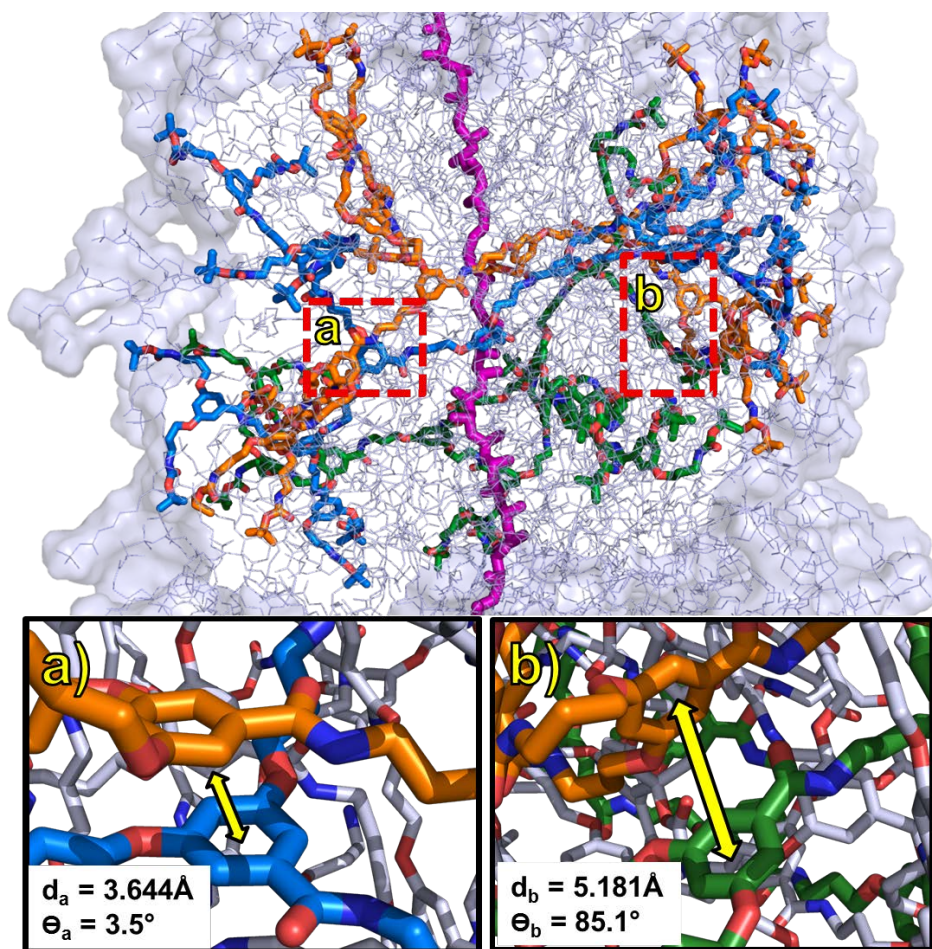


Figure 6.9. Schematic view displaying representative intramolecular π,π -interactions in T- *D* and RT- *D* dimers: (a) sandwich configuration, and (b) T-shaped configuration. Different colors in the amplified view have been used to identify dendrons belonging to different repeat units.

D. Furthermore, for a single chain the amount of sandwich π,π -interactions is higher than half of the interactions detected for dimers with high interpenetration but it is similar to half of the interactions found in dimers with low interpenetration. Figure 6.9 displays representative π,π -intramolecular interactions with T-shaped and sandwich configurations. This interplay of planar and T-shaped interactions should strongly depend on generation as well.

The amount of intermolecular π,π -interactions is only appreciable for T-40 and RT-40 dimers, being negligible, or even completely absent, in T- *D* and RT- *D* with $D = 60, 65$ and 70 . Amazingly, for complexes with $D = 40$ the population of interactions with a T-shaped configuration is higher than that with a sandwich configuration. This feature

indicates that the intrinsic structural properties of PG4 are altered in dimers with a high interpenetration. Representative intermolecular π,π -interactions are depicted in Figure 6.10.

Overall, the results discussed in this and the previous subsections reveal that the formation of specific interactions, such as hydrogen bonds and π,π -stacking, in weakly interpenetrated PG4 dimers is relatively scarce. This should be attributed to the steric hindrance caused by densely branched repeat units, which restricts severely the mobility of the backbone and the inner dendrons. This picture is supported by recent structural studies [24] and is in agreement with the picture emerging from the viscoelastic response [23]. Thus, the colloid-like response of PG4 is essentially controlled by the topological constraints due to neighboring colloidal anisotropic molecules, while the polymer-like behavior of PG1 reflects the life-time of attractive intermolecular interactions, bearing analogies with ionomers [41,42]. The population of intermolecular hydrogen bonds and π,π -interactions is expected to be significantly higher in PG g with $g < 4$ than in PG4, which is consistent with the influence of the generation number on the rheological response of DPs [23].

6.1.3.4. EXPERIMENTAL INVESTIGATION OF THE STABILITY OF PG4

The stability of PG4 was explored experimentally as well. In particular, for 2 different batches that were used at different times, we performed linear viscoelastic measurements with different instruments and different protocols (dynamic frequency sweeps, DFS, and

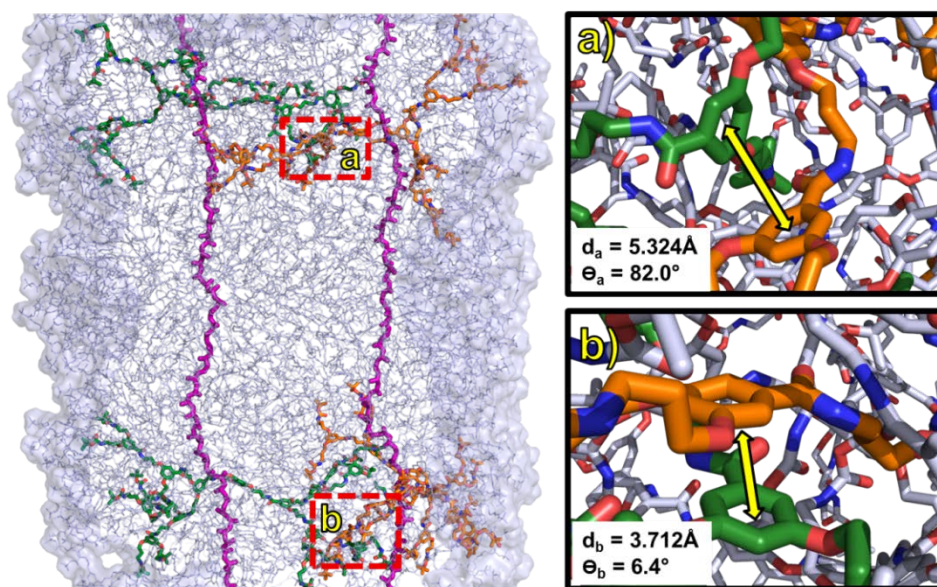


Figure 6.10. Schematic view displaying representative intermolecular π,π -interactions in T- D and RT- D dimers: (a) T-shaped configuration, and (b) sandwich configuration. Different colors in the amplified view have been used to identify dendrons belonging to different chains.

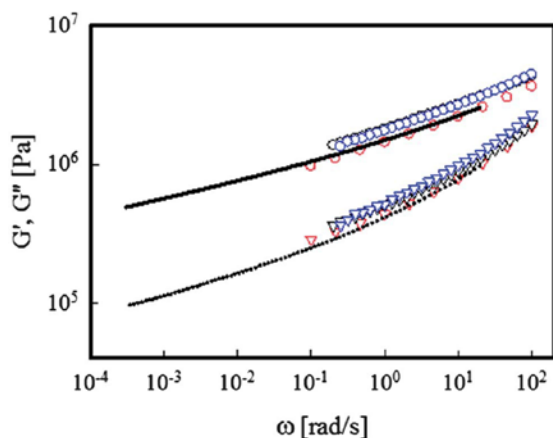


Figure 6.11. Viscoelastic moduli as a function of frequency at 110 °C for sample PG4. Different symbols correspond to different instruments and annealing times. \circ : G' measured with a strain controlled rheometer ARES; \bigcirc : G' measured after annealing the sample for one week; \bigcirc : G' measured with a stress controlled rheometer Physica. ∇ : G'' measured with a strain controlled rheometer ARES; ∇ : G'' measured after annealing the sample for one week, ∇ : G'' measured with a stress controlled rheometer Physica. The lines are viscoelastic moduli data converted from creep tests (Physica).

creep tests which were subsequently converted into frequency spectra [23]), different annealing procedures and measurement times. The linear viscoelastic response was confirmed by dynamic strain sweep tests at different strains, whereas the initial steady-state conditions were confirmed by dynamic time sweeps at a given strain amplitude and frequency lasting typically for 45 min [23]. These experiments were performed with a strain controlled ARES 2kFRTN1 rheometer (TA, USA) and a stress-controlled Physica MCR-501 rheometer (Anton Paar, Austria), the latter operating in the strain-control mode.

All experiments were performed with parallel plate geometry (invar copper–iron alloy or stainless steel, with a diameter of 8 mm) at 110 °C, in a nearly inert (nitrogen) atmosphere. Before each test, the sample was annealed for about 12 hours in a vacuum oven at 110 °C. In addition, DFS was conducted after long annealing of the samples which were kept in a vacuum at 110 °C for one week. Finally, creep tests were converted into DFS as discussed in ref. [23]. The results of all these measurements are compiled in Figure 6.11. The main conclusion is that PG4 is stable, hence these results reflect equilibrium (thermodynamic) properties. This is considered important, as DPs may possibly degrade, although the extent of degradation, the temperature range and the role of degree of polymerization and generation are currently being investigated. The small differences among data observed in the figure is attributed to small differences in sample loading and temperature calibration (nearly always unavoidable when measuring in different laboratories and with different instruments) and is not considered important. Therefore, in practice conclusions remain unaffected.

6.1.3.5. DENSITY PROFILES, CROSS-SECTIONAL RADIUS AND MOLECULAR LENGTH

Figure 6.12a and Figure 6.12b show a comparison of the variation of the density as a function of the radial distance r from the macromolecular backbone (MB) of T-D and

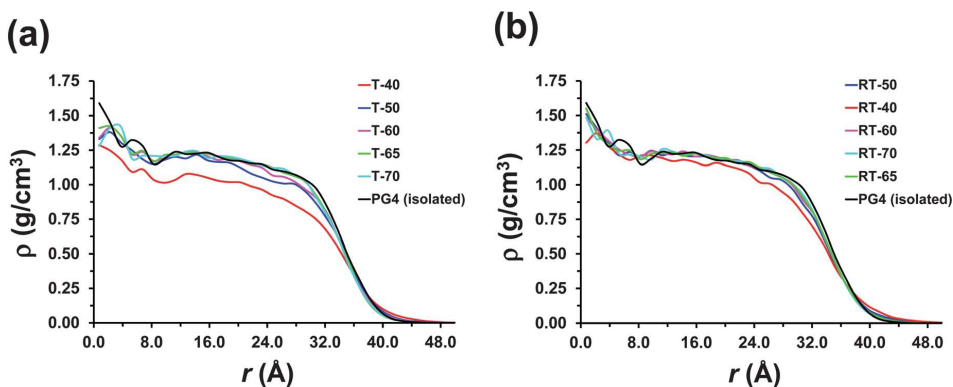


Figure 6.12. Density profile for a PG4 chain in (a) T- D and (b) RT- D dimers representing the density (ρ) against the distance to the backbone measured using the vector perpendicular to the helix axis (r). The profile displayed for each DP corresponds to an average considering different cross-sections within all the analyzed snapshots. The density profile derived from simulations of an isolated PG4 chain is included for comparison.

RT- D dimers, respectively, with that of an isolated PG4 chain. In addition to these local density descriptions, the average values of radial density ($\langle \rho \rangle$) are listed in Table 6.1 for all the investigated systems. As it can be seen, the radial density profiles and $\langle \rho \rangle$ values calculated for PG4 chains in dimers are very similar to those derived from simulations on a single chain in all cases with the exception of T-40. Thus, for the latter the radial density decreases by 17.8% with respect to that of an isolated chain, whereas for the rest of T- D and all RT- D dimers the maximum reduction is only 5.7% (T-50) and 2.2% (RT-40), respectively. Moreover, differences in the density are negligible or even null for dimers with $D \geq 60$.

The radius of PG4 chains in dimers was determined considering a proportionality between the radial probability distribution and the radial density profiles, $p(r) \propto \rho(r)$, and that the density profile, before it approaches zero, is approximately constant as for a homogeneous cylinder of radius R . This case satisfies $p(r) \approx 1/r^2$ subject to normalization, $\int_0^r p(r) dr^2 = 1$, with $dr^2 = 2r dr$, and thus

$$\langle r^2 \rangle^{1/2} = \frac{R}{\sqrt{2}} \approx 0.71 \times R \quad (6.1)$$

Equation (6.1) has been used to obtain estimates of R from the calculated $\langle r^2 \rangle^{1/2}$ values Table 6.1 includes the radius obtained by averaging over a large number of cross-sections of these cylindrical molecules ($\langle R \rangle$), which were selected in the region of interpenetration in dimers. As it can be seen, $\langle R \rangle$ decreases by 0.9 and 0.4 Å in T- D and RT- D series, respectively, when D increases from 40 to 70 Å. This represents a relative reduction of only 2.4% and 1.1%, respectively. Furthermore, the largest change with respect to the $\langle R \rangle$ value calculated for an isolated PG4 chain is lower than 1.4%. The

small influence of molecular interpenetration on the cross-sectional radius was an unexpected result since, *a priori*, this structural parameter was thought to be sensitive to both the formation of intermolecular interactions and conformational rearrangement of dendrons. Still, the polymers are weakly swelling radially with increasing amount of interpenetration, which is consistent with the picture emerging from rheological [23] and structural studies [24].

Finally, the molecular length has been determined by evaluating the end-to-end distance of the backbone, $\langle L \rangle$. The values displayed in Table 6.1 clearly indicate that intermolecular interactions produce an increase of the molecular length, this effect

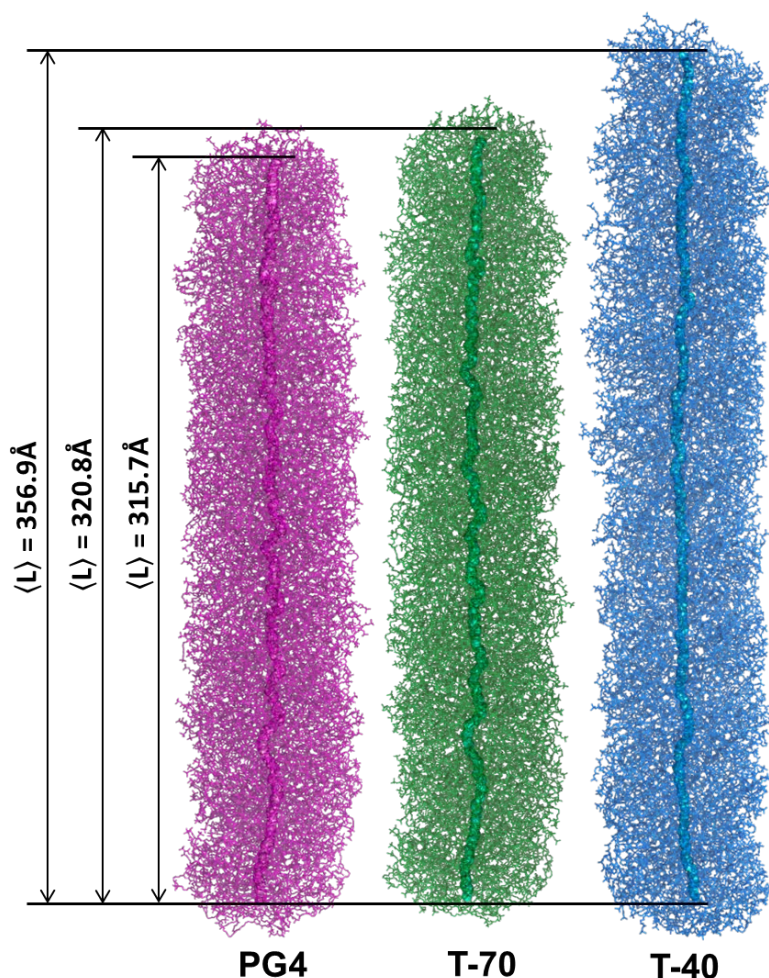


Figure 6.13. Comparison of a single PG4 chain extracted from the last snapshot of simulations on T-40 dimer (right), T-70 dimer (middle) and an isolated chain (left). The backbone corresponds to the central solid lines. Differences in the average molecular length, $\langle L \rangle$, are represented.

increasing with the degree of interpenetration. Thus, the $\langle L \rangle$ values obtained for PG4 in T-40 and RT-40 dimers are 13% and 4%, respectively, larger than that derived from simulations on a single chain. This enlargement decreases to 2% and 1% for T-70 and RT-70, respectively, which is fully consistent with the behavior discussed above for the variation of the amount of intermolecular interactions as a function of the separation distance D in both T- D and RT- D . Figure 6.13 provides a visual description of the effect of the interpenetration on the molecular length, enlargement being evidenced by showing the superposition of PG4 chains extracted from the last snapshot of simulations on T-40, T-70 and a single molecule.

6.1.4. CONCLUSIONS

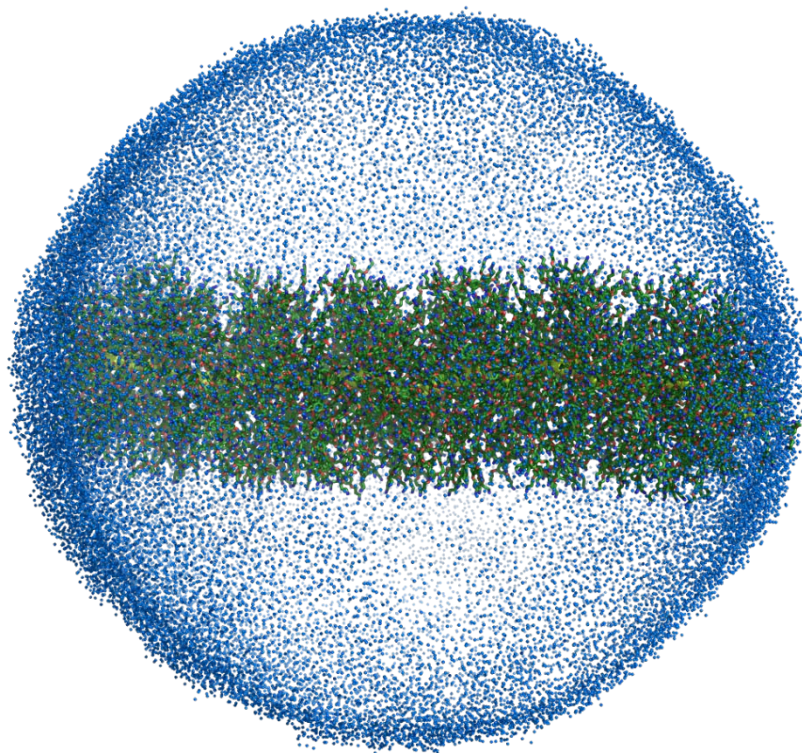
MD simulations on PG4 dimers with different degrees of interpenetration have been carried out to characterize intra- and intermolecular hydrogen bonding and π,π -stacking interactions. The intramolecular interactions have been found to be significantly more frequent than the intermolecular ones in all cases. The predominance of intramolecular interactions is consistent with the calculated energies, the RT- D dimer being more stable than the T- D one for each D . Approximately 11% of the amide groups are involved in hydrogen bonds while $\sim 15\%$ of aromatic rings participate in π,π -interactions. The amount of intermolecular hydrogen bonds has been found to increase with the degree of interpenetration while the opposite tendency has been detected for intramolecular hydrogen bonds. In spite of this, it should be remarked that intermolecular hydrogen bonds represent only 8% and 4% of the total in the dimers with the highest interpenetration (*i.e.* T-40 and RT-40, respectively). Regarding the π,π -stacking, intramolecular interactions represent 80% and 95% interactions in T-40 and RT-40, respectively. However, for dimers with $D > 40 \text{ \AA}$, the amount of intermolecular π,π -interactions becomes practically negligible, or even null (*i.e.* RT-70). Among intramolecular π,π -interactions, those with the two aromatic rings arranged in a sandwich configuration are the most populated, even though the amount of T-shaped interactions is also significant (*i.e.* $\sim 40\%$).

Interpenetration has been found to have an anisotropic effect on the DP structure. We find that the molecular length increases by 13% (T-40) and 4% (RT-40) in dimers with the highest interpenetration, whereas the variation of the cross-sectional radius is lower than 1.4%. The structural variations produced by interpenetration are consistent with the behavior of intermolecular interactions. Furthermore, the overall picture emerging from these results supports the scenario put forth in recently reported structural and rheological studies, which suggests the colloidal-filament nature, dense hexagonal packing in solution and associated solid-like viscoelastic response in the melt of PG4. This behavior could be attributed to the dominant topological interactions in weakly interpenetrated PG4 rather than to specific intermolecular hydrogen bonds and π,π -

stacking interactions. DPs should be considered as a unique family of organic materials with unusual microscopic properties and behavior which can be tailored molecularly from polymeric to colloidal.

6.2. INTERNAL STRUCTURE OF CHARGED DPs

The internal structure and solvent absorption ability of positively charged DPs, made of regularly branched dendrons of generations $g = 1-6$, have been investigated by atomistic molecular dynamics simulations in aqueous solution. Charged DPs are obtained by deprotecting the neutral analogues through the elimination of the blocking *tert*-butyloxycarbonyl groups (Boc groups), which transforms the peripheral amine moieties into ammonium. As a consequence of this procedure, which mimics the divergent synthesis approach, the internal organization of deprotected polymers remains relatively similar to that of neutral polymers. Thus, the electrostatic strain induced by charges at the ammonium groups only provokes a moderate stretching of the backbone, which is manifested through a reduction of the density, while the thickness of the cylindrical nano-object and the amount of backfolding of external dendrons remain relatively independent of deprotection. Analysis of the water density indicates that water penetrates inside the structure of all charged DPs. However, the relative degree of penetration decreases with



increasing g due to the backfolding, which increases with g . On the other hand, the number of water molecules per repeat unit forming hydrogen bonds with deprotected DPs increases from 14 ± 2 for $g = 1$ to 275 ± 14 for $g = 6$. However, water molecules inside the DPs structures are confined in reduced regions affecting the distribution of hydrogen bond angles (*i.e.* $\angle O\cdots H-N$ and $\angle O-H\cdots O$), which do not show clear preferences towards values higher than 120° .

6.2.1. INTRODUCTION

Although DPs are an important class of dendritic architecture [5,43], their properties have been studied in lesser detail than dendrimers so far. DPs can be seen as wormlike molecular objects of cylindrical cross section [4,17,24]. The mass per repeat unit of the polymer backbone increases non linearly with the generation number (g), which modulates properties like the rigidity, diameter and concentration of functionalities [4,16].

In the last years a homologous series of polymethacrylate-based DPs (Figure 6.14), whose repeat units are regularly branched dendrons of generation g , has been synthesized and systematically studied [3,4,16,17,24,44]. The shape and dimensions of these compounds, which have been denoted PG_g , were investigated using atomic force microscopy (AFM), transmission electron microscopy (TEM) and small angle X-ray scattering (SAXS) [3,4,16,17,24], structural information being related with properties like the viscosity, the thermal properties and the viscoelastic response [23,44]. The structure of PG_g has been investigated at the atomic level using MD simulations, which indicated that the backbone of DPs with $g \leq 4$ presents an elongated shape while PG_5 and PG_6 exhibit a helical conformation [18,19]. Also, atomistic simulations have been used to characterize inter- and intramolecular interactions (*i.e.* hydrogen bonds and π , π -stacking) evidencing that intramolecular interactions dominates over intermolecular ones, which support the idea of treating DPs as long colloidal molecules [45]. Due to their properties, these DPs have also attracted great attention for biomedical applications, emerging as a new class of nanomaterials to stabilize therapeutic proteins in the gastrointestinal tract [46] and both to copy [47] and to immobilize enzymes [15].

As the external amine functional groups are blocked by the common *tert*-butyloxycarbonyl protecting group (Figure 6.14a), the stability of PG_g resides on the balance between the repulsive steric interaction and the attractive hydrogen bonding and π - π staking interactions [45]. Deprotection of PG_g is achieved by removing the Boc protecting groups attached to the external amines with trifluoroacetic acid [4,17]. The resulting deprotected DPs, hereafter denoted *de* PG_g (Figure 6.14a), carry positively charged ammonium groups at their peripheral end groups. Although the densely packed dendrons around the backbone render the *de* PG_g shape cylindrical, repulsive long-range

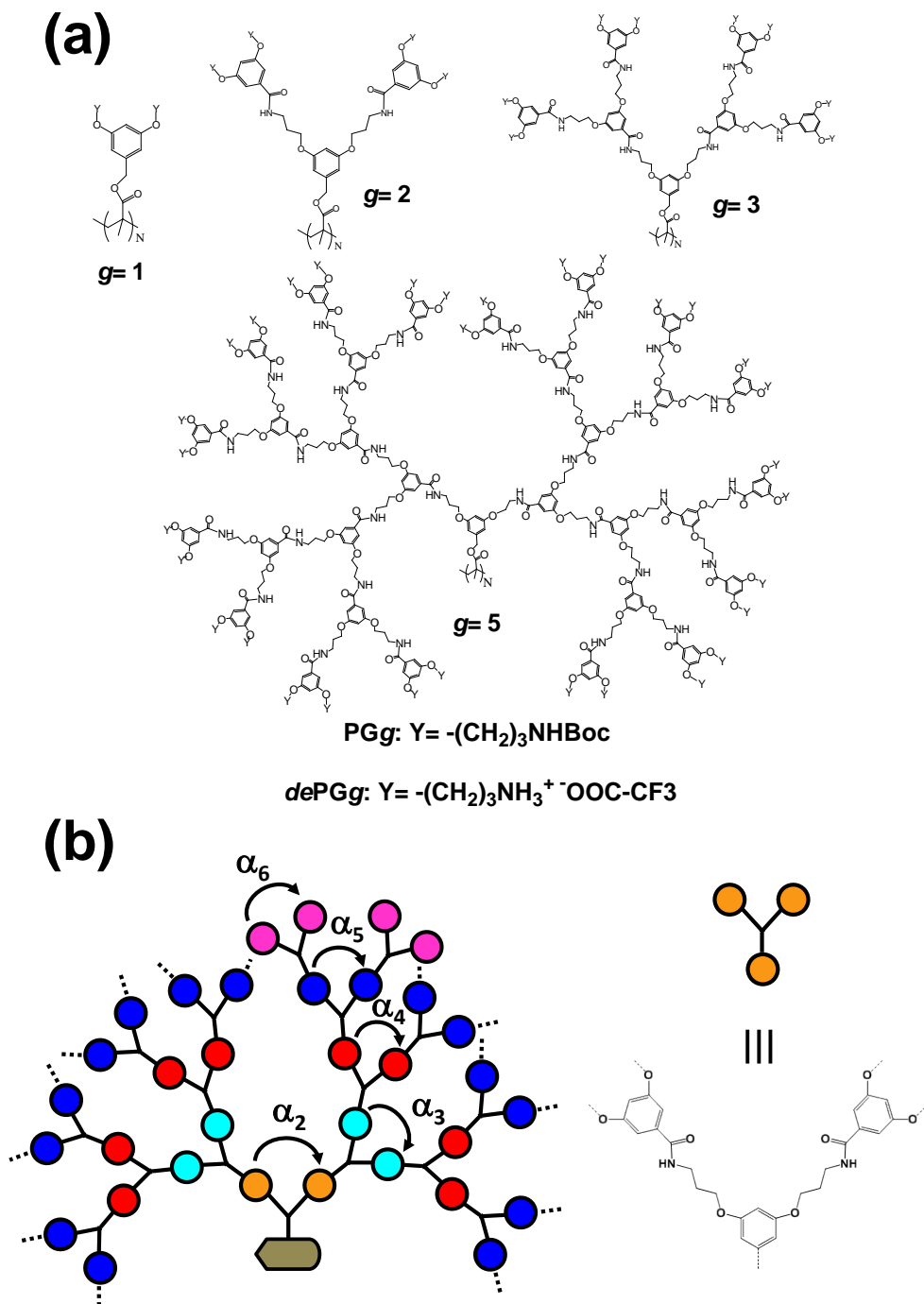


Figure 6.14. (a) Chemical formula of PGg and dePGg with $g=1, 2, 3$ and 5 . (b) Schemes illustrating the definition of the branching angles α_i used to examine the organization of the dendrons at PGg and dePGg.

electrostatic interactions, which are expected to be the dominant, provoke significant differences in both the dimensions and the internal organization with respect to PG g .

The dimensions of cylindrical *de*PG g molecules in solution was indirectly estimated using double electron-electron resonance (DEER) [48]. The radius of the cylinder, R_{DEER} , was found to grow with g , as occurs for PG g . Furthermore, the behavior of *de*PG3, *de*PG4 and *de*PG5 in solution was described as that of molecular objects (*i.e.* environmentally independent dimensions) [48]. More recently, *de*PG g with g ranging from 1 to 5 adsorbed on mica were studied AFM imaging in mildly acidic medium [49]. As expected, the apparent height and width of these molecules were found to increase with g . Furthermore, the adsorbed chains showed a uniform envelop up to *de*PG4 but a pronounced pearl-necklace structure was observed for *de*PG5, which was corroborated with single molecule force spectroscopy [49]. These pearls were attributed to the large hydrophobicity of the polymer backbone.

In spite of the deprotection of PG g is expected to have a large impact in the internal organization, molecular dimensions, density and ability to load solvent molecules, the only charged DP studied at the molecular level using atomistic computer simulations is *de*PG5 [19]. This is because PG5 and *de*PG5 show an exceptional behavior within the homologous series of g -generation. More specifically, polymethacrylate-based DPs of $g = 5$ show a heterogeneous distribution of the atoms, which lead to a region with low density surrounding the backbone. The particular internal structures of PG5 and *de*PG5 are due to the size of the side groups, which are large enough to promote backbone transition from the elongated conformation of PG g with $g \leq 4$ to the helix but too short to enable the significant degree of backfolding found for PG6 [19]. Although PG5 and *de*-PG5 models were found to share the main characteristics, elimination of the Boc protecting groups and protonation of the free amines provoked an elongation of the backbone and a reduction of both the density and the backfolding. These changes resulted from the induced repulsive interactions between the positively charged ammonium groups and led to a structure with a spongy-like appearance for *de*PG5 [19].

In this work, we report on investigations with atomistic MD simulations of the structure of *de*PG g of generations $g = 1-6$, excluding $g = 5$, in aqueous solution. All terminal amine groups of the studied DPs are positively charged, allowing us to determine the effect of the electrostatic strain in the properties of these highly branched materials by comparison with results obtained for PG g [18,19,45]. More specifically, the effects of deprotection on the internal organization of DPs have been examined by comparing the backbone conformation, backfolding of the external dendrons, density and molecular dimensions (*i.e.* length and thickness) of *de*PG g and PG g . On the other hand, water density profiles have been used to evaluate the penetration of water inside the *de*PG g structure, which has been found to be related with the amount of backfolding. Finally, water...*de*PG g interactions have been analyzed.

6.2.2. METHODS

6.2.2.1. MOLECULAR MODELS

Polymethacrylate-based DPS were obtained by divergent synthesis (*i.e.* step-by-step dendronization). According to this procedure, PG_g is deprotected with trifluoroacetic acid and the resulting dePG_g reacts with blocked dendrons to yield $\text{PG}(g+1)$ [4,16,17]. Therefore, the conformation of PG_g is already stabilized before the deprotection of the amino-terminated groups. Considering the steric strain induced by the large side groups, deprotection of PG_g is not expected to produce drastic conformational re-organizations but to induce re-arrangements, especially at the peripheral end groups, because of the electrostatic strain. Furthermore, positively charged amino groups may also affect the backbone of DPS with $g > 3$ due to their pronounced backfolding [18].

Charged DPS have been modeled by constructing the starting geometries from the models proposed for PG_g . These correspond to an elongated conformations for DPS with $g \leq 4$ and to a helical conformation for the DP with $g = 6$. The conformations essentially differ in their alternating (elongated) or regular (helical) twist with respect to the macromolecular axis, at similar average distance between repeat units (2.1-2.3 Å). More specifically, PG_g models were transformed into the dePG_g ones by eliminating the protecting Boc groups of the amine functional groups from each external dendron, the resulting free amines being protonated to obtain positively charged ammonium groups at the end of the external layer. A trifluoroacetate anion (${}^-\text{O}_2\text{CCF}_3$), which was used as counterion, was positioned facing each ammonium group to provoke the electrical neutrality of the system. The number of repeat units used to construct the dePG_g models was $N = 100$ for $g \leq 4$ and $N = 75$ for $g = 6$.

Simulations were carried out in aqueous solution, using explicit water molecules to represent the solvent. A spherical solvent cap was defined around the starting models and filled with water molecules. The radii of the solvent caps was 107 (dePG_1), 118 (model dePG_2), 136 (dePG_3), 126 (dePG_4) and 120 Å (dePG_6), which contained 159559, 209831, 315230, 221532 and 136583 water molecules, respectively. Accordingly, the total number of explicit particles (*i.e.* including atoms of the polymer chain, counterions and solvent molecules) represented in each of these models was 485179 (dePG_1), 644795 (model dePG_2), 978592 (dePG_3), 732698 (dePG_4) and 549401 (dePG_6).

6.2.2.2. COMPUTATIONAL DETAILS

Force field parameters of the charged dendrons and ${}^-\text{O}_2\text{CCF}_3$ counterions were taken from GAFF [33]. Atomic charges for dePG_5 and counterions were obtained using RESP strategy [34]. Water molecules were represented by the TIP3P model of Jorgensen and co-workers [50]. All simulations were carried out using the NAMD [31] software and the potential energy function of AMBER [32]. Van der Waals interactions were calculated by

applying an atom pair distance cutoff at 10 Å. Electrostatic interactions were extensively computed by means of Ewald summations. The real space term was defined by the van der Waals cutoff, while the reciprocal space was computed by interpolation into an infinite grid of points (particle mesh Ewald) with maximum space grid being 1.2 Å [51]. Bond lengths involving hydrogen atoms were constrained using the SHAKE algorithm with a numerical integration time step of 2 fs [36].

Before running the production MD simulations, different consecutive rounds were performed to equilibrate and thermalize each system. First, structures were minimized using a conjugate gradient method. After this, water molecules were thermally relaxed by two consecutive MD runs, while the polymer chain was kept frozen during 0.5 ns of isothermal and 1.0 ns of isobaric relaxation. Hereafter, all atoms of the system were submitted to 1 ns of heating until the target temperature was reached (298 K), followed by 3 ns of thermal equilibration. Temperature was controlled by the weak coupling method [35], using a time constant for the heat bath coupling of 1 ps. After this, the MD production run of each system at 298 K and 1 atm was 15 ns long. The coordinates of the production run was saved every 5000 steps (1500 snapshots for each model).

Averages were obtained using the structures recorded during the last 10 ns of the simulation. The equilibration phase was generally followed by monitoring the system's energy, the end-to-end distance and the radius of gyration.

6.2.3. RESULTS AND DISCUSSION

6.2.3.1. ANALYSIS OF *dePGg* CONFORMATION

The impact of the peripheral charged ammonium groups in the organization of the dendrons has been examined by calculating the angles α_i that correspond to the angles between adjacent branching units as defined in Figure 6.14b (i ranges from 2 to g for *dePGg* and *PGg* with $g > 1$). The average α_i values, which have been obtained considering all repeat units and snapshots recorded during the last 10 ns of the production simulations, are displayed in Table 6.4 with the corresponding standard deviations. Apparently, deprotection does not provoke any important change in the organization of external and internal dendrons for DPs with $g = 2, 3$ and 4. Thus, the largest change in α_i occurred for $g = 3$, α_3 decreasing only 7° upon elimination of the Boc groups. In contrast, deprotection of *PG6* results in a very important re-organization of the both the internal (*i.e.* α_2 decreases 21°) and peripheral dendrons (*i.e.* α_5 and α_6 increase 21° and 17°, respectively). This should be attributed to the large amount of backfolding detected in *PG6* [18], which enhances the electrostatic strain induced by the positive charges.

Figure 6.15 displays atomistic representations of *dePGg*, those reported for *PGg* [18,19] being also displayed for comparison. Interestingly, the backbone conformations of

Table 6.4. Average Values of α_i (degrees; see Figure 6.14b) Calculated for *dePGg* and *PGg* with $g=2, 3, 4, 5$ and 6 . Standard Deviations are also Displayed.

	<i>dePG2</i>	<i>PG2</i>	<i>dePG3</i>	<i>PG3</i>	<i>dePG4</i>	<i>PG4</i>	<i>dePG5</i> ^a	<i>PG5</i> ^a	<i>dePG6</i>	<i>PG6</i>
α_2	128±20	125±18	128±16	126±14	155±13	155±13	70±15	70±16	91±10	112±14
α_3			109±28	116±29	92±22	93±23	66±16	65±16	90±16	91±31
α_4					66±28	66±28	74±21	69±19	81±19	87±31
α_5							69±24	63±21	85±24	64±30
α_6									76±30	59±25

^a Results for *dePG5* and *PG5* have been calculated using the simulations reported in reference [19].

protected and deprotected DPs are apparently very similar. Thus, DPs with $g \leq 4$ display an elongated conformation, while a DP with $g = 5$ and 6 exhibits a helical backbone. In spite of this similarity, the backbone conformations obtained for *dePGg* are stretched with respect to those reported for *PGg*. This feature, which is not evident from Figure 6.15 because MD simulations on *PGg* and *dePGg* were carried out using a different number of repeat units, has been quantified by calculating the average height of each repeat unit (h) with respect to the macromolecular backbone (MB). Results are shown in Table 6.5, the relative elongation induced by deprotection of the external dendrons being also displayed. As it can be seen, the length is systematically lower for *PGg* than for *dePGg*, independently of g , the enlargement provoked by the electrostatic strain ranging from 1.3% to 3.0%.

Figure 6.16 compares the variation of density as a function of the radial distance r from the MB of *dePGg* with those reported for *PGg*. For the calculation of the mass density profiles, the MB was associated over the extension of the atomistic backbone to the macromolecular axis (MA), which was determined from the coordinates of the atomistic backbone by linear regression. Profiles displayed in Figure 6.16 were obtained by averaging over different cross-sections of the resulting cylindrical models. As it was already described for *PGg* [18], density profiles calculated for *dePGg* are also influenced by the structural phenomena associated to the generation g . More specifically, the backbone conformation, which is elongated for $g \leq 4$ or helical for $g > 4$, and the backfolding of the dendrons, which increases with g , affect severely the spatial distribution of the atoms. For all DPs the highest density region is close to the backbone. After this, the density of all polymers with $g \neq 5$ drops and remains approximately constant over some range of distances, and finally decreases progressively until the external layer of the cylinder section has been reached. In contrast the density profiles of both *dePG5* and *PG5* show a drastic decay of the density at the region nearest to the backbone and a subsequent increase, which is consequence of the peculiar heterogeneous distribution of the atoms in these two DPs [19].

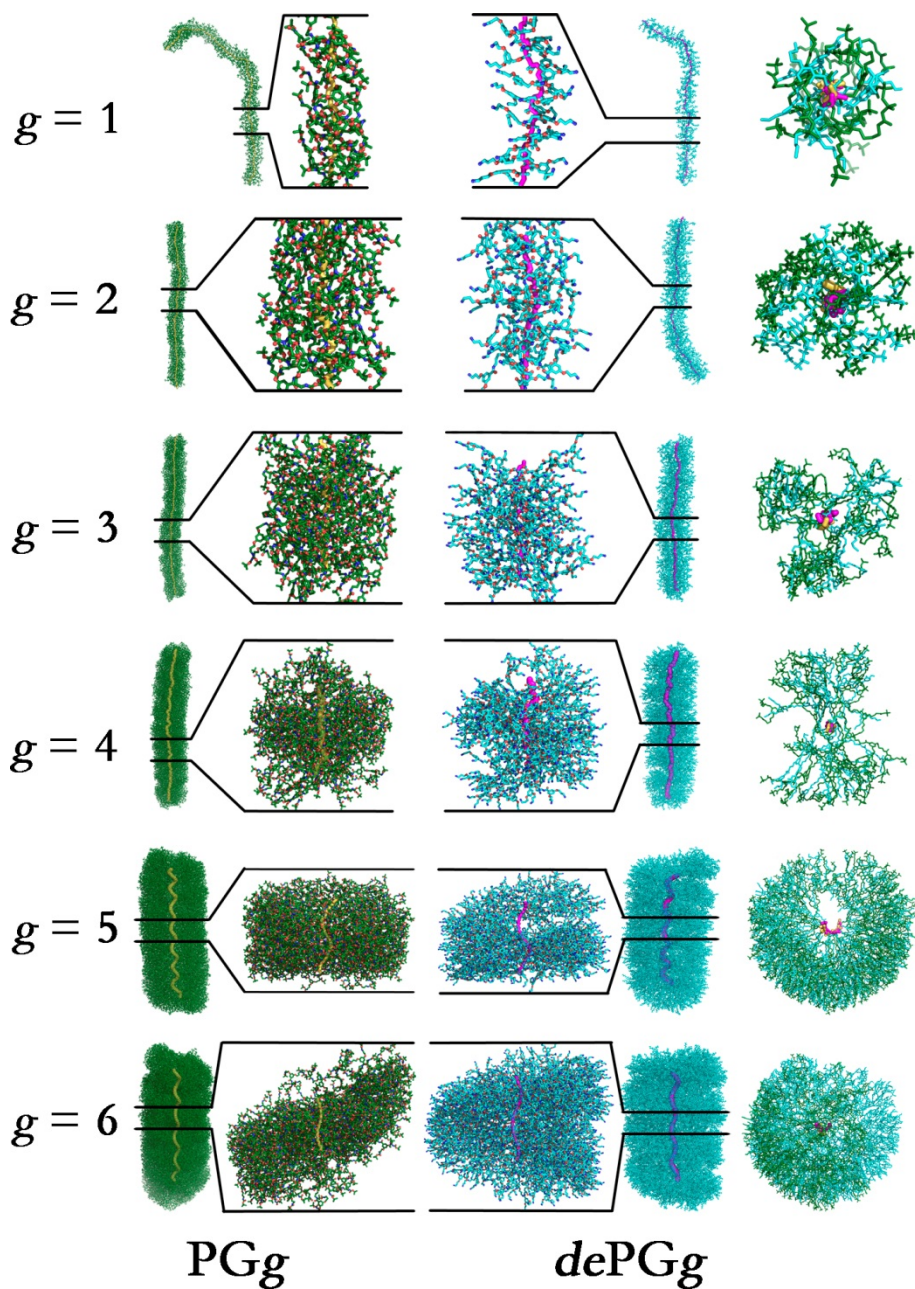


Figure 6.15. Atomistic conformations for PGg (left) and $dePGg$ (right). The complete axial projections represent the whole calculated systems, the number of repeat units being $N = 150$ for PGg with $g=1-4$, 100 for $PG5$ and $dePGg$ with $g=1-4$, and 75 for $PG6$ and $dePGg$ with $g=5-6$. The magnified axial projection involves 20 repeat units in all cases, whereas the equatorial projection involves 5 ($g=1-4$) or 10 ($g=5-6$) repeat units. Figures of PGg and $dePGg$ are only comparable for the same g since the zoom decreases with increasing g .

Table 6.5. Average Height per Repeat Unit (\bar{h}), Average Density (ρ_{av}) and Radius (R and R^*) for $dePGg$ and PGg . Relative Elongation upon Deprotection and Maximum Water Penetration Degree (W_p) for $dePGg$.

	\bar{h} (Å)	ΔL (%)	ρ_{av} (g/cm ³)	R (Å) ^a	R^* (Å) ^b	W_p (%) ^c
$dePG1$ / $PG1^d$	2.146 / 2.114	1.5	0.87 / 0.97	11.0 / 11.7	11.8	82.8
$dePG2$ / $PG2^d$	2.218 / 2.182	3.0	0.94 / 1.03	16.2 / 17.0	17.4	67.2
$dePG3$ / $PG3^d$	2.251 / 2.218	1.5	0.88 / 1.02	23.3 / 24.2	26.0	53.6
$dePG4$ / $PG4^d$	2.161 / 2.105	2.6	0.97 / 1.07	34.9 / 36.2	36.0	37.2
$dePG5$ / $PG5^e$	1.974 / 1.949	1.3	0.57 / 0.86	52.7 / 52.5	54.9	-
$dePG6$ / $PG6^d$	1.991 / 1.964	1.4	0.94 / 1.11	58.0 / 58.7	60.3	20.8

^a Calculated using (6.1). ^b Calculated considering water molecules and the trifluoroacetate anions directly interacting with the periphery of the DP through hydrogen bonds or electrostatic interactions, respectively. ^c Calculated using (6.2). ^d Values for PGg taken from reference [18]. ^e Values for $dePG5$ and $PG5$ taken from reference [19].

For a given g the density decreases upon deprotection due to electrostatic strain, which provokes an enlargement of the molecular length (Table 6.5) and the re-organization of external dendrons, especially for $g > 4$ (Table 6.4). This effect is very apparent in Table 6.5, which lists the average values of the density (ρ_{av}) for all DPs. Independently of g , the density of PGg polymers decreases upon transformation into $dePGg$ by elimination of the Boc groups. For the DPs studied in this work, this reduction ranges from 8.7% ($g = 1$) to 15.3% ($g = 6$), even though a reduction of 33.7% was observed for $g = 5$ in previous work [19].

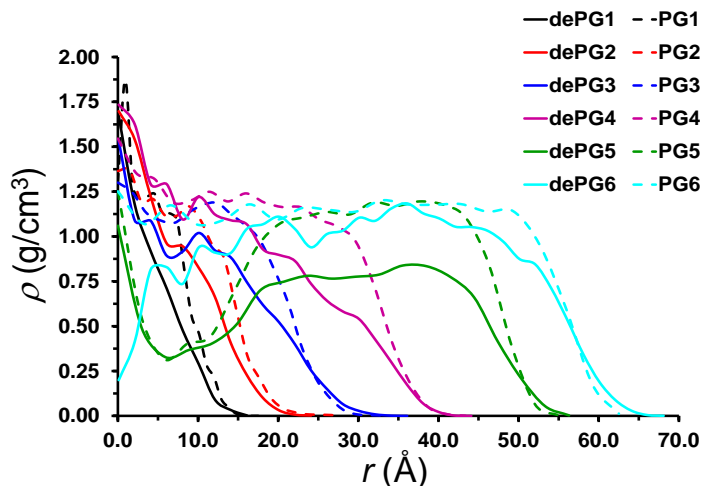


Figure 6.16. Density profiles for the $dePGg$ and PGg models representing the density (ρ) against the distance to the backbone measured using the vector perpendicular to the helical axis (r). The profile displayed for each model corresponds to an average considering different cross-sections within a given snapshot. Data were obtained by averaging over the snapshots taken during the last 10 ns of the MD relaxation runs.

The radius (R) of $dePG_g$ has been evaluated using the density profiles displayed in Figure 6.16. More specifically, the radius was determined from the radial probability distribution profile, $p(r) \propto \rho(r)$. Considering that the density profile is approximately constant, for a homogeneous cylinder of yet unspecified radius $R^{(1)}$ (where the super-index 1 refers to the first approach) that satisfies $p(r) \approx 1/r^2$ subject to normalization, $\int_0^R p(r) dr^2 = 1$, with $dr^2 = 2rdr$, one has

$$\langle r^2 \rangle^{1/2} = \frac{R^{(1)}}{\sqrt{2}} \approx 0.71 \times R \quad (6.2)$$

Table 6.5 lists the R values obtained for $dePG_g$ for g ranging from 1 to 6, the values reported for PG_g [18,19] being also included for comparison. As it can be seen, R grows with increasing generation for both $dePG_g$ and PG_g . This is in agreement with DEER studies on $dePG_g$ in solution [48] ($g = 1-4$) and with both TEM and AFM measures of PG_g deposited onto solid surfaces [16,17] ($g = 1-5$). Although in previous work the R values predicted for PG_g were quantitatively compared with those obtained by TEM [18], direct comparison between the R values displayed in Table 6.5 for $dePG_g$ and the DEER estimates is not possible, unfortunately, because of the different assumptions used to approach molecular dimensions. Although the insensitivity of DEER for low distances precludes reliable estimates for $dePG_g$ with $g \leq 2$, the values obtained for higher generations indicate that the radius increases $\sim 11 \text{ \AA}$ when g grows from 3 to 4. This increment is in excellent agreement with our theoretical prediction, according to which the radii of $dePG_3$ and $dePG_4$ differ in 11.6 \AA . On the other hand, it is worth noting that the R values obtained for $dePG_g$ and PG_g are relatively similar, indicating that the elimination of the Boc groups and the electrostatic strain induced by the positive charges do not provoke significant changes in the thickness of these nanoscopic objects. Furthermore, the similarity between the radii of $dePG_g$ and PG_g is consistent with the small re-organizations suggested by the variations of the branching angles α_i (Table 6.4). Thus, dendrons tend to be slightly more stretched in $dePG_g$ than in PG_g to minimize the repulsive electrostatic effects induced by deprotection. On the other hand, the radii of $dePG_g$ have been also determined considering the water molecules and the trifluoroacetate anions directly interacting with the periphery of the DP through hydrogen bonds or electrostatic interactions, respectively. The resulting values, named R^* in Table 6.5, evidenced a small increment, which ranged from 3.1% ($dePG_4$) to 11.6% ($dePG_3$) in relative terms (the increment ranged from 0.8 to 2.7 \AA in absolute terms).

Figure 6.17 compares the radial probability distribution of the external ammonium and Boc groups for $dePG_g$ and PG_g (see Figure 6.14), respectively, as a function of the distance from the MB ($g_{Boc-b}(r)$ and $g_{N-b}(r)$, respectively). In general, the behaviors of $dePG_g$ and PG_g are similar. The peaks observed for $g = 2, 3$ and 4 become smaller and broader with increasing g , evidencing the backfolding of the external dendrons.

Accordingly, ammonium and Boc groups approach the backbone and reside at radial distances shorter than parts of the same dendron. The inner tails obtained for DPs with $g = 5$ and 6 indicate that the amount of backfolding, which is quantified by the area under such tails, is significantly high. The similarity in the backfolding between charged $dePG_g$ and neutral PG_g has been attributed to the unique architecture of the dendrons, which upon deprotection does not allow major reorganizations but only local rearrangements. This feature is fully consistent with the similarity between the R values previously discussed.

The overall of the results indicate that the conformation of $dePG_g$ is relatively similar to PG_g . As it was found for $dePG_5$ and PG_5 [19], the main difference between the structures calculated for deprotected and protected DPs refers to the sponginess

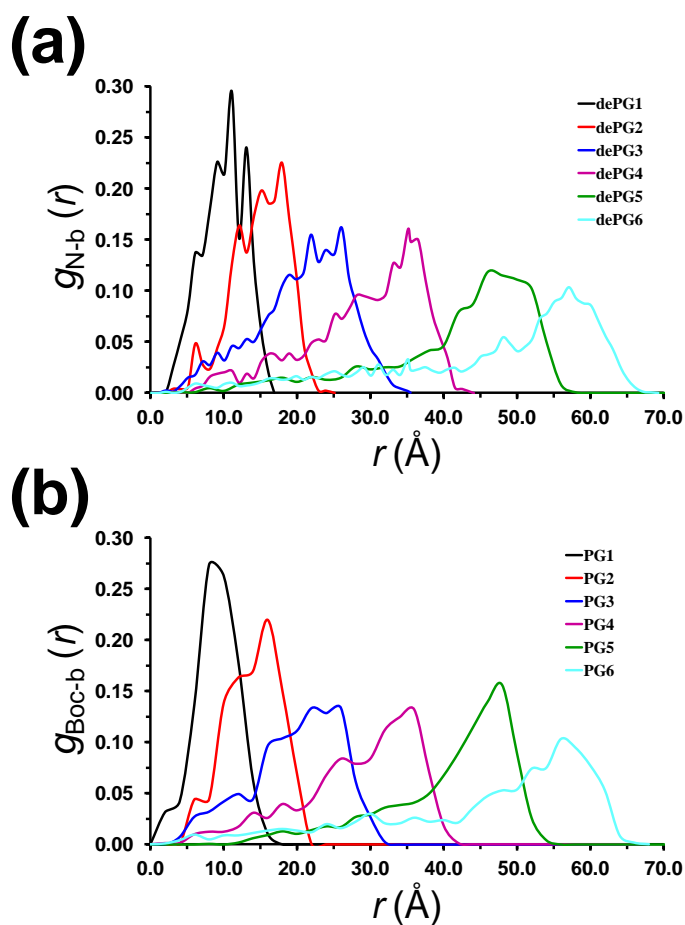


Figure 6.17. Radial distribution function of the dendrons of the external layer for (a) $dePG_g$ and (b) PG_g models measured through the end ammonium (g_{N-b}) and Boc (g_{Boc-b}) groups, respectively.

provoked in the former by the reduction of density. However, the increment of the sponginess does not affect to the backfolding. On the other hand, it is expected that the reduction of density of *dePG**g* is accompanied of the absorption of water molecules inside the DP structure (*i.e.* swelling), which should provoke a decrease of the repulsive interactions between the positively charged ammonium groups. In order to examine this hypothesis, water penetration has been examined in the next sub-section.

6.2.3.2. PENETRATION OF WATER MOLECULES

Water absorption in *dePG*5 was studied in detail in previous work [19]. However, the conformational characteristics of this charged DP are different from those of the rest of the homologous series. Thus, *dePG*5 presents a pore (*i.e.* region with low density in Figure 6.15) surrounding the backbone filled with water, which is not present in elongated *dePG**g* with $g \leq 4$ and helical *dePG*6. In this section we focus on the water absorption in *dePG**g* with $g \neq 5$, which has not been studied before.

Figure 6.18a represents the water density profiles as a function of the radial distance r from the backbone, measured using the vector perpendicular to the helical axis, for *dePG**g*. As it can be seen, the amount of water located inside the DP is very significant and increases with g . However, this increment is not proportional to the enlargement of the radius with g , as is evidenced by the average water density inside the cylinder (ρ_w) associated to each DP. The values of ρ_w , which were calculated by averaging the densities that are below the intersection of water density profiles with the lines representing the radius of each *dePG**g* (dashed lines in Figure 6.18a), are $\rho_w = 0.35, 0.27, 0.22, 0.16$ and 0.10 g/cm³ for *dePG**g* with $g = 1, 2, 3, 4$ and 6 , respectively. This behavior is due to the fact that the distance between the penetrated water molecules and the MB increases with

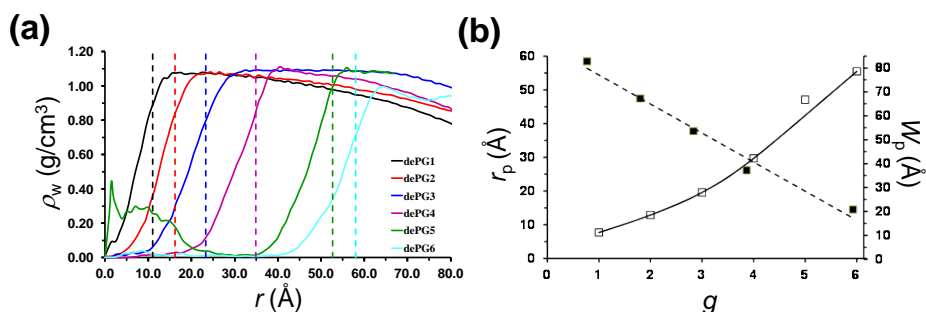


Figure 6.18. (a) Density profile for the *dePG**g* models representing the water density (ρ_w) against the distance to the backbone measured using the vector perpendicular to the helical axis (r). The profile displayed for each model corresponds to an average considering different cross-sections within a given snapshot. Data were obtained by averaging over the snapshots recorded during the last 10 ns of the MD relaxation runs. The profile displayed for *dePG*5 has been taken from reference [19]. It should be noted that decay of ρ_w at large values of r is due to boundary effects of the spherical solvent cap used for the simulations. (b) Graphical representation of the cross point (r_p ; filled squares) between the DP and water density profiles and the degree of water penetration (W_p ; empty squares) against g for *dePG**g*.

g . On the other hand, the distribution of water molecules inside these DPs is completely different from that reported for *dePG5* [19]. For example, for *dePG4* and *dePG6* the amount of water molecules filling the DP at a distance shorter than 22 and 43 Å, respectively, is practically negligible. In contrast, for *dePG5* water was mainly located at the pore close to the MB (for comparison Figure 6.18 includes the water density profile calculated for *dePG5*) [19]. The average water density inside the cylinder associated to *dePG5* is 0.23 g/cm³.

Figure 6.19 displays the superposition of the water (Figure 6.18) and the DP (Figure 6.16) density profiles for *dePG g* . The cross-point of the two profiles, which gives a rough estimation of the penetration of water into *dePG g* structure, occurs at $r_p = 7.7, 12.9, 19.6, 29.7, 47.1$ and 55.5 Å for $g = 1, 2, 3, 4, 5$ and 6 , respectively. Representation of r_p against g for *dePG g* with $g \neq 5$ (Figure 6.18b) indicates a parabolic dependence. As expected, the behavior of *dePG5* departs from the adjusted profile because of the unique structure of this DP. The incorporation of water at the outer parts of the DPs rather than at the internal ones is explained by complementarity between the water and DP density profiles (Figure 6.19). Thus, water does not penetrate into polymeric matrices as individual molecules but grouped in clusters [52]. The high DP density precludes the adsorption of such clusters of water clusters at the internal region while the DP density decreases at the outer regions.

The maximum water penetration degree (W_p) into DPs has been defined as follows:

$$W_p = \frac{|r(\rho_w = 0) - R|}{R} \cdot 100 \quad (6.3)$$

where $r(\rho_w = 0)$ is distance r from the backbone, measured using the vector perpendicular to the helical axis, with $\rho_w = 0$ and R is the radius of the DP (6.2). As occurred above, this definition cannot be applied to *dePG5* because of the particular distribution of water inside its heterogeneous structure (Figure 6.18a). The values of W_p , which are listed in Table 6.5, indicate that maximum water penetration decreases linearly with g (Figure 6.18b). This should be attributed to the fact that the backfolding, which increases with g , hinders the diffusion of water molecules inside the DP.

6.2.3.3. WATER...*dePG g* INTERACTIONS

As deduced from the chemical formulas displayed in Figure 6.14a, interactions between *dePG g* and water molecules surrounding (*i.e.* first hydration shell) or located inside the DPs structure essentially occur through $H_w \cdots O$ and $O_w \cdots H(-N)$ hydrogen bonds, where H_w and O_w refer to the hydrogen and oxygen atoms of water and $H(-N)$ corresponds to both amide and ammonium groups of the polymer. Figure 6.20a and Figure 6.20b represent the partial radial distribution function of $H_w \cdots O$ (g_{H_w-o}) and $O_w \cdots H(-N)$ (g_{O_w-H}) pairs, respectively.

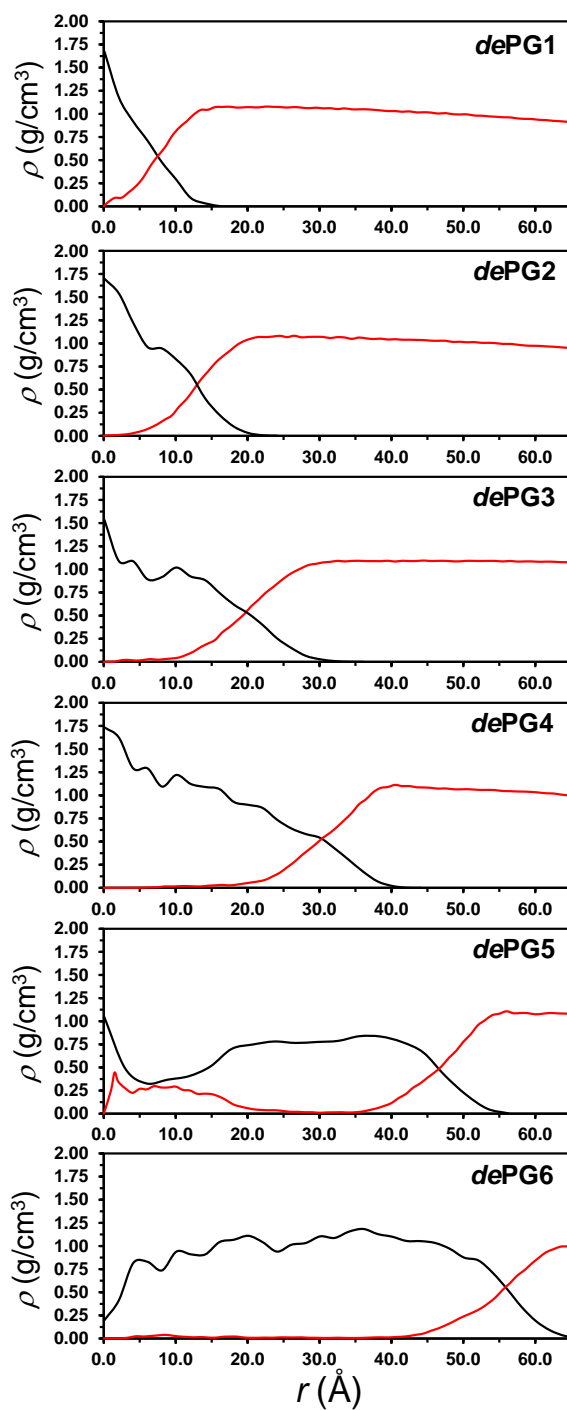


Figure 6.19. Superposition of the water (red) and *dePG*_{*g*} (black) density profiles. Profiles were calculated profiles as a function of the radial distance r from the DP backbone, measured using the vector perpendicular to the helical axis.

The $H_W \cdots O$ profiles, which were calculated considering the oxygen atoms located at both the amide and ether oxygen atoms of the DPS, reflect that the number of pairs increases with g . A peak centered at 1.85 Å is observed for $dePG_g$ with $g=1-6$, which has been attributed to the conventional $H_W \cdots O=C$ (amide) or $H_W \cdots O-C$ (ether) hydrogen bonds [53]. Furthermore, a small shoulder centered at 3.35 Å is detected in the g_{H_W-O} functions of $dePG_g$ with $g \geq 2$. Such shoulders transform into relatively pronounced peaks when the g_{H_W-O} functions are calculated excluding the oxygen atoms of the ether groups (not shown). According to this feature and previous studies on polyamines and polyimines [52], the shoulder has been associated with the formation of small water clusters around the amide groups [52]. Water molecules organized similarly around the oxygen atoms of $dePG_5$, as was previously discussed [19]. The g_{O_W-H} profiles represented in Figure 6.20b show a peak centered at around 1.80 Å. Furthermore, a small shoulder is also detected at ~ 3.2 Å that, as occurred above, has been attributed to the

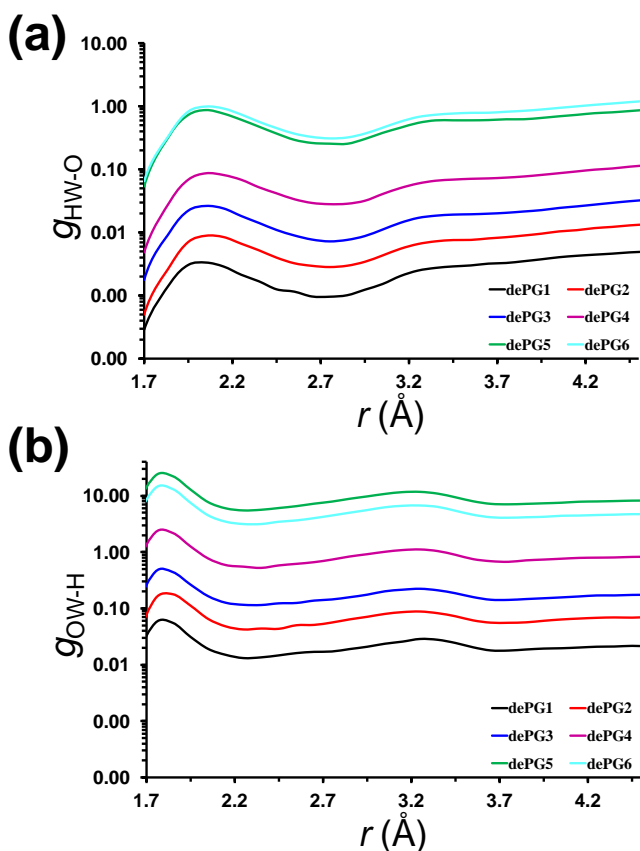


Figure 6.20. Radial distribution function of (a) $H_W \cdots O$ (g_{H_W-O}) and (b) $O_W \cdots H(-N)$ (g_{O_W-H}) pairs for hydrated $dePG_g$. H_W and O_W refer to the hydrogen and oxygen atoms of water molecules, respectively.

formation of small water clusters. Also, comparison between the g_{O_W-H} and g_{H_W-O} indicates that $O_W \cdots H(-N)$ hydrogen bonds are more abundant than the $H_W \cdots O$ ones.

The average number of water molecules directly interacting with atoms of $dePGg$ through either $H_W \cdots O$ or $O_W \cdots H$ hydrogen bonds (*i.e.* a cutoff $H \cdots O$ distance ≤ 2.5 Å) is $N_W = 14 \pm 2$ ($g = 1$), 28 ± 3 ($g = 2$), 76 ± 6 ($g = 3$), 130 ± 11 ($g = 4$), 154 ± 13 ($g = 5$) and 275 ± 14 ($g = 6$) per repeat unit. It should be emphasized that N_W includes both the water molecules located inside the DP and the water molecules surrounding the cylindrical structure of the DP since the interactions with the external ammonium groups have been also accounted. The small standard deviations indicate that the values of N_W are very stable along the trajectories. On the other hand, the total number of water molecules located inside the DP, which include both water molecules hydrogen bonded to atoms of the DP as well as those hydrogen bonded to other water molecules, summed to water molecules interacting with the external ammonium groups ($N_{T,W}$) is very similar to N_W (*i.e.* the difference between $N_{T,W}$ and N_W is lower than 7% in all cases, with $N_{T,W} > N_W$). According to $N_{T,W}$, the percent volume occupied by water molecules inside the cylinder (ρ_w) associated to each $dePGg$ is 63% ($g = 1$), 55% ($g = 2$), 52% ($g = 3$), 42% ($g = 4$), 27% ($g = 5$) and 33% ($g = 6$). This high amount of volume can be occupied, totally or partially, by other different compounds, as was proven in a recent study in which the DPs studied in this work were used as carriers of fatty acids [54].

The orientation of water molecules surrounding (*i.e.* distance ≤ 2.5 Å) the oxygen and nitrogen atoms of the DPs has been evaluated by determining the $O_W-H_W \cdots O$ or $O_W \cdots H-N$ angular distribution functions (Figure 6.21a and Figure 6.21b, respectively). The most favorable orientation of $\angle O_W-H_W \cdots O$ angle ranges from 57° ($dePG1$) to 83° ($dePG6$). The relatively small influence of g has been attributed to the fact that penetrated water molecules are confined in regions of reduced dimensions, which makes difficult the re-orientation of water molecules to improve the hydrogen bonding interaction with ether and amide oxygen atoms. The situation is relatively similar for $O_W \cdots H-N$ angular distribution functions, which also reflect that a large number of hydrogen bonded water molecules form $\angle O_W \cdots H-N$ angles smaller than 120° .

6.2.4. CONCLUSIONS

MD simulations of $dePGg$ in aqueous solution have been used to investigate the effects produced by the deprotection of PGg in the divergent synthesis approach, in which the Boc groups attached to the external amines are eliminated. Electrostatic strain provokes the enlargement of the molecular length and a small rearrangement and stretching of the dendrons, which results in a reduction of the density (9-15%) with respect to PGg . Despite of this, for each g both the cylinder radius and amount of backfolding of peripheral dendrons remain relatively similar for $dePGg$ and PGg . Therefore, from a

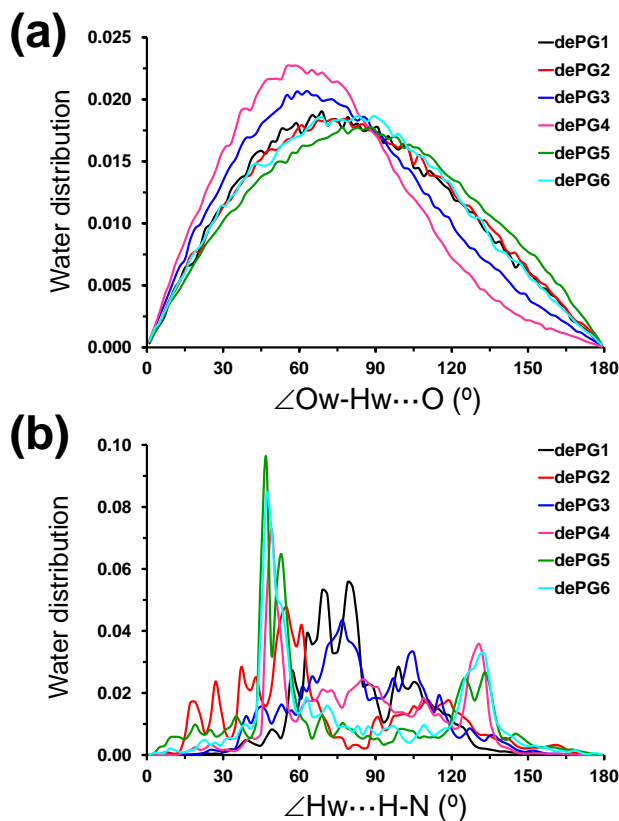


Figure 6.21. Angular distribution functions for water \cdots dePG g hydrogen bonding interactions: (a) $\angle O_w-H_w \cdots O$; and (b) $\angle O_w \cdots H-N$. Hydrogen bonds were defined using a H \cdots O cutoff distance of 2.50 Å

structural point of view elimination of the Boc groups located at the external layer of PG g and the introduction of positive charges do not provoke significant changes but only the appropriated conditions to facilitate the penetration of water.

Water density profiles calculated as a function of the radial distance r from the MB indicates that the distance between the dePG g helical axis and the penetrated water molecules increases with g . The reduction of the water degree penetration has been attributed to the backfolding, which increases with g . Thus, the approximation of the external dendrons to the dePG g backbone hinders the progress of water molecules inside the structure. Furthermore, the reduced dimensions of the regions in which water molecules are confined inside the DPS preclude the formation of water \cdots dePG g interactions with optimum hydrogen bonding angle. Despite of this, the number of water molecules interacting with deprotected DPS increases rapidly with g , growing from 14 ± 2 ($g = 1$) to 275 ± 14 ($g = 6$) per repeat unit.

REFERENCES

- [1] A.D. Schluter; *A covalent chemistry approach to giant macromolecules with cylindrical shape and an engineerable interior and surface*; Top Curr Chem **245**, 151 (2005).
- [2] H. Frauenrath; *Dendronized polymers - building a new bridge from molecules to nanoscopic objects*; Prog Polym Sci **30**, 325 (2005).
- [3] H. Yu, A.D. Schluter, B.Z. Zhang; *Synthesis of dendronized polymers by a "n+2" approach*; Macromolecules **45**, 8555 (2012).
- [4] Y.F. Guo, J.D. van Beek, B.Z. Zhang, M. Colussi, P. Walde, A. Zhang, M. Kroger, A. Halperin, A.D. Schluter; *Tuning polymer thickness: synthesis and scaling theory of homologous series of dendronized polymers*; J Am Chem Soc **131**, 11841 (2009).
- [5] A.D. Schluter, J.P. Rabe; *Dendronized polymers: Synthesis, characterization, assembly at interfaces, and manipulation*; Angew Chem Int Edit **39**, 864 (2000).
- [6] Z.S. Bo, J.P. Rabe, A.D. Schluter; *A poly(para-phenylene) with hydrophobic and hydrophilic dendrons: Prototype of an amphiphilic cylinder with the potential to segregate lengthwise*; Angew Chem Int Edit **38**, 2370 (1999).
- [7] V. Percec, C.H. Ahn, T.K. Bera, G. Ungar, D.J.P. Yeardley; *Coassembly of a hexagonal columnar liquid crystalline superlattice from polymer(s) coated with a three-cylindrical bundle supramolecular dendrimer*; Chem-Eur J **5**, 1070 (1999).
- [8] C.O. Liang, B. Helms, C.J. Hawker, J.M.J. Frechet; *Dendronized cyclopolymers with a radial gradient of polarity and their use to catalyze a difficult esterification*; Chem Commun, 2524 (2003).
- [9] B.M.J.M. Suijkerbuijk, L.J. Shu, R.J.M.K. Gebbink, A.D. Schluter, G. van Koten; *Single-site catalysts on a cylindrical support beyond nanosize*; Organometallics **22**, 4175 (2003).
- [10] Z.N. Bao, K.R. Amundson, A.J. Lovinger; *Poly(phenylenevinylene)s with dendritic side chains: Synthesis, self-ordering, and liquid crystalline properties*; Macromolecules **31**, 8647 (1998).
- [11] A.P.H.J. Schenning, R.E. Martin, M. Ito, F. Diederich, C. Boudon, J.P. Gisselbrecht, M. Gross; *Dendritic rods with a poly(triacetylene) backbone: insulated molecular wires*; Chem Commun, 1013 (1998).
- [12] T. Sato, D.L. Jiang, T. Aida; *A blue-luminescent dendritic rod: Poly(phenyleneethynylene) within a light-harvesting dendritic envelope*; J Am Chem Soc **121**, 10658 (1999).
- [13] D. Joester, M. Losson, R. Pugin, H. Heinzelmann, E. Walter, H.P. Merkle, F. Diederich; *Amphiphilic dendrimers: Novel self-assembling vectors for efficient gene delivery*; Angew Chem Int Edit **42**, 1486 (2003).
- [14] I. Gossel, L.J. Shu, A.D. Schluter, J.P. Rabe; *Molecular structure of single DNA complexes with positively charged dendronized polymers*; J Am Chem Soc **124**, 6860 (2002).
- [15] S. Fornera, T.E. Balmer, B. Zhang, A.D. Schluter, P. Walde; *Immobilization of peroxidase on SiO₂ surfaces with the help of a dendronized polymer and the avidin-biotin system*; Macromol Biosci **11**, 1052 (2011).
- [16] B.Z. Zhang, R. Wepf, M. Kroger, A. Halperin, A.D. Schluter; *Height and width of adsorbed dendronized polymers: electron and atomic force microscopy of homologous series*; Macromolecules **44**, 6785 (2011).

- [17] B.Z. Zhang, R. Wepf, K. Fischer, M. Schmidt, S. Besse, P. Lindner, B.T. King, R. Sigel, P. Schurtenberger, Y. Talmon, Y. Ding, M. Kroger, A. Halperin, A.D. Schluter; *The largest synthetic structure with molecular precision: towards a molecular object*; *Angew Chem Int Edit* **50**, 737 (2011).
- [18] O. Bertran, B.Z. Zhang, A.D. Schluter, A. Halperin, M. Kroger, C. Aleman; *Computer simulation of dendronized polymers: organization and characterization at the atomistic level*; *Rsc Adv* **3**, 126 (2013).
- [19] O. Bertran, B. Zhang, A.D. Schlüter, M. Kröger, C. Alemán; *Computer simulation of fifth generation dendronized polymers: impact of charge on internal organization*; *J Phys Chem B* **117**, 6007 (2013).
- [20] J. Barner, F. Mallwitz, L.J. Shu, A.D. Schluter, J.P. Rabe; *Covalent connection of two individual polymer chains on a surface: An elementary step towards molecular nanoconstructions*; *Angew Chem Int Edit* **42**, 1932 (2003).
- [21] A. Zhang, L. Okrasa, T. Pakula, A.D. Schluter; *Homologous series of dendronized poly methacrylates with a methyleneoxycarbonyl spacer between the backbone and dendritic side chain: Synthesis, characterization, and some bulk properties*; *J Am Chem Soc* **126**, 6658 (2004).
- [22] A.K. Andreopoulou, B. Carbonnier, J.K. Kallitsis, T. Pakula; *Dendronized rigid-flexible macromolecular architectures: Syntheses, structure, and properties in bulk*; *Macromolecules* **37**, 3576 (2004).
- [23] R. Pasquino, B. Zhang, R. Sigel, H. Yu, M. Ottiger, O. Bertran, C. Aleman, A.D. Schluter, D. Vlassopoulos; *Linear viscoelastic response of dendronized polymers*; *Macromolecules* **45**, 8813 (2012).
- [24] A. Kroeger, B.Z. Zhang, C. Rosenauer, A.D. Schluter, G. Wegner; *Solvent induced phenomena in a dendronized linear polymer*; *Colloid Polym Sci* **291**, 2879 (2013).
- [25] F. Rodriguez-Roperio, M. Canales, D. Zanuy, A. Zhang, D. Schluter, C. Aleman; *Helical dendronized polymers with chiral second-generation dendrons: atomistic view and driving forces for structure formation*; *J Phys Chem B* **113**, 14868 (2009).
- [26] A. Zhang, F. Rodriguez-Roperio, D. Zanuy, C. Aleman, E.W. Meijer, A.D. Schluter; *A rigid, chiral, dendronized polymer with a thermally stable, right-handed helical conformation*; *Chem-Eur J* **14**, 6924 (2008).
- [27] Y. Ding, H.C. Ottinger, A.D. Schluter, M. Kroger; *From atomistic simulation to the dynamics, structure and helical network formation of dendronized polymers: The Janus chain model*; *J Chem Phys* **127** (2007).
- [28] K.C.F. Leung, P.M. Mendes, S.N. Magonov, B.H. Northrop, S. Kim, K. Patel, A.H. Flood, H.R. Tseng, J.F. Stoddart; *Supramolecular self-assembly of dendronized polymers: Reversible control of the polymer architectures through acid-base reactions*; *J Am Chem Soc* **128**, 10707 (2006).
- [29] W. Stocker, B. Karakaya, B.L. Schurmann, J.P. Rabe, A.D. Schluter; *Ordered dendritic nanorods with a poly(p-phenylene) backbone*; *J Am Chem Soc* **120**, 7691 (1998).
- [30] D.K. Christopoulos, A.F. Terzis, A.G. Vanakaras, D.J. Photinos; *Helix formation in linear achiral dendronized polymers: A computer simulation study*; *J Chem Phys* **125** (2006).
- [31] J.C. Phillips, R. Braun, W. Wang, J. Gumbart, E. Tajkhorshid, E. Villa, C. Chipot, R.D. Skeel, L. Kale, K. Schulten; *Scalable molecular dynamics with NAMD*; *J Comput Chem* **26**, 1781 (2005).
- [32] W.D. Cornell, P. Cieplak, C.I. Bayly, I.R. Gould, K.M. Merz, D.M. Ferguson, D.C. Spellmeyer, T. Fox, J.W. Caldwell, P.A. Kollman; *A 2nd generation force-field for the simulation of proteins, nucleic-acids, and organic-molecules*; *J Am Chem Soc* **117**, 5179 (1995).
- [33] J.M. Wang, R.M. Wolf, J.W. Caldwell, P.A. Kollman, D.A. Case; *Development and testing of a general amber force field*; *J Comput Chem* **25**, 1157 (2004).
-

- [34] P. Cieplak, W.D. Cornell, C. Bayly, P.A. Kollman; *Application of the multimolecule and multiconformational resp methodology to biopolymers - charge derivation for DNA, RNA, and proteins*; J Comput Chem **16**, 1357 (1995).
- [35] H.J.C. Berendsen, J.P.M. Postma, W.F. Vangunsteren, A. Dinola, J.R. Haak; *Molecular-Dynamics with coupling to an external bath*; J Chem Phys **81**, 3684 (1984).
- [36] J.P. Ryckaert, G. Ciccotti, H.J.C. Berendsen; *Numerical-integration of cartesian equations of motion of a system with constraints - molecular-dynamics of n-alkanes*; J Comput Phys **23**, 327 (1977).
- [37] I.K. McDonald, J.M. Thornton; *Satisfying hydrogen-bonding potential in proteins*; J Mol Biol **238**, 777 (1994).
- [38] E.N. Baker, R.E. Hubbard; *Hydrogen-bonding in globular-proteins*; Prog Biophys Mol Bio **44**, 97 (1984).
- [39] M.O. Sinnokrot, E.F. Valeev, C.D. Sherrill; *Estimates of the ab initio limit for pi-pi interactions: The benzene dimer*; J Am Chem Soc **124**, 10887 (2002).
- [40] S. Tsuzuki, K. Honda, T. Uchimaru, M. Mikami; *Ab initio calculations of structures and interaction energies of toluene dimers including CCSD(T) level electron correlation correction*; J Chem Phys **122** (2005).
- [41] R.A. Weiss, W.C. Yu; *Viscoelastic behavior of very lightly sulfonated polystyrene ionomers*; Macromolecules **40**, 3640 (2007).
- [42] L. Leibler, M. Rubinstein, R.H. Colby; *Dynamics of reversible networks*; Macromolecules **24**, 4701 (1991).
- [43] B.M. Rosen, C.J. Wilson, D.A. Wilson, M. Peterca, M.R. Imam, V. Percec; *Dendron-Mediated Self-Assembly, Disassembly, and self-organization of complex systems*; Chem Rev **109**, 6275 (2009).
- [44] B.Z. Zhang, A. Kroeger, A.D. Schluter, G. Wegner; *The viscosity law of dendronized linear polymers*; Macromol Rapid Comm **34**, 1537 (2013).
- [45] E. Cordova-Mateo, O. Bertran, B.Z. Zhang, D. Vlassopoulos, R. Pasquino, A.D. Schluter, M. Kroger, C. Aleman; *Interactions in dendronized polymers: intramolecular dominates intermolecular*; Soft Matter **10**, 1032 (2014).
- [46] G. Fuhrmann, A. Grotzky, R. Lukic, S. Matoori, P. Luciani, H. Yu, B.Z. Zhang, P. Walde, A.D. Schluter, M.A. Gauthier, J.C. Leroux; *Sustained gastrointestinal activity of dendronized polymer-enzyme conjugates*; Nat Chem **5**, 582 (2013).
- [47] A. Grotzky, T. Nauser, H. Erdogan, A.D. Schluter, P. Walde; *A fluorescently labeled dendronized polymer-enzyme conjugate carrying multiple copies of two different types of active enzymes*; J Am Chem Soc **134**, 11392 (2012).
- [48] D. Kurzbach, D.R. Kattnig, B.Z. Zhang, A.D. Schluter, D. Hinderberger; *Assessing the solution shape and size of charged dendronized polymers using double electron-electron resonance*; J Phys Chem Lett **2**, 1583 (2011).
- [49] L. Grebikova, P. Maroni, L. Muresan, B.Z. Zhang, A.D. Schluter, M. Borkovec; *Interactions between individual charged dendronized polymers and surfaces*; Macromolecules **46**, 3603 (2013).
- [50] W.L. Jorgensen, J. Chandrasekhar, J.D. Madura, R.W. Impey, M.L. Klein; *Comparison of simple potential functions for simulating liquid water*; J Chem Phys **79**, 926 (1983).
- [51] T. Darden, D. York, L. Pedersen; *Particle mesh ewald - a n.log(n) method for ewald sums in large systems*; J Chem Phys **98**, 10089 (1993).
- [52] J. Casanovas, M. Canales, G. Fabregat, A. Meneguzzi, C. Aleman; *Water absorbed by polyaniline emeraldine tends to organize, forming nanodrops*; J Phys Chem B **116**, 7342 (2012).
- [53] R. Taylor, O. Kennard; *Hydrogen-bond geometry in organic-crystals*; Accounts Chem Res **17**, 320 (1984).

- [54] D. Kurzbach, D.R. Kattnig, B.Z. Zhang, A.D. Schluter, D. Hinderberger; *Loading and release capabilities of charged dendronized polymers revealed by EPR spectroscopy*; Chem Sci **3**, 2550 (2012).

CHAPTER 7
THIOPHENE-BASED DENDRIMERS AND DENDRONIZED POLYMERS

“There is no subject, however complex, which, if studied with patience and intelligence will not become more complex”

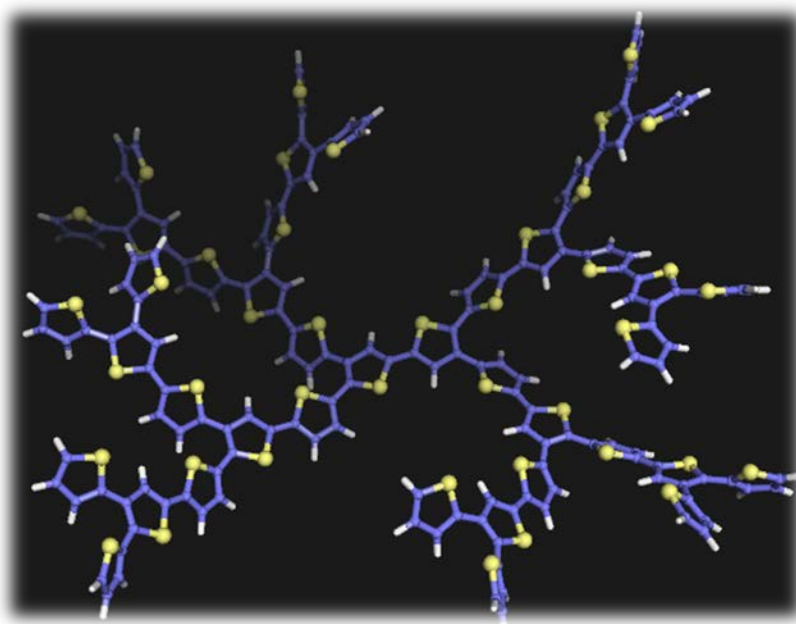
Gordon Rohman

THIOPHENE-BASED DENDRIMERS AND DENDRONIZED POLYMERS

This chapter focusses on the study of both dendrimers and dendronized polymers based on thiophene dendrons through quantum mechanics and molecular dynamics. Section 7.1 analyzes the main properties of symmetric and unsymmetric all-thiophene dendrimers containing up to 45 thiophene rings in the neutral and oxidized state. Results, which were obtained using quantum mechanical approaches, were published in the journal *ChemPhysChem* under the title *Properties of Oligothiophene Dendrimers as a Function of Molecular Architecture and Generation Number* (2012). Section 7.2 is devoted to the study of the internal organization of macromonomers based on all-thiophene dendrons of second and third generation attached to a phenyl core using density functional theory calculations and to the construction of their corresponding dendronized polymers using classical mechanics formalism. The results derived from these studies has been reflected in an article entitled *Internal Organization of Macromonomers and Dendronized Polymers based on Thiophene Dendrons*, which has been recently submitted for publication.

7.1. PROPERTIES OF OLIGOTHIOPHENE DENDRIMERS

Density functional and time-dependent density functional calculations using the B3LYP method combined with the 6-31G(d) and 6-311++G(d,p) basis sets are performed on symmetric and unsymmetric all-thiophene dendrimers containing up to 45 thiophene rings. Calculations consider both the neutral and the oxidized states of each dendrimer. The results are used to examine the molecular geometry, the ionization potential, the lowest π - π^* transition energy, and the shape of the frontier orbitals. The molecular and electronic properties of these systems depend not only on the number of thiophene rings, as typically occurs for linear oligothiophenes, but also on their symmetric/unsymmetric molecular architecture. Two mathematical models developed to



predict the lowest π - π^* transition energy of all-thiophene dendrimers that are inaccessible to quantum mechanical calculations are tested on a dendrimer with 90 thiophene rings.

7.1.1. INTRODUCTION

Dendrimers are ideally perfect monodisperse macromolecules composed of a multifunctional core unit to which a defined number of subunits, known as dendrons, are attached to give a regioregular branched three-dimensional architecture [1-5]. Three topological regions coexist in dendrimers: the inner dense core, the dendritic region around the core, and the external surface. Interest in these shape-persistent molecules with nanometer sizes increases with increasing generation number g , which is defined as the number of dendrons between the inner core and the terminal unit. However, the fabrication of space-filling conjugated dendrimers with rigid structures is a very difficult task, particularly when $g > 2$. In spite of this, phenylacetylene [6,7], phenylene vinylene [8,9], and polyphenylene [10] dendrimers were developed in the late 1990s.

More recently, all-thiophene dendrimers were synthesized and characterized for the first time by Advincula and co-workers [11-13], who prepared n Th dendrimers with $n = 3, 6, 7, 14, 15,$ and 30 (where Th refers to the thiophene ring and n indicates the number of thiophene rings). These systems (Figure 7.1) represented a key stage in the ongoing evolution of the chemistry of conjugated polymers, because of promising applications of oligothiophenes and polythiophenes in the organic semiconductors. Specifically, organic light-emitting diodes, field-effect transistors, and solar cells have been fabricated by using

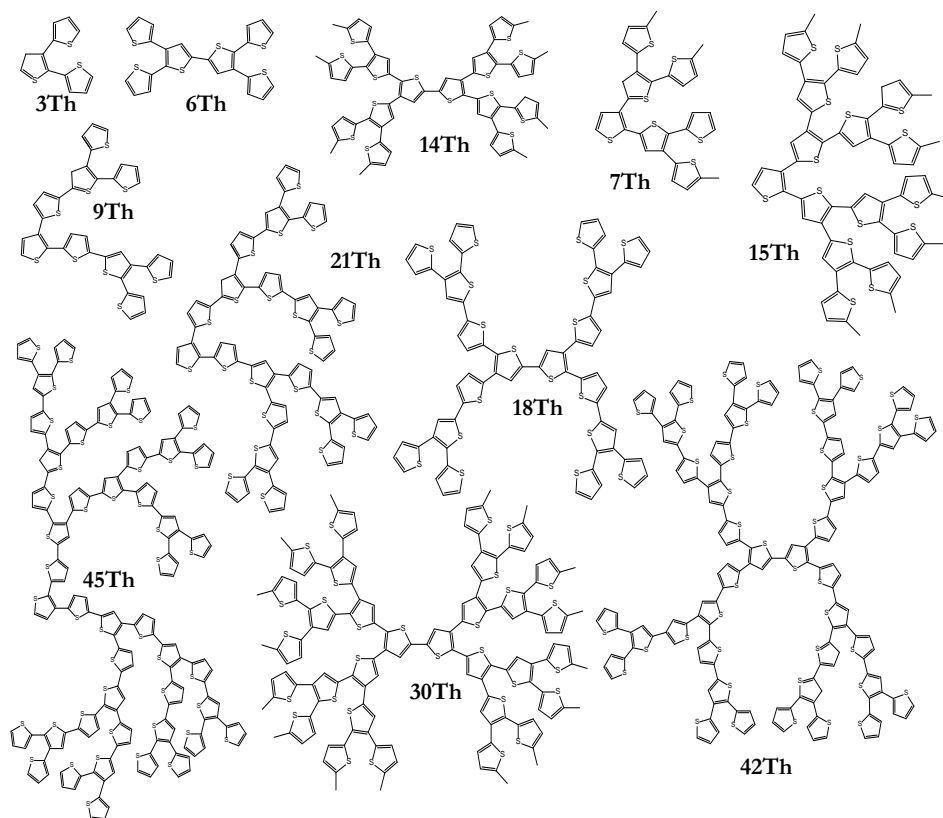


Figure 7.1. Chemical structure of the dendrimers studied in this work.

these conventional all-thiophene systems [14-20]. Besides the Adviculas systems, new all-thiophene dendrimers with excellent nonlinear absorption properties have been reported by Bäuerle and co-workers [21-24].

Given the importance of the electronic properties in the application of all-thiophene dendrimers, theoretical studies based on quantum mechanics are necessary, not only to provide comprehensive understanding at the microscopic level, but also to gain deeper insight into the intrinsic characteristics of these materials. In this context, we recently used quantum mechanical calculations to study the structural and electronic properties of n Th dendrimers with $n = 3, 7, 14, 15,$ and 30 in both the neutral and oxidized (p-doped) states [25]. More specifically, we examined the ionization potential (IP) and the lowest π - π^* transition energy \mathcal{E}_g for these systems using both DFT and time-dependent DFT (TD-DFT) calculations at the (U)B3LYP/6-31G(d) level. The results indicated that the IP per thiophene ring and \mathcal{E}_g decrease with the inverse of the reciprocal α -conjugated chain of the dendrimer (*i.e.*, with increasing generation). Moreover, the \mathcal{E}_g value predicted at the

B3LYP/6-31G(d) level for an infinite generation dendrimer was 2.08 eV, which indicates that these materials are potential candidates for optoelectronic applications.

Herein we extend our previous theoretical study [25] on all-thiophene dendrimers to investigate different aspects of this important family of compounds. Specifically, quantum mechanical calculations of symmetric and unsymmetric n Th dendrimers with $n = 3, 6, 7, 9, 14, 15, 18, 21, 30, 42,$ and 45 (Figure 7.1) were performed to address the influence of n and the molecular architecture on the following issues: 1) molecular geometry; 2) IP and the \mathcal{E}_g ; and 3) the shape of the frontier orbitals. Finally, quantum mechanical results were used to derive simple mathematical models to predict the \mathcal{E}_g of all-thiophene dendrimers with a very large number of rings, independently of g and their symmetric or unsymmetric molecular architectures. These models were developed by considering the dependence of \mathcal{E}_g on the following variables: 1) the number of thiophene rings and g ; and 2) the number of thiophene rings and the molecular architecture (*i.e.* the fraction of $\alpha - \alpha$ and $\alpha - \beta$ linkages).

7.1.2. METHODS

The conformational preferences of 3Th were rigorously characterized in our previous work [25] by calculating the potential-energy surface derived from systematic variation of their inter-ring dihedral angles. The most stable arrangement of 3Th was used to build up 6Th, 7Th, and 9Th, which after complete geometry optimization were used to construct 14Th and 15Th. The initial structures of the remaining n Th dendrimers studied in this work were built by using the same growth principle. The chemical structure and molecular architecture of all investigated dendrimers are displayed in Figure 7.1. These systems can be classified according to both the molecular architecture and generation number. Regarding the former, unsymmetric (*i.e.*, $n = 3, 7, 9, 15, 21,$ and 45) and symmetric (*i.e.*, $n = 6, 14, 18, 30,$ and 42) architectures are found, the latter being derived from dimerization of the former. With respect to generation number, five types are identified by considering the thiophene ring as the basic unit (dendron): $g = 2$ ($n = 3$ and 6), $g = 3$ ($n = 7$ and 14), $g = 4$ ($n = 9, 15, 18,$ and 30), $g = 6$ ($n = 21$ and 42), and $g = 8$ ($n = 45$).

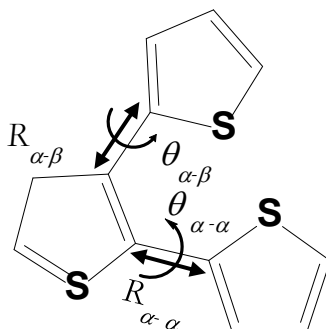
All calculations were carried out with the Gaussian 03 (Revision B.02) program package [26]. Complete geometry optimizations of the n Th dendrimers were performed in all cases by using the B3LYP functional [27,28] combined with the 6-31G(d) [29] and 6-311++ G(d,p) [30,31] basis sets. The molecular geometries of species in the neutral state (closed-shell systems) were optimized by using the restricted formalism of the B3LYP functional, while geometry optimizations of dendrimers in the oxidized state (open-shell systems) were carried out by using the unrestricted formalism (UB3LYP). For n Th and n Th⁺ dendrimers with $n < 30$, frequency calculations were performed to verify

the nature of the minimum state of the stationary points obtained by geometry optimization at the (U)B3LYP/6-31G(d) level. The B3LYP functional was selected not only for consistency with our previous study [25] but also because recent studies [32-36] on linear oligothiophenes with a large number of repeating units (*i.e.*, up to 50) indicated that this is a very accurate method for predicting \mathcal{E}_g and IP of conjugated polymers. Indeed, they evidenced that the excellent agreement between the calculated and experimental \mathcal{E}_g values was partially due to the cancellation of several errors from the B3LYP methodology and from comparison of gas-phase calculations with experimental measures performed in condensed phases. The latter was explicitly shown in a recent study by comparing the IP and \mathcal{E}_g calculated in the gas phase and in solution (acetonitrile and water) of linear oligothiophenes with up to 30 repeating units [36].

The IP of each calculated dendrimer was determined by two different methodologies. The first was the Koopmans' theorem [37], according to which the IPs were taken as the negative of the HOMO (Highest Occupied Molecular Orbital) energy (*i.e.*, $\text{IP}^{\text{KT}} = -\mathcal{E}_{\text{HOMO}}$). Although Koopmans' theorem does not apply to DFT and the energies of Kohn–Sham orbitals do not involve any physical meaning, Janak's theorem [38] was used by Perdew [39] to show the connection between IP and $\mathcal{E}_{\text{HOMO}}$. More accurate values were obtained by calculating the IPs as the energy difference between optimized structures of the oxidized and neutral species ($\text{IP}^{\Delta\text{SCF}} = E_{\text{oxidized}} - E_{\text{neutral}}$). The $\text{IP}^{\Delta\text{SCF}}$ takes into account both the electronic and geometric relaxation of the ionized state, while these two contributions are completely neglected in IP^{KT} .

The \mathcal{E}_g values were estimated by two different strategies. In the first, \mathcal{E}_g was approximated as the difference between the energies of the frontier orbitals: $\mathcal{E}_g = \mathcal{E}_{\text{LUMO}} - \mathcal{E}_{\text{HOMO}}$. In an early work, Levy and Nagy showed that in DFT calculations \mathcal{E}_g can be correctly estimated using this procedure [40]. The second estimation of \mathcal{E}_g was derived from the excitation energies calculated with TD-DFT. This method, which is widely applied to study the UV/Vis spectra of conjugated organic compounds, provides a robust and efficient description of the low-lying molecular states [41-43]. Electronic excitations were evaluated with the B3LYP functional combined with the 6-31G(d) and 6-311++G(d,p) basis sets by using the previously optimized geometries. For open-shell species, the $\langle S^2 \rangle$ values of the ground-state Kohn–Sham determinant obtained with the B3LYP functional lie in the range of 0.75–0.79, that is, the spin contamination is small. In all cases \mathcal{E}_g was extracted from the first low-lying transition with high oscillator strength.

Finally, the theoretically predicted \mathcal{E}_g values were used to derive two simple mathematical models to predict the electronic properties for n Th dendrimers with $n > 45$. The first model considers the dependence of \mathcal{E}_g on the number of thiophene rings n



Scheme 7.1

and the generation number g , while in the second the variables are n , the fraction of $\alpha - \alpha$ linkages ($\chi_{\alpha-\alpha}$) and the fraction of $\alpha - \beta$ linkages ($1 - \chi_{\alpha-\alpha}$).

7.1.3. RESULTS AND DISCUSSION

7.1.3.1. CONFORMATION AND GEOMETRIC PARAMETERS

Complete geometry optimizations of $n\text{Th}$ and $n\text{Th}^+$ with $n = 3, 6, 7, 9, 14, 15, 18, 21, 30, 42,$ and 45 (Figure 7.1) were carried out at the (U)B3LYP/6-31G(d) level. The resulting structures were subsequently used as starting points for complete geometry reoptimization at the (U)B3LYP/6-311++G(d,p) level. Unfortunately, the latter calculations were only possible for dendrimers with $n \leq 21$; the computer resources needed for systems with $n = 30, 42,$ and 45 were prohibitive with such large basis set.

Table 7.1 compares the average inter-ring distance for both $\alpha - \alpha$ and $\alpha - \beta$ linkages ($R_{\alpha-\alpha}$ and $R_{\alpha-\beta}$, respectively; see Scheme 7.1) of the all the calculated systems. The influence of n and the basis set is almost negligible for $n\text{Th}$ with exception of the $R_{\alpha-\beta}$ distance for 3Th. In this case the smallest basis set predicts that this distance is about 0.02 Å smaller than for neutral dendrimers with $n > 3$. Both UB3LYP/6-31G(d) and UBLYP/6-31++G(d,p) geometries are also fully consistent for $n\text{Th}^+$, even though the two inter-ring distances depend on n . Thus, in general $R_{\alpha-\alpha}$ and $R_{\alpha-\beta}$ are slightly shorter for oxidized dendrimers with $n \leq 9$ compared to those with $n > 9$.

The average inter-ring dihedral angles for the $\alpha - \alpha$ and $\alpha - \beta$ linkages ($\theta_{\alpha-\alpha}$ and $\theta_{\alpha-\beta}$, respectively; see Scheme 7.1) of the calculated dendrimers are listed in Table 7.2; the values of the dihedral angle associated with dimerization of symmetric systems (θ_{D-D}) are also displayed. As previously found for the inter-ring distances, the inter-ring dihedral angles predicted by the two basis sets are in excellent agreement, the largest differences being 4.5 and 6.7° for neutral and oxidized systems, respectively. On the other hand, if 3Th and 3Th⁺ are excluded from the analysis because of their small size, the

inter-ring dihedral angles are affected by n , and this feature is particularly pronounced for the oxidized dendrimers. However, such differences are not large enough to alter the general shape of the molecules (*i.e.* maximum deviations of only 11° are detected when different $n\text{Th}^+$ molecules are compared).

Figure 7.2 displays the molecular shape of selected dendrimers in both the neutral and oxidized states after geometry optimization. Oxidation causes some conformational changes independently of the symmetric or unsymmetric molecular architecture and of the generation number. More specifically, the branches are more elongated in the oxidized systems than in the neutral ones, and the structures become less compact on removal of one electron. This change in the molecular shape should be attributed to the rigidity induced by the electronic structure of the oxidized molecules. Thus, the benzenoid-type structure of neutral conjugated polyheterocyclic systems transforms into a quinoid-type structure on oxidation [44-46].

7.1.3.2. IONIZATION POTENTIAL

Figure 7.3 plots IP^{KT} and $\text{IP}^{\Delta\text{SCF}}$ calculated for the investigated $n\text{Th}$ dendrimers against $1/n$. There is a good linear behavior (correlation coefficients $R^2 > 0.92$) in all cases, which is consistent with fact that electron delocalization increases with increasing size of the dendrimers. Recent studies on linear oligothiophenes (*i.e.* adjacent repeating units connected through $\alpha - \alpha$ linkages in all cases) showed a linear relationship between IP and \mathcal{E}_g and $1/n$ for $n < 12$, while second- or higher-order polynomials were required to describe the behavior of oligomers with $n > 12$ [32,33,36,47]. This saturation behavior was obtained by using the same methodological approach as in the present work: gas-phase calculations at the B3LYP/6-31G(d) level on systems with up to $n = 50$. However, no saturation is detected in Figure 7.3 for IP^{KT} and $\text{IP}^{\Delta\text{SCF}}$ of $n\text{Th}$ dendrimers. This is an important difference between linear and dendronized oligothiophenes, which must be attributed to the existence in the latter of $\alpha - \beta$ linkages between adjacent repeating unit, which in turn allow different molecular architectures and generation numbers to be defined (as shown above).

The influence of the basis set on IP^{KT} decreases with $1/n$, whereas for $\text{IP}^{\Delta\text{SCF}}$ it remains approximately constant for $n > 9$. Comparison of IP^{KT} and $\text{IP}^{\Delta\text{SCF}}$ values indicates that electronic and geometric relaxation effects are not negligible, even though they decrease with $1/n$. Thus, the IP^{KT} calculated with the 6-31G(d) basis set for 3Th is approximately 22 % lower than $\text{IP}^{\Delta\text{SCF}}$, and this underestimation decreases to about 8% for 45Th. Similarly, the IP of 3Th is 17 % underestimated by 6-311++ G(d,p) when the electronic and geometric relaxations of the oxidized specie are neglected, while the underestimation is about 10 % for 21Th. These results clearly indicate that the IP^{KT} provided by the B3LYP functional are not predicted satisfactorily; consideration of relaxation effects is necessary.

Table 7.1. Average Inter-Ring Distances (Å) for the $\alpha - \alpha$ and $\alpha - \beta$ Linkages ($R_{\alpha-\alpha}$ and $R_{\alpha-\beta}$, respectively; see Scheme 7.1) of nT and nT^+ Dendrimers Calculated at the (U)B3LYP/6-31G(d) and (U)B3LYP/6-311++G(d,p) Levels. Standard Deviations (Å) are Included.

n	(U)B3LYP/6-31G(d)				(U)B3LYP/6-311++G(d,p)			
	nT		nT^+		nT		nT^+	
	$R_{\alpha-\alpha}$	$R_{\alpha-\beta}$	$R_{\alpha-\alpha}$	$R_{\alpha-\beta}$	$R_{\alpha-\alpha}$	$R_{\alpha-\beta}$	$R_{\alpha-\alpha}$	$R_{\alpha-\beta}$
3	1.457	1.446	1.422	1.432	1.459	1.465	1.420	1.433
6	1.456	1.466	1.433	1.460	1.456	1.466	1.431	1.460
7	1.458±0.001	1.466±0.001	1.435±0.006	1.455±0.009	1.457±0.001	1.465±0.001	1.434±0.001	1.455±0.008
9	1.456±0.001	1.465±0.002	1.434±0.003	1.458±0.009	1.456±0.001	1.465±0.002	1.439±0.003	1.458±0.009
14	1.455±0.001	1.467±0.002	1.443±0.007	1.464±0.004	1.455±0.002	1.465±0.001	1.440±0.008	1.464±0.003
15	1.457±0.002	1.465±0.001	1.445±0.004	1.462±0.004	1.457±0.008	1.465±0.001	1.444±0.004	1.462±0.003
18	1.455±0.002	1.465±0.001	1.444±0.008	1.463±0.005	1.454±0.002	1.465±0.001	1.443±0.009	1.463±0.005
21	1.455±0.002	1.465±0.002	1.446±0.006	1.463±0.005	1.454±0.002	1.465±0.001	1.446±0.006	1.463±0.005
30	1.456±0.002	1.466±0.001	1.449±0.005	1.466±0.003				
42	1.454±0.002	1.465±0.001	1.449±0.005	1.465±0.003				
45	1.454±0.002	1.465±0.001	1.450±0.005	1.465±0.003				

Table 7.2. Average Inter-Ring Dihedral Angles ($^{\circ}$) for the $\alpha - \alpha$ and $\alpha - \beta$ Linkages ($\theta_{\alpha-\alpha}$ and $\theta_{\alpha-\beta}$, respectively; see Scheme 7.1) and Inter-Ring Dihedral Angle Associated with Dimerization of Symmetric Systems (θ_{D-D}) of nT and nT^+ Dendrimers Calculated at the (U)B3LYP/6-31G(d) and (U)B3LYP/6-311++G(d,p) Levels. Standard Deviations ($^{\circ}$) are Included.

n	(U)B3LYP/6-31G(d)						(U)B3LYP/6-311++G(d,p)					
	nT			nT^+			nT			nT^+		
	$\theta_{\alpha-\alpha}$	$\theta_{\alpha-\beta}$	θ_{D-D}	$\theta_{\alpha-\alpha}$	$\theta_{\alpha-\beta}$	θ_{D-D}	$\theta_{\alpha-\alpha}$	$\theta_{\alpha-\beta}$	θ_{D-D}	$\theta_{\alpha-\alpha}$	$\theta_{\alpha-\beta}$	θ_{D-D}
3	125.2	-37.9	-	26.6	28.1	-	123.7	-42.2	-	28.4	28.7	-
6	131.1	-41.7	-163.9	26.1	38.5	170.8	128.2	-45.5	-158.3	26.8	43.0	170.8
7	128.6 \pm 1.2	-38.5 \pm 0.7	-	25.4 \pm 3.0	35.0 \pm 5.6	-	126.5 \pm 0.4	-42.8 \pm 0.9	-	26.9 \pm 2.8	38.1 \pm 5.6	-
9	130.2 \pm 0.9	-40.0 \pm 2.1	-	30.2 \pm 0.4	37.4 \pm 4.9	-	127.7 \pm 0.8	-43.9 \pm 1.6	-	31.9 \pm 0.7	42.0 \pm 6.9	-
14	131.5 \pm 2.8	-40.6 \pm 2.2	167.2	28.2 \pm 4.8	39.8 \pm 2.4	167.0	129.6 \pm 4.1	-45.1 \pm 3.2	-161.5	28.9 \pm 5.2	46.5 \pm 2.7	167.5
15	129.6 \pm 1.4	-40.1 \pm 0.6	-	29.9 \pm 4.0	38.4 \pm 2.6	-	126.8 \pm 1.9	-43.9 \pm 1.3	-	32.4 \pm 3.5	42.0 \pm 4.1	-
18	132.2 \pm 2.1	-41.3 \pm 0.3	-163.8	33.2 \pm 4.5	40.2 \pm 1.8	168.7	129.5 \pm 2.7	-45.0 \pm 1.0	-157.8	35.2 \pm 5.2	44.9 \pm 2.7	167.2
21	131.8 \pm 2.2	-40.7 \pm 1.3	-	35.1 \pm 3.0	39.1 \pm 2.8	-	130.3 \pm 2.3	-45.5 \pm 1.9	-	37.0 \pm 3.4	44.2 \pm 4.3	-
30	131.5 \pm 2.7	-40.8 \pm 1.9	162.3	33.6 \pm 5.2	40.1 \pm 1.7	168.4						
42	132.8 \pm 2.4	-41.3 \pm 0.6	-162.9	37.1 \pm 3.7	40.1 \pm 0.9	170.5						
45	137.7 \pm 3.4	-41.5 \pm 2.7	-	37.7 \pm 3.5	39.3 \pm 2.0	-						

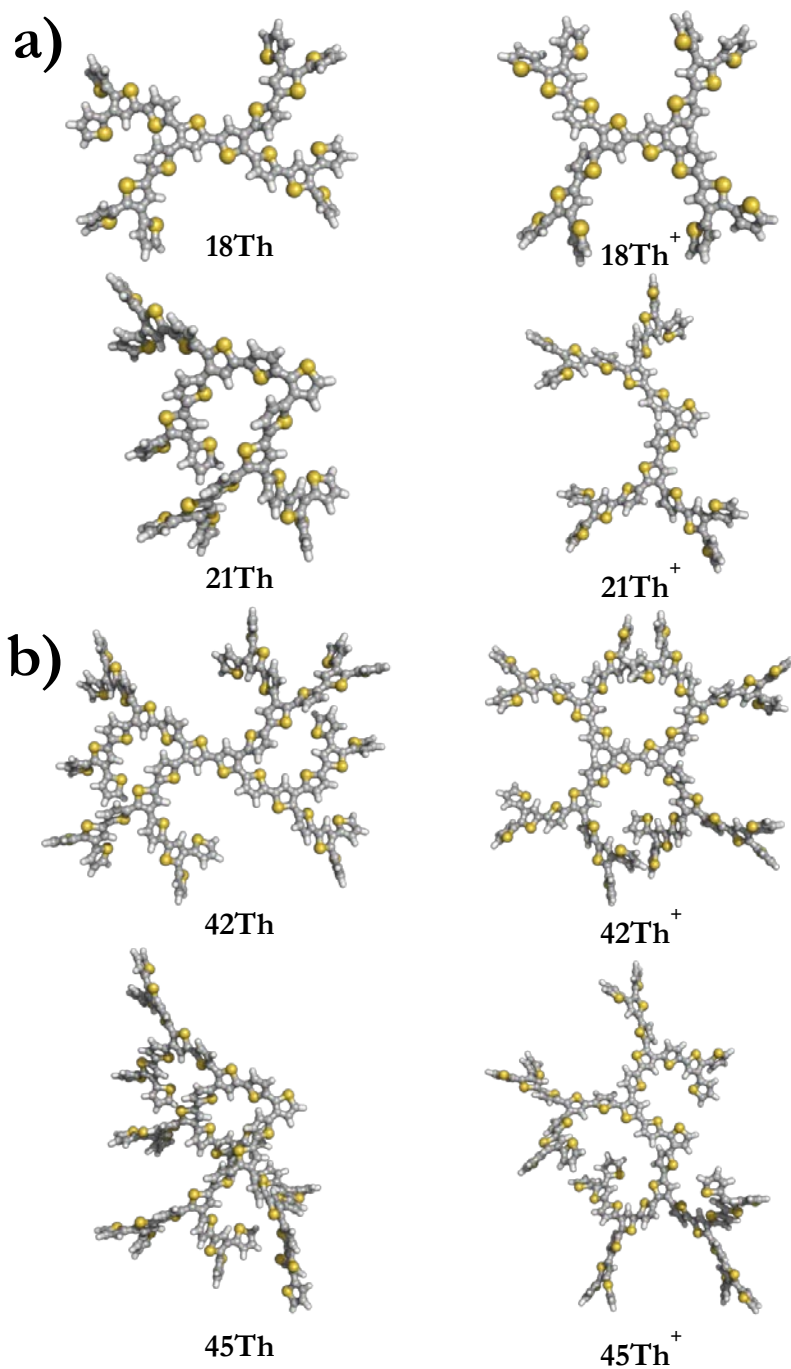


Figure 7.2. Molecular structures of a) 18Th and 21Th dendrimers in both the neutral (left) and oxidized (right) states derived from (U)B3LYP/6-311++G(d,p) geometry optimizations and b) 42Th and 45Th dendrimers in both the neutral (left) and oxidized (right) states derived from (U)B3LYP/6-31G(d) geometry optimizations.

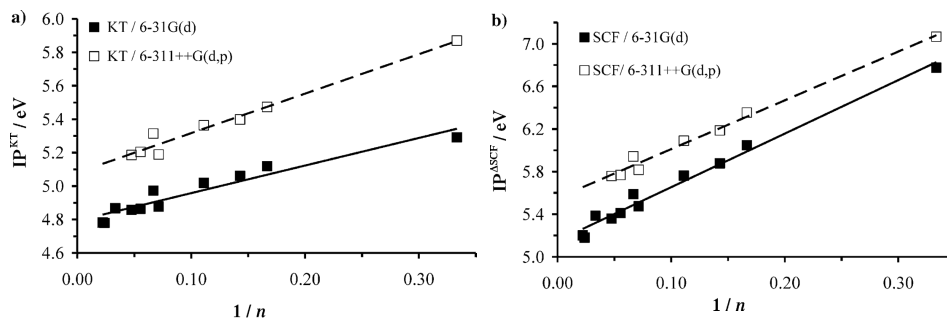


Figure 7.3. Variation of a) IP^{KT} and b) $IP^{\Delta SCF}$ with $1/n$, where n is the number of thiophene rings. Filled and empty squares correspond to the values derived from (U)B3LYP/6-31G(d) and (U)B3LYP/6-311++G(d,p) calculations, respectively. Solid and dashed lines show the linear behavior of the values predicted at these levels of theory.

Comparison between the theoretically predicted IPs and the available experimental data reveals good agreement. The experimental IP reported by Bäuerle and co-workers [21] for 42Th and 45Th were 5.28 and 5.30 eV, and this similarity is also satisfactorily reproduced by (U)B3LYP/6-31G(d) calculations. Specifically, the $IP^{\Delta SCF}$ values predicted for those dendrimers are 5.18 and 5.20 eV, respectively. Note that in their study the above authors measured the oxidation potentials, and converted them to IPs through the following approach: $IP = E_{ox} + 5.1$ [21]. The same approach was used to estimate the experimental IP of 21Th, 5.52 eV [21], while the calculated $IP^{\Delta SCF}$ value is 5.36 eV. On the other hand, the experimental IP for 30Th, estimated by transformation of the oxidation potential reported by Xia et al. [12] by applying the same procedure, is 5.57 eV, while the calculated $IP^{\Delta SCF}$ is 5.38 eV.

7.1.3.3. LOWEST $\pi - \pi^*$ TRANSITION ENERGY

Figure 7.4 shows the \mathcal{E}_g values predicted by DFT calculations for n Th against $1/n$. Table 7.3 compares the \mathcal{E}_g values calculated at the highest DFT level (*i.e.*, with the 6-311++G(d,p) and 6-31G(d) basis sets for dendrimers with $n \leq 21$ and $n > 21$, respectively) with the available experimental data. The (U)B3LYP/6-31G(d) and (U)B3LYP/6-311++G(d,p) predictions are in very good agreement; the values derived from the two basis sets differ by only 2-4 %.

On the other hand, the correlation between the \mathcal{E}_g values and $1/n$ is not particularly good. Thus, the R^2 values derived from the linear fitting of the \mathcal{E}_g values calculated with the two basis sets are 0.85 and 0.86. Furthermore, no polynomial saturation effect, like that obtained for linear oligothiophenes by performing B3LYP/6-31G(d) calculations in the gas phase [32,33,36], is detected in Figure 7.4. Again, this feature must be attributed to the complex molecular architecture of all-thiophene dendrimers. Unfortunately, preliminary trials to improve this correlation (*i.e.* plotting \mathcal{E}_g against $1/n_\alpha$, where n_α is

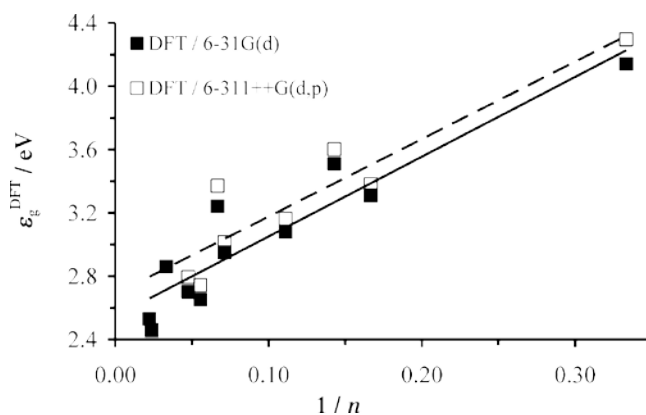


Figure 7.4. Variation of \mathcal{E}_g derived from DFT calculations against $1/n$, where n is the number of thiophene rings, for n Th. The \mathcal{E}_g values determined with both 6-31G(d) (filled symbols) and 6-311++G(d,p) (empty symbols) are displayed. Solid and dashed lines were obtained by linear regressions: $y = a_1x + a_2$.

the number of $\alpha - \alpha$ linkages in the dendrimers) were also unsuccessful, that is, all-thiophene dendrimers need more complex modeling considering simultaneously the size and the architecture. This point will be specifically addressed below.

Figure 7.5 compares the \mathcal{E}_g values derived from DFT calculations with those determined experimentally for n Th [12,21-23]. Although there is a good correlation between the two sets of values ($R^2 = 0.954$), the average relative error amounts to about 31 %. This is because, independent of the basis set, \mathcal{E}_g is systematically overestimated by B3LYP DFT calculations. Moreover, fitting of experimental and DFT values through a

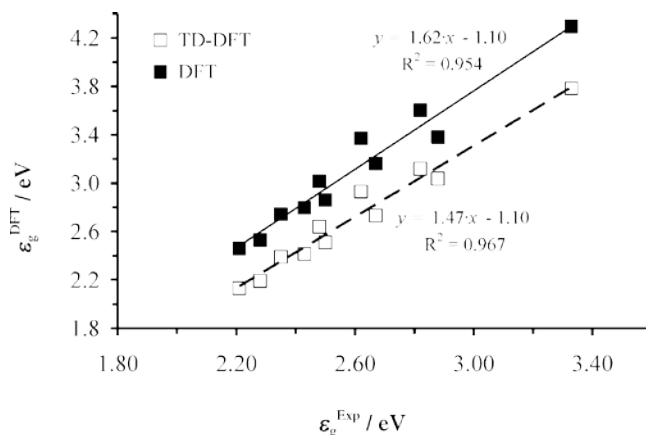


Figure 7.5. Plot of the \mathcal{E}_g values derived from DFT and TD-DFT calculations for n Th dendrimers against the experimental ones. Theoretical values were computed by using the 6-311++G(d,p) basis set for $n \leq 21$ and the 6-31G(d) basis set for $n > 21$. The lines, the equations, and regression coefficients correspond to the linear regressions.

Table 7.3. \mathcal{E}_g Values (eV) Predicted by DFT and TD-DFT Calculations for n Th Dendrimers. The Values Obtained with the Largest Basis Set are Displayed for Each System (i.e. 6-311++G(d,p) for $n \leq 21$ and 6-31G(d) for $n > 21$). Experimental Data (eV) Available for n Th are also Displayed.

n	DFT	TD-DFT	Exp
3	4.29	3.78	3.33 ^a [12]
6	3.38	3.04	2.88 ^b [23]
7	3.60	3.12	2.82 ^a [12]
9	3.16	2.73	2.67 ^b [22]
14	3.01	2.64	2.48 ^a [12]
15	3.37	2.93	2.62 ^a [12]
18	2.74	2.39	2.35 ^b [23]
21	2.79	2.41	2.43 ^b [21]
30	2.86	2.51	2.50 ^a [12]
42	2.46	2.13	2.20 ^b [21]
45	2.53	2.19	2.28 ^b [21]

^a \mathcal{E}_g estimated from electrochemical measurements. ^b \mathcal{E}_g derived from spectroscopic measurements.

simple linear scaling equation $\mathcal{E}_g(\text{DFT}) = c\mathcal{E}_g(\text{Exp})$ (not shown) indicates that the former are overestimated by 20 % ($c = 1.20$) and the regression coefficient is still relatively good ($R^2 = 0.889$). Overall these results clearly indicate that DFT calculations provide a satisfactory description of \mathcal{E}_g , but only from a qualitative point of view. Note that the experimental data were not obtained by using a unique experimental procedure, but are a mix of values derived from electrochemical and spectroscopic measurements (see Table 7.3) [12,21-23]. Moreover, spectroscopic values were more accurate because the electrochemical ones were simply estimated from the oxidation and reduction potentials [21]. Comparison between the electrochemical and spectroscopic values obtained for n Th with $n = 21, 42$, and 45 indicates differences ranging from 0.02 to 0.07 eV [21].

Figure 7.6 plots the \mathcal{E}_g values per thiophene ring predicted by TD-DFT calculations for n Th against $1/n$. The \mathcal{E}_g values calculated with the two basis sets are in excellent agreement in all cases with the exception of 9Th, for which a difference of 8% was obtained. For all other systems differences were smaller than 3%. Furthermore, although correlation of TD-DFT \mathcal{E}_g values with $1/n$ shows some limitations, there is a noticeable improvement with respect to that displayed in Figure 7.4. Table 7.3 includes the \mathcal{E}_g values calculated at the highest TD-DFT level, which correspond to those calculated with the 6-311++G(d,p) and 6-31G(d) basis sets for dendrimers with $n \leq 21$ and $n > 21$,

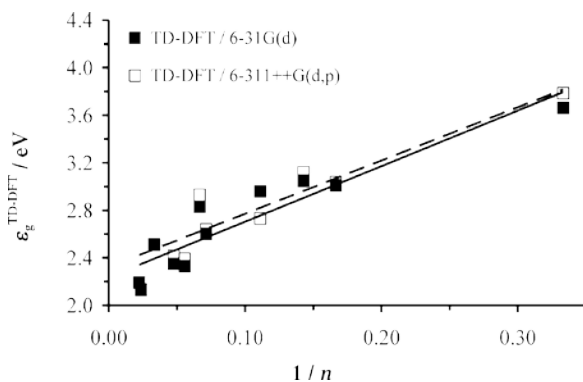


Figure 7.6. Variation of \mathcal{E}_g (eV per thiophene ring) derived from TD-DFT calculations against $1/n$, where n is the number of thiophene rings, for n Th. The \mathcal{E}_g values determined by using both the 6-31G(d) (filled symbols) and 6-311++G(d,p) (empty symbols) are displayed. Solid and dashed lines were obtained by linear regressions: $y = a_1x + a_2$.

respectively. For n Th, the agreement between the experimental and the TD-DFT \mathcal{E}_g values is very noticeable; the average relative error decreases from about 31% for DFT values to only about 16%. This important reduction is because the TD-DFT method systematically corrects the overestimation produced by the DFT method, as is clearly evidenced in Figure 7.5. This feature is also clearly evidenced when experimental and TD-DFT data are fitted to $\mathcal{E}_g(\text{DFT}) = c\mathcal{E}_g(\text{Exp})$ (not shown): the overestimation of experimental data by TD-DFT calculations ($c = 1.05$ with $R^2 = 0.887$) is 15% lower than that obtained for DFT results (see above), even though the regression coefficients are similar in both cases. In spite of this, the TD-DFT transition energies are lower than the experimental values for the larger systems (*i.e.* $n = 42$ and 45), which has been attributed to the exchange term of the B3LYP functional [36,48]. Moreover, the linear regression between the experimental and TD-DFT values shows a correlation of $R^2 = 0.967$, which also represents an improvement with respect to that obtained using DFT values. Accordingly, consideration of excited states through the TD-DFT methodology allows the deficiencies associated with conventional DFT calculations to be corrected.

7.1.3.4. FRONTIER ORBITALS

Figure 7.7 and Figure 7.8 show the HOMO and LUMO for selected unsymmetric and symmetric dendrimers, respectively, considering different generation numbers for each case. More specifically, Figure 7.7 compares the frontier orbitals of 7Th ($g = 3$) and 21Th ($g = 6$) in both the neutral and oxidized states. For each oxidation state, the orbitals of all unsymmetric dendrimers share the same characteristic trends, independent of the generation number. The HOMO of unsymmetric dendrimers shows a major bond-

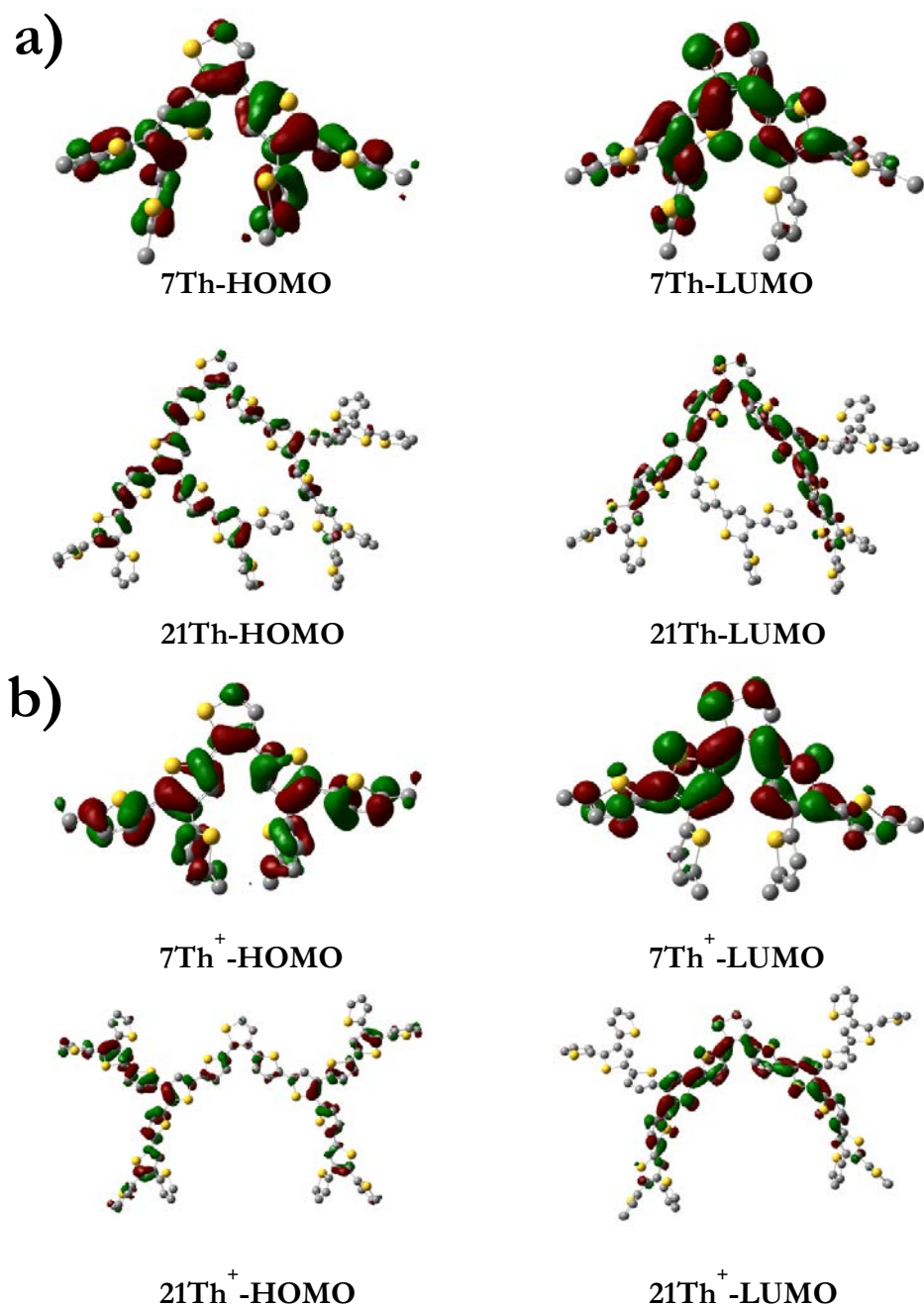


Figure 7.7. Comparison of HOMO and LUMO for unsymmetric dendrimers in a) the neutral and b) the oxidized state.

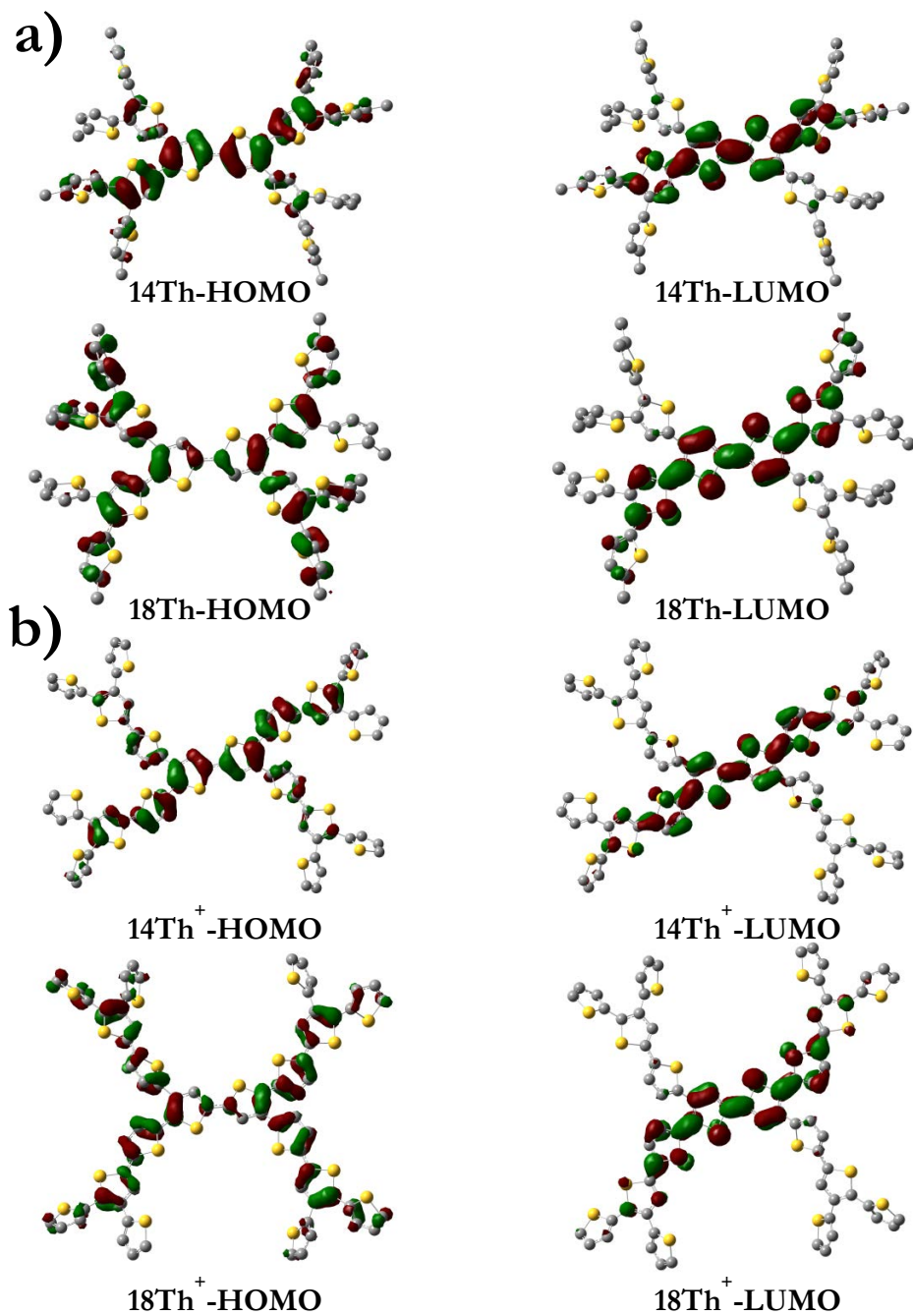


Figure 7.8. Comparison of HOMO and LUMO for symmetric dendrimers in a) the neutral and b) the oxidized state.

bonding character delocalized uniformly along the whole molecule (7Th) or along most of the branches (21Th). Moreover, oxidation enhances such delocalization, as is evidenced by comparison of the HOMOs calculated for 21Th and 21Th⁺. In contrast, lower delocalization is observed for the LUMO, and this effect is independent of the oxidation state. This localization of the LUMO at the central branches is particularly evident for dendrimers with medium and high generation numbers.

Figure 7.8 compares the frontier orbitals calculated for symmetric 14Th ($g = 3$) and 18Th ($g = 4$) dendrimers in both the neutral and oxidized states. The shape of these orbitals is different from that found for symmetric dendrimers (Figure 7.7). Specifically, the HOMO of neutral symmetric dendrimers is mainly delocalized along the segment involving thiophene rings connected by $\alpha - \alpha$ linkages, even though there is also a small delocalization along the immediate neighboring thiophene rings with $\alpha - \beta$ linkages. Interestingly, oxidation promotes delocalization of the HOMO over the whole molecule. The LUMO of symmetric dendrimers is exclusively localized along the central part of segments with $\alpha - \alpha$ linkages, and this localization effect is more pronounced in the neutral systems than in the oxidized ones.

The shapes of the HOMO and LUMO allow us to rationalize differences in the \mathcal{E}_g values experimentally measured for unsymmetric and symmetric all thiophene dendrimers. Thus, the \mathcal{E}_g values determined for symmetric systems (*e.g.* 2.48 and 2.35 eV for 14Th [12] and 18Th [23], respectively) are in all cases lower than those of the slightly larger systems but with an unsymmetric architecture (*e.g.* 2.62 and 2.43 eV for 15Th [12] and 21Th [21], respectively). This inversion in \mathcal{E}_g values with respect to the expected relative order (*i.e.* \mathcal{E}_g decreases when n increases, as is typically observed in linear oligothiophenes [32-36]) should be attributed to the larger delocalization of the frontier orbitals in dendrimers with a symmetric architecture.

7.1.3.5. MODELING \mathcal{E}_g OF ALL-THIOPHENE DENDRIMERS

Modeling was performed by considering two different expressions for \mathcal{E}_g ; equations (7.1) and (7.2):

$$\mathcal{E}_g = a_1(1/g) + a_2(1/n) \quad (7.1)$$

$$\mathcal{E}_g = a_1\chi_{\alpha-\alpha} + a_2(1 - \chi_{\alpha-\alpha}) + a_3(1/n) \quad (7.2)$$

In (7.1) $1/n$ and $1/g$ are variables that take into account the dependence of \mathcal{E}_g on the size of the dendrimer and the generation number, respectively, whereas (7.2) expresses \mathcal{E}_g as a function of the number of thiophene rings and the molecular architecture, which is included through the fractions of $\alpha - \alpha$ and $\alpha - \beta$ linkages: $\chi_{\alpha-\alpha}$ and $\chi_{\alpha-\beta} = 1 - \chi_{\alpha-\alpha}$, respectively. The coefficients a_i , which are listed in Table 7.4, were obtained by minimizing the squared difference between the modeled and the best estimation of \mathcal{E}_g

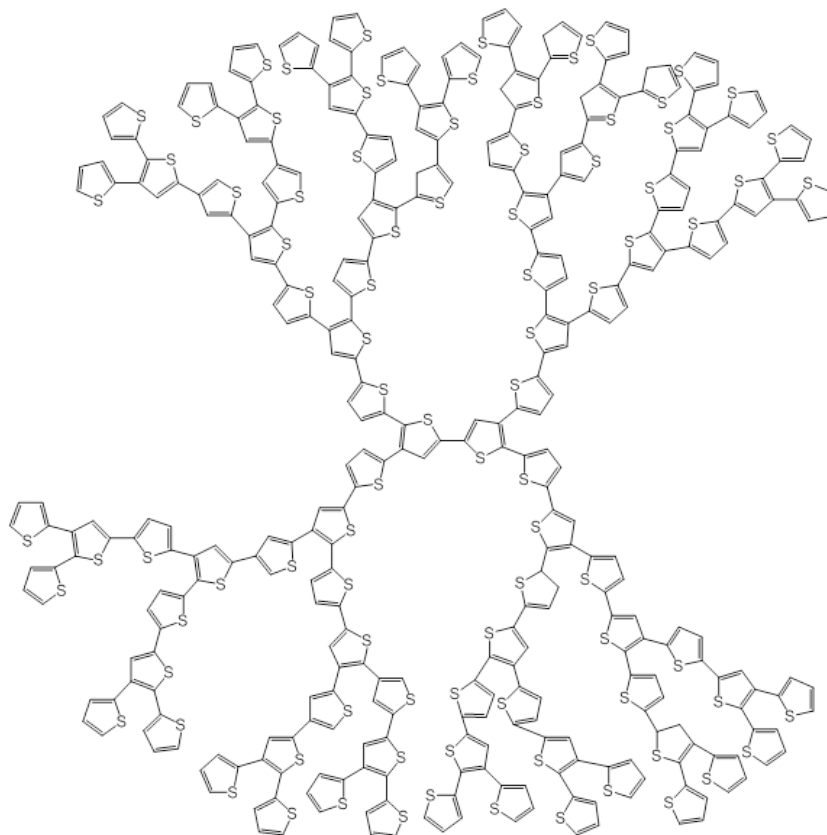
Table 7.4. Coefficients a_i Obtained by Minimizing the Squared Difference between the \mathcal{E}_g Values Derived from DFT and TD-DFT Calculations (see Table 7.3) and the Mathematical Models Proposed in Equations (7.1) and (7.2).

	DFT	TD-DFT
$\mathcal{E}_g = a_1(1/g) + a_2(1/n)$		
a_1	12.3842	10.7075
a_2	-6.5293	-5.3930
sd ^a	6.3329	4.8612
$\mathcal{E}_g = a_1\chi_{\alpha-\alpha} + a_2(1 - \chi_{\alpha-\alpha}) + a_3(1/n)$		
a_1	1.3150	1.0803
a_2	4.7471	4.2087
a_3	3.6701	3.3381
sd ^a	0.3690	0.2578

^a Sum of the squared differences between the \mathcal{E}_g values derived from quantum mechanical calculations and those obtained applying the pro-posed models (7.1) and (7.2).

values obtained at both the DFT and TD-DFT levels (see Table 7.3). Inspection of the values for the coefficients a_i confirms that \mathcal{E}_g is influenced by all the variables included in equations (7.1) and (7.2). However, the importance of such variables in the modeling of \mathcal{E}_g is not the same, as is evidenced by the sum of the squared differences (sd) between the \mathcal{E}_g values derived from quantum mechanical calculations and those obtained applying the two proposed models (sd in Table 7.4). Thus, the molecular architecture plays a more crucial role than the generation number in the modeling of \mathcal{E}_g , the sd of n Th dendrimers being one order of magnitude higher for (7.1) than for (7.2). Moreover, equation (7.1) only provides satisfactory sd values when the data for dendrimers with symmetric and unsymmetric architectures are fitted separately (data not shown); modeling of \mathcal{E}_g with two different sets of parameters of \mathcal{E}_g is not desirable. On the other hand, equation (7.2) indicates that the relative weight of the molecular architecture grows with increasing size of the dendrimer, since $1/n$ becomes smaller. This is an important difference with respect to linear oligothiophenes, in which \mathcal{E}_g exclusively depends on $1/n$ [46,49,50].

The \mathcal{E}_g values modeled for 90Th (Scheme 7.2), which is a symmetric dendrimer with $g = 8$, by using the TD-DFT coefficients obtained for (7.1) and (7.2) are 1.28 and 2.38 eV, respectively. The latter value is in excellent agreement with the experimental data determined from cyclic voltammetry and absorption spectroscopy (2.21 and 2.24 eV, respectively) [22]. Indeed, the difference between the experimental values and the



Scheme 7.2

modeling prediction of equation (7.2) of 0.14–0.17 eV is within the error of the model (i.e. 0.26 eV in Table 7.4). This approximation represents a significant advance since, at present, a quantum mechanical study of 90Th is not accessible. On the other hand, the prediction of 2.74 eV obtained by using the DFT coefficients for (7.2) and the experimental values differ by about 0.5 eV. This is a very reasonable result since, as discussed above, DFT calculations tend to overestimate \mathcal{E}_g values.

7.1.4. CONCLUSIONS

The molecular geometry, IP, \mathcal{E}_g , and frontier orbitals of neutral and oxidized n Th dendrimers have been studied by DFT and TD-DFT calculations in which the (U)B3LYP functional was combined with the 6-31G(d) and 6-311++G(d,p) basis sets. Both the geometric parameters and the molecular shape are not influenced by the size of the basis set, independent of the oxidation state of the dendrimers. However, an important conformational change is detected on oxidation of neutral molecules, independently of

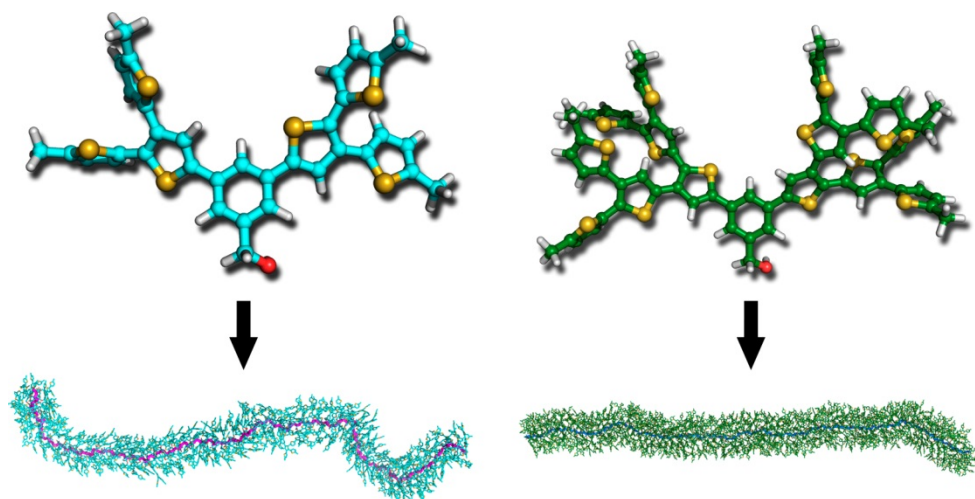
their symmetric or unsymmetric architecture. Specifically, the structures become more elongated and less compact in the oxidized state, which is a consequence of the rigidity imposed by the electronic-structure change, from benzenoid to quinoid form, when the molecules gain a positive charge.

The influence of the basis set on \mathcal{E}_g and, especially, IP is also very small. The IP^{KT} values are significantly lower than the IP^{ASCF} and experimental values, and this evidences the importance of electronic and geometry relaxation effects. Calculated IP^{ASCF} values are in good agreement with available experimental data. Interestingly, the calculated IPs show an excellent correlation with $1/n$, that is, this electronic parameter is mainly dominated by the fact that electron delocalization increases with increasing molecular size. On the other hand, the \mathcal{E}_g values predicted by the DFT method are systematically overestimated with respect to the experimental data. TD-DFT calculations correct this deficiency, providing \mathcal{E}_g estimations that are in very good agreement with values derived from electrochemical and absorption spectroscopy measurements. The correlation of \mathcal{E}_g with $1/n$, as well as with $1/n_\alpha$ and $1/g$, is relatively poor, that is, this electronic property depends on both the number of thiophene rings and the symmetric/unsymmetric molecular architecture of the dendrimers. Analysis of the frontier orbitals provides full rationalization of the latter observation, since both the shape and the delocalization/localization of the HOMO and LUMO depend on these two factors.

A reliable model to predict \mathcal{E}_g of all-thiophene dendrimers that are inaccessible to quantum mechanical calculations (*i.e.* those with $n > 45$) has been developed by considering our best TD-DFT estimates. The validity of this model, which takes into account both the size and the molecular architecture of the dendrimer, has been confirmed for the 90Th system.

7.2. INTERNAL ORGANIZATION OF MACROMONOMERS AND DPs BASED ON TH DENDRONS

The internal organization of macromonomers (MGs) based on all-thiophene dendrons of generation $g=2$ and 3 attached to a phenyl core, as well as of the dendronized polymers resulting from their polymerization (PG2 and PG3, respectively), has been investigated using theoretical methods. The conformational preferences of the MGs, which have been determined using density functional theory calculations, are defined by the relative orientation between the dendrons and the core. The strain of the MGs increases with the generation number and is alleviated by small conformational rearrangements of the peripheral thiophene rings. The conformations obtained for the MGs have been used to construct models for the dendronized polymers. Classical molecular dynamics simulations have evidenced that the interpenetration of dendrons



belonging to different repeat units is practically null for PG2. In contrast, the degree of interpenetration is very high for PG3, which also shows a significant degree of backfolding (*i.e.* occurrence of peripheral methyl groups approaching the backbone). Consequently, PG2 behaves as a conventional linear flexible polymer bearing bulk pendant groups, whereas PG3 is a rigid homogenous cylinder. The two polymers are stabilized by π - π stacking interactions, even though these are significantly more abundant for PG3 than for PG2 (*i.e.* the average number of interactions per repeat unit is 3.0 and 8.8 for PG2 and PG3, respectively). In these interactions the thiophene rings may adopt a parallel or a perpendicular disposition (*i.e.* sandwich and T-shaped configurations, respectively), even though the former is the most abundant in all cases.

7.2.1. INTRODUCTION

Organic molecules with dendritic architectures are typically classified in dendrimers and dendronized polymers (DPs). Dendrimers are the most widely investigated [51-68] and consist of perfectly branched molecules made of tree-like fragments (dendrons) attached to a central core. The internal organization of these well-defined size and monodisperse molecules depends on the generation number, g , of dendrons. Thus, dendrimers of lower generation have relatively loose inner structure while higher generations are densely packed and organized [51-54]. These particular organizations result in unusual properties, as for example liquid-crystalline behavior at high concentrations [55,56], anomalous intrinsic viscosity [57,58], and multivalent molecular surface [59,60]. As a consequence, dendrimers have been proposed for very interesting applications, as for example, drug-delivery systems [61,62], gene vectors [63,64], catalysts [65,66] and organic light-emitting diodes [67,68].

DPs can be seen as wormlike macromolecular objects of cylindrical cross section [69-71]. The mass per repeat unit of the polymer backbone increases non linearly with the generation number, which modulates properties like the rigidity, diameter and concentration of functionalities [71-74]. Due to this particular architecture, DPs currently represent a class of single molecular nanomaterials with potential applications. Among the most promising applications of DPs are nanoscopic building blocks [75,76], functional materials [77,78], organic optoelectronic materials,[79-81] self-assembling vectors for complexation with DNA,[81,82] and nanomaterials to stabilize therapeutic proteins in the gastrointestinal tract [83] and both to copy [84] and to immobilize enzymes [85]. Furthermore, the structure of different families of DPs has been investigated using atomistic simulations, results providing microscopic understanding of the physical properties of these nanomaterials [86-91]. Interestingly, these microscopic studies have revealed that the internal organization and properties are intimately related not only with g but also with the chemical nature of the dendrons. For example, the stability of the right-handed helical conformation found for neutral and charged dendronized polymethylmethacrylates carrying chiral 4-aminoproline based dendrons is essentially due to the formation of networks of specific interactions [86,87]. In contrast, the interactions defined by the backfolding of the external dendrons dominates the properties of dendronized polymethacrylates made of tree-like fragments with amide and aromatic groups separated by polymethylene segments [88,89]. These results supported the idea of treating these DPs as soft elongated colloidal objects [90,91].

Thiophene (Th) based dendrimers and DPs with a fully π -conjugated core are considered as very promising kinds of conducting materials [92]. Since Advincula and co-workers reported on the first Th dendrimer synthesis [11,12], several other Th dendrimers for different energy-related applications have been described [92]. For example, Bäuerle and co-workers [22] synthesized different all-Th dendrimers containing up to 90 Th rings with a divergent/convergent approach to facilitate the inclusion of functionalities in the external surface of the conducting dendrimer. These Th dendrimers were used as entangled photon sensors [23]. Mitchell *et al.* [93] prepared phenyl-cored Th dendrimers for organic photovoltaic devices, their power-conversion efficiency being recently overtaken by hexaperi-hexabenzocornene-cored Th dendrimers described by Wong *et al.* [94] and the hybrid gold-nanoparticle-cored dendrimers of Deng *et al.* [95]. Furthermore, valuable microscopic and electronic information was derived from quantum mechanical studies on several Th-based dendrimers [25,96,97].

In contrast, studies devoted to Th-based DPs are very scarce because of the intrinsic complexity associated to this kind of macromolecular objects. In a pioneering work, a few years ago Schlüter and co-workers [98] reported the synthesis of Th-containing second and third generation dendronized macromonomers with methacrylate polymerizable units as well as their corresponding DPs. More recently, Kimura *et al.* [99] prepared novel all-Th dendritic macromonomers that were subsequently polymerized. The electronic and

electrical properties of the resulting DPs, which showed enhanced conductivity upon doping, were attributed to the spatial overlapping of the Th dendrons through π - π interactions. Very recently, Griffin *et al.* [100] reported the synthesis and characterization of a benzodithiophene/Th alternating copolymers decorated with rigid, singly branched pendant side chains. Photoexcitation of these copolymers resulted in excited states primarily localized on the pendant side chains that excitations were rapidly transferred to the polymer backbone (*i.e.* in less than 250 fs).

In this work we use a multi-scale theoretical approach to characterize at the microscopic level the internal organization of macromonomers and DPs made of branched Th dendrons. More specifically, the molecular and electronic structure of two macromonomers, MG2 and MG3 in Figure 7.9a, have been studied using quantum mechanical methods based on density functional theory (DFT) calculations. After this, in a second step, DPs derived from the polymerization of MG2 and MG3 have been investigated using molecular dynamics (MD) simulations based on classical force-fields. The chemical structure of these DPs, named PG2 and PG3 (with $g = 2$ and 3, respectively), is depicted in Figure 7.9b. It is worth noting that MG2, MG3, PG2 and PG3 are practically identical to the macromonomers and DPs synthesized by Schlüter and co-workers [98]. Thus, the only difference involves the alkyl groups attached to the Th

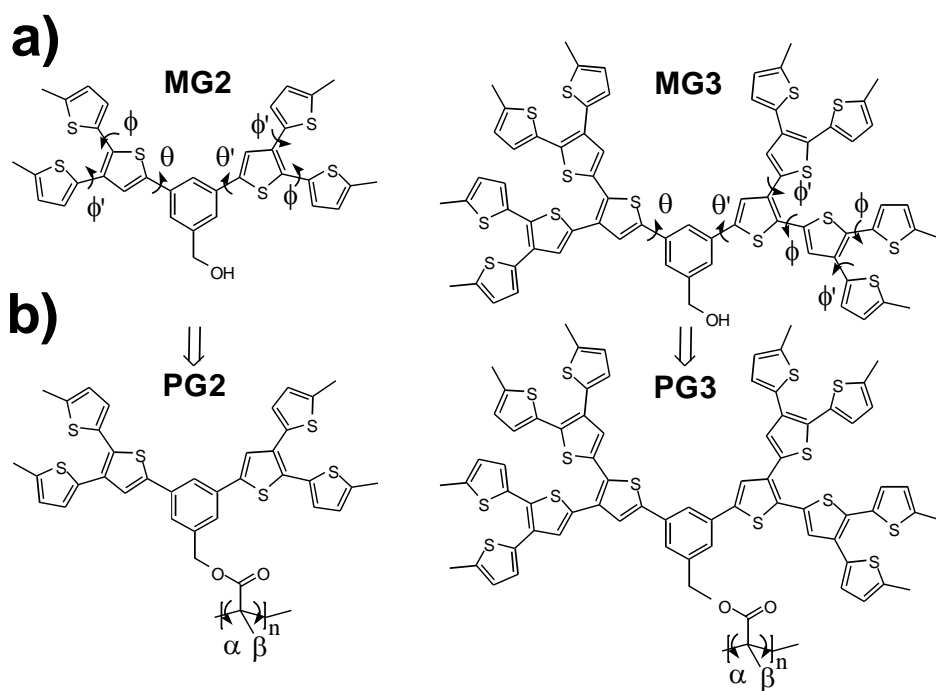


Figure 7.9. Chemical structure of: (a) MG2 and MG3 macromonomers; and (b) PG2 and PG3 DPs.

rings, where we have replaced the hexyl groups of the experimental systems by methyl groups for simplicity.

7.2.2. METHODS

7.2.2.1. QUANTUM MECHANICAL CALCULATIONS

All calculations were performed using the Gaussian 09 computer program [26]. The conformational preferences of MG2 and MG3 were examined using DFT calculations with the wB97X-D functional [101] combined with the 6-311+G(d,p) basis set [30,31], (*i.e.* wB97X-D /6-311+G(d,p) level).

The ionization potential (IP) was estimated using the Koopman's theorem (KT) [37], according to which the IP was taken as the negative of the highest occupied molecular orbital (HOMO) energy ($IP = -\epsilon_{\text{HOMO}}$). It is worth noting that KT is not applied to DFT methodologies since energies of Kohn-Shan orbitals do not involve any physical meaning. However, Janak's theorem [38] was used by Perdew [39] to show the connection between IP and the HOMO energy.

The lowest π - π^* transition energy (ϵ_g) was derived from the excitation energies calculated using time-dependent density functional theory (TD-DFT) [102]. This methodology provides a robust and efficient description of the low-lying molecular states and is widely applied to study the UV-vis spectra of conjugated organic compounds [41,103,104]. Electronic excitations were evaluated using the PB0 [105,106] and B3LYP [27,28] functionals, which are known to be very reliable for the calculation of electronic transitions [107,108], combined with the 6-311+G(d,p) basis set and employing geometries fully optimized at the wB97X-D/6-311+G(d,p) level.

Electron densities of the most stable conformations identified for MG2 and MG3 were determined at the wB97X-D/6-311+G(d,p) level using the Merz-Kollman (MK) scheme [109,110], which assigns point charges to fit the computed electrostatic potential to points on nested Connolly surface with a density of 1 point/Å².

7.2.2.2. CLASSICAL FORCE FIELD SIMULATIONS

The most stable structures of MG2 and MG3 obtained by DFT calculations were used to build the starting geometries for PG2 and PG3. The stability of the resulting structures was investigated in vacuum considering DP chains with $N = 150$ repeat units. Generally speaking, this solvent-free model corresponds to the situation encountered in the poor solvent experiments as was proved in previous studies of other non-charged DPs [88,89]. The backbone conformation of PG2 and PG3 was determined by applying a systematic search strategy. More specifically, 144 trial backbone conformations were constructed for each DP varying the dihedral angles α and β (Figure 7.9b) in steps of 30°. The number of backbone conformations without backbone-backbone, backbone-side group and side

group–side group steric clashes, hereafter denoted *feasible* conformations, was approximately 30% and 20% of the initial trial conformation for PG2 and PG3, respectively. The rest of the conformations (*i.e.* those with atomic overlaps) were directly discarded without perform any calculation.

Energy minimizations and MD simulations of the feasible conformations were performed using the NAMD program [111]. The energy was calculated using the AMBER force-field [112]. All bonding and van der Waals parameters required for PG2 and PG3 were taken from the Generalized AMBER force-field [113] (GAFF) while atomic charges were computed at the wB97X-D/6-311+G(d,p) level using the Restrained ElectroStatic Potential (RESP) strategy (Figure 7.10) [114].

Geometry optimizations of all feasible conformations were performed by applying the conjugate gradient method during 5000 steps. After that, only 15% and 16% of feasible conformations were kept for PG2 and PG3, respectively. Such structures were pre-equilibrated by heating up the system from 0 to 298 K using a rate of 1 K each 1.5 ps. Visual inspection of the structures obtained after such short simulation time (*i.e.* 447 ps) indicated that many of them lost the initial helical regularity during the thermalization process. Thus, only 6 and 4 remained regular for PG2 and PG3, respectively. These structures were submitted to 5 ns of MD for equilibration. Finally, a 20 ns production (“relaxation”) trajectory was carried out for the structure of lowest energy of each DP, which corresponds to that started using $\{\alpha, \beta\} = 180^\circ, 60^\circ$ and $-150^\circ, -60^\circ$ for PG2 and PG3, respectively. Data were saved every 8 ps for subsequent analysis (*i.e.* 2500 snapshots).

Atom-pair distance cut-offs were applied at 14 Å to compute van der Waals and electrostatic interactions. Bond lengths involving hydrogen atoms were constrained using the SHAKE algorithm with a numerical integration step of 1 fs [115]. The temperature was controlled by a weak coupling method, the Berendsen thermostat [116] with a time constant for heat-bath coupling of 1 ps.

7.2.3. RESULTS AND DISCUSSION

7.2.3.1. MG2 AND MG3 MACROMONOMERS

The conformational preferences of the dendron used to prepare MG2 [98], which consists of three Th rings linked by $\alpha - \alpha$ and $\alpha - \beta$ linkages (3Th; Scheme 7.3), was studied in a previous work [25]. More specifically, the potential energy surface derived from the systematic variation of the inter-ring dihedral angles was calculated at the B3LYP/6-31G(d) level. The most stable arrangement reported for 3Th, with $\{\phi, \phi'\} = 125^\circ, -38^\circ$ [25], has been used in this work as starting point for the construction of MG2.

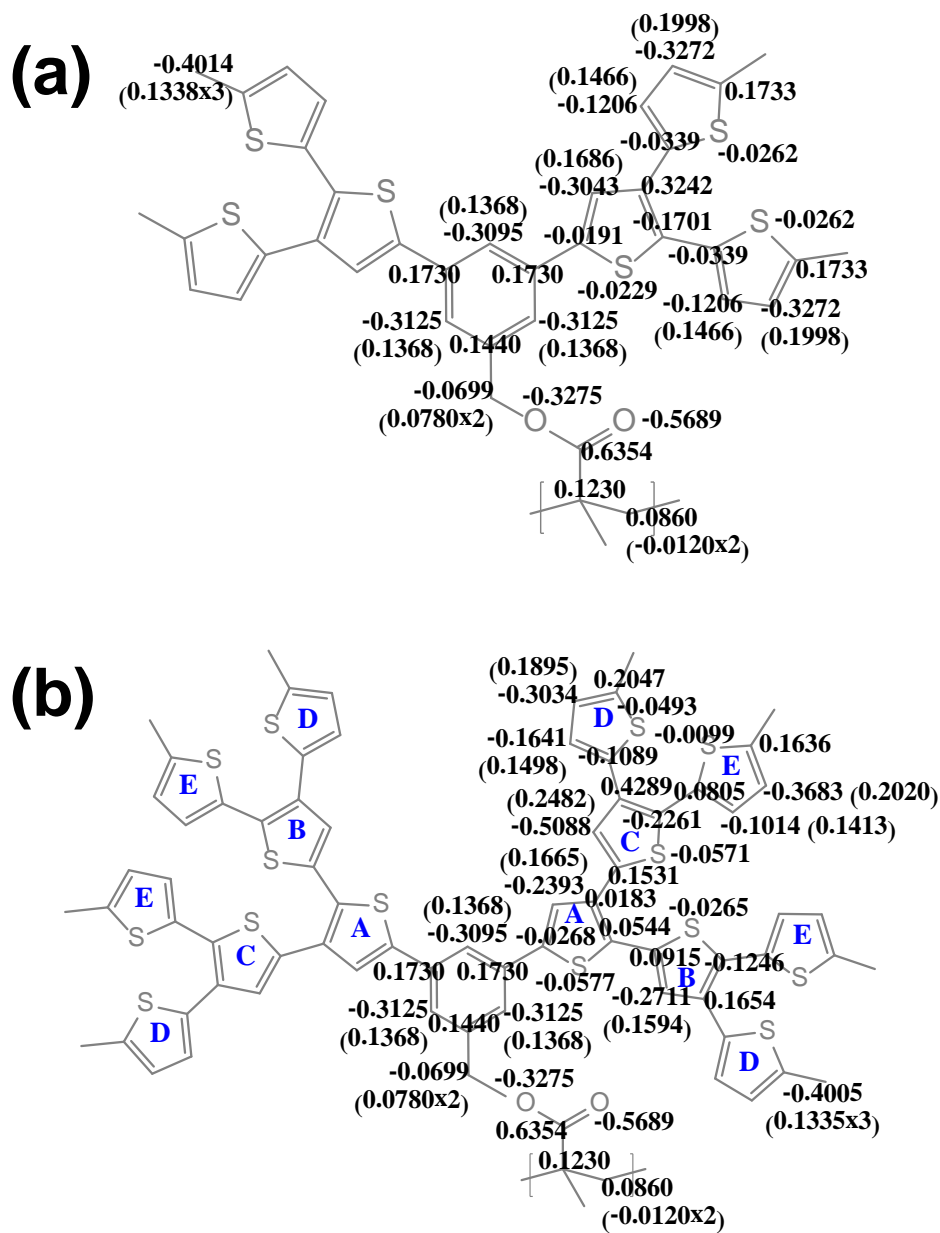
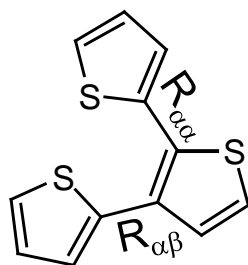


Figure 7.10. Electrostatic parameters determined for the repeat unit of (a) PG2 and (b) PG3. Charges in parenthesis correspond to hydrogen atoms, where $\times n$ refers to the number n of equivalent hydrogens, while charges for carbon, oxygen and sulfur atoms are out of the parenthesis. Charges for equivalent thiophene rings are omitted for clarity. In the repeat unit of PG3, equivalent pairs of thiophene rings have been labelled using letters.



Scheme 7.3. Chemical structure of the dendron (3Th) used to construct MG2

The conformational preferences of MG2 were calculated using a systemic strategy. For this purpose, after construct the starting geometry, the potential energy surface defined by dihedral angles associated to the linkage between 3Th and the phenyl core (θ and θ' in Figure 7.9a) was determined at the wB97X-D/6-311++G(d,p) level. Specifically, θ and θ' were varied between 0° and 360° in steps of 30° , the resulting 144 structures being optimized using a flexible rotor approximation (*i.e.* each structure was submitted to a constrained geometry optimization in which the inter-ring dihedral angles θ and θ' were kept fixed at the initial values).

Figure 7.11 displays the potential energy surface $E = E(\theta, \theta')$ obtained for MG2, which was calculated without imposing any symmetry constraint. As it can be seen, the low-energy regions, which are indicated by blue colors in the map, are located at $\{\theta, \theta'\} \approx \pm 30^\circ, \pm 150^\circ, \pm 150^\circ, \pm 30^\circ, \pm 150^\circ, \pm 150^\circ$ and $\pm 30^\circ, \pm 30^\circ$, where all combinations of signs are possible for each pair of values (*e.g.* $\{\theta, \theta'\} \approx \pm 30^\circ, \pm 150^\circ$ refers to the following four pairs: $+30^\circ, +150^\circ$; $+30^\circ, -150^\circ$; $-30^\circ, -150^\circ$; and $-150^\circ, -150^\circ$). The geometry of these 16 conformations was re-optimized without any constraint in θ and θ' . The dihedral angles and relative energies of the completely optimized representative conformations are displayed in Table 7.5. It should be pointed out that, although the four minima obtained for each pair of $\{\theta, \theta'\}$ values are not formally equivalent because of the lack of molecular symmetry (Figure 7.9a), they are very similar in terms of energy and geometric properties. Accordingly, only one of four minima detected for each $\{\theta, \theta'\}$ pair (that of lowest energy) has been explicitly included in Table 7.5. On the other hand, as the dihedrals ϕ and ϕ' , which refer to the $\alpha - \alpha$ and $\alpha - \beta$ linkages of the two peripheral Th rings to the central one (Figure 7.9a), are very similar for the two dendrons contained in MG2, Table 7.5 lists the average values and the corresponding standard deviations rather than the explicit values for each dendron. Table 7.5 also includes the average values of $\alpha - \alpha$ and $\alpha - \beta$ bond lengths (denoted $R_{\alpha\alpha}$ and $R_{\alpha\beta}$, respectively, in Scheme 7.3).

As it can be seen, the disposition of the peripheral Th rings is very similar for all conformations included in Table 7.5. This feature indicates that the two 3Th dendrons

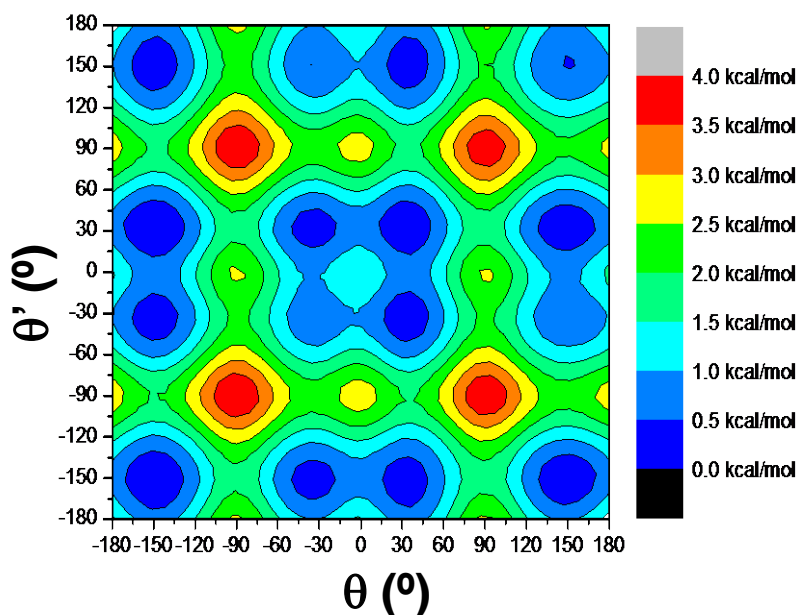


Figure 7.11. Potential energy surface $E = E(\theta, \theta')$ calculated for MG2. The dihedral angles θ and θ' are displayed in Figure 7.9a.

used to prepare MG2 react upon the attachment to the phenyl core, provoking a significant conformational change in one of the peripheral Th rings. Thus, the conformation found for the individual 3Th dendron, $\{\phi, \phi'\} = 125^\circ, -38^\circ$ [25], evolve towards $\{\phi, \phi'\} \approx 120^\circ, 140^\circ$. As occurred for $\{\phi, \phi'\}$, the $R_{\alpha\alpha}$ and $R_{\alpha\beta}$ values obtained for the different optimized conformations do not show appreciable differences. These observations are consistent with the very low relative energies (ΔE) separating the 16 optimized conformations, the energy gap between the most and the least stable conformation being of only 0.6 kcal/mol. The scarce influence of $\{\theta, \theta'\}$ values on the relative stability and geometries facilitates the study and interpretation of MG2 properties, which have been analyzed for the lowest energy conformation only (MG2-1 in Table 7.5).

In the MG2-1 (Figure 7.12a) repulsive S \cdots S interactions involving the Th rings directly attached to the phenyl core are strictly minimized by the dihedrals $\{\theta, \theta'\} = 144.9^\circ, -147.7^\circ$. The ϵ_g and IP values calculated at the PB0/6-311+G(d,p) and B3LYP/6-311+G(d,p) levels for such conformation, which are practically identical to those obtained for the rest of minimized conformations, are in excellent agreement (*i.e.* $\epsilon_g = 3.65$ eV and IP = 5.76 eV at the former level, and $\epsilon_g = 3.48$ eV and IP = 5.56 eV at the latter level). The ϵ_g values derived from TD-DFT calculations slightly overestimate the experimental estimation, 3.00 eV, which was determined by absorption and emission spectroscopy [98]. However, our ϵ_g estimations are significantly lower than the value

Table 7.5. Representative Minimum Energy Conformations Calculated for MG2 at the wB97X-D/6-311++G(d,p) Level. Dihedral Angles (θ , θ' , ϕ and ϕ' ; in degrees), Bond Lengths ($R_{\alpha\alpha}$ and $R_{\alpha\beta}$; in Å) and Relative Energy (ΔE ; in kcal/mol) are Displayed.

#	θ	θ'	ϕ	ϕ'	$R_{\alpha\alpha}$	$R_{\alpha\beta}$	ΔE
MG2-1 ^a	144.9	-147.7	118.9±0.4	141.2±0.6	1.461±0.000	1.463±0.002	0.0
MG2-2 ^b	147.6	33.6	119.5±0.6	140.5±0.1	1.461±0.000	1.465±0.000	0.0
MG2-3 ^c	34.5 ^e	33.0	120.9±0.9	140.0±0.1	1.461±0.000	1.465±0.000	0.0
MG2-4 ^d	31.1 ^e	-148.5	119.3±0.4	142.2±0.8	1.461±0.000	1.465±0.000	0.2

^a The ΔE of minima with $\theta, \theta' = 144.9^\circ, -147.7^\circ$; $-147.9^\circ, -146.1^\circ$; $147.6^\circ, 146.3^\circ$; and $-145.9^\circ, 150.0^\circ$ is lower than 0.2 kcal/mol. Differences in the rest of the geometric parameter are practically inexistent. ^b The ΔE of minima with $\theta, \theta' = 147.6^\circ, 33.6^\circ$; $-145.9^\circ, -34.4^\circ$; $-147.4^\circ, 33.2^\circ$; and $146.3^\circ, -32.4^\circ$ is lower than 0.2 kcal/mol. Differences in the rest of the geometric parameter are practically inexistent. ^c The ΔE of minima with $\theta, \theta' = 34.5^\circ, 33.0^\circ$; $34.0^\circ, -34.3^\circ$; $-35.9^\circ, 31.8^\circ$; and $-30.5^\circ, -32.0^\circ$ is lower than 0.6 kcal/mol. Differences in the rest of the geometric parameter are practically inexistent. ^d The ΔE of minima with $\theta, \theta' = 34.1^\circ, -148.5^\circ$; $-36.2^\circ, -148.3^\circ$; $35.2^\circ, -147.9^\circ$; and $-34.8^\circ, -148.6^\circ$ is lower than 0.4 kcal/mol. Differences in the rest of the geometric parameter are practically inexistent.

calculated for the individual 3Th dendron (*i.e.* the theoretical ε_g obtained using DFT calculations at the B3LYP/6-31G(d) level for 4.13 eV [25] while the experimental measure was 3.33 eV [12]), which is fully consistent with experimental observations. On the other hand, the IP predicted for MG2 by the KT, 0.97 eV per thiophene ring, is lower than that obtained at the B3LYP/6-31G(d) for the individual 3Th dendron (*i.e.* 3.21 eV per thiophene ring) [25]. Inspection of the topology of the highest occupied molecular orbital (HOMO) and the lowest unoccupied molecular orbital (LUMO), which are displayed in Figure 7.12b and Figure 7.12c, evidences that these frontier orbitals are distributed through the aromatic rings of the two 3Th dendrons and the phenyl core. This is fully consistent the homogeneous distribution of the electron density displayed in Figure 7.12d.

The conformational preferences of MG3 were evaluated using the following strategy. The four structures of lower energy identified in a previous study for the all-thiophene dendron used to prepare MG3, which has been denoted 7Th (Scheme 7.4) [25], were attached to the phenyl core considering the following pairs of values for the dihedral angles θ, θ' : $150^\circ, -150^\circ$; $150^\circ, 30^\circ$; $30^\circ, 30^\circ$; and $30^\circ, -150^\circ$. The $4 \times 4 = 16$ starting structures were subjected to complete geometry optimization at the wB97X-D/6-311++G(d,p) level, resulting in 12 different conformations. Interestingly, the structures with $\{\theta, \theta'\} \approx 150^\circ, -150^\circ$ are not stable when the generation number g increases from 2 to 3, reverting in conformations similar to those achieved after optimize the starting points with $\{\theta, \theta'\} \approx 30^\circ, -150^\circ$.

The three conformations of lower energy, which are listed in Table 7.6, are separated by an energy gap of 0.2 kcal/mol only, whereas the relative energy of the remaining opti-

mized structures (not shown) was higher than 0.5 kcal/mol. The most stable conformation (MG3-1 in Table 7.6) is displayed in Figure 7.12a. As occurred for MG2-1, S...S repulsive interactions are minimized in MG3-1. Also, Table 7.6 reflects that the strain of the macromonomer increases with the generation number g . In order to alleviate such strain, inter-ring dihedral angles of different dendrons present larger deviations than

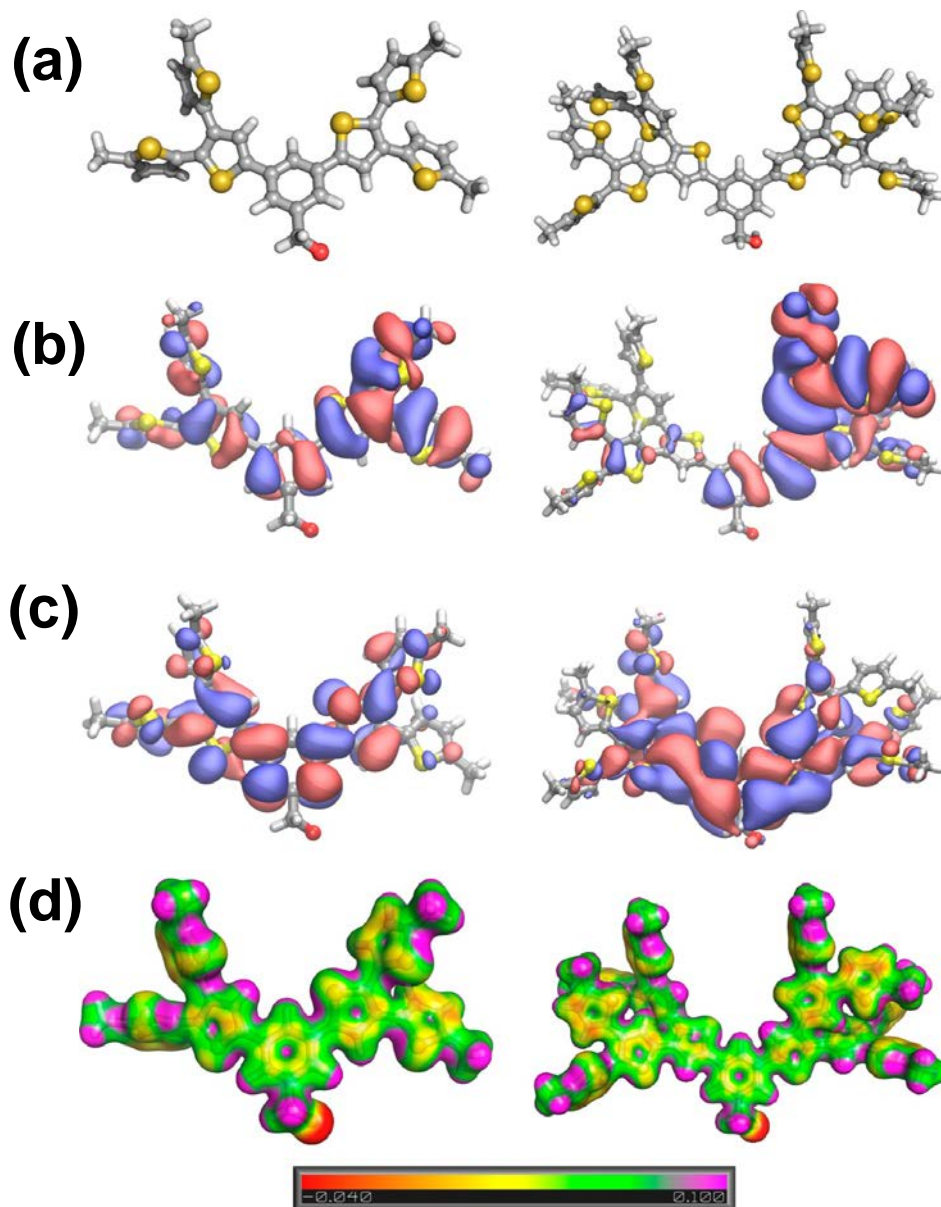
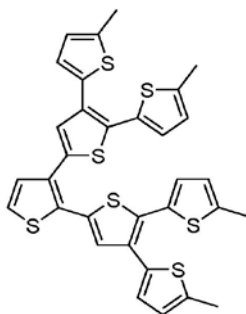


Figure 7.12. (a) Molecular representation, (b) HOMO, (c) LUMO and (d) electron density of the MG2-1 (left) and MG3-1 (right) structures.



Scheme 7.4. Chemical structure of the dendron (7Th) used to construct MG3

in MG2, as is evidenced by the standard deviations of the corresponding averages. In spite of this, it is worth noting that the disposition of the peripheral Th rings is similar for MG2 and MG3, the dihedrals $\{\phi, \phi'\}$ of the minima identified for each macromonomer differing in $\sim 10^\circ$ only.

The ϵ_g values derived for MG3-1 from TD-DFT calculations at the PB0/6-311+G(d,p) and B3LYP/6-311+G(d,p) levels are 3.50 and 3.31 eV, respectively, which represents a slight reduction with respect to MG2-1. This is fully consistent with the ϵ_g values experimentally determined for MG2 and MG3, which reflected a reduction of 0.35 eV [98]. The HOMO extends over two dendrons located of the same branch (Figure 7.12b), which represents a difference with respect to MG2-1. This provokes a slight reduction in the predicted IP values, which are 5.62 and 5.42 eV at the PB0/6-311+G(d,p) and B3LYP/6-311+G(d,p) levels, respectively. In contrast, the delocalization of the LUMO (Figure 7.12c) is similar to that observed for MG2-1. As occurred for MG2, the electron density is homogeneously distributed through the whole molecule (Figure 7.12d).

7.2.3.2. PG2 AND PG3 DPs: STRUCTURAL CHARACTERIZATION

The conformational search strategy explained in the Methods section was applied to PG2 and PG3 chains made of $N = 150$ repeat units. Figure 7.13 represents a complete view of the final atomistic conformations obtained for PG2 and PG3 at the end of the

Table 7.6. Representative Minimum Energy Conformations Calculated for MG3 at the wB97X-D/6-311++G(d,p) Level. Dihedral Angles (θ, θ', ϕ and ϕ' ; in degrees), Bond Lengths ($R_{\alpha\alpha}$ and $R_{\alpha\beta}$; in Å) and Relative Energy (ΔE ; in kcal/mol) are Displayed.

#	θ	θ'	ϕ	ϕ'	$R_{\alpha\alpha}$	$R_{\alpha\beta}$	ΔE
MG3-1	148.8	31.5	110.1 \pm 4.4	148.7 \pm 8.3	1.463 \pm 0.002	1.465 \pm 0.001	0.0
MG3-2	33.6	33.7	110.9 \pm 5.1	149.0 \pm 7.6	1.463 \pm 0.002	1.464 \pm 0.001	0.0
MG3-3	34.6 ^o	-146.7	111.9 \pm 4.1	147.5 \pm 8.4	1.463 \pm 0.002	1.464 \pm 0.001	0.2

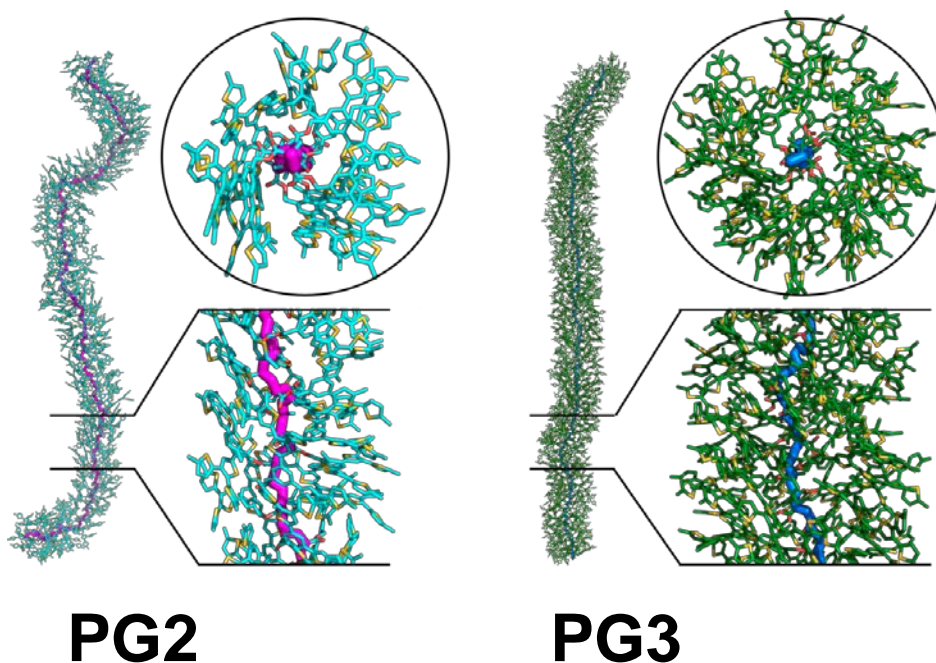


Figure 7.13. Atomistic conformations for PG2 (left) and PG3 (right). The complete axial projections represent the whole calculated systems, the number of repeat units being $N=150$. The magnified axial projection involves 20 repeat units in all cases, whereas the equatorial projection involves 10 repeat units.

MD production phase as well as details on both the backbone conformation and the inter-dendron interactions.

Table 7.7 displays the values of the average end-to-end distance, L_{av} , and the radius, R , derived from MD simulations for PG2 and PG3. As it can be seen, the chain length of the two DPs differs in ~ 100 Å, even though the same number of repeat units was considered in both cases. This should be attributed to the backbone flexibility, which is significantly higher for PG2 than for PG3. As the interpenetration of dendrons belonging to different repeat units is practically null in PG2, the backbone undergoes some irregularities (*e.g.* kinks and folds) (Figure 7.13, left) provoking a reduction of the molecular length. Thus, the conformational behavior of PG2 resembles to that of conventional linear flexible polymers bearing bulk pendant groups. In contrast, the interpenetration of dendrons belonging to different repeat units is very significant in PG3, which results in a significant degree of backbone stiffness (Figure 7.13, right). Thus, PG3 molecules can be viewed as rigid homogenous cylinders. These differences explain the drastic shortening of the end-to-end distance experienced by PG2 with respect to PG3.

The radius R of each DP was determined considering a proportionality between the radial probability distribution and radial density profiles, $p(r) \propto \rho(r)$, and that the

Table 7.7. Properties and Interactions Calculated by MD Simulations for PG2 and PG3. Regarding to Properties, L_{av} , R and ρ_{av} Refer to the Average End-to-End Distance, the Radius and the Average Density, respectively. Regarding to Interactions, the Average Number of π - π Stacking Interactions with T-Shaped and Sandwich Configurations in a Polymer Chain made of 150 Repeat Units are supplied.

	L_{av} (Å)	R (Å)	ρ_{av} (g/cm ³)	π - π Stacking T-shaped	π - π Stacking Sandwich
PG2	222±4	12.9±0.1	1.05	101±11	343±13
PG3	323±1	19.5±0.1	0.99	358±20	955±21

density profile, before it approaches zero is approximately constant as for a homogeneous cylinder of yet unspecified radius R . This case satisfies $p(r) \approx 1/r^2$ subject to normalization, $\int_0^r p(r)dr^2 = 1$, with $dr^2 = 2rdr$, and thus

$$\langle r^2 \rangle^{1/2} = \frac{R^{(1)}}{\sqrt{2}} \approx 0.71 \times R \quad (7.3)$$

As it was expected, R increases with increasing g . Thus, the thickness is 6.6 Å larger for PG3 than for PG2.

Figure 7.14a represents the variation of the density as function of radial distance r from the macromolecular backbone (MB) for PG2 and PG3, obtained by averaging over different cylindrical cross-sections of these macromolecules, while the average values of the density (ρ_{av}) are listed in Table 7.7. It is worth noting that the density profiles reflect all the effects associated with the influence of g on the spatial distribution of the atoms (e.g. changes in backbone conformation). Figure 7.14a indicates that for PG2 the highest density is localized at the region close to the backbone, reaching a value of ~ 1.6 g/cm³. After this, the density of PG2 fluctuates between 1.4 and 1.1 g/cm³ due to conformational irregularities previously mentioned and, finally, it decreases progressively. For PG3 the density remains relatively constant from the backbone to a distance of approximately 9.9 Å and, after this, decreases slowly until the external layer of the cylinder section is reached. As it can be seen in Table 7.7, ρ_{av} is around 1 g/cm³ for both DPs.

Figure 7.14b depicts the radial probability distribution of the peripheral methyl groups (see Figure 7.9b) as a function of the distance from the MB, $g_{Me-b}(r)$, for the two examined DPs. PG2, whose repeat unit presents two external dendrons, shows a single sharp and wide peak centered at around 12.9 Å, which corresponds to the value of R listed in Table 7.7. The peak observed for PG3, centered at approximately 17.3 Å, is smaller and broader than that observed for PG2. In addition of the position of the peak, which is located at a distance 2.2 Å smaller than R (Table 7.7), the $g_{Me-b}(r)$ profile calculated for PG3 shows inner and outer tails. The inner tail is related with the backfolding or looping phenomenon, which refers to the probability of a peripheral

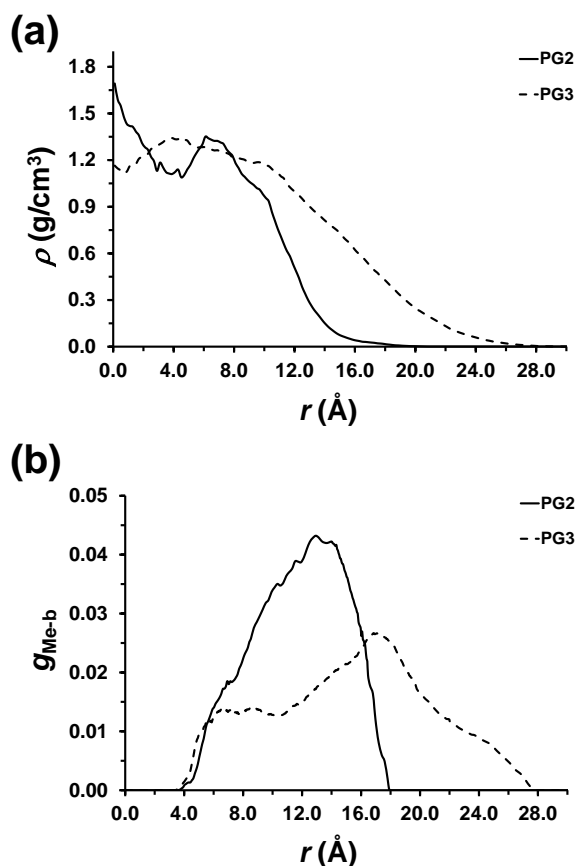
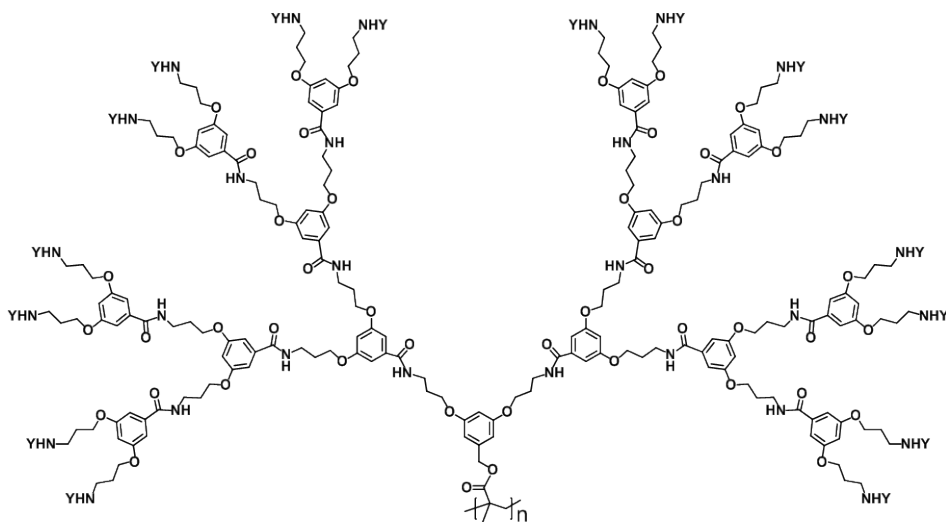


Figure 7.14. (a) Density profile for PG2 and PG3 representing the density (ρ) against the distance to the backbone measured using the vector perpendicular to the helical axis (r). The profile displayed for each DP corresponds to an average considering different cross-sections within a given snapshot. (b) Distribution of peripheral methyl groups (g_{Me-b}) as a function of the distance from the backbone for PG2 and PG3. All data were obtained by averaging over 2500 snapshots taken during the last 20 ns of the MD relaxation runs.

methyl groups to be located at distances lower than $R = 19.5$ Å. For PG3 the broad inner tail indicates that some peripheral methyl groups are very close to the MB (~ 4 Å) and, therefore, evidencing that there must be parts of the same dendron residing at larger radial distances. In contrast, for PG2 the shape of the $g_{Me-b}(r)$ profile indicates that the backfolding is practically null, the wideness of the peak being essentially due to the conformational flexibility of the backbone.

7.2.3.3. $\pi - \pi$ STACKING INTERACTIONS IN PG2 AND PG3

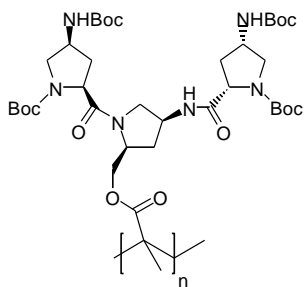
In a recent study we examined intramolecular and intermolecular interactions in DPs composed of a poly(methacrylic acid) backbone and repeat units with regularly branched



Scheme 7.5. Chemical structure of the DP with $g = 4$ studied in reference [89].

dendrons of generation four containing amide and aromatic groups separated by a flexible segment (Scheme 7.5) [90]. After analyze several complexes formed by two interacting macromolecular chains, we concluded that intramolecular interactions are significantly more abundant than the intermolecular ones. Thus, this DP forms rigid cylindrical-like molecules stabilized by intramolecular N–H···O hydrogen bonds and π - π stacking interactions between two aromatic rings arranged in a sandwich or T-shaped configuration, intermolecular interactions being only detected when two molecules interpenetrate considerably. The results supported the scenario put forth in previous structural and rheological studies [73,91], which evidenced the colloidal-filament nature and associated solid-like viscoelastic response in the melt of such DP.

In an earlier study, the helical arrangement identified for the DP obtained from the spontaneous polymerization of a chiral 4-aminoproline-based second generation macromonomer (Scheme 7.6), was found to be stabilized by intramolecular hydrogen



Scheme 7.6. DP studied in references [86,87].

bonding networks that extend along the whole polymer chain [86,87]. Thus, the NH groups of the 4-aminoprolines were found to form this kind of interaction with the amide oxygen atoms of either the neighbor or the same repeat unit, enhancing the stability and stiffness of the right-handed helical conformation.

According to these antecedents, intramolecular interactions are also expected to play a fundamental role in the stability of PG2 and PG3. Based on the molecular details given in Figure 7.9b, the only specific interactions

that may exhibit the two DPs examined in this work correspond to the π - π stacking of Th rings. The presence of these interactions is clearly reflected in Figure 7.15, which represents the partial radial distribution function for pairs of centers of masses of Th rings, $g_{Th-Th}(r)$. The very narrow and sharp peaks at $r = 3.7, 4.1$ and 4.8 Å (see insets) reflect the three inter-ring distances at 3Th units (Scheme 7.3) contained in the side groups of both PG2 and PG3. Some other relatively narrow and sharp peaks are detected for PG2 at $r = 7.3, 8.8$ and 10.9 Å, which also correspond to regular distributions of 3Th units. This is fully consistent with the absence of backfolding in PG2. The shoulder and the small peak centered at 4.4 and 5.2 Å respectively, (marked with arrows in Figure 7.15a), has been attributed to two different types of π - π stacking interactions. More specifically, the shoulder at $r = 4.4$ Å has been attributed to π - π interactions in which the two aromatic rings are coplanar (sandwich configuration) while the two Th rings are perpendicular (T-shaped configuration) in the interaction associated to the peak at $r = 5.2$ Å [117].

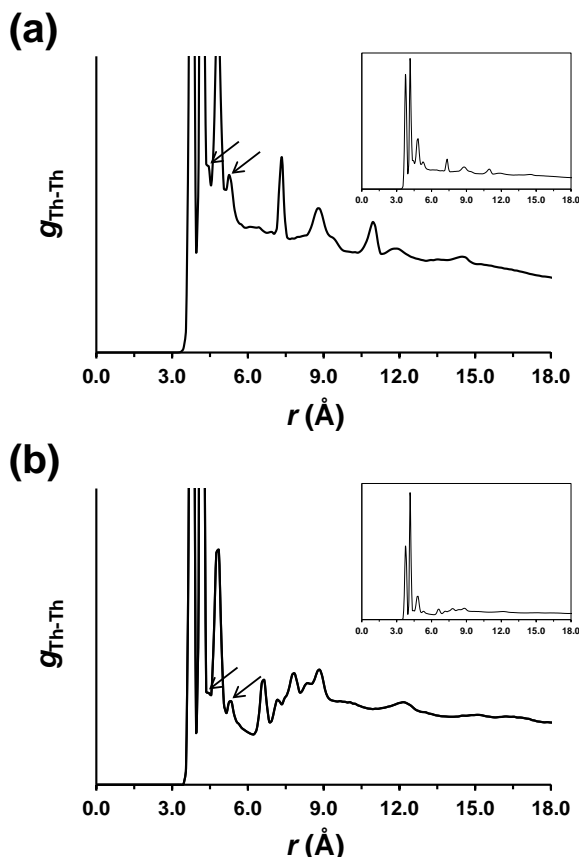
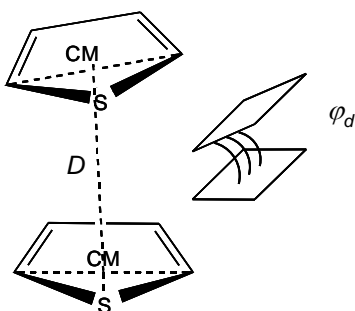


Figure 7.15. Partial radial distribution functions for the pairs of centers of masses of Th rings of (a) PG2 and (b) PG3. Data in were obtained by averaging over 2500 snapshots taken during the last 20 ns of the MD relaxation runs.



Scheme 7.7. Parameters used to define the sandwich and T-shaped configurations

In order to count the number of interactions of each type in PG2, the following cutoffs were considered. For the sandwich configuration the separation between the two Th rings (D in Scheme 7.7) is $\leq 4.5 \text{ \AA}$ and the degree of tilting (φ_d in Scheme 7.7) is $< 45^\circ$ or $> 135^\circ$, whereas for the T-shaped configuration $D \leq 5.5 \text{ \AA}$ and φ_d ranges from 45° to 135° . Results obtained from all the snapshots saved during the production run, which are included in Table 7.7, indicate that the sandwich configuration is 3.4 times more frequent than the T-shaped one in PG2. Accordingly, the average number of π - π interactions per repeat unit of PG2 is 3 (*i.e.* 2.3 and 0.7 participate in sandwich and T-shaped configurations, respectively).

The $g_{Th-Th}(r)$ profile calculated for PG3 show broad peaks at $r = 6.5, 7.8$ and 8.9 \AA (Figure 7.15b), which represents a significant difference with respect to PG2. Thus, the regularity in the position of the Th rings is lost in PG3 due to the backfolding phenomenon discussed above. The shoulder and peak centered at 4.4 and 5.2 \AA (marked with arrows in Figure 7.15b) have been related with π - π stacking interactions, as occurred for PG2. Quantitative analysis indicates that the total number of π - π stacking interactions for PG3 is around three times higher than for PG2 (Table 7.7). Thus, the average number of interactions counted per repeat unit of PG3 is 8.8 (*i.e.* 6.4 and 2.4 participate in sandwich and T-shaped configurations, respectively). According to these values, the relative frequency of the sandwich configuration with respect to the T-shaped one is lower for PG3 (2.7 : 1) than for PG2 (3.4 : 1). This should be attributed to the interpenetration and backfolding phenomena discussed above, which restricts the ability of the dendrons to rearrange and adopt T-shaped configurations.

7.2.4. CONCLUSIONS

The potential energy surface $E = E(\theta, \theta')$ calculated for MG2 reveals that the well-defined conformational preferences of the macromonomers are essentially defined by the relative orientation between the all-thiophene dendrons and the phenyl core. The

disposition of the peripheral Th rings, which is associated to the dihedral angles ϕ and ϕ' , is similar for MG2 and MG3. However, small re-arrangements at these dihedrals allow to alleviate the conformational strain, which increases with g . The calculated electronic properties indicate that both the ϵ_g and the IP decrease with increasing g , which is in good agreement with experimental observations.

Atomistic models of PG2 and PG3, which were constructed using the most favored conformations of MG2 and MG3, evidenced very different internal organizations. PG2 behaves as a flexible linear polymer bearing bulk side group while PG3 is a rigid cylinder. The particular behavior of the latter, which affects the molecular length, is due to both the interpenetration of dendrons belonging to different repeat units and presence of backfolding phenomena. In contrast these effects are practically inexistent for PG2. The different behavior of PG2 and PG3 also affects the radial density profile, which is more uniform for the latter than for former.

Analysis of the inter-dendron interactions in PG2 and PG3 reveals that π - π stacking interactions are significantly more abundant for latter than for the former. This is consistent with the rigidity and backfolding of PG3 and the flexibility of PG2. Deeper analysis show that the interacting Th rings prefer the sandwich configuration with respect to the T-shaped one, this effect being more pronounced for PG2 than PG3.

REFERENCES

- [1] H.E. Katz, L. Torsi, A. Dodabalapur; *Synthesis, material properties, and transistor performance of highly pure thiophene oligomers*; Chem Mater **7**, 2238 (1995).
- [2] W.J. Li, H.E. Katz, A.J. Lovinger, J.G. Laquindanum; *Field-effect transistors based on thiophene hexamer analogues with diminished electron donor strength*; Chem Mater **11**, 458 (1999).
- [3] Z.N. Bao, A.J. Lovinger; *Soluble regioregular polythiophene derivatives as semiconducting materials for field-effect transistors*; Chem Mater **11**, 2607 (1999).
- [4] L. Torsi, A. Dodabalapur, L.J. Rothberg, A.W.P. Fung, H.E. Katz; *Intrinsic transport properties and performance limits of organic field-effect transistors*; Science **272**, 1462 (1996).
- [5] H. Sirringhaus, P.J. Brown, R.H. Friend, M.M. Nielsen, K. Bechgaard, B.M.W. Langeveld-Voss, A.J.H. Spiering, R.A.J. Janssen, E.W. Meijer, P. Herwig, D.M. de Leeuw; *Two-dimensional charge transport in self-organized, high-mobility conjugated polymers*; Nature **401**, 685 (1999).
- [6] J.S. Moore; *Shape-persistent molecular architectures of nanoscale dimension*; Accounts Chem Res **30**, 402 (1997).
- [7] C. Devadoss, P. Bharathi, J.S. Moore; *Energy transfer in dendritic macromolecules: Molecular size effects and the role of an energy gradient*; J Am Chem Soc **118**, 9635 (1996).
- [8] S.K. Deb, T.M. Maddux, L.P. Yu; *A simple orthogonal approach to poly(phenylenevinylene) dendrimers*; J Am Chem Soc **119**, 9079 (1997).
- [9] H. Meier, M. Lehmann; *Stilbenoid dendrimers*; Angew Chem Int Edit **37**, 643 (1998).
- [10] A.J. Berresheim, M. Muller, K. Mullen; *Polyphenylene nanostructures*; Chem Rev **99**, 1747 (1999).
- [11] C.J. Xia, X.W. Fan, J. Locklin, R.C. Advincula; *A first synthesis of thiophene dendrimers*; Org Lett **4**, 2067 (2002).
- [12] C.J. Xia, X.W. Fan, J. Locklin, R.C. Advincula, A. Gies, W. Nonidez; *Characterization, supramolecular assembly, and nanostructures of thiophene dendrimers*; J Am Chem Soc **126**, 8735 (2004).
- [13] J. Locklin, D. Patton, S.X. Deng, A. Baba, M. Millan, R.C. Advincula; *Conjugated oligothiophene-dendron-capped CdSe nanoparticles: Synthesis and energy transfer*; Chem Mater **16**, 5187 (2004).
- [14] F. Geiger, M. Stoldt, H. Schweizer, P. Bauerle, E. Umbach; *Electroluminescence from oligothiophene-based light-emitting devices*; Adv Mater **5**, 922 (1993).
- [15] G. Yu, H. Nishino, A.J. Heeger, T.A. Chen, R.D. Rieke; *Enhanced electroluminescence from semiconducting polymer blends*; Synthetic Met **72**, 249 (1995).
- [16] M.R. Andersson, M. Berggren, O. Inganäs, G. Gustafsson, J.C. Gustafssoncarlberg, D. Selse, T. Hjertberg, O. Wennerstrom; *Electroluminescence from substituted poly(thiophenes) - from blue to near-infrared*; Macromolecules **28**, 7525 (1995).
- [17] R.H. Friend, R.W. Gymer, A.B. Holmes, J.H. Burroughes, R.N. Marks, C. Taliani, D.D.C. Bradley, D.A. Dos Santos, J.L. Bredas, M. Logdlund, W.R. Salaneck; *Electroluminescence in conjugated polymers*; Nature **397**, 121 (1999).
- [18] H.E. Katz, L. Torsi, A. Dodabalapur; *Synthesis, material properties, and transistor performance of highly pure thiophene oligomers*; Chem Mater **7**, 2235 (1995).

- [19] A.J. Lovinger, L.J. Rothberg; *Electrically active organic and polymeric materials for thin-film-transistor technologies*; J Mater Res **11**, 1581 (1996).
- [20] J.H. Schon, A. Dodabalapur, Z. Bao, C. Kloc, O. Schenker, B. Batlogg; *Gate-induced superconductivity in a solution-processed organic polymer film (Retracted article. See vol 422 pg 92 2003)*; Nature **410**, 189 (2001).
- [21] C.Q. Ma, M. Fonrodona, M.C. Schikora, M.M. Wienk, R.A.J. Janssen, P. Bauerle; *Solution-processed bulk-heterojunction solar cells based on monodisperse dendritic oligothiophenes*; Adv Funct Mater **18**, 3323 (2008).
- [22] C.Q. Ma, E. Mena-Osteritz, T. Debaerdemaeker, M.M. Wienk, R.A.J. Janssen, P. Bauerle; *Functionalized 3D oligothiophene dendrons and dendrimers - Novel macromolecules for organic electronics*; Angew Chem Int Edit **46**, 1679 (2007).
- [23] M.R. Harpham, O. Suzer, C.Q. Ma, P. Bauerle, T. Goodson; *Thiophene dendrimers as entangled photon sensor materials*; J Am Chem Soc **131**, 973 (2009).
- [24] G. Ramakrishna, A. Bhaskar, P. Bauerle, C.Q. Ma, T.G. Goodson; *Oligothiophene dendrimers as new building blocks for optical applications*; J Phys Chem A **112**, 6235 (2008).
- [25] F. Rodriguez-Roperro, D. Zanuy, C. Aleman; *Electronic characterization of all-thiophene conducting dendrimers: Molecules and assemblies*; Polymer **51**, 308 (2010).
- [26] M.J. Frisch, G.W. Trucks, H.B. Schlegel, G.E. Scuseria, M.A. Robb, J.R. Cheeseman, G. Scalmani, V. Barone, B. Mennucci, G.A. Petersson, H. Nakatsuji, M. Caricato, X. Li, H.P. Hratchian, A.F. Izmaylov, J. Bloino, G. Zheng, J.L. Sonnenberg, M. Hada, M. Ehara, K. Toyota, R. Fukuda, J. Hasegawa, M. Ishida, T. Nakajima, Y. Honda, O. Kitao, H. Nakai, T. Vreven, J. Montgomery, J. A., J.E. Peralta, F. Ogliaro, M. Bearpark, J.J. Heyd, E. Brothers, K.N. Kudin, V.N. Staroverov, R. Kobayashi, J. Normand, K. Raghavachari, A. Rendell, J.C. Burant, S.S. Iyengar, J. Tomasi, M. Cossi, N. Rega, J.M. Millam, M. Klene, J.E. Knox, J.B. Cross, V. Bakken, C. Adamo, J. Jaramillo, R. Gomperts, R.E. Stratmann, O. Yazyev, A.J. Austin, R. Cammi, C. Pomelli, J.W. Ochterski, R.L. Martin, K. Morokuma, V.G. Zakrzewski, G.A. Voth, P. Salvador, J.J. Dannenberg, S. Dapprich, A.D. Daniels, Ö. Farkas, J.B. Foresman, J.V. Ortiz, J. Cioslowski, D.J. Fox; *Gaussian*, Gaussian 09, Revision A.1, Gaussian Inc. Wallingford CT, 2009.
- [27] A.D. Becke; *A new mixing of hartree-fock and local density-functional theories*; J Chem Phys **98**, 1372 (1993).
- [28] C.T. Lee, W.T. Yang, R.G. Parr; *Development of the colle-salvetti correlation-energy formula into a functional of the electron-density*; Phys Rev B **37**, 785 (1988).
- [29] P. Harihara, J.A. Pople; *Influence of polarization functions on molecular-orbital hydrogenation energies*; Theor Chim Acta **28**, 213 (1973).
- [30] A.D. Mclean, G.S. Chandler; *Contracted gaussian-basis sets for molecular calculations .1. 2nd row atoms, Z=11-18*; J Chem Phys **72**, 5639 (1980).
- [31] M.J. Frisch, J.A. Pople, J.S. Binkley; *Self-consistent molecular-orbital methods .25. supplementary functions for gaussian-basis sets*; J Chem Phys **80**, 3265 (1984).
- [32] S.S. Zade, M. Bendikov; *From oligomers to polymer: Convergence in the HOMO-LUMO gaps of conjugated oligomers*; Org Lett **8**, 5243 (2006).
- [33] S.S. Zade, M. Bendikov; *Study of hopping transport in long oligothiophenes and oligoselenophenes: Dependence of reorganization energy on chain length*; Chem-Eur J **14**, 6734 (2008).
- [34] U. Salzner, J.B. Lagowski, P.G. Pickup, R.A. Poirier; *Design of low band gap polymers employing density functional theory - Hybrid functionals ameliorate band gap problem*; J Comput Chem **18**, 1943 (1997).
-

- [35] U. Salzner, J.B. Lagowski, P.G. Pickup, R.A. Poirier; *Comparison of geometries and electronic structures of polyacetylene, polyborole, polycyclopentadiene, polypyrrole, polyfuran, polysilole, polyphosphole, polythiophene, polyselenophene and polytelluropene*; Synthetic Met **96**, 177 (1998).
- [36] C. Aleman, J. Torras, J. Casanovas; *Influence of polarity of the medium in the saturation of the electronic properties for pi-conjugated oligothiophenes*; Chem Phys Lett **511**, 283 (2011).
- [37] T. Koopmans; *The classification of wave functions and eigen-values to the single electrons of an atom*; Physica **1**, 104 (1934).
- [38] J.F. Janak; *Proof that delta-e-delta-Ni=epsilon-i in density-functional theory*; Phys Rev B **18**, 7165 (1978).
- [39] R.M. Dreizler, J. da Providência, N.A.T.O.S.A. Division; *Density Functional methods in physics*, Springer Dordrecht, 1985.
- [40] M. Levy, A. Nagy; *Excited-state Koopmans theorem for ensembles*; Phys Rev A **59**, 1687 (1999).
- [41] D. Jacquemin, J. Preat, E.A. Perpète, C. Adamo; *Absorption spectra of recently synthesised organic dyes: A TD-DFT study*; Int J Quantum Chem **110**, 2121 (2010).
- [42] J. Preat, D. Jacquemin, E.A. Perpète; *A UV/VIS spectra investigation of ph-sensitive dyes using time-dependent density functional theory*; Int J Quantum Chem **110**, 2147 (2010).
- [43] D. Jacquemin, E.A. Perpète, I. Ciofini, C. Adamo; *On the TD-DFT UV/vis spectra accuracy: the azoalkanes*; Theor Chem Acc **120**, 405 (2008).
- [44] C. Aleman, L. Julia; *Characterization of the quinoid structure for the 2,2'-bithiophene and 2,2',5',2''-terthiophene dications*; J Phys Chem-Us **100**, 14661 (1996).
- [45] C. Aleman; *Spatial extension of the bipolaronic defect in highly conducting polymers based on five-membered aromatic rings*; Macromol Theor Simul **6**, 237 (1997).
- [46] J. Casanovas, C. Aleman; *Comparative theoretical study of heterocyclic conducting oligomers: Neutral and oxidized forms*; J Phys Chem C **111**, 4823 (2007).
- [47] M. Dierksen, S. Grimme; *The vibronic structure of electronic absorption spectra of large molecules: A time-dependent density functional study on the influence of "Exact" Hartree-Fock exchange*; J Phys Chem A **108**, 10225 (2004).
- [48] D. Jacquemin, V. Wathelet, E.A. Perpète, C. Adamo; *Extensive TD-DFT benchmark: singlet-excited states of organic molecules*; J Chem Theory Comput **5**, 2420 (2009).
- [49] O. Bertran, J. Torras, C. Aleman; *Modeling the structural and electronic properties of an optically active regioregular polythiophene*; J Phys Chem C **114**, 11074 (2010).
- [50] O. Bertran, E. Armelin, F. Estrany, A. Gomes, J. Torras, C. Aleman; *Poly(2-thiophen-3-yl-malonic acid), a polythiophene with two carboxylic acids per repeating unit*; J Phys Chem B **114**, 6281 (2010).
- [51] G.R. Newkome, C. Shreiner; *Dendrimers derived from 1 -> 3 branching motifs*; Chem Rev **110**, 6338 (2010).
- [52] M. Ballauff, C.N. Likos; *Dendrimers in solution: Insight from theory and simulation*; Angew Chem Int Edit **43**, 2998 (2004).
- [53] P.K. Maiti, T. Cagin, G.F. Wang, W.A. Goddard; *Structure of PAMAM dendrimers: Generations 1 through 11*; Macromolecules **37**, 6236 (2004).
- [54] Y. Liu, C.Y. Chen, H.L. Chen, K.L. Hong, C.Y. Shew, X. Li, L. Liu, Y.B. Melnichenko, G.S. Smith, K.W. Herwig, L. Porcar, W.R. Chen; *Electrostatic swelling and conformational variation observed in high-generation polyelectrolyte dendrimers*; J Phys Chem Lett **1**, 2020 (2010).
- [55] X.F. Li, T. Imae, D. Leisner, M.A. Lopez-Quintela; *Lamellar structures of anionic poly(amido amine) dendrimers with oppositely charged didodecyltrimethylammonium bromide*; J Phys Chem B **106**, 12170 (2002).

- [56] R. Mezzenga, J. Ruokolainen, N. Canilho, E. Kasemi, D.A. Schluter, W.B. Lee, G.H. Fredrickson; *Frustrated self-assembly of dendron and dendrimer-based supramolecular liquid crystals*; *Soft Matter* **5**, 92 (2009).
- [57] Y.Y. Lu, T.F. Shi, L.J. An, L.P. Jin, Z.G. Wang; *A simple model for the anomalous intrinsic viscosity of dendrimers*; *Soft Matter* **6**, 2619 (2010).
- [58] T.H. Mourey, S.R. Turner, M. Rubinstein, J.M.J. Frechet, C.J. Hawker, K.L. Wooley; *Unique behavior of dendritic macromolecules - Intrinsic-viscosity of polyether dendrimers*; *Macromolecules* **25**, 2401 (1992).
- [59] D. Astruc, E. Boisselier, C. Ornelas; *Dendrimers designed for functions: from physical, photophysical, and supramolecular properties to applications in sensing, catalysis, molecular electronics, photonics, and nanomedicine*; *Chem Rev* **110**, 1857 (2010).
- [60] G.R. Newkome, C.N. Moorefield, F. Vögtle; *Dendrimers and dendrons: concepts, syntheses, applications*, Wiley-VCH, 2001.
- [61] A.M. Caminade, C.O. Turrin; *Dendrimers for drug delivery*; *J Mater Chem B* **2**, 4055 (2014).
- [62] G.M. Soliman, A. Sharma, D. Maysinger, A. Kakkar; *Dendrimers and miktoarm polymers based multivalent nanocarriers for efficient and targeted drug delivery*; *Chem Commun* **47**, 9572 (2011).
- [63] N.K. Voulgarakis, K.O. Rasmussen, P.M. Welch; *Dendrimers as synthetic gene vectors: Cell membrane attachment*; *J Chem Phys* **130** (2009).
- [64] H.M. Liu, Y. Wang, M.M. Wang, J.R. Xiao, Y.Y. Cheng; *Fluorinated poly(propyleneimine) dendrimers as gene vectors*; *Biomaterials* **35**, 5407 (2014).
- [65] L. Ropartz, R.E. Morris, D.F. Foster, D.J. Cole-Hamilton; *Increased selectivity in hydroformylation reactions using dendrimer based catalysts; a positive dendrimer effect*; *Chem Commun*, 361 (2001).
- [66] E. Karakhanov, A. Maximov, Y. Kardasheva, V. Semernina, A. Zolotukhina, A. Ivanov, G. Abbott, E. Rosenberg, V. Vinokurov; *Pd nanoparticles in dendrimers immobilized on silica-polyamine composites as catalysts for selective hydrogenation*; *Acs Appl Mater Inter* **6**, 8807 (2014).
- [67] J.Y. Li, Q. Li, D. Liu; *Novel thieno-[3,4-b]-pyrazines cored dendrimers with carbazole dendrons: design, synthesis, and application in solution-processed red organic light-emitting diodes*; *Acs Appl Mater Inter* **3**, 2099 (2011).
- [68] J.Y. Li, T. Zhang, Y.J. Liang, R.X. Yang; *Solution-processible carbazole dendrimers as host materials for highly efficient phosphorescent organic light-emitting diodes*; *Adv Funct Mater* **23**, 619 (2013).
- [69] A.D. Schlüter, J.P. Rabe; *Dendronized polymers: synthesis, characterization, assembly at interfaces, and manipulation*; *Angew Chem Int Edit* **39**, 864 (2000).
- [70] B.M. Rosen, C.J. Wilson, D.A. Wilson, M. Peterca, M.R. Imam, V. Percec; *Dendron-mediated self-assembly, disassembly, and self-organization of complex systems*; *Chem Rev* **109**, 6275 (2009).
- [71] Y.F. Guo, J.D. van Beek, B.Z. Zhang, M. Colussi, P. Walde, A. Zhang, M. Kroger, A. Halperin, A.D. Schluter; *Tuning polymer thickness: synthesis and scaling theory of homologous series of dendronized polymers*; *J Am Chem Soc* **131**, 11841 (2009).
- [72] B.Z. Zhang, R. Wepf, K. Fischer, M. Schmidt, S. Besse, P. Lindner, B.T. King, R. Sigel, P. Schurtenberger, Y. Talmon, Y. Ding, M. Kroger, A. Halperin, A.D. Schluter; *The largest synthetic structure with molecular precision: towards a molecular object*; *Angew Chem Int Edit* **50**, 737 (2011).
- [73] A. Kroeger, B.Z. Zhang, C. Rosenauer, A.D. Schluter, G. Wegner; *Solvent induced phenomena in a dendronized linear polymer*; *Colloid Polym Sci* **291**, 2879 (2013).
-

- [74] B.Z. Zhang, R. Wepf, M. Kroger, A. Halperin, A.D. Schluter; *Height and width of adsorbed dendronized polymers: electron and atomic force microscopy of homologous series*; *Macromolecules* **44**, 6785 (2011).
- [75] Z.S. Bo, J.P. Rabe, A.D. Schluter; *A poly(para-phenylene) with hydrophobic and hydrophilic dendrons: Prototype of an amphiphilic cylinder with the potential to segregate lengthwise*; *Angew Chem Int Edit* **38**, 2370 (1999).
- [76] V. Percec, C.H. Ahn, T.K. Bera, G. Ungar, D.J.P. Yeardley; *Coassembly of a hexagonal columnar liquid crystalline superlattice from polymer(s) coated with a three-cylindrical bundle supramolecular dendrimer*; *Chem-Eur J* **5**, 1070 (1999).
- [77] C.O. Liang, B. Helms, C.J. Hawker, J.M.J. Frechet; *Dendronized cyclopolymers with a radial gradient of polarity and their use to catalyze a difficult esterification*; *Chem Commun*, 2524 (2003).
- [78] B.M.J.M. Suijkerbuijk, L.J. Shu, R.J.M.K. Gebbink, A.D. Schluter, G. van Koten; *Single-site catalysts on a cylindrical support beyond nanosize*; *Organometallics* **22**, 4175 (2003).
- [79] Z.N. Bao, K.R. Amundson, A.J. Lovinger; *Poly(phenylenevinylene)s with dendritic side chains: Synthesis, self-ordering, and liquid crystalline properties*; *Macromolecules* **31**, 8647 (1998).
- [80] T. Sato, D.L. Jiang, T. Aida; *A blue-luminescent dendritic rod: Poly(phenyleneethynylene) within a light-harvesting dendritic envelope*; *J Am Chem Soc* **121**, 10658 (1999).
- [81] D. Joester, M. Losson, R. Pugin, H. Heinzelmann, E. Walter, H.P. Merkle, F. Diederich; *Amphiphilic dendrimers: Novel self-assembling vectors for efficient gene delivery*; *Angew Chem Int Edit* **42**, 1486 (2003).
- [82] I. Gossli, L.J. Shu, A.D. Schluter, J.P. Rabe; *Molecular structure of single DNA complexes with positively charged dendronized polymers*; *J Am Chem Soc* **124**, 6860 (2002).
- [83] G. Fuhrmann, A. Grotzky, R. Lukic, S. Matoori, P. Luciani, H. Yu, B.Z. Zhang, P. Walde, A.D. Schluter, M.A. Gauthier, J.C. Leroux; *Sustained gastrointestinal activity of dendronized polymer-enzyme conjugates*; *Nat Chem* **5**, 582 (2013).
- [84] A. Grotzky, T. Nauser, H. Erdogan, A.D. Schluter, P. Walde; *A fluorescently labeled dendronized polymer-enzyme conjugate carrying multiple copies of two different types of active enzymes*; *J Am Chem Soc* **134**, 11392 (2012).
- [85] S. Fornera, T.E. Balmer, B. Zhang, A.D. Schluter, P. Walde; *Immobilization of peroxidase on *SiO₂* surfaces with the help of a dendronized polymer and the avidin-biotin system*; *Macromol Biosci* **11**, 1052 (2011).
- [86] A. Zhang, F. Rodriguez-Roperro, D. Zanuy, C. Aleman, E.W. Meijer, A.D. Schluter; *A rigid, chiral, dendronized polymer with a thermally stable, right-handed helical conformation*; *Chem-Eur J* **14**, 6924 (2008).
- [87] F. Rodriguez-Roperro, M. Canales, D. Zanuy, A. Zhang, D. Schluter, C. Aleman; *Helical dendronized polymers with chiral second-generation dendrons: atomistic view and driving forces for structure formation*; *J Phys Chem B* **113**, 14868 (2009).
- [88] O. Bertran, B.Z. Zhang, A.D. Schluter, A. Halperin, M. Kroger, C. Aleman; *Computer simulation of dendronized polymers: organization and characterization at the atomistic level*; *Rsc Adv* **3**, 126 (2013).
- [89] O. Bertran, B. Zhang, A.D. Schlüter, M. Kröger, C. Alemán; *Computer simulation of fifth generation dendronized polymers: impact of charge on internal organization*; *J Phys Chem B* **117**, 6007 (2013).
- [90] E. Cordova-Mateo, O. Bertran, B.Z. Zhang, D. Vlassopoulos, R. Pasquino, A.D. Schluter, M. Kroger, C. Aleman; *Interactions in dendronized polymers: intramolecular dominates intermolecular*; *Soft Matter* **10**, 1032 (2014).

- [91] R. Pasquino, B. Zhang, R. Sigel, H. Yu, M. Ottiger, O. Bertran, C. Aleman, A.D. Schluter, D. Vlassopoulos; *Linear viscoelastic response of dendronized polymers*; *Macromolecules* **45**, 8813 (2012).
- [92] A. Mishra, C.Q. Ma, P. Bauerle; *Functional oligothiophenes: molecular design for multidimensional nanoarchitectures and their applications*; *Chem Rev* **109**, 1141 (2009).
- [93] W.J. Mitchell, N. Kopidakis, G. Rumbles, D.S. Ginley, S.E. Shaheen; *The synthesis and properties of solution processable phenyl cored thiophene dendrimers*; *J Mater Chem* **15**, 4518 (2005).
- [94] W.W.H. Wong, C.Q. Ma, W. Pisula, C. Yan, X.L. Feng, D.J. Jones, K. Mullen, R.A.J. Janssen, P. Bauerle, A.B. Holmes; *Self-assembling thiophene dendrimers with a hexa-peri-hexabenzocoronene core-synthesis, characterization and performance in bulk heterojunction solar cells*; *Chem Mater* **22**, 457 (2010).
- [95] S.X. Deng, T.M. Fulghum, G. Krueger, D. Patton, J.Y. Park, R.C. Advincula; *Hybrid gold-nanoparticle-cored conjugated thiophene dendrimers: synthesis, characterization, and energy-transfer studies*; *Chem-Eur J* **17**, 8929 (2011).
- [96] E. Cordova-Mateo, F. Rodriguez-Ropero, O. Bertran, C. Aleman; *Properties of oligothiophene dendrimers as a function of molecular architecture and generation number*; *Chemphyschem* **13**, 1354 (2012).
- [97] E. Badaeva, M.R. Harpham, R. Guda, O. Suzer, C.Q. Ma, P. Bauerle, T. Goodson, S. Tretiak; *Excited-state structure of oligothiophene dendrimers computational and experimental study*; *J Phys Chem B* **114**, 15808 (2010).
- [98] P. Sonar, H. Benmansour, T. Geiger, A.D. Schlüter; *Thiophene-based dendronized macromonomers and polymers*; *Polymer* **48**, 4996 (2007).
- [99] M. Kimura, A. Kitao, T. Fukawa, H. Shirai; *Rodlike macromolecules through spatial overlapping of thiophene dendrons*; *Chem-Eur J* **17**, 6821 (2011).
- [100] G.B. Griffin, P.M. Lundin, B.S. Rolczynski, A. Linkin, R.D. McGillicuddy, Z.A. Bao, G.S. Engel; *Ultrafast energy transfer from rigid, branched side-chains into a conjugated, alternating copolymer*; *J Chem Phys* **140** (2014).
- [101] J.D. Chai, M. Head-Gordon; *Long-range corrected hybrid density functionals with damped atom-atom dispersion corrections*; *Phys Chem Chem Phys* **10**, 6615 (2008).
- [102] E. Runge, E.K.U. Gross; *Density-functional theory for time-dependent systems*; *Phys Rev Lett* **52**, 997 (1984).
- [103] A.D. Laurent, D. Jacquemin; *TD-DFT benchmarks: A review*; *Int J Quantum Chem* **113**, 2019 (2013).
- [104] C. Adamo, D. Jacquemin; *The calculations of excited-state properties with Time-Dependent Density Functional Theory*; *Chem Soc Rev* **42**, 845 (2013).
- [105] J.P. Perdew, M. Emzerhof, K. Burke; *Rationale for mixing exact exchange with density functional approximations*; *J Chem Phys* **105**, 9982 (1996).
- [106] C. Adamo, V. Barone; *Toward reliable density functional methods without adjustable parameters: The PBE0 model*; *J Chem Phys* **110**, 6158 (1999).
- [107] J. Torras, J. Casanovas, C. Aleman; *Reviewing extrapolation procedures of the electronic properties on the pi-conjugated polymer limit*; *J Phys Chem A* **116**, 7571 (2012).
- [108] D. Jacquemin, E.A. Perpete, I. Ciofini, C. Adamo; *Accurate simulation of optical properties in dyes*; *Accounts Chem Res* **42**, 326 (2009).
- [109] U.C. Singh, P.A. Kollman; *An approach to computing electrostatic charges for molecules*; *J Comput Chem* **5**, 129 (1984).
- [110] B.H. Besler, K.M. Merz, P.A. Kollman; *Atomic charges derived from semiempirical methods*; *J Comput Chem* **11**, 431 (1990).
-

-
- [111] J.C. Phillips, R. Braun, W. Wang, J. Gumbart, E. Tajkhorshid, E. Villa, C. Chipot, R.D. Skeel, L. Kale, K. Schulten; *Scalable molecular dynamics with NAMD*; J Comput Chem **26**, 1781 (2005).
- [112] W.D. Cornell, P. Cieplak, C.I. Bayly, I.R. Gould, K.M. Merz, D.M. Ferguson, D.C. Spellmeyer, T. Fox, J.W. Caldwell, P.A. Kollman; *A 2nd generation force-field for the simulation of proteins, nucleic-acids, and organic-molecules*; J Am Chem Soc **117**, 5179 (1995).
- [113] J.M. Wang, R.M. Wolf, J.W. Caldwell, P.A. Kollman, D.A. Case; *Development and testing of a general amber force field*; J Comput Chem **25**, 1157 (2004).
- [114] P. Cieplak, W.D. Cornell, C. Bayly, P.A. Kollman; *Application of the multimolecule and multiconformational resp methodology to biopolymers - charge derivation for DNA, RNA, and proteins*; J Comput Chem **16**, 1357 (1995).
- [115] J.P. Ryckaert, G. Ciccotti, H.J.C. Berendsen; *Numerical-integration of cartesian equations of motion of a system with constraints - molecular-dynamics of n-alkanes*; J Comput Phys **23**, 327 (1977).
- [116] H.J.C. Berendsen, J.P.M. Postma, W.F. Vangunsteren, A. Dinola, J.R. Haak; *Molecular-dynamics with coupling to an external bath*; J Chem Phys **81**, 3684 (1984).
- [117] F. Rodriguez-Ropero, D. Zanuy, J. Casanovas, R. Nussinov, C. Aleman; *Application of 1-aminocyclohexane carboxylic acid to protein nanostructure computer design*; J Chem Inf Model **48**, 333 (2008).

CHAPTER 8

FINAL DISCUSSION AND CONCLUSIONS

If all scientific knowledge were lost in a cataclysm, what single statement would preserve the most information for the next generation of creatures? How would we best pass on our understanding of the world? [I might propose:] “All things are made of atoms –little particles than move around in perpetual motion, attracting each other when they are a little distance apart, but repelling upon being squeezed into one other.” In that one sentence, you will see there is an enormous amount of information about the world, if just a little imagination and thinking are applied.’

Richard P. Feynman, *The Atom in the History of Human Thought* (1998)

CHAPTER 8

FINAL DISCUSSION AND CONCLUSIONS

8.1. FINAL DISCUSSION

The *leitmotif* of the present Thesis is visibly summarized in its title, *Application of Computer Simulation Approaches to Study the Structure and Properties of Polymeric Systems*. Computational chemistry consists on the application of different theoretical models to analyze and predict the behavior of complex molecular systems, as clearly has been corroborated throughout the last four Chapters. Basically, the studies at the atomic and molecular level of the polymeric systems examined in this dissertation show computer simulation approaches as powerful tools to elucidate both structural features and physicochemical properties at the nanoscopic level. Results presented in this Thesis can be divided mainly in three main research lines, each one involving a different class of polymeric systems and linked to experimental projects developed either within the IMEM group or in collaboration with other groups:

- Conducting Polymers
- Polymeric Cation Exchange Membranes
- Dendritic Polymers: Dendrimers and Dendronized Polymers

Having reached this point, the reader might ask himself, which is the main motivation for the investigation of these subjects? Possibly, the motivation of all the studies presented in this Thesis is easy to envisage after reading the abstract and the introductory section of this dissertation. Basically, it could be summed up by the attempt to contribute to the nanotechnological scientific branch through the inspection of physicochemical properties of innovative polymeric systems with the aim of providing new information for future applications in the design of nanodevices.

On the other hand, which is the common thread of the three different working lines of this Thesis? This question must be answered in the sense that all the polymeric systems investigated in my PhD Thesis present structural and/or electronic properties that allow them to be considered as good candidates for the fabrication of charge transport devices. Moreover, the specific features of all these materials induce great sensing abilities through non-bonded interactions. For this reason some of the key points analyzed and studied for some of these materials throughout this Thesis have been their main electronic properties (*e.g.* lowest π - π^* transition energy and ionization potential), the ability to form secondary interactions (*i.e.* weak and strong hydrogen bonds, π -stacking interactions), the dipole moments and their ability to diffuse charged species. It is worth noting that both the facility to either transport charged species and to recognize external molecules through the formation of specific interaction are strongly related with the structural and chemical architecture of our systems. For this reason, accurate survey of the structural features associated to these polymeric systems is required too. Furthermore, exhaustive conformational analyses considering numerous starting arrangements have been required to obtain suitable stable structures that have been used to initiate the production simulations. These preliminary conformational analyses, which are barely reflected in the articles derived from this Thesis, were crucial for the successful development of all the investigations.

CPs have an extended π -orbital system through which electrons can move almost freely. Within this dissertation both linear and dendritic structures of conducting polymers have been studied with the aim of both provide comprehensive understanding at the microscopic level and gain deeper insight into the intrinsic characteristics of these materials. Certainly, the main motivation for focusing our attention on this promising generation of polymers is the fact that they display many of the desirable properties typically associated with conventional polymers as well as they show electrical and optical properties similar to those of metals and inorganic semiconductors. These traits imply, on the one hand, the possible fabrication of optoelectronic devices based on cheaper and endless resources carbon chemistry and, on the other hand, the development of new biomedical applications using their electroactive properties due to their biocompatibility.

Atomic models derived from quantum mechanical simulations have been performed in the case of linear CPs with the goal of studying their ability to interact and recognize other compounds (*i.e.* morphine and dopamine). The study, on the one side, of the nature of non-bonding interactions (strong hydrogen bonds, C-H \cdots O, π -stacking and/or orbital interactions) between the studied CPs and the recognized species; and on the other side, of the structural rearrangements that take place due to the delocalization of electrons throughout the polymeric main chain; have allowed us to determine the best CP candidates for a nanosensor design based on their affinity towards oxidized dopamine/morphine. Concretely, poly[N-(2-cyanoethyl)pyrrole] showed the strongest affinity towards both molecules (dopamine and morphine) in comparison with other CPs.

In the case of dopamine, the strong electron-withdrawing provoked by the cyano groups located relatively close to the π system induces the reduction of the barrier for electron injection, increase the oxidation potential, and improve the electron-transporting properties. In the study of morphine affinity, the detection based mechanism of poly[N-(2-cyanoethyl)pyrrole] has been found to be completely different. More specifically, energy decomposition analyses showed that the larger charge transfer in morphine...polymer complexes is due to three favorable interactions that takes place because of the higher stability of the single occupied molecular orbital of the polymer.

Dendritic polymers have become a new major class of polymeric architecture due to the unique physical and chemical properties caused by their highly branched topology. Thinking about their singular architecture, highly branched globular dendrimers with a dense inner core based on conducting polymers must present great charge-carrying properties. Effectively, thiophene based dendrimers exhibit large electro-optic response with potential applications in the organic optoelectronic field due to their fully π -conjugated core. Results derived in this dissertation showed that the electronic properties of these systems are closely related to the dendrimer generation number and architecture. Thus, the ionization potential and the lowest π - π^* transition energy values decrease with the inverse of the reciprocal α -conjugated chain of the dendrimer. The lowest π - π^* transition energy predicted for an infinite generation dendrimer is 2.08 eV, which is clearly in the range of semiconducting materials.

It is worth noting that the exponential growth of dendritic branches due to the generation number increase delimits the accessible size of these materials. For this reason, it would be interesting to develop longer dendritic structures with molecular conducting properties. Thiophene-based dendronized polymers have become incredible candidates for this purpose. That is, the use of a polymer as a polyfunctional, polydisperse core and the attachment of polythiophene-based dendrons to the pending functional groups at every repeating unit along the polymeric backbone. The result would be a special case of graft copolymers with conducting properties and cylindrical structures of nanometric thickness. These structures would self-organize into parallel arrays allowing photochemically generated charges to be transported into opposite directions throughout the entire bulk phase. Keeping in mind this perspective, the study of the internal organization of thiophene dendrons is a key point for the resulting dendronized polymer atomic models. Structural analysis of second and third generation of this dendronized polymers evidenced that the interpenetration of dendrons is practically null for second generation polymers while in the case of the third generation it is very high. Consequently, the third generation polymer presents a rigid homogenous cylindrical shape with high degree of charge transport within the same dendron and between different dendron chains. This final assertion is corroborated by the raise of π -stacking interactions between thiophene rings belonging to different dendrons.

Up to here, the systems presented in this discussion shared the feature of possessing important charge-carrying properties, among other powerful structural features, as is the case of thiophene based dendronized polymers. However, due to the synthetic difficulties related with the latter macromolecules, only the second and third generation polymers have been successfully produced. This precludes an exhaustive study for higher generations in the sense of comparing the properties obtained via computational simulations and experimentally. Having gone this far, the study of DPs with a chemical structure not based on CPs but successfully synthesized up to sixth generation, arises as the natural way to continue with the investigation of these unique kind of materials.

The investigation in the field of DPs is fairly new; especially thinking in the publications devoted to the study of these materials in the area of computational chemistry. For this reason the research within this scientific field entails an extra effort in the sense that *creativity* is essential for analyzing the overall data obtained from MD simulations due to the scarce bibliography reported yet. Taking it into account, perhaps the modelling *via* MD of DP systems has become one of the most attractive topics treated in this Thesis.

The second class of DPs showed in this dissertation are composed of a poly(methacrylic acid) backbone and tree-like branches bearing both amide and aromatic groups (PG g). One of the most intriguing features of PG g is their unusual viscoelastic behavior, which is strongly dependent on the generation of the dendron pendants, ranging from liquid-like (PG1) to solid-like behavior (PG4). This evidence was attributed to their elongated conformation and the combination of topological constraints at the whole macromolecular scale as well as the competition of the intra- and intermolecular interactions that take place in aggregates. Thus, with the aim of shed light on this assertion, a characterization of inter- and intramolecular hydrogen bonds and π,π -interactions of two interacting PG4 chains with up to ten arrangements degrees of interpenetration was carried out. Results indicated that intramolecular interactions clearly dominate over intermolecular ones. Moreover, interpenetration was found to have an anisotropic effect on the PG4 (*i.e.* the increase in the molecular length in dimers with the highest interpenetration degree was much more pronounced in comparison with the variation of their cross-sectional radius). These results reinforced the concepts, recently reported through structural and rheological studies, related with the colloidal-filament nature, dense hexagonal packing in solution and associated solid-like viscoelastic response in the melt of PG4.

The peripheral region or surface of DPs plays a key role in their functionalization. That is, the nature of such functional end-groups affects drastically the physical and chemical properties of these organic materials with unusual microscopic behavior. Taking it into account, the next natural step in the inspection of these macromolecules was focused on a comparative study between the PG g and their positively charged analogues from first to

sixth generation. Charged systems (*dePG_g*) were obtained by deprotecting the neutral *PG_g* through the elimination of the blocking Boc groups, which transforms the peripheral amine moieties into ammonium. Furthermore, the simulations were performed in aqueous solution with the aim of not only analyzing the internal structure and the effect of the electrostatic strain in the properties of these highly branched materials but also of understanding their solvent absorption ability. Results showed that, from a structural point of view, elimination of the Boc groups with the subsequent introduction of positive charges does not provoke significant changes but only the appropriated conditions to facilitate the penetration of water. Analysis of the water density indicated that water penetrates inside the structure of all charged DPs. However, the relative degree of penetration decreases with increasing *g* due to the backfolding, which increases with *g*. The molecular dimensions, shape and end-groups functionalization lead us to think in this nanomaterials as densely cylindrical molecular objects with the ability of carrying or immobilizing other compounds *via* long-range electrostatic interactions. This fact was recently evidenced through a fascinating application in the biomedical area, where *dePG1* was used for stabilizing and retaining enzyme activity in the gastrointestinal tract.

The last topic to cover in this discussion refers to ionic transport in cation exchange membranes. Regarding the common thread of this Thesis, computational simulation approaches were applied with the aim of investigating structural rearrangements that take place in a sulfonated P(S-DVB) membrane, as well as the dynamical properties and interaction patterns of charged species crossing it. All these studies were carried out as a function of the electric field strength and using different temperature values.

P(S-DVB) based membranes may be considered; due to their low protonic resistance, good mechanical properties, and high chemical stability; among the best for electro dialysis applications. Consequently, detailed knowledge of the working range of these materials is required before a large-scale commercial production. On the other hand, it is worth noting that many microscopic aspects related with the electric-field-induced transport of ionic species across cation exchange membranes remain still unknown.

Atomistic MD simulations addressed to examine the effect of the electric field and the temperature on both the structure of the P(S-DVB) membrane and the ionic transport showed that hydronium ions follow a diffusive behavior for electric fields ≤ 0.7 V/nm. The diffusion coefficients increase with the electric field. Moreover, these values are systematically higher in the direction of the applied electric field than in the perpendicular directions. Temperature provokes local structural deformations around the sulfonate groups and these distortions affect both the density and porosity of the membranes and become anisotropic upon the application of the external electric field. The dynamical aspects of the interaction between the hydronium ions and the sulfonic acid groups, as well as their interactions with water molecules, have been analyzed and used to discuss,

on the one side, the transport mechanism and, on the other side, the influence of the kinetic energy in comparison with the electric work. Results showed that sulfonate···water interactions are stronger than hydronium···water interactions. This should be attributed to the fact that sulfonate anions tend to be surrounded by three hydronium ions, allowing the formation of a dense attractive network of interactions involving sulfonate anions, hydroniums, and water molecules.

A general overview of all the research work displayed throughout all the previous chapters corroborates the utility of computer simulation approaches to study the structure and properties of novel polymeric systems with powerful applications in nanotechnology. Furthermore, in some cases the investigations presented in this Thesis were thought to support experimental studies while in other ones were designed to shed some light on unknown aspects of the examined materials (*e.g.* transport mechanism of charged species and internal organization of DPs).

8.2. CONCLUSIONS

The main conclusions derived from all the studies presented in this dissertation can be summarized as follows:

CHAPTER 4. DETECTION BASED ON CONDUCTING POLYMERS

- i. Quantum mechanical calculations on CP···DQ and CP···MO complexes evidence that C-H···O interactions play a crucial role in the DA detection process.
- ii. Although PNMPy interacts favorably with DA, the rigidity imposed by the methyl group attached to the N-position of the pyrrole ring affects negatively the neurotransmitter recognition process.
- iii. The flexibility of the cyanoethyl substituent favors the recognition of DA by increasing the strength of the interaction with the polymer length. Thus, the interaction of DA with PNCPy is stronger than with PNMPy, which is consistent with the relative abilities of these two PPy derivatives to detect DA (PNMPy < PNCPy).
- iv. In the recognition of MO participate a number of different interactions, which depend on the chemical nature of the CP and can coexist: C-H···O, π -stacking, N-H···O, O-H···N, C-H···N and charge transfer.
- v. The strength of the examined CP···MO interaction decreases as follows: PNCPy \approx P3MT' \gg PPy > PNMPy > PEDOT.
- vi. The stronger interaction of MO with P3MT' and PNCPy, as compared to the other three studied CPs, is due to the higher stability of their SOMOs, which

favors the transfer of charge from MO to the polymers leading to stronger orbital interactions.

CHAPTER 5. HYDRONIUM TRANSPORT IN CATION EXCHANGE MEMBRANES

- vii. The strength of the electric field affects the transport of hydronium ions in sulfonated P(S-DVB) membranes. The normal diffusive regime is only reached for electric fields ≤ 0.7 V/nm, the diffusion coefficient obtained for the latter electric field being of $62.8 \cdot 10^{-7}$ cm²/s.
- viii. The highest protonic conductivity has been found for an electric field of 0.03 V/nm. This is due to a combination of moderate current density and very low electric field. At higher electric fields, the protonic current density increases too slowly (i.e. for electric fields ≤ 0.7 V/nm) or too rapidly (i.e. electric fields > 0.7 V/nm) resulting in a reduction of the conductivity or in significant structural deformations of the membrane, respectively.
- ix. The membrane undergoes structural changes upon heating, which are essentially localized at the sulfonate groups. The rearrangement of the negatively charged groups is accompanied by a variation of the density and the porosity.
- x. The influence of the temperature in the velocity of the hydronium and water molecules is small in comparison with that exerted by the electric field strength, the latter provoking a remarkable enhancement of the flux.
- xi. The hydration shell of the hydronium ions is not affected by electric fields lower than 1.0 V/nm. In contrast, when the external electric field is higher than 1.0 V/nm, both the size and exchangeability of such hydration shells increase.
- xii. The effect of the temperature in the orientation of water molecules contained in the hydronium hydration shell is negligible while, in opposition, such water molecules reorient upon the application of an external electric field.

CHAPTER 6. ATOMISTIC PROPERTIES OF DENDRONIZED POLYMERS

- xiii. Calculations on interpenetrated complexes of PG4 reveal that the stability and structure of DPs is dominated by intramolecular hydrogen bonds and π - π interactions, which are more frequent than intermolecular interactions.
- xiv. The concentration of intramolecular hydrogen bonds increases when the interpenetration of the two PG4 chains decreases, whereas intramolecular π , π -interactions remain practically insensitive to the amount of interpenetration.
- xv. The strength and frequency of hydrogen bonds and π - π intermolecular interactions decrease very rapidly with interpenetration.
- xvi. The overall of the results obtained for PG4 complexes supports the scenario treating DPs as long colloidal molecules. This behavior has been attributed to the

dominant topological interactions in weakly interpenetrated PG4 rather than to specific intermolecular hydrogen bonds and π,π -stacking interactions.

- xvii. Deprotection of PG g to produce *de*PG g provokes electrostatic strain, which in turn results in small structural re-arrangements that lead to a reduction of the density. Consequently, the elimination of the external Boc groups and the introduction of positive charges facilitate the penetration of water.
- xviii. Water degree penetration in *de*PG g decreases with increasing g . This behavior is due to the increasing backfolding that hinders the progress of water molecules inside the structure. Despite of this, the number of water molecules interacting with *de*PG g increases rapidly with g .

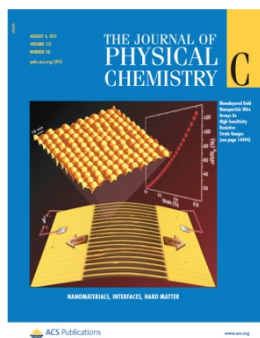
CHAPTER 7. THIOPHENE-BASED DENDRIMERS AND DENDRONIZED POLYMERS

- xix. The conformation of neutral n T dendrimers becomes more elongated and less compact upon oxidation. This feature is due to the rigidity imposed by the quinoid electronic structure of the positively charged molecules.
- xx. The importance of geometry relaxation effects on the IP of n T dendrimers decreases with increasing n . This has been attributed to the dominant role of the electron delocalization contribution, which increases with n .
- xxi. TD-DFT calculations provide ϵ_g estimations that are in very good agreement with values derived from electrochemical and absorption spectroscopy measurements. The correlation of ϵ_g with $1/n$, $1/n_\alpha$ and $1/g$, is relatively poor indicating that the symmetric/asymmetric molecular architecture of n T dendrimers plays a fundamental role in this electronic property.
- xxii. A reliable empiric model to predict the ϵ_g of all-thiophene dendrimers that are inaccessible to quantum mechanical calculations has been developed using the TD-DFT results. The validity of this model has been proven for the 90T system.
- xxiii. MG2 and MG3 macromonomers show well-defined conformational preferences, which are essentially defined by the relative orientation between the all-thiophene dendrons and the phenyl core. Despite of their different generation, the disposition of the peripheral Th rings is similar for MG2 and MG3.
- xxiv. TD-DFT calculations on both MG2 and MG3 reflect that the ϵ_g and the IP decrease with increasing g , which is in good agreement with experimental observations. The electron density is homogeneously distributed through the whole molecule for the two macromonomers.
- xxv. The dendronized polymer derived from MG2 behaves as a flexible linear polymer bearing bulk side group while that obtained by polymerizing MG3 is a rigid cylinder. The particular behavior of the latter, which affects the molecular length, is due to both the interpenetration of dendrons belonging to different

repeat units and presence of backfolding phenomena. Both dendronized polymers are stabilized by π - π stacking interactions.

ANNEX. LIST OF PAPERS

CHAPTER 4. DETECTION BASED ON CONDUCTING POLYMERS



Ultrathin Films of Polypyrrole Derivatives for Dopamine Detection
J Phys Chem C 115, 14933 (2011)



Electroactive polymers for the detection of morphine
J Polym Res 21, 1 (2014)

CHAPTER 5. HYDRONIUM TRANSPORT IN CATION EXCHANGE MEMBRANES



Transport of hydronium ions inside poly(styrene-co-divinyl benzene) cation exchange membranes
J Membrane Sci 428, 393 (2013).



Influence of the Temperature on the Proton Transport in Poly(styrene-co-divinylbenzene) Membranes from Molecular Dynamics Simulations

J Phys Chem C 118, 17643 (2014)

CHAPTER 6. ATOMISTIC PROPERTIES OF DENDRONIZED POLYMERS



Interactions in dendronized polymers: intramolecular dominates intermolecular

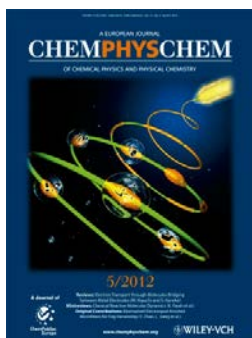
Soft Matter 10, 1032 (2014)



Internal Structure of Charged Dendronized Polymers

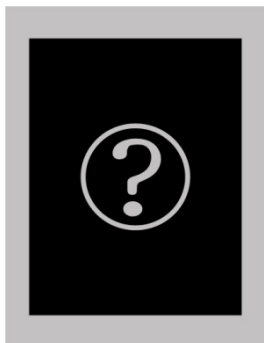
Submitted for publication

CHAPTER 7. THIOPHENE-BASED DENDRIMERS AND DENDRONIZED POLYMERS



Properties of Oligothiophene Dendrimers as a Function of Molecular Architecture and Generation Number

Chemphyschem 13, 1354 (2012)



*Internal Organization of Macromonomers and Dendronized
Polymers based on Thiophene Dendrons*

Submitted for publication

